INVESTIGATING DUAL-TARGETED DOMAIN ANTIBODY FUSION PROTEINS IN A CANCER MODEL

Alex G. Papple

Supervisors
Dr. Jane Sosabowski
Dr. Adam Walker
Prof. Stephen Mather

PhD Thesis

May 2015

ABSTRACT

Developing efficacious, highly specific therapeutics is an ongoing challenge. The domain antibody (dAb) fragment platform has shown promise targeting a dAb-fused therapeutic moiety to a specific tissue. This investigation sought to conclude on the optimum binding affinity combination to maximise tissue-targeting specificity and localised therapeutic potency by using a panel of dAb fusion proteins with varying affinity combinations of asialoglycoprotein receptor (ASGPR)-targeting dAb mutants and human interferon (hIFN) mutants – hIFN-ASGPRdAbs.

The hIFN-ASGPRdAbs were engineered, expressed, 1,4,7-triazacyclononanetriacetic acid (NOTA)-conjugated and purified with binding affinities and potencies characterised. Gallium-68 radiolabelling of the NOTA-hIFN-ASGPRdAbs was optimised using a high activity fraction in a 10 minute reaction at ambient temperature in pH4.4 sodium acetate. HepG2 xenograft mouse models were injected with ^{68}Ga-NOTA-hIFN-dAbs for biodistribution analysis and PET/CT imaging, followed by mRNA expression analysis of the xenograft tissue.

ASGPR binding affinities of the NOTA-hIFN-ASGPRdAbs ranged from 0.73pM to ~528nM, and their hIFN potency ranged from 6.79pM to ~3.87nM. Targeting of HepG2 cells was driven by the dAb-mediated ASGPR targeting. Ga-68 radiolabelling efficiencies up to 98.4% and specific activities up to 2.47MBq/μg were achieved. Xenograft uptake was significantly increased through dAb-mediated ASGPR targeting compared to the non-ASGPR targeted control ^{68}Ga-NOTA-hIFN-CTRLdAb, achieving 2.42%ID/g vs. 0.68%ID/g, respectively. A trend of increasing xenograft uptake correlated with increasing ASGPR binding affinity for the panel of mutants, in spite of very high murine liver uptake. Increased xenograft uptake also correlated with a more potent hIFN-mediated anti-proliferative mRNA response in the xenograft tissue. A dAb with a mid-range affinity for ASGPR and maximum affinity hIFN was concluded to be the optimum combination.

These results showed that the efficacy of a dAb fusion protein can be influenced by the two intrinsic binding affinities. Hence, dAb-mediated tissue targeting of a fused therapeutic and engineered affinity synergism strategies may hold the key to novel, selectively cytotoxic biopharmaceutical drugs.

ACKNOWLEDGEMENTS

This project was jointly funded by Queen Mary University of London, GlaxoSmithKline (GSK) and the EPRSC. I would like to thank them for enabling this project to proceed. The PhD wet work was performed primarily in the Cancer Imaging group of Molecular Oncology at Barts Cancer Institute, Queen Mary University of London with additional *in vitro* work performed during extended stays at GlaxoSmithKline in Cambridge. It has thus involved the efforts of many people at both institutions.

My primary supervisor, Jane Sosabowski, is the respected matriarch of the Cancer Imaging department, rightfully in constant demand for her knowledge and experience. On top of this she had to stoically endure my ramblings and flights of scientific fantasy on a daily basis, and tussle to ground me back in the realms of scientific reality. Jane has thus been instrumental in ensuring I had the scientific competency and understanding necessary to complete this project, keeping the project focussed and spending innumerable hours troubleshooting with me. Stephen Mather, as my supervising professor, has my gratitude and respect for using his wealth of experience and incisive scrutiny of data to always help me find solutions with his sharp intellect always invaluable in making the big project decisions.

As I didn't hold an animal license, I was highly reliant on the skill sets of other *in vivo* specialists. Julie Foster's *in vivo* experience was unrivalled and cheerfully trained me in dissection. Julie performed the majority of the xenograft injections, and aided in a plethora of other techniques but particularly PET/CT where Julie reconstructed images for time course analysis. I owe a debt of gratitude to Julie Andow-Cleaver who went above-and-beyond to accommodate my fluid experimental requirements as early as 7am, and was always willing to help out. Julie performed the majority of *in vivo* handling, injections (HepG2 cells and radioactive), and also helping significantly with performing PET/CT work and a number of dissections. Also, Stella Adamou, without whom the biodistribution work may never have been completed because Stella was always willing to give up her spare time to perform dissections, as well as ensuring I did not lose my sanity in the process. Ciara Finucane for her welcome *in vivo* input, and excellent VivoQuant training. I am further thankful to Julius Leyton and Jerome Burnet who performed some of the initial injections and dissections, and Chantelle Hudson and Roxana Kashani for their help with tissue culture.

I am grateful to all at GSK Targeted BDU (Domantis) who were always happy to discuss experiments and spend their time on demonstrating new techniques.

Adam Walker, as my GSK supervisor, played a crucial role in formulating the best strategy for achieving the project aims and was always constructive in his analysis of my

ideas. Indeed it was easy to trust Adam's judgement, as his knowledge of the liver-targeting dAbs science is unrivalled. Prior to Adam, Elena De Angelis was my GSK supervisor and provided excellent project guidance and intellectual input from the outset. Thil Batuwangala made an inestimable contribution to this project in spite of having absolutely no obligation to do so, selflessly allowing me to adopt him as an unofficial lab mentor. Thil was instrumental in almost all aspects of the *in vitro* work by training me in almost all the techniques performed. Ed Coulstock was a ray of sunshine, fountain of optimism, and more seriously of great intellectual help to this project. Ed also facilitated the majority of the MS data, personally overseeing many of the runs.

Milan Ovecka was an oracle on all matters Biacore, training me on the Biacore T200 and patiently troubleshooting all my glitches. Jayne Colebrook was fantastically proactive with planning and implementation of the TaqMan experiments. Rob Prince taught me how to perform HEK-Blue assays. Laura Goodall happily aided my competency in Flow Cytometry. Katy Childerley graciously performed HEK293e mammalian transfections in my absence and often harvested the cells too. I would also like to acknowledge the lab help and data interpretation input of Marie Davies, Chris Herring, Daniel Badcock, Armin Sepp, Oliver Schon, Joanne McGregor, Dan Rycroft, Chris Plummer, Gavin Jones, Ksenia Rotislavleva, Clare Mudd, Nadine Clemo, Andrew Sanderson, Helen Sanderson, and Gaby Dos Santos Cruz De Matos. My time at GSK ran so much smoother thanks to the help of the lab assistants Clare and Jamie, and the administrative staff Grace, Julie & Caron. Finally, Laurent Jespers for supporting the project since inception.

Discussions with fellow students stimulated new avenues of enquiry and discovery of fresh techniques so I am also grateful to Mark Jackson, Chris Cobb, Constantia Pantelidou, Delphine Guillotin, Michael Walsh, Aine McCarthy, Roxana Koshani, Ana Boshoff, Benedikt Sandhöfer, Marian Meckel and Berit Kühle.

I am infinitely grateful to Camilla Tørnqvist-Johnsen for her unwavering belief and cheerleading throughout, and in spite of the PhD findings will remain my most amazing discovery at the BCI. Moreover, my parents Karen Johnston and Gordon Papple for their continued support of my baffling interests.

TABLE OF CONTENTS

FIGURES & TABLES

Introduction

Methods

HepG2 Xenograft Targeting of 68Ga-NOTA-hIFN-dAb

Optimising HepG2 Xenograft Targeting of hIFN-dAbs

Conclusions & Future Work

Appendices

ABBREVIATIONS

%ID/g	% injected dose per gram
^{177}Lu	lutetium-177
^{124}I	iodine-124
^{18}F	fluorine-18
^{44}Sc	scandium-44
^{44}Ti	titanium-44
^{68}Ga	gallium-68
^{68}Zn	zinc-68
^{89}Zr	zirconium-89
^{82}Rb	rubidium-82
^{90}Y	yttrium-90
^{99m}Tc	technetium-99m
2D	two-dimensional
3D	three-dimensional
AA	amino acid
ADCC	antibody dependent cell mediated cytotoxicity
Alexa647	goat anti-mAb pAb with Alexa647 fluorophore
AM	ammonia-methanol
APD	avalanche photodiodes
ASGP	asialoglycoprotein
ASGPR	asialoglycoprotein receptor
B-FN	fibronectin isoform B
BSA	bovine serum albumin
bsmAb	bi-specific monoclonal antibody
CA	citric acid
CCV	clathrin coated vesicle
cDNA	complementary deoxyribonucleic acid
CDR	complementarity determining region
cgH2O	clinical grade water
CRD	carbohydrate recognition domain
CT	computer tomography
Cu	copper
CV	column volumes
dAb	domain antibody
ddH2O	double deionised water

DMEM	Dulbecco's Modified Eagle Medium
DNA	deoxyribonucleic acid
DOTA	1,4,7,10-tetraazacyclododecanetetraacetic acid
DR	death receptor
ds-RNA	double-stranded ribonucleic acid
DTPA	diethylene triamine pentaacetic acid
DTT	dithiothreitol
EC	electron capture
EDTA	ethylenediaminetetraacetic acid
EEF2	elongation factor 2
EGFR	epithelial growth factor receptor
EMAX	maximum end point energy
EpCam	epithelial cell adhesion molecule
EtOH	ethanol
F-18	fluorine-18
Fab	fragment binding antibody
FACS	fluorescence-activated cell sorting
FBS	fetal bovine serum
FC	flow cell
Fc	fragment crystallisable
FcRn	neonatal Fc receptor
FDA	Food and Drug Administration
FDG	fluorodeoxyglucose
FeIII	ferric iron
FPKM	fragments per kilobase of exon per million fragments mapped
Ga-68	gallium-68
Gal	galactose
Gal-Nac	*N*-acetylgalactosamine
GAPDH	glyceraldehyde-3-phophate
Ge-68	germanium-68
GSK	GlaxoSmithKline
GuHCl	guanidine hydrochloric acid
HAIC	hepatic arterial infusion chemotherapy
HBED	*N*,*N*'-bis(2-hydroxybenzyl)-ethylenediamine-*N*,*N*'-diacetic acid
HCC	hepatocellular carcinoma
HCV	hepatitis C virus
HER2	human epidermal growth factor receptor 2

hIFN	human interferon
HPLC	high pressure liquid chromatography
HSA	human serum albumin
HU	Houndsfield units
ID	injected dose
IFN	interferon
IFNAR	interferon alpha receptor
IFNGR	interferon gamma receptor
IgG	immunoglobulin G
IL-12	interleukin-12
IL-1RA	interleukin-1 receptor antagonist
IL-2	interleukin-2
IMAC	immobilised metal ion affinity chromatography
IRF9	interferon regulatory factor 9
ISG	interferon stimulated gene
ISGF3	interferon stimulated gene factor 3
ISRE	interferon stimulated response element
JAK	Janus kinase
KML	chelator stability constant
L-Trp	L-tryptophan
mAb	monoclonal antibody
MAPK	mitogen activated protein kinase
mASGPR	murine asialoglycoprotein receptor
MCSP	melanoma chondroitin sulphate proteoglycan
MEK	mitogen activate protein kinase/extracellular signal regulated kinase
mIFNAR	murine interferon alpha receptor
MRI	magnetic resonance imaging
mRNA	messenger ribonucleic acid
MWCO	molecular weight cut off
NaAc	sodium acetate
NEB	New England Biolabs
NFκB	nuclear factor kappa-light-chain-enhancer of activated B cells
NHS	*N*-hydroxysuccinimide
NHS-NOTA	2,2'-(7-(2-((2,5-dioxopyrrolidin-1-yl)oxy)-2-oxoethyl)-1,4,7-triazonane-1,4-diyl)diacetic acid
NK	natural killer
NO	nitrous oxide

NOTA	1,4,7-triazacyclononanetriacetic acid
OAS	2',5'-oligoadenylate synthetase
OSEM	ordered subset expectation maximisation
pAb	polyclonal antibody
PBS	phosphate buffered saline
PCR	polymerase chain reaction
PET	positron emission tomography
PI	propidium iodide
PKR	protein kinase R
PMT	photomultiplier tube
PVDF	polyvinylidene fluoride
RHL-1	rat hepatic lectin
RNase	ribonuclease
ROI	region of interest
RT-PCR	reverse transcription polymerase chain reaction
RU	resonance units
scFv	single chain variable fragment
SCID	severe combined immunodeficiency
SCN-Bn-NOTA	S-2-(4-Isothiocyanatobenzyl)-1,4,7-triazacyclononanetriacetic acid
SDM	site directed mutagenesis
SDS-PAGE	sodium dodecyl sulphate polyacrylamide gel electrophoresis
SE-HPLC	size exclusion high pressure liquid chromatography
SOC	optimal broth with catabolite suppression
SOE	Splice Overlap Extension (PCR)
STAT	signal transducers and activators of transcription
TLC	instant thin layer chromatography
TNF	tumour necrosis factor
TRAIL	TNF-related apoptosis inducing ligand
UV	ultraviolet
Vκ	variable kappa
VEGF	vascular endothelial growth factor
V_H	variable heavy
V_{HH}	*Camelidae* heavy chain antibody
V_L	variable light
WEA	Water-Ethanol-Ammonia

I

INTRODUCTION

1.1 THESIS RATIONALE

It is an ongoing challenge to develop therapeutics with not only enhanced efficacy, but also increased specificity, thus ameliorating side effects and toxicity from off target activity. There are many examples of potent molecules, such as cytokines, which are limited in their application as therapeutics due to prohibitively broad toxicity. They could therefore benefit from increased specificity against only diseased tissue. Combining such therapeutics with a targeting moiety designed to selectively interact with a target disease tissue could deliver the attached therapeutic payload to its intended site of action at a localised efficacious concentration, thus reducing non-specific toxicity by decreasing systemic exposure and precluding activating concentrations in off-target tissues. Engineered selective targeting is achievable utilising antibody-derived protein fragments. Therefore it is an attractive prospect to engineer potentially highly selective and efficacious fusion proteins comprised of cytotoxic therapeutics fused with targeted antibody fragments.

One such fusion protein technology is the domain antibody (dAb) fusion protein[1]. The dAb technology is a highly adaptable single polypeptide antibody fragment platform. Their small size (11-15kDa), low-immunogenic fully-humanised scaffold, high stability in physiological conditions and ease of *in vitro* genetic manipulation mean dAbs hold great potential as the targeting moiety of a therapeutic fusion protein. Hence, the development of dAb fusions may be useful in the development of highly efficacious biopharmaceutical drugs for patients, perhaps as one of the initial steps towards personalised medicine.

However, dAb fusions have a potential problem arising from the presence of two competing intrinsic binding affinities. There is a molecular level tussle between the specific tissue targeting of the dAb and the systemic 'off-target' binding (interacting with receptors outside the target tissue) of the fused therapeutic. Conventional wisdom would ordinarily dictate that the highest possible achievable binding affinities are appropriate. However, it may require much more subtlety to create the most optimised dAb fusion. A maximised dAb target affinity may increase specific tissue uptake, but it may also prevent effective tissue percolation or prevent effective delivery of the attached therapeutic to its respective receptor target[2-4]. A maximised therapeutic binding affinity may increase potency but target tissue

concentration-limiting systemic interactions and dose dependent side effects may compromise the overall efficacy[5,6].

Hence, it is clear that there may be a delicate balancing act to be performed in engineering the binding affinities of the targeting moiety and therapeutic payload in an optimised fusion protein. This investigation will seek to investigate how best to maximise tissue targeting specificity and localised therapeutic potency with two binding affinity influences, by experimenting with different binding affinity combinations *in vivo*.

Hypothesis

The efficacy – targeting selectivity and localised potency – of a dAb fusion protein will be significantly influenced by its two intrinsic binding affinities

Testing the hypothesis necessitates a model system to analyse tissue targeting and a tool dAb fusion comprised of a tissue selective dAb and a potent therapeutic with a systemically distributed receptor. A dAb fusion protein consisting of human interferon (hIFN) fused to an asialoglycoprotein receptor (ASGPR)-targeting dAb, a IFN-ASGPRdAb, is a possible tool for investigating the approach. Such a molecule has been conceived as a potential treatment for liver malignancies. hIFN derivatives are already the primary treatment for the hepatitis C virus (HCV) and are indicated in treating hepatocellular carcinoma (HCC), but are linked to severe side effects. ASGPRdAbs have been engineered to discretely target liver tissue. Hence the hIFN and dAb proteins' genetic sequences have been fused as an in-line genetic fusion, conferring the resultant recombinant fusion protein with a dual-targeting capability for ASGPR and IFNα receptor (IFNAR).

ASGPR is abundantly expressed almost exclusively on the liver hepatocytes beneath the endothelium, and so a dAb engineered to target ASGPR allows liver tissue specificity. This contrasts with IFN binding to the ubiquitously expressed IFNAR activating the JAK-STAT intracellular signalling pathway, which can activate downstream mechanisms such as anti-proliferation, apoptosis and immune system activation.

IFN-ASGPRdAbs thus possess dual affinity for ASGPR and IFNAR. Therefore, these two potentially conflicting binding properties can be probed in

order to assess the validity of the hypothesis. IFN-ASGPRdAb mutants, with varying binding affinity combinations, can be engineered for testing in an *in vivo* model system.

In order to quantify the targeting of the IFN-ASGPRdAbs *in vivo*, it is a fortuitous opportunity to develop gallium-68 (Ga-68/^{68}Ga) labelling of IFN-ASGPRdAbs. Ga-68 is an increasingly promising imaging isotope but is yet to have been utilised for radiolabelling dAbs. The positron emitting Ga-68 in conjunction with a chelator such as 1,4,7-triazacyclononanetriacetic acid (NOTA) also enables the use of radioactive biodistribution studies and positron emission tomography (PET) computed tomography (CT) to quantify uptake of dAb fusion in xenograft tissue over time, which would be an important addition to the experimental toolbox for dAb fusion development.

It is important to note that the motivation is thus not to create a new therapeutic hIFN-ASGPRdAb for liver disease but rather this is a convenient model for a proof of principle based on the hypothesis.

1.2 DOMAIN ANTIBODIES

1.2.1 Domain Antibody Engineering

Immunoglobulins are the B-cell antigen-recognition molecules of the adaptive immune system and are secreted as antibodies[7]. Antibodies recognise a discrete target molecule, the antigen, by interacting with a specific antigenic component sequence known as the epitope. Full antibody isotype immunoglobulin G (IgG)1 is the most abundant immunoglobulin in human serum and the most exploited antibody technology for engineering therapies[8]. It is a large ~150kDa protein comprising two identical ~50kDa heavy peptide chains and two identical ~25kDa light chains arranged in a tetrameric quaternary 'Y' conformation connected by disulphide bridges and non-covalent interactions. A dAb is comprised of a single variable domain of an antibody variable region and is thus the smallest functional antigen binding unit of an immunoglobulin at 11-15kDa[7]. Therefore, the small size of a dAb markedly contrasts with the full IgG, comprising approximately one twelfth of the mass of an entire IgG whilst maintaining binding activity.

The dAb comprises only a single variable domain, and is a purely targeting antibody fragment. A variable domain is comprised of four highly conserved framework β-sheet barrel regions linked by three hypervariable region loops. It is through the hypervariable sequence diversity that antigen-epitope specific binding activity is encoded and together form a complementary antigen-binding site. Hence they are termed the complementarity determining regions (CDRs). A dAb thus has three CDRs with a V_H or variable kappa (V_κ) domain framework forming its antigen-binding site. This contrasts with the six CDRs in a full antibody afforded by the presence of both a variable heavy (V_H) and a variable light (V_L).

The potential of dAb antibody fragments was first described in the late 1980s* by Ward et al[1]. Three dAb sequences were isolated from anti-lysozyme antibody D1.3 and the deoxyribonucleic acid (DNA) of the variable domains of murine-derived anti-lysozyme antibodies by polymerase chain reaction (PCR)[9], and subsequently expressed in *E. coli* and homogenously purified as single functional polypeptides. They were shown to maintain a low nanomolar affinity for lysozyme, similar to those of the full antibody. Hence, this indicated that the rest of the

* Initially at the MRC lab in Cambridge and were subsequently developed, patented and pioneered by Domantis, now a subsidiary of GlaxoSmithKline (GSK)

antibody protein scaffold, including the other associated variable domain, was not essential to achieve independently mediated V_H antigen binding.

However, the lack of partnering variable domain initially caused problems with dAb synthesis attempts. They demonstrated poor solubility, dimerisation, aggregation and precipitation[1,10] because of the solvent exposure of hydrophobic residues ordinarily shielded by the interaction with the other variable domain[11]. Heating at low concentrations lead to irreversible aggregation[12]. For a potential therapeutic this was less than ideal, as high concentrations are needed for administration and aggregation increases immunogenicity. This V_L-absence hydrophobicity problem had in fact already been solved by evolution twice: *Elasmobranchii* Nurse Shark antigen receptors[13] and *Camelidae* heavy chain antibodies (HCAbs). The latter are naturally occurring antibody analogues possessing only 3 CDRs, similar to dAbs, and lack light chains[14]. This just leaves a single variable heavy (V_{HH}) domain functionally binding antigens in the absence of V_L domains. *Camelidae* have evolved conserved V_{HH} mutations to hydrophilic residues in the framework sequences and an increase in CDR1 CDR3 length. These prevent a hydrophobic interface exposure due to the absence of a V_L domain and increase specific epitope binding potential respectively[15-18]. V_{HH} domains thus exist as highly soluble monomeric species under physiological conditions and can even maintain specific binding activity up to 90°C[19] and resist aggregation in spite of exposure to extremes[20]. The human V_H3 family of dAbs are the most similar in stability to V_{HH} compared to the unfolding energies of other variable domain families[18,21]. Therefore, one strategy was for the 'camelisation' of the V_H dAb protein framework sequences by selectively mutating the hydrophobic residues to hydrophilic residues conforming to conserved *Camelidae* germline substitutions (such as G44E, L45R and W47I[22]) in addition to CDR3 elongation[23]. This indeed allowed selection of viable thermostable soluble dAbs[24,25].

Furthermore, it is also possible to achieve 'camelisation-like' results whilst maintaining a native V_H residue sequence. Selection for an elongated CDR3 to mask the hydrophobic residues[26], decreased CDR hydrophobicity[27], decreased beta sheet folding[28], reoriented residues to mask hydrophobic patches[12], or rare native mutations (such as G44K[29]) have also been shown to allow for the purification of active highly soluble monomeric dAbs. Moreover, having an isoelectric point away from physiological pH appears to correlate with aggregation-resistance. This is

particularly the case if the CDRs contain kosmotropic negatively charged residues aspartate or glutamate[30] or by the selection of charged residues at the periphery of the CDRs[27], both of which can be introduced by mutagenesis. However, these modifications are dAb specific relative to the charged residues' spatial distribution and the net charge of the protein as a whole[31].

An effective method of dAb selection was to create a selection pressure during initial dAb isolation from a library. For instance, high transient heating to 80°C of candidate human V_H3 family dAb proteins expressed on the surface of bacteriophage promoted full dAb unfolding followed by re-cooling to promote refolding, allowed identification of thermostable aggregation-resistant dAbs by Protein A ELISA capture assay, thus yielding the sequences of highly stable V_H3 dAbs that can be produced at high titres[24,28,32,33].

The generation of dAbs traditionally involves the creation of a phage display library[34,35], allowing a vast repertoire of potential dAbs to be amassed[36]. Error prone PCR, mutator bacterial strains, CDR shuffling, and oligonucleotide mutagenesis can efficiently create an indefinite array of affinity matured sequences of dAb biophysical phenotypes, mimicking the endogenous mammalian hypermutagenic engineering of antibody CDRs in response to exogenous antigen challenge[32,37,38]. The hypermutated dAb genetic sequences are encoded in filamentous bacteriophage by genetic fusion to gene III which encodes minor coat protein III, expressed at the tip of the phage[39], and is ordinarily responsible for attachment to bacterial pili. The phage thus express protein III-dAb fusion proteins, displaying their encoded dAb on their tip and so screening the library against a target antigen by affinity capture can rapidly match phenotype to genotype[40] in an entirely automatable process, enriching phages encoding candidate dAb. After several more rounds of amplification in *E. coli* and further affinity capture refinement, the bacteriophage DNA of this subset of active antigen-binders can be sequenced to analyse for consensus. The genetic template is subsequently cloned into an *E. coli* expression vector and the affinity matured to encode a recombinant dAb protein structure with the desired biophysical properties[41]. This generation method bestows the dAb platform with a vast potential antigen-targeting repertoire without the need for animal immunisation and harvest.

A primary limitation of the phage display platform includes the biology of the phage-host system and its interaction with the displayed protein, which can lead to

library censorship[42], and so precludes some domain antibody sequences. There is a limit to the potential library size/diversity (10^{15} sequences) through sequence bias against sequences deleterious to the host[43,44]. For instance, there may be too high a metabolic strain on the parasitised bacterial host to produce the display progeny phage, inhibition of the insertion of the pIII protein into the assembling virion, poor pIII translocation within the bacterium, or disruption to viral protein-protein interactions such as through interfering disulphide bonding of odd numbers of encoded cysteine residues. Alternative strategies could be mRNA or ribosomal display with their larger libraries (10^{17} sequences)[45].

The *in vitro* bacteriophage based method of dAb generation contrasts with exploiting *in vivo* antibody generation. Native antibodies are 'bio-engineered' in mammals through hypermutation in B-lymphocyte germinal centres[46] so as to attain antibodies for specific antigens. Therefore originally host mammals were challenged repeatedly with the antigen and the serum harvested, attaining a polyclonal antibody (pAb) mix. However attaining standardised therapeutic sera with consistent pAb yields was not possible. The Nobel Prize in Physiology or Medicine 1984 was shared by Jerne, Köhler and Milstein for theorising and developing monoclonal antibodies (mAbs)[47], solving the pAb problems. They created immortal hybridomas by fusing sheep red blood cell immunised mouse spleen cells with myeloma cells[48,49], which were refined to only produce specific mAb species[50]. Nevertheless effective hybridoma generation is constrained by the initial immunised hosts' endogenous antibody generation, thus the repertoire attained is restricted and requires long dosing regimes, bleeds and sacrifice to attain the genetic sequences conferring immunity. On the other hand, phage display is theoretically only limited by the number of plasmids encoding the dAbs.

Another drawback of non-human mammalian antibody derivatives such as hybridoma mAbs is the presence of 'foreign' non-human protein sequences which may cause an immune response in humans. Strategies can be employed to minimise the foreign protein sequences by 'humanising' the antibody scaffold (non-CDRs)[51], for instance, by selectively mutagenising non-human sequences of a chimeric recombinant mAb[52] or grafting the CDR sequences into a full human antibody scaffold[53]. However, the CDRs may still nonetheless contain foreign immunogenic sequences. By contrast phage-display generated dAbs have a lower potential

immunogenicity owing to a fully humanised recombinant scaffold and human CDR3 sequences. Nevertheless, this is no guarantee against an anti-idiotypic reaction in some patients as seen with fully-humanised phage display selected tumour necrosis factor (TNF) antagonist adalimumab[54].

A dAb lacks the fragment crystallisable (Fc) domain that is present on full antibodies. The Fc domain is responsible for the long serum half-life of immunoglobulin through the endothelial cell neonatal Fc receptor (FcRn) endocytosis recycling system[55] and Fcγ receptor effector interactions such as phagocytosis by macrophages and neutrophils[2], Antibody-Dependent Cell-Mediated Cytotoxicity (ADCC) by Natural Killer (NK) cells[56] and instigating a classical complement dependent cytotoxicity by interacting with C1q[57]. These Fc interactions may contribute to the positive pharmacokinetics and potency of antibody therapies, such as for adalimumab[58,59] but particularly anti-tumour rituximab and trastuzumab (Section 1.3.1). Therefore, the lack of Fc in dAbs can be considered a drawback of the dAb technology as it precludes dAbs from the FcRn recycling mechanism, concordantly lowering dAb half-life compared to Fc constructs. This also precludes dAbs as potential direct antagonistic therapies for immune system mediated clinical response strategies. Nonetheless, the upside is that the decreased immunogenicity from not engaging the immune system, whether mediated by antigenic sequence motifs or Fc, increases the potential applications for dAbs as non-immunogenic targeting agents.

The dAb's 12-15kDa size, although potentially beneficial for increased tissue penetration[2], may result in rapid renal clearance. In conjunction with no FcRn recycling mechanism, these factors conspire towards a dAb terminal circulatory half-life of approximately 25 minutes in *in vivo* murine models[7]. An alternative perspective though is that the small size potentially allows more homologous biodistribution to access the maximum number of possible targets, and rapid clearance ought to ensure that the dAb only accumulates locally at high concentrations of target. These properties would be especially useful if dAbs were to be utilised as tracers in molecular imaging, for instance. Nevertheless increasing the half-life sufficiently to ensure an efficacious response to a dAb-mediated therapy is an important developmental challenge.

1.2.2 Domain Antibody Biopharmaceuticals

One of the first applications of the dAb platform was for extending the half-life of quickly metabolised therapeutics such as IFN (Introduction 1.5). IFN is an important HCV treatment but it has poor pharmacokinetics. However, extending the half-life of IFN improves its antiviral efficacy. For example, IFN was enhanced with polyethylene glycol pegylation, extending IFN's *in vivo* half-life from approximately 8 to 40 hours due to an increase in hydrodynamic radius decreases renal clearance rates and the inert coating of the protein protects against proteolysis[60]. This concordantly led to an improved sustained virological response was obtained with a weekly subcutaneous dosing strategy[61-63]. However, heterogeneous pegylated IFN production challenges[64] left the door open for alternative half-life extension technologies.

The dAb platform was utilised for achieving increased IFN *in vivo* serum half-life through mediating an association between IFN and the 67kDa human serum albumin (HSA) protein[65]. HSA has a circulatory half-life of approximately three weeks owing to protection from non-specific pinocytotic-lysosomal degradation by pH-dependent FcRn-mediated recycling of HSA back to the extracellular matrix[66]. Hence, association with HSA would both increase size and limit proteolysis, as seen with the pegylation strategy, thus increasing IFN half-life. Therefore, dAb fusions of hIFNα2b fused N-terminally by a small peptide linker to a dAb with affinity for HSA called an AlbudAb were engineered, such as hIFNα2b-DOM7h-14[67]. This compares to a strategy based on the same principles with Albuferon, achieved by genetically fusing human IFN-alpha 2b (hIFNα2b) N-terminally directly to HSA[68], with a reported increased half life of effective concentrations *in vivo* up to seven days allowing less frequent dosing in comparison to pegylated IFN[69,70].

It was shown, however, that in comparison to an Albuferon equivalent, the IFN-AlbudAbs possessed a 1.5x longer serum half-life, a 5.8 fold greater antiviral effect on encephalomyocarditis virus in a A549 lung carcinoma cell line, and a significant retardation of human melanoma xenograft growth in severe combined immunodeficient (SCID) mice. *In vitro,* neither AlbudAb or Albuferon demonstrate anti-viral efficacy greater than IFN-α2b alone due to the steric hindrances of their respective extensive additional protein scaffold, however *in vivo* the increased half-life through FcRn mediated recycling through the HSA association evidently

compensated for the decrease in potency as the IFN-AlbudAb's half-life was 19-fold higher than IFN alone.

An increase in efficacy was similarly observed with AlbudAbs fused to interleukin-1 receptor antagonist (IL-1RA) (an approved treatment for rheumatoid arthritis[71]) in an arthritis model, with a significantly decreased disease progression over IL-1RA alone[72]. This was linked to an albumin-mediated increase in half-life owing to a comparable IL-1RA-AlbudAb half-life as rat serum albumin in rats, which was a 20% half-life improvement over non-targeted IL-ra-dAb.

Hence, the AlbudAb platform presented a viable treatment improvement in different disease states, and clear demonstrations that IFN-dAb fusions can be efficacious *in vivo*.

The dAb research has now progressed to the concept of selectively targeting a therapeutic agent to a diseased tissue by way of dAb mediated tissue targeting whereby the therapeutic agent and the dAb are expressed as a single recombinant protein fusion known as a dAb fusion. In principle, the targeting leads to discrete biodistribution and thus localised high concentration, therefore enhancing therapeutic efficacy. This has been applied to targeting IFNα directly to the liver in the treatment of hepatitis C[73] (Section 1.5.4), rather than extending the half-life as seen with AlbudAbs. The first published data involved a murine IFNα genetically fused with a dAb targeting ASGPR, an ASGPRdAb (Section 1.4), which was shown *in vitro* to retain both ASGPR targeting and IFN function as a fusion protein. *In vivo* specific ASGPR targeting accounted for a 23.8% increase in liver uptake at 3h versus a non-targeted IFN fusion protein control[74].

1.3 IMMUNO-TARGETING CANCER

1.3.1 Cancer Targeting Antibody Derivatives

The anti-neoplastic chemotherapeutics have serious toxic side effects for the host in the treatment of cancer. These include alkylating agents, anti-metabolites and plant alkaloids. Therefore antibody biopharmaceuticals have been developed to increase targeted cytotoxicity to supplement chemotherapy. There is currently no published data on the targeting of cancerous cells or tissues utilising dAbs. However, alternative antibody based derivatives (Figure 1.1) provide numerous precedents for targeting cancerous cells *in vivo*, functioning as antagonistic therapeutics or tracers.

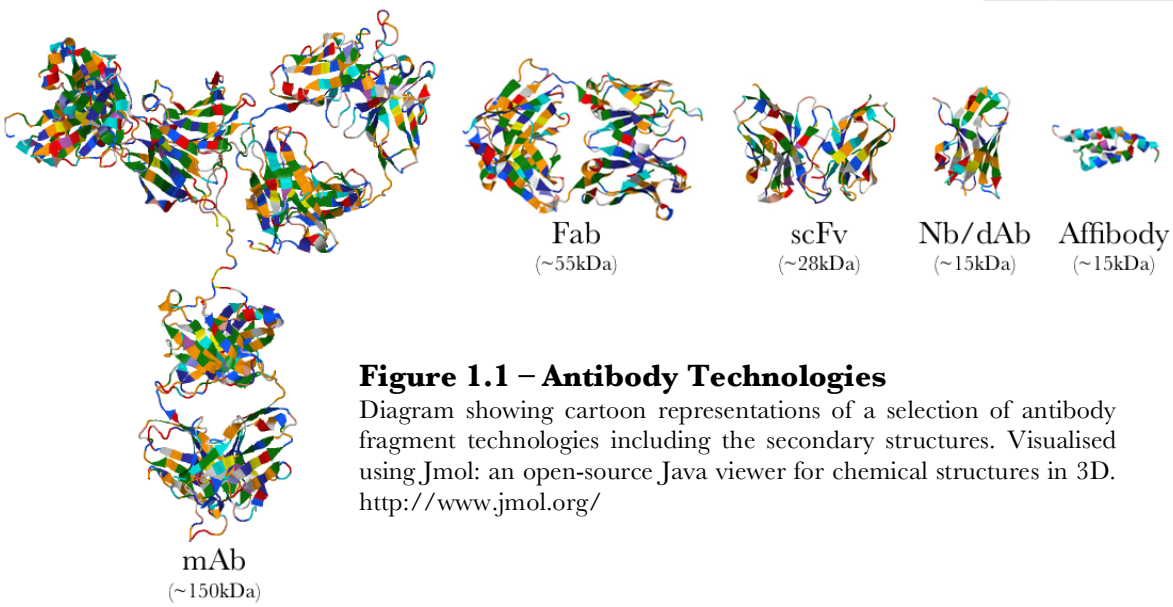

Figure 1.1 – Antibody Technologies
Diagram showing cartoon representations of a selection of antibody fragment technologies including the secondary structures. Visualised using Jmol: an open-source Java viewer for chemical structures in 3D. http://www.jmol.org/

In 1997 the first approved anti-cancer antibody therapy called Rituximab was released against B cell non-Hodgkin's lymphoma[75]. A chimaeric monoclonal anti-CD20 IgG1 antibody[76], Rituximab sensitises B-Cells to chemotherapy, inducing ADCC and crosslinking CD20 to induce apoptosis[77]. The first approved biopharmaceutical against an epithelial malignancy was the breast cancer treatment monoclonal humanised IgG1 trastuzumab, which targets the epidermal growth factor receptor Her2.[78] Trastuzumab is efficacious in 20-30% of cases[79], which constitutes a predominantly poor prognosis patient subset, increasing response rates by 14% independently[80] and ~37% in combination with chemotherapy[81]. Trastuzumab's clinical effect is through a combination of ADCC[82] and targeting the Her2 receptor for ubiquitination[83]. There are also anti-CD52 leukaemia therapy

altuzumab[51,84] which was subsequently redeveloped for treating multiple sclerosis[85], plus cetuximab[86] and panitumumab[87] targeting the epidermal growth factor receptor (EGFR) overexpression in metastatic colorectal cancer[88].

However, mAbs have proven widely ineffective against solid tumours even in those where they are the primary indication[89,90]. Indeed the majority of oncological antibody therapies focus on haematological malignancies. The optimum molecular size for tumour penetration is <100kDa. Hence, smaller antibody fragment biopharmaceuticals open up the potential for hitting intratumoural and intracellular epitopes, owing to greater tumour percolation[91].

Fragment antigen binding (Fab) antibodies (Figure 1.1) are produced by enzymatic cleavage of the Fc region above the hinge[91]. Ranibizumab is a recombinant monoclonal anti-vascular endothelial growth factor (VEGF) humanised Fab derived from parent IgG1 bevacizumab. It was developed for the treatment of age-related macular degeneration. Ranibizumab inhibits vascular growth and could theoretically perform the same role in a cancerous disease state.

Bi-specific mAbs (bsmAb) demonstrate dual-targeted efficacy. BsmAbs are derived from two independent mAbs with discrete targets to create a hybrid comprised of the one heavy and one light chain from each mAb. For instance, the first approved trifunctional bsmAb, catumaxomab for the treatment of malignant ascites, is a rat-mouse hybrid[92,93]. The hybridisation bestows the bsmAb with both anti-epithelial cell adhesion molecule (EpCam)[94] (a tumour associated proliferative signal transducer[95]) and anti-CD3[96,97] variable domains. Therefore it will target EpCam positive ascites and also sequester CD3-positive T Cells to stimulate an ADCC or phagocytosis against the ascites tissue.

Single chain variable fragments (scFv)[98,99] possess a V_H domain linked to a V_L domain via a polypeptide linker (Figure 1.1)[100]. Fibronectin isoform B (B-FN)[101] is expressed in neoplastic blood vessels, such as in actively angiogenic tumours[102], and an scFv targeting B-FN demonstrated the cancer targeting potential *in vivo* by specifically accumulating in the vessels of actively growing teratocarcinomas by infrared-fluorescent tagging[103]. Furthermore, anti-human epidermal growth factor receptor 2 (HER2) scFvs demonstrated specific accumulation in SKOV-3 xenografts[104]. SKOV-3 targeting increased with scFv-HER2 affinity[3], dimerisation and phage display derivation[105]. Conversely, SKOV-3 uptake was limited by renal clearance and lower tumour diffusion was observed with higher HER2 affinities[4].

Nanobodies[106], also known as single domain antibodies or V_{HH} domains, are homologous to dAbs but crucially are derived by cleaving V_{HH} domains from isolated from HCAbs harvested from immunised *Lama glama*[16,107]. The V_{HH} undergo genetic recombination from the harvested V_{HH} sequences for *in vitro* scaffold humanisation[108]. V_{HH} domains also possess many non-canonical CDR architectures[109]. Nanobodies have been raised against the angiogenic and metastasis facilitating chemokine receptors CXCR4[110] and CXCR7[111], inhibiting the invasive phenotype through antagonising the interaction with ligand CXCL12. Hepatocyte growth factor targeting nanobodies antagonising c-Met proliferative signalling have demonstrated glioblastoma xenograft outgrowth regression. EGFR targeting nanobodies have been utilised as imaging agents[112,113] and solid tumour xenograft antagonists[114], including in combination with albumin half-life extension[115] (Section 1.2.2) or multiparatopic strategies[116] to increase efficacy. Anti-HER2 nanobodies are potentially promising tracers for diagnostic PET breast cancer imaging[117,118].

Affibodies[119] are only 7kDa 58 amino acid (AA) scaffolds arranged in a three-helix bundle structure (Figure 1.1)[120], possessing low picomolar target affinities[121,122]. They are however not derived from antibodies but rather from staphylococcal protein A[123,124], which could be problematic for achieving low-immunogenicity with repeat dosing. However, the rationale for affibody development is similar to dAbs as they are small and highly specific with potential for therapeutic half-life extension[125] and are also selected utilising phage display library (Section 1.2.1)[126]. In development for the diagnostic imaging of HER2-positive metastases, the platform could be extended to deliver a cytotoxic. HER2 diagnostic imaging is the predominating goal, correlating imaged receptor number with likely prognosis[127]. Radiolabelled ^{68}Ga-1,4,7,10-tetraazacyclododecanetetraacetic acid (DOTA) anti-HER2 affibodies with injected into an *in vivo* HER2-overexpressing xenograft model demonstrated specific accumulation of the affibody in the tumour at higher concentrations than the non-targeted affibody and in comparison to other tissues (ex. kidneys), with rapid blood clearance of unbound ligand[128]. Furthermore, a correlation between receptor density and affibody tumour concentration was demonstrated utilising PET-CT of xenografts derived from cell lineages with varying HER2 expression profiles. Similar results were achieved with fluorine-18 (F-18/^{18}F) labelling[129,130], in addition to nanoparticle fluorescence imaging of significant tumour affibody targeting versus tissues not involved in excretion[131].

1.3.2 Dual-Targeted Fusion Proteins targeting Cancer

The dAb fusion platform has been shown to allow discrete liver tissue targeting *in vivo* by a dual-targeted hIFN-dAb[74], however it is yet to be demonstrated for cancer tissue. Nonetheless there are a number of precedents for *in vivo* cancer tissue targeting with an antibody derivative linked to a therapeutic cytotoxic payload. Many of these antibody-drug conjugate strategies involve chemically conjugated antimitotic chemotherapies such as the United States Food & Drug Administration (FDA)-approved anti-CD30 brentuximab monomethyl auristatin E conjugate for B-cell lymphomas[132,133] or anti-HER2 trastuzumab-DM1 for HER2-positive metastatic breast cancer[134,135]. However, this investigation is focussed on the recombinant biopharmaceutical drug strategy with spliced fusion proteins targeted towards solid tumours.

A humanised mAb-derived scFv fusion is Oportuzumab-monatox. The scFv component binds an EpCam epitope whereupon it delivers its cytotoxic payload to the tumourous tissue. Exotoxin A from *Pseudomonas aeruginosa*, as designated by 'monatox', is an adenosine diphosphate ribosyltransferase which inhibits eukaryotic elongation factor 2 (EEF2) and thereby causes cessation of polypeptide synthesis, killing the cell[136-138]. The cytotoxic payload could also be an enzyme such as ribonuclease (RNase), for example amphibian onconase, with survival time in SCID mice increased ~150%[139].

Cytokines have potent anti-tumourigenic properties and serious potential side effects for bystander cells with systemic application, which can be expeditiously controlled by the employment of targeting as antibody-cytokine fusion proteins. Endogenous tumouricidal mechanisms can be stimulated by scFv controlled delivery of cytokine TNF Fas ligand to effector sites by targeting fibroblast activation protein inhibiting tumour outgrowth in 78% of models whilst crucially not instigating septic shock[140].

Anti-EGFR nanobody fused with TNF-related apoptosis inducing ligand (TRAIL) was shown to localise in glioblastoma xenografts and retard tumour growth[141]. Similarly, melanoma chondroitin sulphate proteoglycan (MCSP), a poor-prognosis marker for metastatic melanoma, targeted by an anti-MSCP scFv fused to

TRAIL also significantly retarded outgrowth synergistically by sensitising and instigating an apoptotic state in a melanoma xenograft model[142].

An anti-B-FN scFv fused with heterodimeric interleukin-12 (IL-12), a mediator of T-cell and NK cell activation, had 100% greater xenograft uptake over the non-targeted control. The scFv improved the therapeutic index (tumour volume, metastasis, histochemical analysis of cytokine recruitment to the tumour neovasculature) of IL-12 approximately 25-fold against teratocarcinoma and by 400% against adenocarcinoma[143]. However, the tumour:organ ratios were quite low, indicating potential non-specific off-target uptake. Indeed there was evidence of side effects in immuno-competent models.

The same anti-B-FN scFv fused with interleukin-2 (IL-2), another lymphocyte mediator, accumulated in the tumour vasculature, recruited lymphocytes and instigated teratocarcinoma necrosis[144]. This therapeutic significantly reduced orthotopic pancreatic tumour load to 2% that of untreated disease by NK cell recruitment[145]. An scFv targeting tenascin-C, a multifunctional extracellular matrix glycoprotein strongly expressed in breast cancer neovasculature but low in normal tissue[146], fused to IL-2 exhibited specific xenograft uptake in a breast cancer model. However, significant therapeutic efficacy relied upon synergism with a high dose of chemotherapeutic[147].

Another anti-fibronectin scFv fused this time with IFNα formed a non-covalent diabody targeted to the tumour neovasculature. It demonstrated selective tumour uptake in teratocarcinomas and melanoma murine-xenograft models[148]. However, this failed to correlate with a significant targeting-linked therapeutic effect in spite of a 20-fold higher uptake. On the other hand, fusion with IFNγ demonstrated low xenograft uptake[149] owing to IFNγ-mediated off-target sequestering. However, if off-targeting was artificially circumvented by IFNγ receptor knock-out or blocking, then a therapeutic effect was witnessed[150].

These outlined studies employ a highly similar therapeutic fusion strategy to the one to be investigated in this study and exemplify the ability of antibody fragment cytokine based fusion proteins to target *in vivo* xenografts and instigate a measurable response.

1.4 ASIALOGLYCOPROTEIN RECEPTOR

A target protein for a dAb must be preferably abundantly and discretely expressed in the selected diseased tissue. Cell surface markers, such as receptor proteins, are of particular merit owing to the relative ease of access for a circulating biopharmaceutical. In the instance of a therapeutic dAb fusion designed to modify cellular function, rather than for example antagonising a receptor-ligand interaction, the target receptor must also facilitate the therapeutic payload's cellular interaction. In this instance, IFN must be targeted discretely to the liver as part of a dAb fusion. A potential target receptor adhering to these criteria is ASGPR, thus rationalising the creation of the ASGPRdAb.

1.4.1 ASGPR Function

ASGPR, also known as the Ashwell Receptor[151] or Human Hepatic Lectin, was first identified in 1974 in rats[152-154]. ASGPR is a mammalian long-form C-type lectin, a carbohydrate binding glycoprotein reliant on Ca^{2+} ions containing three disulphide bridges[155-158]. ASGPRs are expressed on parenchymal epithelial hepatocytes' sinusoidal plasma membranes[159]. The ASGPRs are concentrated in clathrin coated pits facing capillaries[160,161], and are effectively absent from the apical membrane, thus prioritising maximum exposure to macromolecules through the fenestrated endothelium[162]. This localisation highlights the suitability of ASGPR for targeting because circulatory access may enable effective targeting dynamics.

The ASGPR mediates stochastic endocytosis of desialyted (terminal sialic acid removed) N-linked glycoproteins with terminal galactose (Gal) or *N*-acetylgalactosamine (Gal-NAc) residues, i.e. asialoglycoproteins (ASGP)[163]. Spatial interaction of an ASGP with ASGPR causes a conformational change in ASGPR's structure which instigates the internalisation of the ASGPR-ASGP complex into a clathrin coated vesicle (CCV)[164,165], thus removing ASGPs from circulation by receptor mediated endocytosis[166] for degradation in lysosomes via the endosome[167]. The acidic conditions of the endosome propagate the release of ASGP from the complex, probably by the dissociation of the complexed Ca^{2+} [168], and ASGPR is rapidly recycled back constitutively to the cell plasma membrane[161,169]. Owing to the dissociation at low pH, ASGP binding by ASGPR is reliant on >pH6.5[157]. This

ASGPR cycle occurs within 6.5min *in vitro*[170], with ~60% ASGPR available on the surface at anytime[171]. This mechanism has implications for the potential fate of an ASGPRdAb fusion binding ASGPR (Section 1.4.4.1), avoiding the degradation pathway.

In vivo, ASGPR is thought to regulate von Willebrand factors such as coagulation factor VIII[172] and to prevent the accumulation of deleterious circulating glycoproteins, such as cancer mucins[173] and desialyted platelets[151], maintaining glycoprotein homeostasis[174]. The hepatitis viruses HAV, HBV and HCV also exploit ASGPR for cell entry[175-177]. However, generally, endogenous ligands of ASGPR are not well characterised in the literature as they exist endogenously in a sialyted state and are therefore degraded. This necessitates a binding efficiency between the dAb and ASGPR which may out-compete the endogenous ligands, assuming the epitopes overlap in order to ensure therapeutic levels of payload delivery. However, given the high receptor density and the recycling of ASGPR, there ought to be minimal interference with overall ASGPR function *in vivo* and therefore one would expect no side effects from the interaction of the dAb and ASGPR. Indeed the knock out of ASGPR is a non-deleterious phenotype[178]. Moreover, ASGPR has no downstream effectors given its purpose as a delivery medium to the endosome. Therefore, binding ASGPR ought not to have a modulatory effect on the cells. This is beneficial experimentally as it removes a potential variable, ensuring that observed cellular effects are likely to be the result of the attached therapeutic payload.

1.4.2 ASGPR Structure & Interactions

Human ASGPR exists as a heterooligomer of two integral type-II single-span transmembrane subunits designated H1 (major subunit 46kDa) and H2 (minor subunit 50kDa). The two are further subdivided into homologous RNA splice variants: H1a, H1b, H2a, H2b, and H2c[179-181]. H2b for instance has a five AA insertion at the C-terminus versus H2a. H1 and H2 have a protein sequence homology of 58%[180] and are also highly conserved between mammals. Although cellular messenger ribonucleic acid (mRNA) encoding H1 & H2 is approximately equal, they are expressed at a ratio of 6:1 respectively *in vitro*[171,180].

The structure of H1 includes a ~40AA N-terminal cytoplasmic domain, ~20AA hydrophobic single-span transmembrane domain, with the ectodomain

consisting of an ~80AA extracellular stalk oligomerisation domain, and the ~140AA Ca^{2+}-reliant (for example, three Ca^{2+} in H1) carbohydrate recognition domain (CRD)[158,182,183].

Figure 1.2 – ASGPR-H1 Carbohydrate Recognition Domain Crystal Structure
Diagram showing cartoon representation of the secondary structure of the carbohydrate recognition domain of the H1 subunit of ASGPR including co-ordinated Ca^{2+} ions (green spheres) and amino acids (various colours). Visualised using Jmol: an open-source Java viewer for chemical structures in 3D. http://www.jmol.org/

The native plasma membrane conformation of ASGPR involves a stable complex of H1a, H1b, H2b, and H2c[179], which are cotranslationally inserted into the rough endoplasmic reticulum before glycosylation and maturation in the Golgi apparatus[163]. The exact composition of H1 & H2 is poorly understood but is proposed to be at least a 2:1 heterotrimer[184] or 3:1 heterotetramer but potentially a 2:2 heterotetramer[185] or even H1 homotrimers. The heterooligomeric conformation, achieved through an α-helical coiled-coil interaction of the respective subunits' heptad repeats of the extracellular stalk domains[186], is necessary for ASGPR's high specific binding affinity for ASGPs[187]. The H1 subunit must associate with the H2 subunit to function effectively, because the interaction arranges the high affinity ASGP binding conformation of the CRDs[188], and H2 must make the association for transport to the plasma membrane[184]. The function of the CRD is independent of glycosylation[189].

There are reports of a soluble ASGPR variant consisting of the H1b and H2a, which has been hypothesised to be a buffer against a rapid increase in ASGPs

during infection[179]. It is reported H1b lacks an effective transmembrane domain when translated alone and so can be excreted from the cell, where it can oligomerise with H2a, which is proteolytically cleaved from the plasma membrane into the extracellular fluid. Therefore this could explain the reported uncomplexed 'third' of H2 protein detected on plasma membranes[190]. The presence of this soluble ASGPR complex is relevant when choosing an epitope for the ASGPR targeting dAb, thus favouring a subunit of the native membrane-bound ASGPR.

The structural nuances and subunit expression profiles of ASGPR suggest that an anti-ASGPR dAb ought to be targeted to H1, as it is more highly expressed. Furthermore, the dAb ought to be preferably targeted to the H1a subunit, thus avoiding potential off-target non-cellular binding to H1b of the soluble ASGPR. However the differences between H1a and H1b lie in the transmembrane domain, which is unavailable for targeting. Hence, given the stalk domain interactions, the most freely accessible extracellular domain is the CRD. Therefore, dAbs ought to be selected to target a H1 CRD epitope, with the caveat that blood sequestration by soluble ASGPR is a possibility.

1.4.3 ASGPR Expression Profile

The liver is an attractive organ to target with biopharmaceuticals because the high blood volume supply increases the chances for successful dAb fusion delivery at a therapeutic concentration. The primary reason cited for ASGPR's selection as a target for liver-specific drug delivery is that ASGPR is "exclusively expressed"[191], and has "selective expression on hepatocytes"[192]. Indeed, the tissue mRNA expression data shows conserved predominantly liver transcription of ASGPR-H1 and ASGPR-H2 transcripts (Table 1.1)[193-197]. Studies of liver parenchymal cell lineages has demonstrated a high ASGPR expression level in the order of $1x10^5$ to $5x10^5$ receptors per cell[170,198], even up to $1.2x10^6$ depending on the reaction conditions for quantitative functional binding of the trace ligand[199].

There are examples, however, of expression on non-hepatic tissues. Expression of the rat hepatic lectin 1 (RHL1), which is highly H1 homologous, on rat thyrocyte apical membranes has been identified with rabbit polyclonal serum[200]. This is in addition to RHL1 mRNA in rat brain and kidney[201]. In this instance RHL1 is

responsible for binding and internalising thyroglobulin[202]. However, dAb fusion liver targeting ought to predominate as expression levels of RHL1 are 80% lower than in rat liver and, crucially, thyroid ASGPR is expressed on the apical plasma membrane, thus circulating ASGPRdAb fusion is unlikely to encounter the thyroidal ASGPR. A RHL2 homolog was identified on the dorsal spermatid tip[203], but given the locale and lack of RHL1 subunit, there would be no interference with liver targeting.

Table 1.1
ASGPR Subunit Human Tissue Expression Levels

	Tissue															
Receptor Subunit	Adipose	Adrenal	Appendix	Bladder	Bone Marrow	Brain	Breast	GI Tract	Gall Bladder	Heart	Kidney	Leukocyte	Liver	Lung	Lymph Node	Ovary
ASGPR-H1	0.7	2.0	4.0	1.0	0.8	7.0	0.7	2.0	2.0	-	0.8	7.0	265	1.4	-	-
ASGPR-H2	0.6	2.0	8.0	1.0	4.0	0.7	-	-	9.0	-	1.4	31	344	1.0	0.9	-

Units: Fragments Per Kilobase Of Exon Per Million Fragments Mapped (FPKM)
Data compiled from several studies, as accessed on Expression Atlas http://www.ebi.ac.uk

A study with mAb ASSA-1 against H1 indicated ASGPR expression on activated T-cells[204], although it is conceded that this is a seemingly non-logical result and perhaps the epitope is homologous to another C-type lectin which are common on immunological cells. Similarly identification in immature dendritic cells[205] could be another C-type lectin.

The most compelling potential alternative interfering ASGPR locale is in the kidneys. Both H1 & H2 subunits have been identified in renal proximal tubular epithelial cells by mRNA analysis, histology, flow cytometry and confocal microscopy[206]. There is no receptor density quantification and thus it is unclear if the kidney would detract from liver targeting. Furthermore given that the kidneys will most likely excrete unbound dAb fusion, deciphering specific from non-specific kidney targeting would be difficult *in vivo*.

Therefore, there is evidence for extra hepatic expression, thus raising implications for ASGPR targeted dAb-fusions to tissues other than hepatic. Nevertheless, it is apparent that ASGPR liver expression predominates. A dAb selected for its ability to bind ASGPR should therefore allow the discrete delivery of a therapeutic payload to liver endothelial tissue rather than a homogenous systemic distribution as the abundant expression in the liver should reduce any potential off-tissue binding.

There are also some doubts over the expression of ASGPR in the disease state. H1b expression has been observed *in vitro* to decrease in hepatic cells infected with HBV/HCV, and H1a with HCV[179]. However, this was an mRNA study *in vitro* and thus may not reflect expression *in vivo*. ASGPR is the cell entry medium for the hepatitis viruses, and so it would seem logical for a down regulation of ASGPR post infection.

Moreover, an investigation of hepatic cell carcinoma patients found a negligible level of ASGPR activity on the cancerous cells, including a correlation between tumour size and hyperasialoglycoproteinemia thus indicating reduced endocytic function by ASGPR[207]. There could be potential for application in glycomic patient stratification[208]. This is supported by the observation that hepatocytes with low ASGPR expression levels have a higher proliferative tendency[209,210]. The former investigation was however only performed with 30 patients, which raises a question of significance. Furthermore there is no data to suggest that the ASGPR is no longer being expressed on the plasma membrane but rather only that ASGPR is functioning sub-optimally. This could perhaps be due to tissue restructuring, an issue with endocytosis, or pH in the tumour microenvironment; all of which ought to have no bearing on the ability of an ASGPRdAb to bind the ASGPR. The latter studies are related to proliferation for artificial liver growth and are not related to cancer, and so the ASGPR expression may be due to cell cycle stage rather than a clinical phenotype.

In fact in another study, HCC tissue histology showed an increase in ASGPR expression and no change in binding affinity[211]. Nonetheless, for the purposes of this investigation, cancerous hepatic cell lines can be selected which do express ASGPR at relatively high levels such as HepG2 (Section 1.6.2).

1.4.4 Targeting ASGPR

There are precedents for the selection of ASGPR as the target of biopharmaceuticals for therapeutic payload delivery. Foremost examples are gene delivery for hepatocyte gene therapy applications utilising asialyted glycosylated liposomes[212,213], such as Gal-pOrn-mHA2[214].

More relevant to this investigation, the indirect delivery of a therapeutic protein payload via ASGPR as a proxy target has been shown to augment therapeutic effect. For instance with IFNβ, an increased therapeutic effectiveness was observed through desialytion of the branched oligosaccharide chain on the Asn80-Glu81-Thr82 tripeptide sequence[215] by neuraminidase, producing asialo-IFNβ[191]. A significant anti-HBV effect was observed versus conventional IFNα/β utilising viral particle and downstream effector quantification *in vitro* and *in vivo* inhibition of HBV in athymic nude mice. Hence, targeting ASGPR, an extracellular receptor with no downstream effector functionality, can still produce significant therapeutic results.

A strategy to target ASGPR with antibody fragment technology to deliver an immunotoxin has been developed. A payload of cytotoxic EEF2 inhibitor B11-PE38KDEL, a potential HBV therapeutic, was delivered to various hepatic cell lines through fusion to an anti-ASGPR scFv[216]. The scFv-fusion targeted the extracellular H1 domain, whereupon internalisation reputedly instigated cell death[217,218]. B11-PE38KDEL delivery was shown to be ASGPR dependent through Gal competition assays[216], and although it is assumed the mechanism involves internalisation followed by cytoplasmic release of the cytotoxin, there was however no evidence to confirm the exact mechanism of ASGPR involvement. The scFv-fusion is shown to be less efficacious than application of PE-KDEL alone *in vitro.* However the low IC_{50} nanomolar concentrations necessary to induce cell death demonstrate dual targeting does not forego effective cytotoxicity. Furthermore, it is conceded that the scFv binding affinity is not fully matured. Hence, there is positive evidence for antibody fragment mediated therapeutic payload delivery via ASGPR targeting.

1.4.4.1 ASGPR Targeting Fates

As described, the majority of treatments thus far have selected ASGPR with the aim of internalisation. The interaction of a dAb fusion with the ASGPR receptor can have essentially three different outcomes. Firstly the dAb may bind the ASGPR without inducing the conformational change necessary to induce CCV internalisation, and hence remain on the periphery of the cell[219]. This scenario would involve the dAb simply associating with ASGPR and then dissociating, hopefully allowing the therapeutic payload moiety to engage its receptor whether by cis, as seen with nanobody-IFN fusion proteins[220], or trans .

A second potential interaction would cause endocytosis of the ASGPR dAb-fusion complex into a CCV, transporting the complex to the endosome. The endosome is mildly acidic[221] (pH5-6), therefore the affinity of the dAb for ASGPR may not be overcome, thus not releasing the dAb fusion into the lumen. The recycling of ASGPR to the plasma membrane would in turn return the dAb-fusion to the extracellular space for further interactions.

The third possibility would follow the second except that there is no recycling of the dAb-fusion to the plasma membrane. This could either occur because complexing the dAb fusion prevents the ASGPR recycling mechanism, or the dAb fusion dissociates into the lumen such as with dendrimer delivery of chemotherapeutics[222]. Assuming there is no re-binding, the dAb fusion could be broken down.

All three scenarios would allow kinetic modelling of ASGPR interactions and would require investigation to determine which model is appropriate. As the binding affinities may be an inextricable determining factor in receptor complex fate, it is especially imperative to this study. The latter retention scenario would not be conducive to delivery of the therapeutic moiety and so ASGPR would prove to be a poor target choice. However, the two former possibilities do not preclude an IFN therapeutic payload binding its receptor, as the receptor is similarly recycled via CCVs[223,224]. Indeed the IFN moiety may potentially bind its receptor simultaneously, exerted either in a cis (same cell[192]) and/or trans (bystander cell[225,226]). Hence, the tissue-targeting efficacy of a dAb fusion may prove to be linked to the dAb binding affinity for ASGPR.

1.5 INTERFERON

IFN has been cited as a potential anti-HCC therapeutic after numerous years in the clinic as a treatment for HCV, and even championed as a cancer cure-all in Time Magazine March 31st 1980[227]. However, despite IFNα being a multi billion dollar treatment for hepatitis, IFN has not reached its full potential owing to several major drawbacks. In this investigation, IFNα is fused to a liver targeting ASGPRdAb, with a view to harnessing IFN's cytotoxicity by controlling its biodistribution, potentially localising IFN to the diseased tissue to maximise therapeutic efficacy. Therefore it is important to comprehensively understand IFN's endogenous activity, in order to optimise its utilisation in the IFN-ASGPRdAb fusion.

1.5.1 Interferon Protein

IFN was seminally attributed the role of a vertebrate antiviral, blocking active intracellular influenza viral replication[228]. IFNs, as a part of the innate immunity, act as the first line defence against viruses[229] and other pathogens, but are also known to be immunomodulatory[230] and anti-neoplastic[231]. The IFN cytokine family members are classified based on the receptor through which they signal. Type-I subtypes such as the thirteen variants of IFNα or IFNß bind IFNAR. The immune cell specific Type-II IFNγ binds IFNγ-Receptor (IFNGR), although it can cross-talk with the IFNα/β signalling pathways [232]. In spite of only two known receptors, the different IFNs have highly coordinated, discrete, synergistic effects for specific cell types and disease states[233-235]. For instance, IFNα5 can instigate a stronger anti-viral response than IFNα2 through the IFNAR in HCV infected liver cells.

Human IFNα exists as twelve 19kDa mature protein subtypes, encoded by thirteen *IFNA* genes (*IFNA1* and *IFNA13* encode for an identical IFNα), with the hydrophobic 23 amino acid signalling peptide cleaved during post-translation modification[236]. The 165-residue mature peptide sequences share broad amino acid consensus of ~80%*. IFNα2 is an exception owing to a single D44 deletion, plus three additional polymorphic forms. For example, the predominating 165-amino acid K23R His34† IFNα2b[237], which is also unusual for its post-translational

* UniProt BLAST search against P01563 IFNA2_Human, performed 02/06/14
† UniProt ALIGN analysis of H2DF54_HUMAN vs IFNA2_HUMAN

heterogeneous O-linked glycosylation on Thr106 comprised of a core disaccharide galactosamine-GalNAc with varying α-*N*-acetylneuraminic acid (Neu5Ac) residues[238,239]. There are seven reported glycan variants*. The specific implications of glycosylation for IFNα2 are currently un-established but glycosylation generally plays an important role in protein folding and pharmacokinetics[240], perhaps by slowing dynamic tertiary structure conformation modifications[241]. Indeed in feline IFNα variants, which is 60% homologous to human IFNα†, glycosylation has been linked to increased stability and *in vitro* bioactivity[242]. Nevertheless most human variants have a Val106 residue‡, and so glycosylation cannot be entirely essential to function.

IFN forms a conserved cuboidal tertiary structure consisting of five alpha helices linked by loops[243]. The largest, the 30 residue AB loop, being the predominating site for subtype sequence variation and also critical receptor interactions[244] (Section 1.5.2). IFNα subtypes have four conserved cysteine residues, which form two disulphide bridges (C1-C98 & C29-C138)[245] critical to anti-viral function[246]. IFNα2b has been observed to reversibly dimerise *in vitro* in the presence of Zinc $(Zn)^{2+}$ through interaction of superficial charged residues[247] in a pH and concentration dependent manner[248], although the *in vivo* relevance remains unresolved.

1.5.2 IFNAR Structure & Interactions

Human IFNAR is the receptor protein complex responsible for transducing the signalling cascade for all type I IFNs and comprises two heterologous transmembrane subunits designated 1 & 2: IFNAR1 & IFNAR2[249,250].

IFNAR1 exists as the 135kDa full chain[251] or as the IFNAR1s splice variant lacking exons 4-6[252], although this latter conformation has been challenged[253], and has a unique extracellular domain (ECD). IFNAR2 has three variants: soluble (IFNAR2a), short (IFNAR2b), which is thought to be a dominant negative regulator of IFNα/β[254], and long (IFNAR2c)[255,256]. Two apposing subunits are always found in the full quaternary hIFNAR, and the most stable conformation is believed to be IFNAR1+IFNAR2c[257] binding opposing sides of IFN[258] (Figure 1.3). IFNAR2c binds

* UniCarbKB GlycoSuiteDB database searched with Interferon Alpha 2b 18/06/14
† UniProt BLAST search against Q8MIL4_FELCA performed 02/06/14
‡ UniProt BLAST search against P01563 IFNA2_Human, performed 14/06/14

IFN via a discrete aliphatic hydrophobic patch[259,260] interacting with the AB loop of IFNα2[247] which also possesses a highly motile electrostatic segment for interaction[243]. However, IFNAR1 is necessary to induce the highly potent 'active' ternary hIFNAR structure as a result of, for instance, IFNα2 helix C's[247,261] highly plastic interaction at Val69 and Tyr70[262-264] which transduces the signal through the IFNAR1 ectodomain[265]. IFNAR1 has differential binding chemistry to each IFN subtype[266,267] creating a tertiary conformation unique to each subtype thus inducing discrete signalling[268].

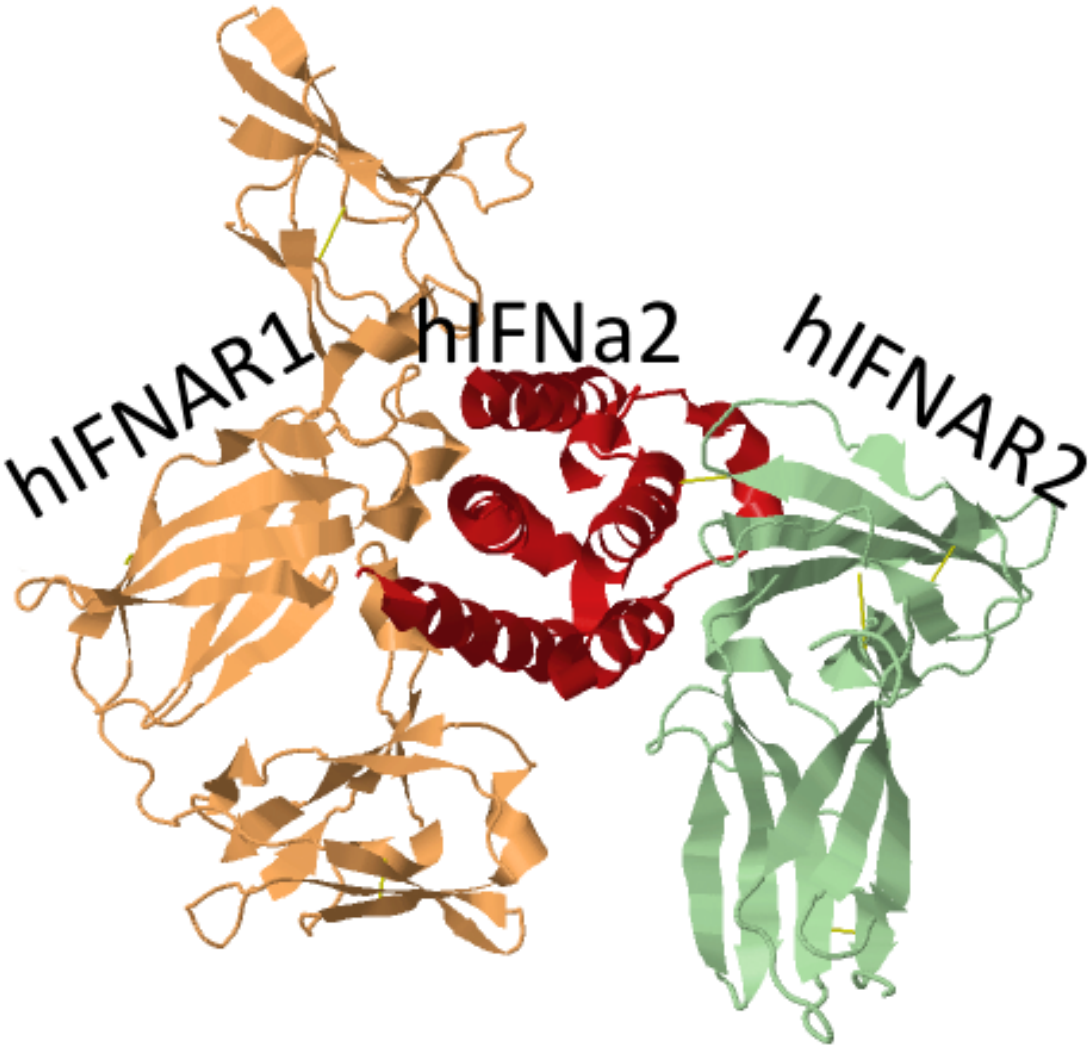

Figure 1.3 – Interaction of hIFNα2 with hIFNAR
Diagram showing cartoon representation of the discrete binding of hIFNα2 (red) to the ECDs of the hIFNAR1 (orange) and hIFNAR2 (green) subunits of the hIFNAR, in the specific ternary conformation for hIFNα2 signalling. Visualised using Jmol: an open-source Java viewer for chemical structures in 3D. http://www.jmol.org/

Therefore, it would appear that the optimum strategy for interacting with the hIFNAR within cancerous tissue utilising an IFN-dAb fusion would be to create a hIFN with decreased affinity to IFNAR2. This would decrease off-target binding and thus would potentially reduce side effects (Section 1.5.5). The affinity reduction would be compensated through the increase in localised target-tissue concentration mediated by a dAb. Additionally an increase in affinity to IFNAR1 would stabilise the ternary receptor conformation thus increasing potency[262]. Hence, the dAb-fusion would be highly potent only in the target hepatic tissue. Nevertheless modifying the ternary interaction with hIFNAR could completely change the signalling cascade profile creating a different cellular phenotype[263,269].

Both IFNAR subunits' mRNA is found systemically transcribed (Table 1.2)[193,194,196,197,270]. The expression of IFNAR1 is related to the disease state[271] and is down-regulated in many cancers, significantly negating response to IFN[272] and so must be established for each cell lineage specifically.

Table 1.2
hIFNAR Subunit Human Tissue Expression Levels

	Tissue															
Receptor Subunit	Adipose	Adrenal	Appendix	Bladder	Bone Marrow	Brain	Breast	GI Tract	Gall Bladder	Heart	Kidney	Leukocyte	Liver	Lung	Lymph Node	Ovary
hIFNAR1	18	13	19	21	9.0	11	17	13	17	7.3	12	31	17	17	16	16
hIFNAR2	13	16	37	25	10	6.0	9.0	7.8	20	5.7	7.7	34	7.3	14	18	18

Units: FPKM
Data compiled from several studies, as accessed on Expression Atlas http://www.ebi.ac.uk

1.5.3 IFN Signal Transduction

IFNα is most markedly upregulated during infection, signalling a diverse cellular response (Figure 1.4). For example, T-lymphocytes (T-Cells) produce IFN in response to viral antigen recognition[273]. Alternatively, a potent initiator is the detection of double-stranded ribonucleic acid (ds-RNA) by ds-RNA detecting protein kinase R (PKR), which inhibits nuclear factor of kappa light polypeptide gene enhancer in B-cells inhibitor to allow nuclear factor kappa-light-chain-enhancer of activated B cells (NFκB) to upregulate IFN production[274].

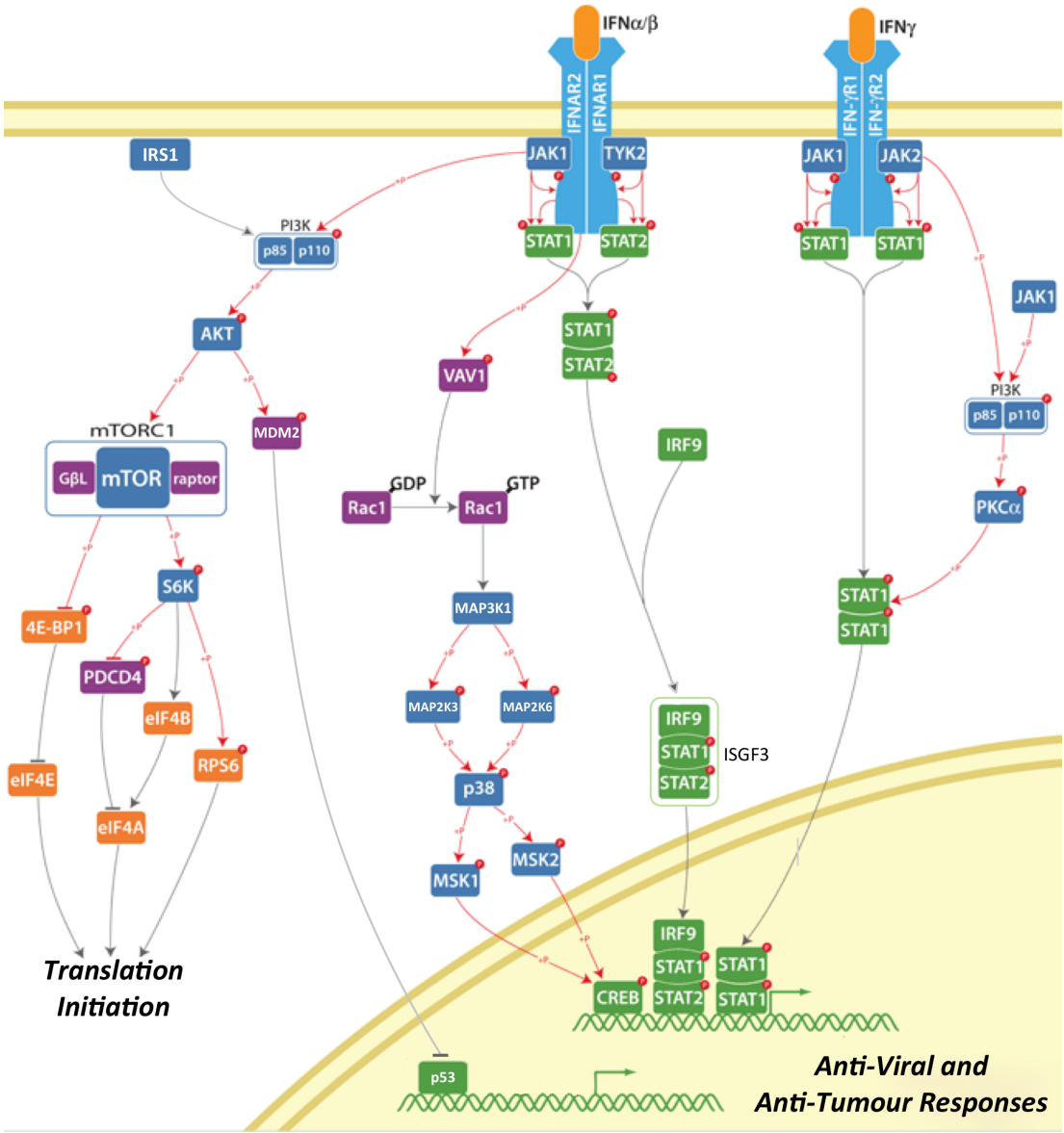

Figure 1.4 – Human Interferon α/β and γ Signalling Pathways
Diagram showing an abridged representation of the protein signalling cascades of the interferon pathways integrating a discrete cellular response, including the cross-talk with the MAPK and PI3K signalling pathways. Adapted from Life Technologies Cell Signalling Pathways, accessed September 2014.
http://www.lifetechnologies.com/uk/en/home/life-science/cell-analysis/signaling-pathways.html

IFN's influence is pleiotropic, with binding of IFNα to IFNAR (Section 1.5.2) inducing transcription of a diverse 'interferome' of over 300 IFN stimulated genes (ISGs)[275,276]. IFNAR1 and IFNAR2c have no endogenous kinase activity and therefore interact with Janus kinases (JAKs). Tyrosine kinase 2 (Tyk2) is constitutively associated with IFNAR1[277] and JAK1 interacts with IFNAR2c via a non-Box1 motif upon formation of the ECD IFNα complex[278], resulting in transphosphorylating of Tyr residues. These activated JAKs then phosphorylate associated signal transducers and activators of transcription (Stat) proteins, which results in a Stat1αβ/Stat2 heterodimer [279,280]. Stat1/Stat2 interacts with IFN-regulatory factor-9 (IRF9) to form the IFN-stimulated gene factor 3 (ISGF3)[281] which translocates to an interferon stimulated response element (ISRE) of an ISG in the nucleus[282]. IFNα/β can self-regulate by inducing IFNAR inhibitors such as UBP43 enzyme[283], SHP phosphatase[284] and SOCS-1[285]. There are numerous ISG expression products which integrate the IFNα induced phenotype[286]. PKR inhibits protein production through phosphorylation of the α-subunit Ser51 of eukaryotic initiation factor-2[287], leading to translational arrest[288-290]. 2',5'-oligoadenylate synthetase (OAS) is also upregulated[291], which can inhibit protein production through activating dimeric endoribonuclease RNAseL[292], resulting in mRNA degradation[293,294].

IFNα/β utilises p53, for instance, to integrate an apoptotic response[295]. The tumour suppressor protein p53 has been described as 'the guardian of the genome'[296], inducing apoptosis if stress signals are detected to suppress tumour outgrowth. The downstream influence of p53, to achieve tumour suppression and induce mitochondrial-mediated apoptosis, is wide ranging. IFNα/β stimulates the induction of p53 transcription *in vitro*[231,297], notably in liver malignant cell line HepG2. Inhibition of the ISGF3 complex demonstrated a decrease in p53 levels *in vitro*[231], and *TP53* contains two characteristic ISRE sequences within its intron. However, p53 is not so readily expressed as OAS for instance. Through p53, IFNα/β has been shown to indirectly increase apoptotic factors FasR and Bcl-2, and p53 inhibitor Mdm2[295].

IFNα has no reported effect on p53 activation (Ser54 phosphorylation) but rather primes the cell with increased p53 concentrations to counteract, for example, human papilloma virus E6 induced ubiquitin degradation of p53[298], pre-empting stress signals. IFN lacks specificity to only cancerous cells, and the dAb doesn't discriminate beyond ASGPR expressing hepatic cells. Hence, there is the potential

for collateral damage to bystander normal non-compromised cell populations within the hepatic tissue. However, the action of IFN on non-compromised cells is to modify the cell's transcriptome to resist hijacking of the cellular machinery[231]. Additional aberrations must be present in the cell to instigate the apoptotic signal cascades, thus making IFN cytotoxicity specific to abnormal cells. Thus the potential for bystander death ought not be an issue for IFN-dAb fusions.

IFN's reliance on p53 is however a potential drawback. Inactivation of p53 and its pathways is an almost universal step in cancer progression[299], and the p53 downstream redundancy attempts to counteract this cancerous selective pressure. IFN tumour suppression, as with other chemotherapeutics[300], has decreased efficacy with tumour stage due to decreasing influence of p53 with cancer progression[301]. The *TP53* gene encoding p53 is mutated in ~50% cancers, and so a key connection between cell damage detection and apoptosis is lost[302]. This would logically indicate that IFN is a poor therapeutic choice as IFN's intrinsic action may be impotent. However, IFN can be an effective anti-HCC agent in certain patient subsets (Section 1.5.4), which may have a mutation profile conducive to treatment such as, for example, non-mutated *TP53*, and/or functional PKR and OAS. Furthermore, decreasing p53 concentrations ensures only high affinity promoters are engaged, which encode apoptotic responses[303-305].

In addition to ISGF3 formation, IFNα/ß stimulated Jak-Stat signal transduction can also cross talk with additional signalling pathways such as the mitogen-activated protein kinase (MAPK)/extracellular signal response kinase (MEK) signalling pathway[306], inhibiting MEK to prevent cell-cycle progression at the G_o/G_1 checkpoint, thus inhibiting cellular proliferation[307,308]. Furthermore IFNα/ß interferes with cyclin A expression, which is overexpressed in 40% of hepatic malignancies[309], to stall the cell in S-phase[310].

The marshalling of extrinsic factors may also become more influential, i.e. the effect on the immune system (Section 1.1.4.2). IFNγ is referred to as the 'immune' IFN[311], however IFNα can also stimulate indirect effects through an immunomodulatory influence. IFNα stimulates expression of TRAIL on the surfaces of NK cells[312,313], T-Cell lymphocytes[314], $CD11c^+$ dendritic cells[315] and monocytes[316]. Also, TRAIL's promoter contains an ISRE for ISGF3 TF binding[312]. TRAIL binds death receptor (DR)-4 or DR-5 to instigate a FAS-associated death domain mediated

apoptotic signal cascade leading to caspase cancer cell death [317]. In monocytes a decrease in DR-5 expression was also noted[316], which is presumably to desensitise them to the increase in extracellular TRAIL, and an increase in nitric oxide (NO) synthase with concordant antiviral NO production[318]. IFNα/β can also stimulate the expression of major histocompatibility complex-I on the cell surface of lymphocytes[319] to increase compromised cell recognition. IFNα/β increases memory T-cell turnover, extending their half-lives[320].

It is thought TRAIL can act in a p53 independent manner if the *TP53* gene is damaged, although this is not substantiated in human tissue[321,322]. Furthermore, there are additional indications as it has been suggested that IFNα/β anti-metastatic effects are mediated by $CD4^+$ T-Cells in ESb lymphomas[323] and $CD8^+$ T-Cells in adenocarcinoma[324]. IFNα/β has been observed to be less effective in immuno-compromised mice[325,326], further supporting the necessity for the immune system.

1.5.4 IFN as a Cancer Therapeutic

IFNα has been chosen for this investigation owing to the wide systemic expression of IFNAR, in contrast to the hepatic tissue specific expression of ASGPR. In addition, IFN is widely utilised as a treatment for various cancers. Injection with anti-IFNα/ß polyclonal antiserum abrogates syngeneic/xenogeneic tumour implantation rejection by an immuno-competent mouse host[327,328]. This indicates the importance of IFN's role in endogenous anti-tumour activities. IFN has also been reported to negatively influence cancerous phenotypes such as angiogenesis[329] and cell motility[330].

IFNα2b administration in patients with high-risk cutaneous melanoma showed a statistically significant increase in disease-free survival and overall survival[331], and is currently the only FDA approved treatment for this malignancy. Previously, IFNα has been trialled for multiple malignancies with varied success[332], particularly in renal cell carcinomas.

An anti-cancer combination therapy of IFNα and fluorouracil was first characterised in colorectal cancer[333], before being demonstrated as a treatment to illicit a partial response in HCC patients[334]. Subsequently studies have provided clinical support for this combination therapy showing a number of those examined reaching steady state disease[335,336]. However, none of the studies analysed a large

patient subset to provide total confidence and survival appears patient specific. Therefore, it is apparent that within the HCC population there is a subset of tumours that will respond to IFN treatment with a full disease remission.

It has been hypothesised that endogenous IFNs are involved in 'cancer immunosurveillance', whereby stress ligands or cancer antigens are recognised, and immune response elicited[337]. However, a potential effect is an immunoselective 'Darwinian' environment for the 'fittest' tumour cells from a heterogeneous population, promoting an immunoevasive plastic phenotype, thus facilitating tumour outgrowth[338-340]. This has been termed 'immunoediting'[341]. These are similar to the selective pressures applied by such classical mechanisms of regulation, such as growth factor regulation, the evasion of which comprise one of the original 'hallmarks of cancer' [342]. Immunoevasion and inflammatory response are now cited to be new hallmarks [343].

Cancerous tissues acquire a multifactorial, high mutation, resistance phenotype. It has been argued that genomic instability is a phenotype of cancerous cells rather than a single crisis event, therefore leading to a highly heterogeneous and continually 'evolving' population of cells. Hence, the application of IFN results in a new selective niche for a reduced immunogenic cancer cell subpopulation to thrive, potentially later resulting in cancer progression and an ever increasingly poor prognosis. It is a comparable scenario to the effect of antibiotic over usage on bacterial strains [344].

The tumour phenotype is thus a product of its immunological environment. Tumours harvested from *Ifnar1*$^{-/-}$ knock-out mice subsequently transplanted into wild-type hosts showed increased immunogenicity (lymphocyte-dependent rejection) in comparison to tumours harvested from immunocompetent hosts which form progressive tumours in a wild-type recipient[340]. This may be seen as counterintuitive, as it may be expected a tumour growing in the presence of a fully competent immune system to be severely compromised and unable to progress in a new host. Hence, this is strong evidence for immunoediting of the tumour through the action of IFN in the fully competent immune system, creating a less immunogenic cancer phenotype.

Immunoediting highlights the need for patient stratification based on their likely prognosis, perhaps utilising the principles of theranostics[345], by for instance a cancer tissue specific dAb as a radiotracer. It would also necessitate multi-targeted

combination strategies attempting to obviate the evolution of resistant tumours through different angles of attack[346]. The combination of therapeutic antibodies and small molecule drugs[347] is the standard for breast cancer with trastuzumab plus DNA intercalater doxorubicin and mitosis inhibitor paclitaxel.

Thus, IFN has been shown to be an effective treatment for cancer in defined patient subsets with drawbacks related to cancer immunoediting. It also serves as an additional rationale for IFN targeted delivery localised to the tumour at subsequently more efficacious concentrations, by for example a dAb fusion, which can then integrate an anti-tumour effect[6].

1.5.5 IFN Treatment Side Effects

Treatment with IFN has prohibitive side effects that limit optimal dose schedules[348]. Side effects of chronic IFN therapy include neutropenia[349], flu-like symptoms[350], and serious cognitive impairments such as depression[351]. In one trial on Western HCC patients more than 50% of participants had to withdraw owing to side effects, resulting in a non-significant survival rate versus control[352]. The treatment durations are substantial, lasting months or years, requiring regular injections, which further decreases patient compliance. Even with the decreased dosing of Albuferon treatment, for instance, side effects remain similar to pegylated IFN[5] (Section 1.2.2).

The neuropsychiatric episodes experienced by patients receiving IFN treatment are attributed to pro-inflammatory cytokine interference with mood pathways and neuroprotection in the brain. Precisely, L-Tryptophan (L-Trp) catabolism is channelled through the kynurenine pathway through the action of IFN increasing the activity of enzymes indoleamine 2–3, dioxygenase and kynurenine 3-monooxygenase, inhibiting astrocyte neuroprotection and modifying microglia metabolism[351]. L-Trp is normally channelled into the serotonin pathway, a neurotransmitter responsible for euphoria. The diversion of L-Trp, thus decreasing serotonin levels, could be the root of the depression associated with IFN treatment.

One solution to decrease side effects was Hepatic Arterial Infusion Chemotherapy (HAIC) whereby a catheter is inserted into the hepatic artery to deliver a localised high concentration dose[336,353]. HAIC is highly invasive and can thus introduce more complications than it solves, particularly patient discomfort. It is an unsuitable alternative to routine parenteral administration.

Therefore, localising therapeutic IFN to the diseased tissue would hopefully decrease the aforementioned side effects. A decrease in off-target binding to systemically expressed IFNAR may be potentially achieved by coupling IFN to a highly stringent ASGPRdAb. This could be assessed *in vivo* by perhaps monitoring markers of depression during a long term toxicity study, such as the hormones of the hypothalamic-pituitary-adrenal axis[354] including cortisol levels by the dexamethasone suppression test[355]. Alternatively, subjective assessments of behaviour could be performed such as measures of appetite, lethargy or stress[356].

1.6 HEPATOCELLULAR CARCINOMA

1.6.1 HCC Overview

The chosen model for testing the hypothesis in this investigation is a HCC xenograft model, specifically a subset of cells expressing ASGPR and IFNAR. Thus HCC is good choice for a cancer model to analyse specific xenograft tissue targeting by hIFN-ASGPRdAbs. Also, investigating the targeting hypothesis may also demonstrate a quantifiable anti-tumour effect. Therefore, it is useful to put HCC in context, even though this investigation is not tasked with creating a HCC therapeutic.

In 2012 14.1 million people were diagnosed with cancer worldwide, with 8.2 million succumbing to the disease[357]. Liver cancer was the second highest cause of mortality accounting for 9.1% of the total deaths. Prognosis for liver cancer is poor, with a 95% mortality rate. The predominating liver cancer is HCC with a 3-5% incidence rate of HCC development in cirrhosis patients observed globally[358]. The underlying cirrhosis is often caused by alcohol abuse, chronic hepatitis, diabetes and potentially cigarette smoke[359], linked to patient genotype. HCC is most prevalent in Eastern Asia and Sub-Saharan Africa. The underlying cause has been mooted as ingestion of mouldy grains, whereby exposure to hepatocarcinogenic aflatoxins exacerbates the carcinogenic effects of an underlying hepatitis infection[360].

There are presently no unequivocal treatments for HCC. Sofranib has been approved by the FDA as a treatment for HCC, but it has been rejected by United Kingdom regulators for its lack of cost effectiveness, as the average patient life expectancy is increased by only 6 months. The dire lack of treatments is highlighted by the use of herbal remedies in Eastern Asia[361]. IFN has been widely researched as a therapeutic for HCC and the frequently underlying hepatitis but has been restricted by its inhibitory side effects (Section 1.5.5).

Therefore investigation of a targeted IFN treatment in the form of an IFN-ASGPRdAb fusion could be a useful addition to the field where new treatments are desperately needed. This however is a secondary consideration in this investigation.

1.6.2 HepG2 HCC Model Cell Line

The most studied cell lines for endogenous ASGPR activity have been rat hepatocytes or human HepG2 cell lines. The HCC epithelial cell line HepG2 (Figure1.5) was immortalised from a 15-year-old adolescent human male[362]. Under the correct conditions they will form sub-cutaneous xenograft tumours in an immuno-compromised mouse[363] and are frequently utilised to model HCC *in vivo*. ASGPR is known to be expressed on the cell surface of the HepG2 cell line[364]. Therefore, HepG2 cells present themselves as the appropriate cell line for inducing ASGPR expressing xenografts.

1.7 RADIOCHEMISTRY

1.7.1 Positron Emission Tomography

Non-invasively imaging the biodistribution of a radiolabelled molecule (a radioligand) *in vivo* at the molecular level facilitates an invaluable insight into the biochemical properties of the molecule and biological mechanisms within an organism. PET is a molecular imaging modality that exploits a radioisotopic subset with unique positron emission decay characteristics to trace a radioligand's biodistribution. Acquired three-dimensional (3D) spatial data is utilised to construct a 3D image of radioligand biodistribution.

PET is a highly sensitive imaging modality, which is derived from capturing a high proportion of decay events within the scope of the scanner, and thus the derived signal is directly proportional to the radioactivity present. This facilitates an extrapolation to the molar concentration of the ligand or target, within 3D space, through compartmental modelling. Current microPET scanners have a resolution of 1.2mm. Hence, the biophysical parameters of the radioligand can be calculated.

PET utilises the radioactive beta decay properties of radioisotopes that undergo weak force mediated nuclear transmutation, involving a proton decaying to a neutron. Specifically, beta positive decay whereby a positron ($ß^+$), the anti-particle to an electron[365], along with a negative neutrino (√), are emitted from the atomic nucleus. For example, the radioactive isotope Ga-68:

$$^{68}Ga \rightarrow {}^{68}Zn + ß^+ + \surd$$

A positron is emitted with kinetic energy equating to a proportion of an observed maximum endpoint energy (E_{max}). *In vivo,* as the positron encounters local proton rich tissue, the repulsive forces result in the positron's emission vector being erratic. These repulsive nuclear interactions dissipate the positron's kinetic energy and the positron is attracted to an electron. The positron and electron interact to form a very short-lived ($1x10^{-7}s$) non-nuclear 'element' known as a positronium[366]. As the electron and positron combine, the positronium annihilates and the mass is converted into gamma (γ) photon radiation. The total energy of the annihilation can

be calculated using the principles of mass-energy equivalence dictated in Einstein's Theory of Special Relativity:

$$\begin{aligned}\mathbf{E} &= mc^2 \\ &= m_e c^2 + m_p c^2 \\ &= (9.11\text{x}10^{-31} \text{ x } (3.00\text{x}10^{8})^2) \text{ x } 2 \\ &= 1.64\text{x}10^{-13} \text{ J} \\ &= \mathbf{1.022\ MeV} \text{ (3dp)}\end{aligned}$$

The momentum of the positronium at annihilation is close to zero, therefore conservation of momentum dictates that the energy is emitted simultaneously in coincidence as anti-parallel γ photons. Hence the energy of each γ photon is thus 511 keV (to 3 significant figures). This emission energy is constant for all positron-emitting radioisotopes and is independent of the positron E_{max}. Higher order annihilations such as four emissions at right angles occur in only 0.003% of annihilations

The γ photons from a positron annihilation event can traverse biological tissues and air to impinge on the scintillation medium of photomultiplier tubes (PMTs), positioned within a cylindrical PET scanner to detect both of the anti-parallel 511keV γ photons. The co-linearity of the detected γ photons allows the use of electronic collimation to determine the line of coincidence, along which the loci of the annihilation events can be predicted within 3D space. For instance, Filtered Back Projection, Expectation Maximised Algorithms or Ordered Subset Expectation Maximisation (OSEM) computed tomographic calculations assimilate the coincidence data to quantitatively iterate the total radioactivity along the lines of coincidence between detector pairs into cross sectional two dimensional (2D) images. The data is collectively reconstituted into 3D pixels, known as voxels, which are assigned an intensity value relative to the detected radioactivity present at the represented locus within the tissue, and thus a 3D image of radiotracer biodistribution is attained.

'Time of flight' modelling can also predict the locus of the annihilation event along the line of coincidence by measuring the difference in detection time of the γ photons. This 'time of flight' method, however, can yield poor resolutions due to the

lack of technology capable of measuring the necessary picosecond differentials. For instance, an accuracy to within 300ps would only equate to a resolution of ~4.5cm.

The significant gains in sensitivity provided by PET through not excluding decay events from detection, compared to for example Single Photon Emission Computed Tomography (SPECT) (Section 1.7.1.2), results in a necessity to correct for unwanted detected events such as random decay events or scattered γ photons. Also corrections must be made for the decreased PMT sensitivity with the varying angles of incidence and the dead-time increase from the volume of detected events.

Furthermore, there is a need to correct for tissue attenuation of the γ photons to correct for decay in deeper tissues. Another error is due to non-colinearity, whereby the small momentum of the positronium causes a small deviation from 180° by ±0.25°. Moreover, the annihilation point is utilised as an approximation for the location of the β+-emitting radioisotope, and thus the attached ligand, as the two points are relatively very close[367]. Error in this approximation is related to the E_{max}, as the higher the energy, the further the positron is likely to travel before annihilation. However, the current detector technologies do not have sufficient resolution for these differences to be significant, and can be broadly corrected within the reconstruction algorithms.

1.7.1.1 PET-CT

PET is utilised in unison with a tissue imaging modality, such as X-Ray CT scanning (PET-CT). CT images are derived from the differential tissue absorption of X-Rays, which are detected in cross sections for interpretation and reconstruction into 3D image utilising computerised attenuation algorithms. Therefore, CT images hyperdense tissues rich in heavy atoms appear white on scans. For example, dense bones appear very prominently (3000 Houndsfield Units (HU)), as do dense carbon-rich tumours. Hypodense soft water (~0HU) rich tissues are poorly imaged and appear black. Therefore, PET-CT multimodality approach delivers morphological data to spatially position PET data relative to hyperdense tissues.

The poor soft tissue contrast prejudices CT against accurate anatomical positioning of PET data to a specific tissue type. Magnetic Resonance Imaging (MRI) scanning offers higher contrast resolution and thus tissue discrimination. MRI utilises a strong magnetic field to manipulate the spin of hydrogen atoms' proton nuclei in the imaged tissues[368], systematically altering their magnetic alignment with radio

pulses at the Lamor frequency[369]. As the nuclei realign to their thermodynamically stable spin they emit at a detectable radiofrequency. Stacking of the 2D isotropic resolution images, and defining the threshold of penetration, allows subsequent compilation into a high-resolution anatomical image. There is the additional option of acquiring functional MRI to attain blood flow data or magnetic resonance spectroscopy spectrums to ascertain the metabolite composition within the tissues. Therefore, PET-MRI would overcome some of the drawbacks of PET-CT and provide additional imaging options[370].

Nonetheless, although progress is continually being made towards a robust PET-MRI machine[371], MRI is presently expensive and requires long acquisition times to produce high-resolution images. Moreover, its combination with PET is a troublesome exercise in engineering as traditional PET PMTs are extremely sensitive to magnetic fields[372], and MRI is incompatible with the metal components of the PET imager, thus impractical levels of shielding are necessary. However, there are efforts to develop PET-MRI with components that do not interfere with the imaging of either system. This could be solved with sequential imaging and computerised image reconstruction, although this would potentially decrease the imaging accuracy due to decay correction and imperfect image alignments from subject movement. A simultaneous acquisition would be more beneficial with initial attempts utilising fibre optics to carry scintillation light outside the MRI shielding for detection[373]; however, this diminishes resolution and field of view. A more effective solution is the use of silicon based avalanche photodiodes (APD), which are not magnet sensitive. By inserting an APD PET into an existing MRI, *in vivo* functional PET data plus morphological MRI data was acquired[374]. The MRI even provided tumour morphological indications, such as inflammation. Nonetheless the system was affected by temperature fluctuations, space restrictions, and an inability to neither instigate attenuation correction utilising MRI data nor scatter correction. Hence, owing to the outlined challenges there is yet to be a commercially available pre-clinical isochronous fully integrated PET-MRI. It is however possible to acquire separate image data and stitch the images back together using appropriate software[375]. This tissue targeting study would benefit from the additional tissue uptake discretion offered by MRI, however a xenograft is relatively hyperdense so will be visible using conventional CT.

1.7.1.2 SPECT Imaging

There is presently a debate about the relative merits of PET versus SPECT[376-378]. SPECT captures γ photon and X-ray emissions from electron capture (EC), via lead collimators, with a ring of detectors. The collimator allows precise directional sourcing of a decay event emission to within 1mm resolution after computed tomography of all detected events, whereas PET can achieve 1.2mm with tight scintillation crystal densities. However, the collimator precludes the detection of 99.9% of decay events, and thus the sensitivity is over 100x less than for PET. In order to compensate for SPECT's reduced sensitivity, image acquisition times must be extended and a higher radioactive dose injected.

SPECT radioisotopes can emit photons at a variety of energies, therefore multiple radioisotopes can be employed within the same host and the individual biodistribution of their attached ligands be discriminated. On the other hand, as all positron decay annihilation events emit at an energy of 511keV, PET cannot discern between different radioisotopes and thus only one radioligand can be employed per scan. However, there is no requirement for detecting multiple ligands in this study, only whole tissue targeting. SPECT would be a viable alternative to PET but for this investigation Ga-68 will be utilised and so the comparison is academic.

1.7.2 Gallium-68 as a Radiopharmaceutical

The post-transition metal $_{31}$Ga stably exists as ^{69}Ga and ^{71}Ga. Ga has an electronic configuration $3d^{10}\ 4s^2\ 4p^1$, existing in the +3 oxidation state Ga(III)[379]. Ga is classified as a 'hard' metal and thus coordinates stably predominantly with oxygen and nitrogen electron donors forming a spherically symmetrical tripositive cation arrangement. Ga is not a biologically essential metal as ferric iron Fe(III) has very similar chemistry and is more abundantly available in the natural environment[380].

A radioisotope of $_{31}$Ga is ^{68}Ga. ^{68}Ga decays to ^{68}Zn with the emission of a positron and a neutrino (Section 1.7.1), of which positrons comprise 89% of ^{68}Ga nuclear decay emissions. This high abundance of positron emissions enables the use of ^{68}Ga in quantitative PET imaging. ^{68}Ga's half-life is 67.71min, which provides a useful tracer window of approximately 4.5hours (depending on dosage)[381]. ^{68}Ga's positron emission E_{max} is 1.90MeV. The short half-life and relatively high E_{max} are ^{68}Ga's primary drawbacks, as this precludes studying long time points and decreases

resolution in preclinical imaging respectively. However, ^{68}Ga is well suited for studying biomolecules with rapid pharmacokinetics such as in preclinical imaging, and minimising patient radiation burden in the clinic[382,383].

^{68}Ga was first utilised for clinical positron scintillation imaging of the brain through complexation by ethylenediaminetetraacetic acid (EDTA)[384]. ^{68}Ga today is increasingly being utilised for PET imaging through conjugation to biomolecules, as ^{68}Ga is readily attained from a germanium-68 (^{68}Ge)/^{68}Ga generator (Section 1.7.3) for immediate experimentation. A primary goal of some within the field is to develop pharmaceutical agents which can be utilised for both diagnoses through molecular imaging but similarly utilise this targeting to deliver a therapeutic radioactive dose. This is achieved by exchanging the PET radionuclide for a β^- emitter, such as Yttrium-90 (^{90}Y) or Lutetium-177 (^{177}Lu). The diagnostic data from PET, including target quantification, can be utilised to determine patient dosimetry for therapeutic isotopes. This combination of the diagnostic and therapeutic has been coined 'Theranostics'[345]. This is particularly prevalent with small peptide imaging agents.

Indeed the most developed usage of ^{68}Ga labelling is for small peptide molecular probes. For instance, the somatostatin analogous octreotide derivatives 68Ga-DOTA-[Tyr^3]-octreotide (^{68}Ga-DOTA-TOC), ^{68}Ga-DOTA-[Nal^3]-octreotide (^{68}Ga-DOTA-NOC) and ^{68}Ga-DOTA-[$_D$Phe^1]-[Tyr^3]-octreotide (^{68}Ga-DOTA-TATE) target overexpressed somatostatin receptors for octreoscan scintigraphic diagnostic imaging of neuroendocrine tumours[385-388], in addition to therapeutic β^- emitter ^{90}Y or ^{177}Lu therapeutic dose delivery[389-391]. Moreover, there is research with labelled RGD based peptides for targeting cancer $\alpha_v\beta_3$ vitronectin receptor integrins for angiogenesis in ischemic tissues[392-394].

Radioimmunoconjugates have been researched for over 50 years, either pretargeting cancers[395-397] or direct targeting of coupled radionuclides[398] for radioimmunodetection or radioimmunotherapy. The use of bsmAbs (Section 1.3.1) for ^{68}Ga imaging, involving affinity for a cancer marker and ^{68}Ga labelled hapten, has been investigated to improve tumour contrast versus conventionally directly labelled antibody derivatives[399,400]. This is achieved by chase blocking all circulatory hapten binding sites before administering the ^{68}Ga-hapten, which binds the pre-administered tumour localised bsmAbs, thus giving a low background signal[401].

Affibodies (Section 1.3.1) have been extensively labelled, including for PET ^{18}F imaging[129,130], demonstrating that small antibody fragments can be successfully

utilised for PET imaging. DOTA (Section 1.7.4) conjugated anti-HER2 affibodies labelled with ^{68}Ga were shown to have high tissue retention in HER2-positive xenografts, in addition to a high tumour-to-blood/organ ratio post injection due to rapid renal clearance of circulating labelled affibodies[127]. This was in comparison to ^{111}In labelled affibodies which demonstrated poorer pharmacokinetic properties.

However, the main precedent comparable to this investigation involves nanobodies (Section 1.3.1). NOTA conjugated (Section 1.7.4.1) α-HER2 nanobodies were successfully ^{68}Ga labelled for non-invasive detection of HER2-positive breast cancers[118]. A 4% injected dose per gram (%ID/g) uptake was observed versus 0.26%ID/g in HER2-negative cells, and good molecular stability.

Hence these examples demonstrate ^{68}Ga is likely an effective labelling strategy *in vivo* for an IFN-dAb fusion.

Nevertheless, ^{68}Ga usage has some associated issues. A Ga(III) ion is a redox-inert 'hard' metal acid (E_{red} = -0.6) and so under acidic conditions is stable as a free hydrated ion with a pK_a of 2.6[380,402]. Hence, when eluted from a generator with 0.1M HCl, ^{68}Ga will exist as free hydrated ions. However, with increasing pH above pH3.0 Ga(III) will begin to form insoluble amphoteric hydroxy complexes that redissolve to gallate $Ga(OH)_4^-$ ions, known as ^{68}Ga-Colloid. Once added to a chelation reaction mixture and exposed to free hydroxy ions at a higher pH, the gallate ion formation will preclude high labelling efficiencies. A low pH alone is not sufficient to prevent hydrolysis, however[403]. Therefore a high kinetic rate multi-dentate chelator, combined with a low pH, should minimise ^{68}Ga hydrolysis by biasing the equilibrium away from hydrolysis (Section 1.7.4). An alternative is to use a ligand-exchange reaction using a low affinity but rapidly binding chelator, such as citrate, but this is time consuming for an isotope with a 68min half-life.

Another possible problem *in vivo* concerns transferrin, whose natural biological ligand is Fe(III). Transferrin is the blood plasma glycoprotein responsible for controlling free Fe(III) levels in biological fluids. Before undergoing transferrin-receptor mediated endocytotic internalisation, transferrin sequesters two Fe(III) ions. An intra-vesicle increase in H^+ ion concentration facilitates release of the Fe(III) ions into the cytoplasm. The highly similar inorganic properties of Fe(III) to Ga(III), such as charge density, mean that transferrin also has a high affinity for Ga(III) . Indeed transferrin's affinity for Ga and mechanism for removal is the basis of ^{67}Ga scanning

and ^{68}Ga-citrate infection site imaging. Therefore, *in vivo* a chelator must offer greater thermodynamic stability than transferrin in order to prevent transchelation and thus loss of radiolabelling.

Moreover, unlike the use of covalently bonded ^{18}F or an imaging agent fused in the protein structure[404], ^{68}Ga must be chelated to the protein. This can result in a stoichiometry greater than one to one thus potentially making subsequent quantitation less robust (Section 1.7.4.1).

Thus, the favoured predisposition to Ga hydrolysis, and *in vivo* transchelation to transferrin, necessitates a chelator with more favourable thermodynamic properties, for example NOTA (Section 1.7.4.1).

1.7.2.1 Alternative Ga Radioisotopes and Positron Emitters

There are several Ga radioisotopes, of which three are important to Nuclear Medicine: ^{66}Ga, ^{67}Ga and ^{68}Ga. ^{66}Ga and ^{67}Ga are both produced from bombardment of Zn or copper (Cu) in a cyclotron. ^{66}Ga's half-life of 9.5 hours makes it an attractive radioactive label for long-lived biomolecules. Various circulatory proteins have been labelled with ^{66}Ga but it provides poor spatial resolutions when imaged due to its high-energy positron (4.15 MeV) and an undesirable subject radiation dosage owing to 4.0 MeV gamma emissions. Moreover, the necessary cation exchange chromatography purification step can actually introduce numerous metal impurities[405]. Hence, ^{66}Ga is not appropriate for this study quantitatively imaging a small biomolecule.

On the other hand, ^{67}Ga has been widely utilised as a ^{67}Ga-citrate or ^{67}Ga-nitrate radiotracer for Gallium Scanning whereby inflammation marking is used as a proxy for tumour staging. Indeed ^{67}Ga was for a long time the gold standard for cancer detection but has since been superseded by fluorodeoxyglucose (FDG)-PET[406]. FDG is a glucose uptake quantification imaging strategy exploiting increased tumour metabolism. A Gamma Camera or SPECT imaging visualises ^{67}Ga distribution by its EC decay emissions. ^{67}Ga's emissions are over a range of energies (93.3keV, 184.6keV, and 0.2keV) bestowing ^{67}Ga with a highly detectable emission profile. Despite being a very feasible isotope for this study, as PET is the preferred imaging system, ^{67}Ga could be a viable alternative if required.

The alternative positron emitting isotopes to ^{68}Ga include ^{18}F, which has a slightly longer half-life of 109.8min. Hence, this would provide more experimentation

time with a higher activity by comparison to ^{68}Ga. Moreover, ^{18}F has a smaller E_{max} of 0.63MeV and thus would provide higher resolution (tissue range ~0.3mm vs. ~1mm for ^{68}Ga), in addition to 97% decay by positron emission providing a higher initial activity from source. However, the source of ^{18}F is a cyclotron and must be specially created to order from an oxygen-18 target, compared with the convenience of a ^{68}Ga generator[407]. The ^{18}F must also be covalently bonded to the protein which adds additional complex reaction steps.

Another alternative is incorporating the positron emitting isotopes carbon-11, nitrogen-13 and oxygen-15 directly into the structure of the entity one wishes to study for PET imaging[408-410]. This reduces the uncertainty regarding whether detected radiation is still attached to the entity of interest, rather than existing as free entities through endogenous proteolytic cleavage events, as may be the case with chelated isotopes for instance. However, these must also be produced in a cyclotron and instantly be utilised in the synthesis reaction, thus precluding these isotopes as practical for a protein labelling application despite recent progress in microfluidic reactors[411].

Iodine-124 (^{124}I) and Zirconium-89 (^{89}Zr) are additional alternatives[412,413]. They have relatively long half-lives of 4.17 days and 3.27 days respectively, which would allow a longer imaging strategy to be performed, and this has made them popular for labelling mAbs. Their E_{max} is high which would likely decrease resolution, and most importantly only 23% of decay is by positron emission and so a lot of activity is required to compensate for the lower signal this causes. ^{89}Zr must be produced in a cyclotron and its chelation chemistry is still unproven[414], so it has its drawbacks, even though it has been utilised to create an imaging agent through labelling anti-EGFR nanobodies with a deferoxamine chelator[113]. ^{64}Cu also has positron emissions[415,416], and has been used previously to label cetuximab[417], but it emits beta-particles which are cytotoxic thus potentially introducing an unwanted variable, and has an unfavourable redox potential. Therefore, if ^{68}Ga is utilised in efficient protocols, to negate the downsides of its relatively short half-life, then it is preferable to ^{18}F, ^{124}I, ^{89}Zr and ^{64}Cu for chelation-based labelling.

1.7.3 PET Isotope Generators

Generators offer the convenience of providing on-demand high-activity radioisotopes for instant radiopharmaceutical synthesis, and are often mooted as the way forward for nuclear medicine in the clinic[418]. An effective generator must provide radiochemically pure daughter radionuclides effectively separated from the decayed parent radionuclide. The Molybdenum-99/Technetium-99m (^{99m}Tc) generator provided the radiation source for approximately 80% of all nuclear medicine applications in the first decade of this century. It provided convenient access to the ^{99m}Tc SPECT isotope, but most importantly was good manufacturing practice approved and in reliable kit-friendly form, thus allowing extensive use in humans[419].

^{68}Ga can be generated *in situ* from a ^{68}Ge source based generator, rather than relying on a cyclotron[418]. ^{68}Ge decays by EC with a half-life of 270.95 days, to evolve ^{68}Ga(III) ions. The principle has been in existence since the 1960s with the first ^{68}Ge/^{68}Ga 'Cows' 'milked' for ^{68}Ga-EDTA, but this required a laborious process to achieve free ^{68}Ga(III) ions for further experimentation[420,421].

Modern commercially available generators, such as the Eckert & Ziegler IG100 (Figure 1.6) or Cyclotron Co Obninsk, adsorb the ^{68}Ge onto an inorganic matrix resin of TiO_2, and ^{68}Ga(III) can be eluted with 0.1M HCl. Alternatives are the SnO_2 based IDB Holland iThemba or the organic silica matrix ITG generator, which requires only weak acid elution. Elution is routinely followed by microfluidic anionic[422,423] or cationic[424,425] chromatography exchange columns to remove any free metal contaminants and increase the activity per unit volume[128], which can improve labelling efficiencies[426] and specific activity in order of 1GBq/nmol. However in some instances yields can be compromised and imaging time wasted, even with automation[427].

There are at least seven potential parent/daughter PET radionuclide combinations other than ^{68}Ge/^{68}Ga[428], however most are undeveloped due to daughter radionuclides with very short half-lives in the order of minutes which are only relevant for perfusion studies. Labelling of pharmaceuticals with these isotopes would be inappropriate, as the life of the radioactivity does not reflect that of the drug.

Rubidium-82 (^{82}Rb) is a commercially available generator-produced PET radioisotope, derived from parent isotope Strontium-82, and has proven clinical applications[429]. However, ^{82}Rb's 1.2min half-life restricts its usage to rapid low-dose imaging such as myocardial perfusion PET imaging.

A titanium-44 (^{44}Ti)/scandium-44 (^{44}Sc) generator system would produce the PET isotope ^{44}Sc, with $t_{1/2}$ 3.93h and 94% β^+ emission[430], presents a potentially superior PET imaging agent by comparison to ^{68}Ga in contexts where a longer physical half-life is necessitated[431,432]. However this generator is not commercially available due to radiochemical challenges with ^{45}Sc(p,2n)^{44}Ti production. Hence, ^{68}Ga is alone as an efficient commercially available generator derived PET imaging radioisotope.

Figure 1.5 – ^{68}Ge/^{68}Ga Generator IG100
Image of the IGG100 gallium-68 generator for *in situ* production from the contained Germanium-68 core.

http://www.icmedical.eu/pet-imaging/eckert-ziegler

However generators are not devoid of drawbacks. There is the possibility for parent isotope such as ^{68}Ge breakthrough into the eluate, in addition to any contaminating metal impurities. Contamination can be reduced by regular generator usage and purging consumables and glassware with HCl. As the generator's parent isotope decays, yield activity concentrations decrease. Experimental time points are restricted by the necessity to allow the generators to re-generate. The necessity for HCl elution produces an eluate at pH1.0, which must be buffered to prevent

degradation of a protein ligand. Radioactivity is eluted in a relatively large volume, which can impact on specific activity. Nevertheless, these negative points are however outweighed by the outlined benefits. Also the IG100 generator is noted for its low ^{68}Ge breakthrough and the ITG for its >90% yields within the first 200days.

The alternative means of isotope production is in a cyclotron, an electromagnetic particle accelerator that manipulates charged particles to hit target nuclei at high energies of approximately 10s MeV and collects the resultant products of the collision. The process is reliable and can produce numerous radioactive isotopes merely by changing the target nuclei. However, potential contamination sources, especially when utilising aqueous targets, include metals from the target body cooling housing and these can preclude efficient labelling yields in downstream reactions. However, niobium usage has forgone this problem to an extent[433]. Cyclotrons are limited to specialist institutions, which are few in number, and therefore their availability is significantly restricted. Moreover the costs are very high. Hence, the relatively simple ^{68}Ga generator is preferential[434].

1.7.4 Chelators

Trivalent radioisotope cations such as ^{68}Ga(III) do not ordinarily strongly interact with a protein structure and the protein must be chemically altered to allow radioisotope chelation. This is achieved by first bioconjugating a specifically designed chelating agent to the protein before the addition of the isotope to promote a thermodynamically stable interaction, thus creating the radioligand.

When selecting a chelating agent one must consider numerous factors. Firstly, and most importantly, the agent must have a strong interaction to the radionuclide even within the biological ionic environment of the host. The chelator-radionuclide complex must be kinetically inert *in vivo*. Free isotopes may give potentially false positive results and a high background. Furthermore, the conjugation of the chelator with the protein must not affect the others' ability to function whether sterically or chemically. Each radioisotope requires a specialist chelator whose structure reflects the coordination chemistry required to maximise thermodynamic chelation stability.

Chelator properties are inherent to their structure. Acyclic chelators have fast metal binding rates due to their open structure[435], which is an advantage when utilising short-lived radioisotopes, however this is at the expense of kinetic inertness.

Macrocyclic chelators are comparably more stable and resistant to transchelation[436]. It is difficult to predict *in vivo* stabilities *in vitro*[437] although good indications can be obtained from a serum stability assay for instance, but only *in vivo* performance data provides the necessary elucidation.

^{68}Ga(III) will strongly bind to a chelator featuring multiple anionic pendant arm oxygen donors due to ^{68}Ga(III) being a hard acidic cation (Section 1.7.2). ^{68}Ga(III) also has a good affinity for thiolates, such as in N,N'-Ethylenedi-L-cysteine[438] and 1,4,7-tris(2-mercaptoethyl)-1,4,7-triazacyclononane (TACN-TM). A successful ^{68}Ga(III) chelator must prevent transchelation with the biological iron transporter transferrin. Therefore, a macrocyclic chelator will be most appropriate for ^{68}Ga chelation.

^{68}Ga(III) has a maximum coordination number of 6, which preferably involves a distorted octahedral geometry in a macrocyclic structure for maximum stability, but tetradentate chelators do exist. There are many chelator complexes identified for usage with ^{68}Ga(III). EDTA is a highly effective metal chelator with a stability constant (K_{ML}) of 21.0 for Ga(III)[439] but it is acyclic. Diethylene triamine pentaacetic acid (DTPA) derivatives (K_{ML} = ~26) and *N*,*N*'-bis(2-hydroxybenzyl)-ethylenediamine-*N*,*N*'-diacetic acid (HBED) derivatives (K_{ML} = ~38) have been utilised to successfully label mAbs and antibody fragments[440,441]. HBED's high stability ^{68}Ga(III) chelation allows high specific activities to be achieved at ambient temperatures. A similar chelator named CP256 can achieve over double the radiolabelling efficiency of HBED[442]. Similarly, 6,9,15-tetraazabicyclopentadeca-1(15),11,13-triene-3,6,9-triacetic acid (PCTA) can be ^{68}Ga-labelled to 99% within 5min at room temperature, although this decreased temporally post-conjugation[443]. Triazacyclononane-phosphinic acid (TRAP) chelator has been shown to incorporate ^{68}Ga(III) with ligand concentrations as low as 0.1μM with >90% efficiency at 25°C[444], which is the highest published efficiency achieved at the time of writing. However, these highly efficient chelators are not currently commercially available.

DOTA is the current 'gold standard' for ^{68}Ga labelling of small peptides due to the long *in vivo* stability of peptide conjugates and reliable chemistry. DOTA conjugation has been exhaustively investigated for somatostatin analogues (Section 1.7.2) in addition to gastrin receptor substrates[445] and glucagon-like peptide 1

receptor[446]. However DOTA's large macrocyclic cavity size can create poor thermodynamic stability and potential non-selectivity under the wrong conditions. Moreover, the hexadentate coordination can leave a deprotonated carboxylate group at physiological pH, which can lead to rapid kidney clearance[447].

In relation to dAbs, however, DOTA has a major drawback. DOTA requires a high temperature (~100°C) to rapidly chelate ^{68}Ga or extended incubation time at lower temperatures due to DOTA's slow complexing kinetics, therefore precluding its use to rapidly label heat labile proteins such as a dAb. Furthermore, these DOTA properties are not conducive to ^{68}Ga's 67.71min half-life and optimum imaging radioactivity. For example, for EGFR-targeted scFv and 50kDa diabodies, HBED was preferred[440]. DOTA labelling has been performed at 37°C for conjugated antibody fragments[443,448,449], but this necessitated additional purification steps, 20min reaction time and high pHs, which is detrimental to effective ^{68}Ga labelling.

NOTA, or a derivative thereof, has been utilised previously for the labelling of the octreotide small peptides and RGD peptides in place of DOTA. NOTA is itself a derivative of TACN with an additional tris-acetate pendant arm[450]. NOTA envelops its chelated metal atom in the macrocyclic cavity through a N_3O_3 distorted octahedral conformation[451-453] as deciphered by X-ray crystallography (Figure 1.7). This conformation confers a Ga(III) chelating stability constant of 31.0[454], affording inertness in nitric acid for up to 6 months for instance[453], with the pendant carboxymethyl arms providing transchelation protection from nucleophilic attack on the Ga(III). NOTA derivatives possess modified pendant groups, which allows influence over final charge or peptide conjugation (Section 1.7.4.1).

NOTA's primary advantage over its commercially available chelation peers is the favourable reaction conditions in which it can be radio labelled with ^{68}Ga(III). If the half-life of ^{68}Ga is not to be restrictive the reaction must be quick (Section 1.7.2), and at low pH to inhibit the formation of ^{68}Ga-colloid. NOTA can be successfully labelled within 10min at an optimum pH3.5[381] which meets the desired criteria. The published data does not provide details of specific activities achieved, instead focussing on labelling efficiencies, which is a misleading measure as it does not take into account the amount of protein present in the assay; although greater than

1GBq/nmol has been suggested*. Moreover, the NOTA labelling reaction can be performed at room temperature without major loss of labelling efficiency, which is perfect for not denaturing a folded protein as was the main issue with DOTA labelling. The thermodynamic stability of Ga-NOTA is reported to be ten-fold higher than Ga-DOTA[454]. This initial evidence from the literature and unpublished anecdotal NOTA usage from fellow researchers has created a compelling case for choosing NOTA as the chelator for labelling the IFN-dAb fusion proteins with Ga-68.

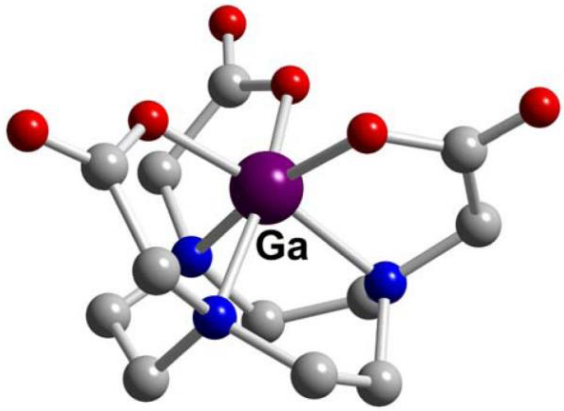

Figure 1.6 – NOTA Chelating a Gallium atom
Cartoon representation of the chelation of a Ga^{3+} ion by NOTA in a distorted octahedral hexadentate formation, as determined by X-Ray Crystallography.

Wadas, T.J. et al. (2010)

1.7.4.1 Bifunctional NOTA Derivatives

NOTA can be chemically bestowed with a variety of reactive cross-linker groups to facilitate covalent bioconjugation to a protein. These bifunctional NOTA compounds each have unique reactive properties that, in addition to controlled reaction conditions, enable NOTA bioconjugation to discrete sites on the protein.

For instance, an isothiocyanate reactive group can interact with amino acid nucleophile groups such as amines of histidine's imidazolyl nitrogen and arginine's guanidinyl group, a tyrosine phenolic hydroxyl group, or sulphydryl groups on cysteine residues[455]. However, the only reactions yielding stable products are akylation reactions with the primary N-terminal α-amines or lysine side chain ε-amines. Therefore, NOTA with an isothiocyanate reactive group can be bioconjugated to proteins specifically through an amine group.

A commercially available isothiocyanate derivative of NOTA is S-2-(4-Isothiocyanatobenzyl)-NOTA (SCN-Bn-NOTA). The isothiocyanate group can react with α/ε-amines by nucleophilic addition reaction under basic conditions, such as in carbonate buffer[393,456,457] (Figure 1.8). The alkaline pH yields a reactive unprotonated

* Prof. Bengt Långström, personal communication

primary amine group, with free electrons able to instigate nucleophilic attack on the electrophilic carbon of the isothiocyanate. The electron-rich nitrogen will subsequently abstract a proton, creating a covalent isothiourea bond between the protein and the Bn-NOTA[458].

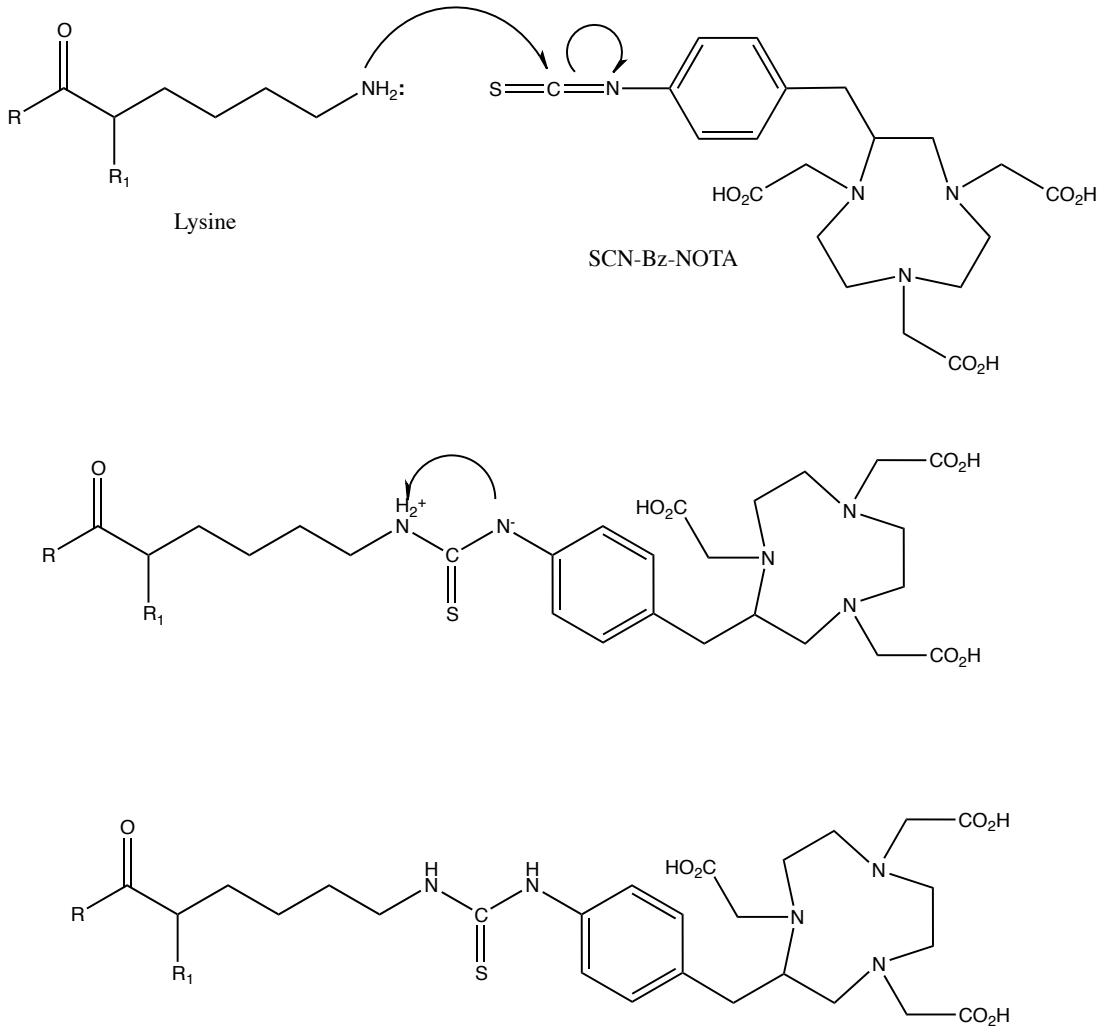

Figure 1.7 – SCN-Bn-NOTA Nucleophilic Addition reaction with Lysine

Diagram representing the nucleophilic substitution reaction of the isothiocyanate group of a SCN-Bn-NOTA with the ε-amine of a lysine amino acid side chain by nucleophilic addition reaction under basic conditions, yielding the NOTA-conjugated protein by a isothiourea bond.

The alkaline pH at which the amine groups become deprotonated varies with the pK_a range of the group *in situ*. The pK_a of N-terminal α-amines with a pK_a range 7.6-8.0 (also quoted 8.0-9.0) is lower than that of the ε-amine lysine groups with a pK_a range 9.3-9.5 (also quoted as 9.8-10.4). Based on these values, according to the Henderson-Hasselbach equation, pH9.0 reaction conditions will equate to ≥91% of α-amines in an unprotonated state compared to <50% ε-amine[458]. Therefore, controlling the pH to bias ionisation of the α-amine groups can promote coupling to the protein N-termini, yielding a predominantly singularly bioconjugated protein species[459].

However, in reality the microenvironmental influences of the protein superstructure on the ionisation potential of the amine groups can cause a decrease in the pK_a range. For instance, α-lymphocyte monoclonal antibody Lym-1 was selectively bioconjugated at the N-terminus at neutral pH7 with ε-amine bioconjugation predominating at pH9.0[460], and both α- and ε-amine NOTA-conjugated metabolites of a disulphide-stabilised Fv antibody of could be detected[461] after bioconjugation at pH8.5[462]. Moreover, the number of lysines available within the amino acid sequence, and their polar hydrophilic nature resulting in protein surface localisation, can shift the equilibrium towards ε-amine bioconjugation. Therefore, the ability to control the conjugation reaction comes with the caveat that it is very much protein specific and must be determined experimentally.

The foremost alternative to an isothiocyanate reactive group for stable coupling of NOTA primarily with α-/ε-amines is a *N*-hydroxysuccinimide (NHS) ester reactive cross-linker, such as 2,2'-(7-(2-((2,5-dioxopyrrolidin-1-yl)oxy)-2-oxoethyl)-1,4,7-triazonane-1,4-diyl)diacetic acid (NHS-NOTA). The NHS ester undergoes a nucleophilic acylation reaction with the unprotonated amine via the carbonyl group to form a covalent amide bond between the protein and the NOTA, with the NHS being released.

The chemistry is efficient but using a NHS ester has several drawbacks. Like the isothiocyanate reaction, the pH must be elevated to promote efficient amine reactivity, and so the same issues with α-/ε-amine specificity will be realised. Even at pH7.0 five chelator units per protein can be achieved[463]. However the more acute issue is that NHS esters are very susceptible to hydrolysis[464] with increasing pH[465] with the equilibrium shifting towards hydrolysis over amide formation above pH8.5

under certain conditions. The half-life could be a matter of minutes at room temperature in aqueous solution. Hydroxide ions are more reactive nucleophiles than water[466], hence the increase in hydrolysis with increasing pH. An isothiocyanate group is electrophilic and so is also vulnerable to hydrolysis in aqueous reaction conditions because a water molecule or hydroxide ion hydrates the isothiocyanate carbon by nucleophilic addition* yielding a thiocarbamic acid derivative of Bn-NOTA. However, the half-life of SCN-Bn-NOTA is substantially higher than NHS-NOTA in aqueous conditions. The lability of NHS-NOTA is therefore a major drawback to NHS chemistry, and must be overcome by using wasteful concentrations of material to improve the reaction kinetics, making SCN-Bn-NOTA the most appropriate choice.

* The nitrogen is oxidised and will abstract a proton from water

1.8 CONCLUDING REMARKS

The evidence from the literature provides a compelling evidence base for pursuing the objectives of this investigation (Section 1.1) with Ga-68 radiolabelled, NOTA conjugated hIFN-ASGPRdAbs *in vivo*.

The properties of dAbs of small size, low immunogenicity, ease of genetic manipulation for desired pharmacodynamics, and high target specificity bestow the platform with potential for applications as novel antibody molecules. The efficacy of the IFN-AlbudAbs for half-life extension and IFN-ASGPRdAb for specific liver uptake (Section 1.2.2) demonstrates the potential of the therapeutic dAb fusion platform to yield quantifiable efficacy improvements *in vivo*. The dAb platform fits into a well established history of efficacious antibody based therapies (Section 1.3.1) and dual targeting of antibody derivatives in combination with biological cytotoxic proteins now has precedents for effective xenograft uptake *in vivo* (Section1.3.2). Examples include an anti-EGFR nanobody fused to TRAIL, anti-B-FN scFv-IL12, and anti-fibronectin scFv-IFNα.

ASGPR's characteristics make it a highly suitable target for localised tissue concentration as there are no signalling functions or downstream effectors to antagonise (Section 1.4.1 & 1.4.2), it is predominantly expressed in the liver (Section 1.4.3), in addition to targeting precedents *in vivo* (Section 1.4.4). There is though a caveat that the molecule fate upon binding could influence the targeting result (Section 1.4.4.1).

The hIFN has a discrete interaction with the systemically expressed hIFNAR (Section 1.5.2) to initiate a diverse cellular response (Section 1.5.2), priming for a potent anti-viral or anti-proliferative phenotype (Section 1.5.3 & 1.5.4). This potency comes at a cost as it also results in debilitating side effects due to off-target interactions. Hence, it is prime candidate for dAb-mediated localised targeting.

Ga-68 (Section 1.7.2) labelling of dAb fusions is a novel approach for *in vivo* tracing of the dAb fusion pharmacology. It can be readily produced *in situ* from a Ge-68/Ga-68 generator, and emits 89% positrons for effective potential PET-CT quantitation (Section 1.7.1.1). The short half-life could be a drawback, but the dAb fusions' expected systemic half-lives are conducive to Ga-68 use. SCN-Bn-NOTA (Section 1.7.4.1) presented itself as a conjugation mechanism to reliably synthesise a broadly homogenous species of stable NOTA conjugated protein, in mild reaction

conditions and without necessitating protein modification. The NOTA is also known to stably chelate Ga^{3+} ions without stringent reaction conditions. SPECT sensitivity is low, and PET-MRI is presently unavailable (Section 1.7.1.2); thus in a study focussing on the quantitation of tissue uptake, the highly sensitive PET-CT presents itself as the optimum imaging modality to quantitatively visualise dAb-fusion receptor targeting *in vivo*.

The chosen model system to build upon this knowledge base is an immuno-compromised murine HepG2 xenograft model of HCC (Section 1.6.1). Modelling targeting in a liver cancer model provides a tissue exhibiting discrete expression of ASGPR and IFNAR expression within a full biological system comprising many potential non-specific binding sites. Through diligent comparison to control molecules, it will be possible to discern specific HCC xenograft tissue targeting mediated by ASGPR. Moreover, as a model of human disease, it also allows analysis of the activity of the targeting methodology as a therapeutic strategy.

II

METHODS

2.1 MUTANT FUSION PROTEIN EXPRESSION & PURIFICATION

For the initial pilot study as to whether hIFN-dAbs could target tissue *in vivo* stocks of two HEK293-expressed tool hIFN-dAb fusion proteins were supplied: hIFN-MAXdAb and hIFN-CTRLdAb* (as utilised in Chapter III, starting with Methods 2.2 onwards). However, a further panel of affinity mutant hIFN-ASGPRdAbs were required for more detailed analysis of tissue targeting (Chapter IV). These latter mutants were chosen to be fusion proteins of hIFN mutants hIFN(A), hIFN(C) and hIFN(E) with ASGPRdAb mutants HidAb, MidAb and LodAb (Table 4.1). The DNA templates for these individual proteins were supplied in holding vectors†. Therefore, it was necessary to clone the sequences and splice them together as in line hIFN-ASGPRdAb genetic fusion expression cassettes within a mammalian expression pDOM50 vector with subsequent HEK293e expression and ÄKTA purification (see Appendix Figures 6.4 & 6.5 for a schematic overview).

2.1.1 Expression Vector Construction

This section details the construction of the pDOM50-hIFN-ASGPRdAb expression vectors, specifically: pDOM50-hIFN(A)-HidAb, pDOM50-hIFN(C)-HidAb, pDOM50-hIFN(E)-HidAb, pDOM50-hIFN(A)-MidAb, pDOM50-hIFN(C)-MidAb, pDOM50-hIFN(E)-MidAb, pDOM50-hIFN(A)-LodAb, pDOM50-hIFN(C)-LodAb, and pDOM50-hIFN(E)-LodAb.

2.1.1.1 PCR Cloning & Amplification of the hIFN Mutants

High fidelity *Pwo*‡ PCR reactions were performed for each individual hIFN mutant to clone and amplify its sequence from its holding vector. The sense primer AGP-P1 (Table 2.1) was complementary to the 5' end of the hIFN sequences and introduce a BamHI restriction site (GGATCC) and the mammalian post-translational cleavage/excretion leader sequence Threonine-Glycine (ACCGGC) as

* Kindly supplied by Dr Adam Walker and Dr Ed Coulstock, GSK.
† Kindly supplied by Dr Thil Batuwangala and Dr Armin Sepp, GSK.
‡ *Pwo* is a proofreading polymerase and so is 18x more accurate than *Taq* polymerase for DNA <3kb

a 5' overhang. The anti-sense primer AGP-P2 maintained the 3'-end of the hIFN sequence.

The 50µl PCR reaction mixture of 1µl respective hIFN vector DNA (1ng), 1µl (2µM final) AGP-P1 primer, 1µl (2µM final) AGP-P2 primer, 25µl Roche *Pwo* MasterMix and 22µl clinical grade water (cgH_2O) underwent PCR cycling in a Bio-Rad DNA Engine Tetrad 2 Peltier Thermal Cycler using the protocol outlined in Table 2.2.

Table 2.1
PCR Primers for hIFN-ASGPRdAb Expression Cassette

Primer Name	Primer Sequence*	Tm (°C)
AGP-P1 (Sense)	5′-ggatccaccggcTGTGATCTGCCTCAAA-3′	46
AGP-P2 (Anti-Sense)	5′-TTCCTTACTTCTTAAACT-3′	46
AGP-P3 (Sense)	5′-gaaagtttaagaagtaaggaaGAGGTGCAGCTGTTGGA-3′	54
AGP-P4 (Anti-Sense)	5′-aagcttcattaGCTCGAGACGGTGACC-3′	54
AGP-P1s (Sense)	5′-GGATCCTGTGATCTGC-3′	50
AGP-P4s (Anti-Sense)	5′-AAGCTTCAGCTCGAGAC-3′	52

*lower case represents overhang DNA

The temperature decrease between the denature step and anneal step was slowed using a cooling gradient of 2.5°C/s. The PCR machine lid temperature tracked 5°C above the sample temperature. The amplified DNA was isolated by PCR Purification into 50µl cgH_2O (Appendix 6.1.3.1) and visualised by DNA gel electrophoresis (Appendix 6.1.3.2).

Table 2.2
***Pwo* PCR for hIFN Mutant Amplification**

Step	Temperature (°C)	Time (min:s)	# Cycles
Initial Denaturation	94	2:00	1
Denature	94	0:30	30
Anneal	42	0:30	
Extension	72	2:00	
Final Extension	72	10:00	1
Soak	4	∞	1

2.1.1.2 PCR Cloning & Amplification of the ASGPRdAb Mutants

High fidelity *Pwo* PCR reactions were performed for each individual ASGPRdAb mutant to clone and amplify its sequence from its holding vector. The sense primer AGP-P3 (Table 2.1) was designed to anneal to the 5' end of the ASGPRdAb sequences and introduce a splice overlap extension (SOE) PCR overhang complementary to the hIFN mutants' 3' sequence. The dAb anti-sense primer AGP-P4 (Table 2.1) introduced a double transcriptional stop codon (TAATGA) and a HindIII restriction site (AAGCTT).

The 50µl PCR reaction mixture of 1µl of the respective ASGPRdAb vector DNA (1ng), 1µl (2µM final) AGP-P3 primer, 1µl (2µM final) AGP-P4 primer, 25µl Roche *Pwo* MasterMix and 22µl cgH_2O underwent PCR cycling in a Bio-Rad DNA Engine Tetrad 2 Peltier Thermal Cycler using the protocol outlined in Table 2.3.

The temperature decrease between the denature step and anneal step was slowed using a cooling gradient of 2.5°C/s. The PCR machine lid temperature tracked 5°C above the sample temperature. The amplified DNA was isolated by PCR Purification into 50µl cgH_2O (Appendix 6.1.3.1) and visualised by DNA gel electrophoresis (Appendix 6.1.3.2).

Table 2.3
***Pwo* PCR for ASGPRdAb Mutant Amplification**

Step	Temperature (°C)	Time (min:s)	# Cycles
Initial Denaturation	94	2:00	1
Denature	94	0:30	30
Anneal*	51	0:30	
Extension	72	2:00	
Final Extension	72	10:00	1
Soak	4	∞	1

2.1.1.3 SOE PCR of hIFN-ASGPRdAb Expression Cassette

The constructs for the required hIFN and ASGPRdAb sequences (Table 4.1) were spliced together and amplified by SOE PCR to create the hIFN-ASGPRdAb fusion sequences as blunt-ended expression cassettes.

The 50µl PCR reaction mixture of 1µl (1ng) PCR product encoding the respective hIFN mutant, 1µl (1ng) PCR product encoding the respective ASGPRdAb mutant with SOE overhang, 25µl Roche *Pwo* MasterMix, 21µl cgH_2O underwent

PCR thermal cycling in a Bio-Rad DNA Engine Tetrad 2 Peltier Thermal Cycler as outlined in Table 2.4. After four cycles 1µl (2µM final) sense primer AGP-P1s (Table 2.1) and 1µl (2µM final) α-sense primer AGP-P4s (Table 2.1) were added.

The temperature decrease between the denature step and anneal step was slowed using a cooling gradient of 2.5°C/s. The PCR machine lid temperature tracked 5°C above the sample temperature. The amplified fused DNA sequences were isolated by gel extraction purification (Appendix 6.1.3.3) and visualised by DNA gel electrophoresis (Appendix 6.1.3.2).

Table 2.4
SOE *Pwo* PCR for hIFN-ASGPRdAb Splicing

Step	Temperature (°C)	Time (min:s)	# Cycles
Initial Denature	94	2:00	1
Denature	94	0:30	4
Anneal	55	0:30	
Extension	72	2:00	
Soak	4	∞	1
ADD PRIMERS			
Denature	94	0:30	26
Anneal	55	0:30	
Extension	72	2:00	
Final Extension	72	10:00	1
Soak	4	∞	1

2.1.1.4 Constructing the Recombinant pDOM50-hIFN-ASGPRdAb Expression Vectors

Each of the hIFN-ASGPRdAb expression cassettes was recombined into the expression vector pDOM50, a vector based on pTT5 vector derivative with an N-terminal Kozak consensus sequence and a murine-derived secretion V-J2-C signal sequence (Appendix Figure 6.6).

Firstly, the Invitrogen Zero Blunt TOPO PCR Cloning Kit was utilised to clone all the hIFN-ASGPRdAbs' blunt end SOE PCR constructs into pCR-Blunt II-TOPO holding vector for amplification of the hIFN-ASGPRdAb expression cassette*. The 6µl reaction mixture consisted of 1µl (25ng) pCR-Blunt, 4µl (4ng)

* The covalently attached TOPO isomerases catalyse the direct insertion of the blunt ended hIFN-ASGPRdAb constructs into the pCR-Blunt vectors.

hIFN-ASGPRdAb SOE construct and 1µl Salt Solution. This was incubated at room temperature for 10min, before resting on ice. The reaction mix was then utilised immediately to transform DH5α E. coli (Appendix 6.1.3.4) with kanamycin selective culturing. Colony *Taq* PCR (Appendix 6.1.3.5) of subsequent cultures utilised the insert's internal annealing sense primer AGP-P1s (1µM final) (Table 4.3) and the pCR-Blunt specific anti-sense primer M13R (1µM final) to confirm the correct pCR-Blunt-hIFN-ASGPRdAb recombination orientation was achieved based on the presence of a PCR product as seen by DNA gel electrophoresis (Appendix 6.1.3.2). The chosen clones were sequenced using commercial primers M13F & M13R (Appendix 6.1.3.6) and any non-recombinant or incorrectly mutated clones were excluded and a colony selected for each mutant pCR-Blunt-hIFN-ASGPRdAb construct. The selected pCR-Blunt-hIFN-ASGPRdAb recombinant plasmids from those colonies were subsequently amplified and purified by DNA MiniPrep (kanamycin selection pressure during growth) (Appendix 6.1.3.7). The purified pCR-Blunt-hIFN-ASGPRdAb plasmids were resolved by DNA gel electrophoresis, the concentrations measured by UV spectrophotometry at 260nm and DNA sequencing performed.

A BamHI/HindIII (12.5U) double restriction digest in buffer SuRE/Cut B (Appendix 6.1.3.8) was then performed on all the MiniPrep pCR-Blunt-hIFN-dAb samples (~2µg) in addition to the pDOM50 vector. The cut constructs and pDOM50 were purified by gel extraction (Appendix 6.1.3.3).

T_4 DNA ligase recombined the respective pDOM50-hIFN-ASGPRdAb expression constructs. A 10µl reaction mix consisted of 1µl (25ng) cut pDOM50 vector DNA, 5µl (5ng) cut insert DNA, 1µl 10x T_4 Ligase Buffer, 2µl ddH_2O and 1µl New England Biolabs (NEB) T_4 DNA Ligase. This was incubated for 10min at room temperature, before being immediately used in its entirety to transform DH5α E. coli with carbenicillin selective culturing. Colony *Taq* PCR of subsequent cultures utilising the pDOM50 upstream sense primer DT039 AATGACATCCACTTTGC (1µM) and the pDOM50 downstream anti-sense primer DT045 TCAGGTTTAGTTCGTCCGGG (1µM) was performed to confirm recombination was achieved by DNA gel electrophoresis. The chosen clones were then sequenced using the DT039 and DT045 primers, with any non-recombinant or incorrectly mutated clones excluded and a colony selected for each mutant pDOM50-hIFN-ASGPRdAb construct. These chosen colonies were subsequently used in DNA

MiniPrep (carbenicillin selection pressure during growth) to amplify the respective pDOM50-hIFN-ASGPRdAb expression vectors. The purified vectors were resolved by DNA gel electrophoresis and the concentrations measured by UV spectrophotometry at 260nm. As above, the process of DH5α transformation followed by Colony *Taq* PCR and sequencing was used to select a colony for each pDOM50-hIFN-ASGPRdAb. These colonies were used to amplify and purify the pDOM50-hIFN-ASGPRdAbs by DNA MegaPrep (carbenicillin selection pressure during growth) (Appendix 6.1.3.9). The purified pDOM50-hIFN-ASGPRdAb plasmids were resolved by DNA gel electrophoresis and the concentrations of a 1:100 TE dilution sample measured using UV spectrophotometry at 260nm, plus DNA sequencing with DT039 and DT045 to confirm full fidelity to the designed sequences.

2.1.2 HEK293E hIFN-ASGPRdAb Expression

A HEK293E mammalian cell expression system was utilised to produce the hIFN-ASGPRdAb mutants as recombinant proteins with full post-translational modifications* with one preparation for each pDOM50-hIFN-ASGPRdAb.

HEK293e cells were incubated at 37°C 5% CO_2 in 500ml Geneticin-selective Gibco 293 Freestyle Expression Medium with 10ml Anti-Shear contained in Erlenmeyer flasks with 125rpm horizontal shaking. The cells were grown to a seeding density between ~$1.75x10^6$ cells/ml and a viability >95% for transfection†.

Transfection reagent 293Fectin was added to 10ml Opti-MEM media to a 1.33µl/ml final concentration and incubated at room temperature for 5min. The relevant pDOM50-hIFN-ASGPR (50µg) was added to 10ml Opti-MEM and incubated at room temperature for 5min. The 293Fectin and plasmid solutions were mixed and incubated at room temperature for 30min before addition to the primary cell culture. Cells were returned to 125rpm shake incubation 37°C 5% CO_2 until cellular viability had reached <90% (~5 days).

To harvest the protein, the cell culture was transferred to a 500ml centrifuge tube and centrifuged for 30min at 3600rpm 4°C and the supernatants vacuum filtrated with a 500ml Rapid-Flow 0.2µm filter unit.

* Graciously performed in my absence by Katy Childerley
† Cells were not utilised beyond passage 25

2.1.3 hIFN-ASGPRdAb Protein Purification by ÄKTA HiTrap mAbSelect Xtra Chromatography

Each batch of hIFN-ASGPRdAb from the panel of nine proteins underwent purification using this method.

All lines and pumps of the ÄKTA Purifier were purged with 6M guanidine hydrochloric acid (GuHCl) followed by 20% ethanol (EtOH) by executing the SamplePumpPurify protocol. All pump lines were purged of air using a 20ml syringe. Lines were primed with 0.1M pH6 sodium acetate (NaAc) and 0.1M pH3.3 NaAc. A HiTrap mAb-Select Xtra 5ml column* was installed, taking care not to introduce any air bubbles. The column was primed with 4 column volumes (CV) 6M GuHCl followed by 4CV 20% EtOH. A column wash with 4CV 0.1M pH6 NaAc completed the column priming. A 96-well deep plate was filled with 500µl 1M pH6 NaAc per well and loaded onto a FC950 fraction collector. The method parameters, as assigned in UNICORN software, included 480ml of protein expression filtered supernatant loaded at a 5ml/min flow-rate, followed by 1.5ml fraction collection in the 96 well plate with a serpentine elution pattern and an elution gradient of 20CV 0.1M pH6 NaAc with 0-100% 0.1M pH3.3 NaAc.

Sodium dodecyl sulphate polyacrylamide gel electrophoresis (SDS-PAGE) (Appendix 6.1.3.10) was performed on 9µl of those wells containing protein eluate, as indicated by the UV elution trace, to qualify the amount of protein present as well as assess its purity. All fractions with a high concentration of expressed protein were pooled and 0.22µm filtered. The final concentration was measured by UV spectrophotometry at 280 nm and purity was determined by SDS-PAGE (2µg).

Fractions were flash frozen using ethanol freezing (Appendix 6.1.3.11) and stored at -20°C.

* 5mg/ml maximum load

2.2 NOTA Conjugation of Fusion Proteins and *in vitro* Functional Analysis

In order to radiolabel the dAb fusions they were first conjugated with NOTA and then their new biophysical and biological *in vitro* properties characterised, as detailed in these methodologies (see Appendix Figure 6.1 for a schematic overview).

2.2.1 NOTA Conjugation & Purification

2.2.1.1 NOTA Conjugation Reaction

The hIFN-MAXdAb, hIFN-CTRLdAb and all nine of the hIFN-ASGPRdAb mutants (Table 4.2; created in Methods 2.1) were NOTA conjugated.

All buffers were formulated with TraceSelect reagents. The fusion protein (up to 3 ml) was dialysed for ≥16hours at room temperature using a GeBAflex Maxi 3.5kDa dialysis tube immersed in Chelex-containing 0.05M pH9.2 HCO_3^- buffer, with pH adjustment with TraceSelect 0.1M HCl or additional Chelex. The dialysed protein was transferred to a 2ml Lo-Bind tube. The protein concentration was measured using UV spectrophotometry at 280 nm to calculate recovery.

A 10µg/µl solution of Macrocyclics p-SCN-Bn-NOTA was prepared in 0.05M pH 9.2 HCO_3^- buffer immediately before addition to the dialysed protein in a 10:1 NOTA:protein molar ratio. The reaction was incubated at room temperature in the dark for ~4 hours with 20rpm rocking, and stored at 4˚C until purification.

2.2.1.2 Protein-A Batch Purification of NOTA Conjugates

All buffers were formulated with TraceSelect reagents. GE Healthcare Protein A Sepharose 4 FastFlow was bedded in a 10ml Bio-Rad Poly-Prep chromatography column using 1ml of Protein A sepharose per 5mg of fusion protein and equilibrated with 20CV 25mM pH6 NaAc.

The respective NOTA conjugation reaction mix from Method 2.2.1.1 was loaded onto the column and the eluate collected. The eluate was reloaded onto the

column ≥5 times to ensure all dAb fusion was captured, as confirmed by SDS-PAGE loading 9µl (Appendix 6.1.3.10) and UV spectrophotometry at 280nm.

The column was washed with 20CV 25mM pH6 NaAc. The flow-through was analysed by SDS-PAGE loading 9µl and UV spectrophotometry at 280nm for protein breakthrough.

The column was eluted in 5 fractions of 1CV 25mM pH3.3 NaAc into 0.02CV 1M pH6 NaAc pre-loaded into 2.0ml polypropylene tubes. Fraction protein concentration was measured using UV spectrophotometry at 280 nm and the sample purity was analysed by SDS-PAGE (2µg). Free NOTA contamination was also determined using ^{111}In labelling (see Section 2.3.3 without the purification step), with Ammonia:Methanol (AM) instant Thin Layer Chromatography (iTLC) analysis (Section 2.3.4). Fractions were flash frozen using ethanol freezing (Appendix 6.1.3.11) and stored at -20°C.

2.2.1.3 Mass Spectrometry of Fusion Proteins

Samples of the fusion proteins were diluted as required in pH4.5 NaAc to 0.5mg/ml, in a total volume of 50µl, and transferred into 300µl fused glass insert vials with a 9mm Screw Top seal. A Micromass LCT Mass Spectrometer, in conjunction with an Agilent 1100 Series High Pressure Liquid Chromatography (HPLC) machine, was utilised to analyse samples. Samples were arranged in the auto-sampler and the runs controlled by MassLynx software.

Alternatively, proteins were prepared in the same manner and sent away to GSK Analytical Chemistry Services (GSK, Stevenage) for mass spectroscopic protein mass fingerprinting analysis. The data was analysed utilising Waters MassLynx Mass Spectrometry software.

2.2.2 SPR Kinetic Analysis of the Fusion Proteins' interactions with ASGPR & hIFNAR

GE Healthcare Biacore SPR was utilised to determine the kinetics of the various fusion proteins (with and without NOTA conjugation) with their target receptors ASGPR and hIFNAR. The Biacore machines were used based on availability with a preference for the Biacore T200. The hIFN-MAXdAb, NOTA-

hIFN-MAXdAb and NOTA-hIFN-CTRLdAb's interaction with ASGPR was determined on both the Biacore T200 and Biacore 3000, and their interaction with hIFNAR on the Biacore 3000. The hIFN-ASGPRdAb mutant's interaction with ASGPR was determined on both the Biacore T200 and Biacore 3000, whereas the NOTA-hIFN-ASGPRdAb mutants were analysed only on the Biacore 3000. The hIFN-ASGPRdAbs and the NOTA-hIFN-ASGPRdAb mutants' interactions with hIFNAR were determined on the Biacore 3000 only.

The respective protocols, as described in Methods 2.2.2.1 and 2.2.2.2, were performed the same regardless of the sample analytes.

2.2.2.1 Biacore T200 Surface Plasmon Resonance

Before each new run the Biacore T200 system was desorbed and sanitised with the GE Healthcare Biacore Maintenance Kit, and primed with HBS-P+ buffer*.

A Biacore S-Series CM5 chip coated with approximately 500RU of the recombinant ASGPR-H1-CRD ligand† by amine coupling to the carboxymethylated dextran surface in pH5.5 NaAc (Appendix 6.1.3.12) was primed with HBS-P+ at a flow rate 30µl/min until the baseline RU value stabilised to less than 3 resonance units (RU) drift in all flow cells (FC).

Sample analytes were prepared in a 1:2 serial dilution from 64nM to 0.5nM in HBS-P+ buffer from 1µM protein stock solutions in a 96 Square Well Storage Plate. The HBS-P+ buffer flow rate was constant at 30µl/min and the chip compartment at 25°C (sample bay was cooled to 4°C). Samples were injected in a randomised order onto the chip in an association phase totalling 30s, followed by a dissociation phase of 300 seconds. Samples were interspersed with HBS-P+ 'Blank' injections to monitor baseline drift and provide a baseline RU value during analysis The chip surface was regenerated by a single 6µl Glycine 2.0 injection, in addition to two conditional regeneration repeats to maintain a less than 3 RU baseline drift.

Results were analysed using BIA Evaluation software and the curves exported to Microsoft Office Excel. The chip was stored in HBS-P+ buffer at 4°C.

* This was to remove any EDTA present in the system as this would chelate the Ca^{2+} ions necessary for effective ASGPR function

† Kindly provided by Peggy Luong and Dr Thil Batuwangala

2.2.2.2 Biacore 3000 Surface Plasmon Resonance

Before each new run the Biacore 3000 system was sanitised and desorbed with the GE Healthcare Biacore Maintenance Kit, then rinsed and primed with degassed HBS-P+ buffer.

A Biacore CM5 chip was coated with approximately 500RU of self-made recombinant ASGPR-H1-CRD (Appendix 6.1.9.3) and R&D Systems recombinant hIFNAR2 by amine coupling to the carboxymethylated dextran surface in pH5.5 NaAc (Appendix 6.1.3.12) (FC was left blank, whilst FC2 was coated with ASGPR and FC3 with hIFNAR2). Before each usage, the CM5 chip was primed with degassed HBS-P+ at a flow rate of 30µl/min at 25°C until the baseline RU value stabilised to less than 3RU sensogram drift in all flow cells.

Samples were prepared in serial dilution, normally 1:2 from 250nM to 1nM in HBS-P+ buffer from 1µM protein stock solutions in a 96-well round-bottom plate. A text file (Appendix 6.1.3.13) was written detailing constant HBS-P+ buffer flow rate of 30µl/min, sample injections in ascending concentration order (interspersed with HBS-P+ 'Blank' injections), an association phase totalling 30s, followed by a dissociation phase of 300 seconds and regeneration by two 5µl Glycine 2.0 injections.

Results were analysed using BIA Evaluation software and exported to Microsoft Office Excel. The chip was stored in HBS-P+ buffer at 4°C.

2.2.3 HEK-Blue Reporter Assay for hIFN Bioactivity Quantitation

HEK-Blue cells were cultured to ~70%-80% confluency in a humidified incubator at 37°C 5% CO_2 (Appendix 6.1.4.1). The weakly adherent cell monolayer was gently washed with 10ml PBS, resuspended with the addition of 10ml culture medium and pipetted over the cell culture surface to ensure full re-suspension of all HEK-Blue cells. The total live cell count was determined by Trypan Blue automated counting (Appendix 6.1.4.4), and the cells were pelleted by centrifugation at 1250rpm 4°C for 5min, and resuspended to a final cell density of $1x10^6$cells/ml in culture medium.

HEK-Blue cell suspension aliquots of 50µl were pipetted to each relevant well of a 96-Well Flat Bottom Cell Culture Plate, for a cell count of 50000 cells per well. Cell plates were incubated in a humidified incubator at 37°C 5% CO_2 until required.

Sample proteins were diluted in a 1:3.33/1:3 logarithmic serial dilution of 1nM to 3fM starting from 300µl 2nM, by a 90µl serial transfer into alternating 210µl and 180µl volumes of culture medium with thorough mixing. Sample aliquots of 50µl were pipetted in series into the cell culture plate in triplicate. A hIFNα positive control row and a culture medium only negative control row were included on each plate. Reaction plates were incubated at 37°C 5% CO_2 for 16 hours.

A sachet of QUANTI-Blue reagent was reconstituted in 100ml of ddH_2O. The reaction culture plates were mirrored into fresh optical flat-bottomed 96 well plates by transferring 40µl of all supernatants and 160µl QUANTI-Blue reagent added to each well. Plates were developed at room temperature until the hIFNα 1nM control well had reached approximately 1.0A colour intensity, as observed on a Bio-Rad Spectrophotometric Plate Reader at an optical density of 640nm.

Data was analysed using GraphPad Prism graphical software, with plates normalised relative to the hIFNα control for inter-plate comparisons.

2.2.4 FACS Flow Cytometry Assays of hIFN-dAb Whole Cell Binding to HepG2 and U937 cells

Fluorescence-Activated Cell Sorting (FACS)* was performed on NOTA-hIFN-MAXdAb, hIFN-MAXdAb, NOTA-hIFN-CTRLdAb, hIFN-CTRLdAb, MAXdAb, hIFN, and all the NOTA-hIFN-ASGPRdAb mutants to measure their binding to whole cells HepG2 (ASGPR+/hIFNAR+) and U937 (ASGPR-/hIFNAR+).

The HepG2 and U937 were first incubated with the primary analyte in suspension, followed by staining with either a secondary anti-dAb mouse mAb for dAb detection or a secondary anti-hIFN mAb, and finally stained with a tertiary goat anti-mAb pAb carrying the Alexa647 fluorophore (Alexa647) (Figure 3.11). The cells were also stained with DNA binding Live/Dead PI stain, a cell membrane impermeant. Data on 50000 events was collected for each analyte sample. Cells were

* Adapted from a protocol provided by Dr Laura Goodall (personal communication)

first gated based on their uptake of PI stain into live (i.e. no PI staining) and dead cells based on their 614nm emissions (Appendix Figure 6.11). The live cells were subsequently analysed for the presence of Alexa647 at 647nm (representing hIFN-dAb binding) and a histogram plotted of the FL4-H intensity data. The calculated mean intensity can thus be used as a semi-quantitative proxy for binding levels*.

In addition to the analyte samples, data was acquired for the presence of the receptors with anti-ASGPR, anti-hIFNAR1, and anti-hIFNAR2 mouse mAbs by running these mAbs in the same manner. Non-specific binding by the analyte detection secondary antibodies anti-dAb and anti-hIFN was similarly controlled for. The general non-specific binding background was controlled for using an irrelevant IgG1 mouse λ isotype control with no specific affinity for either cell line. Non-specific staining was controlled for using PI, Alexa647 and PI+Alexa647 only controls and necessary primary and secondary antibody controls to gauge non-specific staining.

HepG2 and U937 cells were cultured to 70-80% confluency in a humidified incubator at 37°C 5%-CO_2. Cells were processed to the pellet stage of their respective subculture protocol (Appendix 6.1.4.1) Sample proteins were diluted to 1μM in FACS Buffer (Table 2.5), all antibodies were diluted to 1μg/ml in Staining Buffer and propidium iodide (PI) dead cell stain to 1μg/ml in PBS.

The supernatant was aspirated and the cell pellet resuspended in 20ml Dulbecco's Modified Eagle Medium (DMEM) supplemented with 1% (v/v) Fetal Bovine Serum (FBS) by gentle mixing. The total live cell count was determined, and the cell resuspension was centrifuged again at 1250rpm 4°C for 5min, and then resuspended in DMEM supplemented with 1% (v/v) FBS for a final concentration of $5x10^6$ cells/ml.

Table 2.5
Flow Cytometry Buffer Recipes

REAGENT*	COMPONENTS	VOLUME (ml)
FACS Buffer	PBS (+Mg^{2+}/Ca^{2+})	500
	FBS	50
Staining Buffer	PBS (+Mg^{2+}/Ca^{2+})	500
	FBS	5

*Stored at 4°C

* Assumes a 1:1 stoichiometry for the primary antibodies with their respective targets and binding of Alexa647 being equal for each of the primary antibodies – a multimeric primary antibody stoichiometry or multiple Alexa647 binding profiles would artificially amplify the signal giving false positive data – and so the relevance of data must be judged on their individual merits

Cells were multipipetted as 200µl aliquots into relevant wells of a 96-Well V-bottom plate for $1x10^6$ cells per well. The cells were then pelleted by centrifugation at 1200rpm 4°C for 3min. The supernatants were discarded by carefully inverting the plate over a sink and the pellets dried by gently striking the upturned plate against a pile of paper towel. The pellets were washed with 200µl of FACS Buffer, and then re-pelleted by centrifugation at 1200rpm 4°C for 3min and the liquid removed as before.

Cell pellets were resuspended either in 50µl 1µM sample protein PBS+ solution or 50µl FACS Buffer only for controls. The cell plates were then incubated at 4°C for 1 hour before cells were then pelleted by centrifugation at 1200rpm 4°C for 3min. The cell pellets were subsequently washed with 200µl FACS Buffer, pelleted by centrifugation at 1200rpm 4°C for 3min, and the supernatants discarded. This wash process was repeated twice more.

Cell pellets were resuspended in 100µl of the relevant 1µg/ml primary antibody Staining Buffer solution and relevant control pellets resuspended in 100µl Staining Buffer only. The cell plates were then incubated at 4°C for 30min before cells were then pelleted by centrifugation at 1200rpm 4°C for 3min. The cell pellets were subsequently washed with 200µl FACS Buffer three times as above.

Cell pellets were resuspended in 100µl of AlexaFluor 647 1µg/ml primary antibody Staining Buffer solution and relevant control pellets resuspended in 100µl Staining Buffer. The cell plates were then incubated at 4°C for 30min before cells were then pelleted by centrifugation and washed three times as above.

Cell pellets were resuspended in 100µl PI stain PBS+ solution and relevant control pellets resuspended in 100µl PBS+. The cell plates were then incubated at 4°C for 10min. The cells were transferred to 5ml FACS tubes containing 1ml PBS. Cells were kept in suspension by gentle vortexing.

Cell staining data was acquired using a BD Biosciences FACSCalibur equipped with a 15mW argon ion laser emitting at 488nm (Alexa647) in addition to a 635nm red laser (PI Stain). Cells were gated with BD FACSDiva software, and 50000 events captured. Results were analysed using FlowJo analysis software.

2.2.5 ^{68}Ga Radioligand Binding Assay

A radioligand binding assay was developed for a 96-well format to attempt to quantify binding of Ga-68 radiolabelled NOTA-hIFN-MAXdAb and NOTA-hIFN-CTRLdAb to whole HepG2 cells.

HepG2 cells were cultured to 70-80% confluency in a humidified incubator at 37°C 5%-CO_2 (Appendix 6.1.4.1). The cells were washed with 10ml of PBS before adding 5ml of Gibco Cell Dissociation Buffer for cell detachment. The flasks were returned to 37°C incubation until all cells were detached before resuspension with an additional 5ml DMEM 10%-FBS.

Cell resuspensions were combined and centrifuged at 1250rpm 4°C for 5min. The supernatant was aspirated and the cell pellet resuspended in 20ml Binding Buffer (Table 2.6) by gentle mixing. The total live cell count was determined by Trypan Blue cell counting. The cell resuspension was centrifuged again at 1250rpm 4°C for 5min, and then resuspended in Binding Buffer to a final concentration of $2x10^6$ cells/ml.

The cell suspension was multi-pipetted in 50µl aliquots ($1x10^5$ cells) into a v-bottomed 96 well plate, three wells per radioligand and competitor concentration, in addition to a row for total protein quantitation. Plates were stored at 4°C until required. A 4µM competitor mix stock of hIFN-MAXdAb alone was prepared in Binding Buffer and 25µl aliquots were pipetted into competitor wells. All remaining wells were topped up with 25µl Binding Buffer.

Table 2.6
Radioligand Binding Assay Buffer Recipes

Reagent	Components	Volume (ml)
Binding Buffer	DMEM	500
	FBS	5
Wash Buffer	PBS w/ Mg^{2+}/Ca^{2+}	500
	FBS	5

The NOTA-hIFN-MAXdAb and NOTA-hIFN-CTRLdAb were radiolabelled with Ga-68 using the 1M NaAc labelling method (see Method 2.3.2) with an extended 15min incubation and no EDTA reaction quench*. The 1µM Ga-

* Reaction was not quenched with EDTA to avoid Ca^{2+} chelation which is necessary for ASGPR binding

68 reaction mix was serially diluted 1:2 in Binding Buffer to give a serial dilution series ranging from 128nm-1nm in a final volume of 200µl*.

25µl aliquots of the serially diluted radioligand were multi-pipetted into the binding and competitor wells of the cell plate and 10µl aliquots of each radioligand concentration added to 0.5ml tubes in triplicate as counting controls. The total protein wells were topped up with 25µl binding buffer.

The plate was incubated at 18°C for 1 hour , centrifuged at 1200rpm for 5mins and the supernatant removed.. The cell pellets were resuspended in 150µl Wash Buffer (Table 2.15) and re-centrifuged at 1200rpm for 5min. The wash step was repeated twice more, and finally re-pelleted by centrifugation at 1200rpm for 5min.

The cell pellets were resuspended in 100µl PBS and multi-pipetted to 0.5ml tubes and counted along with the controls in a LKB Wallac 1282 Compugamma CS Universal Gamma Counter. Data was analysed using Microsoft Excel and GraphPad Prism.

To estimate the amount of protein added to each well, the Bio-Rad DC Protein Assay was carried out ontotal protein wells.e. Cell pellets were resuspended in 50µl 1M NaOH and incubated at room temperature for 10mins. The samples were made up to 100µl with PBS. A 10mg/ml BSA in ddH_2O mix was created by the same preparation process as the cell samples, before serial dilution 1:2 to create a BSA standard curve. Aliquots of 5µl of samples and standards in triplicate were added to a 96-Well flat-bottomed optical microtitre plate followed by 25µl of Reagent A and 200µl of Reagent B. The plate was agitated to mix the reagents and left for 15mins at room temperature. The plate was read using a Bio-Rad Spectrophotometric Plate Reader at 640nm, and the standard BSA protein curve utilised to estimate the total protein content of the cells.

* 75µl for binding assay wells n=3, 75µl for blocking assay wells n=3, and 30µl for loading controls n=3

2.3 RADIOLABELLING

2.3.1 Gallium-68 Elution Design & Operation

An Eckhert & Ziegler 370MBq (1MCi) IG100 $^{68}Ge/^{68}Ga$ Generator was used to produce ^{68}Ga for all experimentation, and was eluted using 0.1M HCl made with TraceSelect reagents. The generator was eluted at least once within 24 hours prior to experimentation and no more than once every four hours.

An elution system was designed applying the principles of ALARP with lead shielding >1cm in thickness used as appropriate and the generator housed within a Hot Cell. Fluorinated ethylene propylene tubing, in conjunction with polypropylene Luer-Luer connectors and polyvinylidene fluoride (PVDF) three-way stopcocks, were utilised to construct an adaptable manual elution system for $^{68}GaCl_3$ collection, which could be controlled from outside the Hot Cell (Figure 2.1). The system also included a Bio-Rad peristaltic pump with a timer to facilitate automatically eluting the generator every 24hours. An inline airlock protected the generator from gaseous contaminants. No rubber was used within the system, neither in airlock seals nor

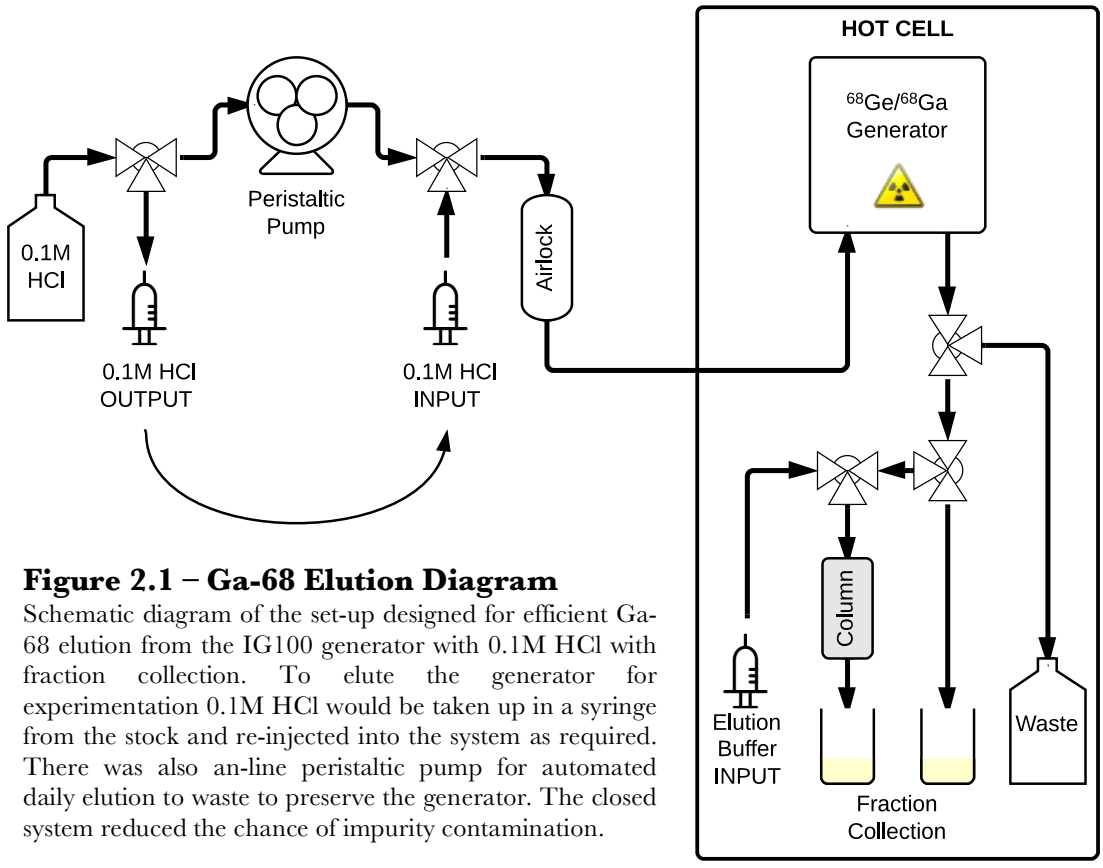

Figure 2.1 – Ga-68 Elution Diagram
Schematic diagram of the set-up designed for efficient Ga-68 elution from the IG100 generator with 0.1M HCl with fraction collection. To elute the generator for experimentation 0.1M HCl would be taken up in a syringe from the stock and re-injected into the system as required. There was also an-line peristaltic pump for automated daily elution to waste to preserve the generator. The closed system reduced the chance of impurity contamination.

syringes. The valves allowed for direct injections, bypassing the pump, for the manual elutions. The outflow could be directed for collection or to a shielded waste bottle by three-way PVDF stopcock. The outflow was either connected to a catheter for accurate elution volumes or a cationic exchange column. Another three-way valve prior to the outflow allowed injection of buffers or air directly onto an attached cationic exchange column.

Radioactivity measurements were performed using a Capintec CRC-15PET radioisotope dose calibration chamber. Labelling was quantified in all instances by a combination of AM)-iTLC, Citric Acid (CA)-EDTA iTLC and 2% bovine serum albumin (BSA) solid phase with water-ethanol-ammonia (WEA) liquid phase iTLC, and corroborated with size exclusion (SE)-HPLC as appropriate.

2.3.2 1M NaAc ^{68}Ga-NOTA-hIFN-dAb Labelling

Radiolabelling and subsequent purification of ^{68}Ga-NOTA-hIFN-MAXdAb, ^{68}Ga-NOTA-hIFN-CTRLdAb, and all the mutant ^{68}Ga-NOTA-hIFN-ASGPRdAbs was performed as detailed below.

All buffers were formulated with TraceSelect reagents. NOTA conjugated fusion proteins were rapidly thawed to room temperature prior to starting the assay. The generator was manually eluted with 0.1M HCl. Fractions of 500µl (radioligand binding assays and biodistribution studies) or 250µl (PET studies) were collected covering the top of the elution peak (Appendix Figures 6.12 & 6.13).

A 200µl aliquot of the eluted $^{68}GaCl_3$ in 0.1M HCl was pipetted from the high activity fraction into a 2ml Lo-Bind tube. This was followed by 30.6µl of 1M NaAc*, pipetted slowly with gentle pipette swirling to ensure homogeneity and minimise colloid formation. NOTA conjugated protein in 0.14 M pH 4.5 NaAc was added to give a final concentration of ~2µM for radioligand binding assays and biodistribution studies or 1.1µM for PET studies made up to a total reaction volume of 250µl with 0.14M NaAc pH4.5. The reaction was gently mixed, the total activity measured and incubated at room temperature (37˚C for PET studies) for 10min. A control reaction with a relevant volume of 0.14M NaAc pH4.5 replacing the protein,

* Method was devised utilising the Henderson-Hasselbach equation to reliably buffer the reaction to pH4.4

was run in parallel. Radiolabelling efficiency was quantified by a combination of 0.02M CA-EDTA iTLC and WEA-iTLC (Section 2.3.4). At this stage the specific activity (MBq/µg) could be calculated for t=0:

$$= \frac{\left((Activity\ MBq) \times e^{\left(-\left(0.693 * \left(\frac{(0-(Time\ mins))}{67.629} \right) \right) \right)} \times \frac{Radiolabelling\ Efficiency\ \%}{100} \right)}{Mass\ \mu g}$$

A PBS equilibrated PD MiniTrap G-25 column was used to purify labelled product from radiochemical impurities into PBS. The column was equilibrated with ~4ml PBS without Ca^{2+}/Mg^{2+} (PBS-) by gravity flow. The whole radiolabelling reaction (250µl) was loaded onto the column and topped up with PBS to a total stacked volume of 0.5ml. The purified radiolabelled product was eluted in a 0.5ml PBS primary fraction (radioligand binding assays), or two of 0.25ml and the second fraction utilised (biodistribution and PET studies). Recovery purity was quantified by a combination of 0.02M CA-EDTA iTLC and WEA-iTLC and the activity of the recovered fraction was measured.

The total radiolabelled protein recovery was calculated from the iTLC values and the activity measurements:

$$= \left(\frac{Fraction\ Purity\ \%}{100} \right) \times \frac{(Fraction\ Activity\ MBq) * e^{\left(-\left(0.693 * \frac{(0-(Time\ mins))}{67.629} \right) \right)}}{(Specific\ Activity\ MBq/\mu g)}$$

2.3.3 Indium-111 Labelling

The NOTA-hIFN-MAXdAb and NOTA-hIFN-CTRLdAbs were radiolabelled with In-111 for the 24 hours biodistribution time point.

A 20µl aliquot of $^{111}InCl_3$ in 0.1M HCl was added to a 0.5ml polypropylene tube, followed by 0.2M pH5 NaAc buffer and the NOTA conjugated fusion protein for a final protein concentration of 3µM in a total reaction volume of 80µl. The reaction mix was gently mixed and the total activity measured using a Capintec CRC-15PET radioisotope dose calibration chamber. The reaction was incubated at 37°C for 2hrs. A control containing 0.14M pH4.5 NaAc buffer instead of the protein

aliquot was incubated in parallel. Labelling was quantified by a combination of 0.02M CA-EDTA iTLC and WEA-iTLC (Section 2.3.4).

A PBS equilibrated PD MiniTrap G-25 column was subsequently used to purify into PBS as described above (Section 2.3.2). Purity was subsequently quantified by a combination of 0.02M CA-EDTA iTLC and WEA-iTLC (Section 2.3.4). The specific activity and radiolabelled protein recovery could be calculated as in Section 2.3.2 exchanging the half-life from 67.629min to 4038.77min.

2.3.4 Instant Thin Layer Chromatography

Three types (Table 2.7) of iTLC were utilised to differentiate between the radioactive species present at the end of radiolabelling reactions (radioligand and radioimpurities), and are relevant for both Ga-68 and In-111 radiolabelling. AM-iTLC identified free NOTA. CA-EDTA iTLC showed the amount of free unreacted radioactivity. WEA-iTLC showed the amount of radioactive colloid. The two values for the radioimpurities together allow the deduction of the radiolabelling efficiency of the radioligand, e.g. ^{68}Ga-NOTA-hIFN-MAXdAb, as a percentage.

Chromatographic Instant TLC Silica Gel (iTLC-SG) was cut into strips of approximately 1cm width and 8cm height. Strips were dried overnight in a 50°C oven and were stored in a sealed container with silica gel desiccant.

Table 2.7
Thin Layer Chromatography Recipes

iTLC Name	Stationary Phase	Mobile Phase*	
		Reagent	Volume (ml)
AM	iTLC-SG	Ammonia 35%	0.1
		Methanol 100%	1
		ddH_2O	0.9
0.02M CA-EDTA	iTLC-SG	Citric Acid 0.04M	1
		EDTA 0.1M	1
WEA	2%-BSA iTLC-SG	Ammonia 35%	0.25
		Ethanol 100%	0.5
		ddH_2O	1.25

* 2ml Total Volume

To make iTLC-SG 2%-BSA strips, iTLC-SG strips were submerged in an excess of 2%(w/v) BSA in ddH_2O at room temperature with gentle rocking for 3

hours. The strips were then baked in an oven at 50°C for ~16 hours. The strips were stored in a sealed container with silica gel desiccant.

For the analysis, a 1µl sample of the radiolabelling reaction was centrally spotted 2cm above the base of the iTLC-SG strip. Once the spot had air-dried onto the strip, it was placed in a 50ml tube and eluted with 2ml of freshly prepared mobile phase. The strips were exposed to a phosphoscreen for ~30s, before being removed from the cassette in a darkened room and scanned using a PerkinElmer Cyclone Phosphor Imager. Images were analysed using PerkinElmer OptiQuant Software.

2.4 *IN VIVO* ANALYSES

2.4.1 Animal Research Statement

All *in vivo* work was performed using SCID Beige mice from Charles River Laboratories, kindly shared by Dr John Maher (Kings College London, London).

All procedures were carried out under the Home Office project license of Professor Stephen Mather (Queen Mary University of London, London) by Home Office individual licensees. All animal work was ethically reviewed and carried out in accordance with the Animals (Scientific Procedures) Act 1986 and the GSK Policy on the Care, Welfare and Treatment of Animals.

Experimental design was guided by the principles of the 'Three Rs'. All *in vitro* avenues of data acquisition were performed before proceeding to *in vivo* data collection.

2.4.2 HepG2 Xenograft Murine Models

HepG2 cells were cultured to 70-80% confluency in a humidified incubator at 37°C 5%-CO_2 (Appendix 6.1.4.1). Cells were incubated with 10ml Cell Dissociation Buffer per flask for ~10min in the incubator until cells had dissociated. Cells were resuspended with the addition of 10ml DMEM, 10% FBS Cell resuspensions from several flasks, with total cell count sufficient to exceed $5x10^6$ cells per xenograft injection, were combined and centrifuged at 1250rpm 4°C for 5min. The supernatant was discarded and the cell pellet resuspended in 20ml DMEM 10%-FBS. The total live cell count was determined using a Trypan Blue cell counting

(Appendix 6.1.4.4) after which the cell resuspension was centrifuged as before and resuspended in DMEM, 10% FBS to a final concentration of $25x10^6$ cells/ml.

A 1ml syringe and attached 23-gauge needle were purged of air using DMEM 10%-FBS, and a 200µl xenograft dose ($5x10^6$ cells) drawn up. This process was repeated for each dose, and the cell suspension was constantly agitated to ensure a homogenous cell concentration for even xenograft dosing.

The murine SCID Beige mice were dosed subcutaneously in the left flank for biodistribution studies or left shoulder for PET studies. Xenografts were grown for ~20 days, until they had reached a mass of ~250µg, before further experimentation.

2.4.3 Radioactivity Biodistribution Studies

The radiolabelled NOTA-hIFN-MAXdAb, NOTA-hIFN-CTRLdAb, NOTA-hIFN(A)-HidAb, NOTA-hIFN(E)-HidAb, NOTA-hIFN(A)-MidAb, NOTA-hIFN(C)-MidAb, NOTA-hIFN(E)-MidAb, NOTA-hIFN(A)-LodAb and NOTA-hIFN(E)-LodAb were used for *in vivo* biodistribution studies to determine HepG2 xenograft tissue uptake (see Appendix Figures 6.2 & 6.3 for a schematic overview).

The NOTA conjugated protein was radiolabelled with Ga-68 (Section 2.3.2) or In-111 (Section 2.3.3) to a specific activity sufficient for a total activity greater than 0.5MBq/dose at injection. The subsequently purified 250µl G-25 eluate was diluted with PBS supplemented with 1%(w/v) BSA* to the final required radiolabelled protein concentration in 200µl doses (mostly 1µg at 0.005µg/µl†) with an excess for dosing standards. The 200µl doses were injected into the tail veins of female SCID Beige HepG2 xenograft bearing mice (Section 2.4.2). The dose syringe was both weighed and the dose radioactivity measured in a Capintec CRC-15PET radioisotope dose calibration chamber before and after injection.

At pre-determined timepoints (1h, 3h or 24h) the mice were anaesthetised for cardiac puncture procedure to remove blood and subsequently euthanasia confirmed by cervical dislocation. The carcass was weighed and the tissues and organs were dissected out. The tumour was placed in a labelled, pre-weighed scintillation tube and the new tube mass noted. RNAlater was then added to the tube at approximately 2X the xenograft volume. The intestines, spleen, pancreas, stomach,

* The additional of BSA could reduce the residual dose adhering to the syringe by up to 500%
† For higher injected doses, cold protein was added to give the necessary concentration e.g. 6µg/16µg

kidneys, liver, heart, lungs, blood, muscle and tail were deposited in pre-weighed gamma counter tubes.

Tubes were counted using a 1282 Compugamma CS Universal Gamma Counter, alongside weighed dosing standards (to allow calculation of injected dose). Samples were counted for 60 seconds over a 177-277 energy window with half-life and dead time corrections applied. The tubes with their enclosed tissue were weighed to determine tissue mass. The tumour samples in RNAlater were stored at 4°C for a minimum of 24 hours before being stored at -80°C until required for TaqMan analysis. Results were analysed in Microsoft Excel and graphed using GraphPad Prism.

2.4.3.1 Blocking Dose Biodistribution Study

To test if xenograft tissue uptake binding was specific then an excess of cold MAXdAb ligand was co-injected with a 1µg ^{68}Ga-NOTA-hIFN-MAXdAb dose.

Unconjugated MAXdAb protein was concentrated to 204µM in 0.14M pH6.5 NaAc (a pH that allows direct IV injection into mice, whilst avoiding the pI of the protein thus preventing potential protein aggregation) using a Sartorius Vivaspin-6 5kDa molecular weight cut off (MWCO) concentrator column.

Preparing a blocking dose followed the same protocol as for a normal 1µg biodistribution dose (Section 2.4.3) using a 2µM Ga-68 reaction, attaining post-G25 purified ^{68}Ga-NOTA-hIFN-MAXdAb in PBS. At this stage the eluate was divided to make three normal 1µg doses of ^{68}Ga-NOTA-hIFN-MAXdAb diluted with PBS supplemented with 1%(w/v) BSA in 200µl and three blocking 1µg doses of ^{68}Ga-NOTA-hIFN-MAXdAb diluted with the 204µM MAXdAb solution. This resulted in ~333µg of MAXdAb in the blocking doses. The remainder of the protocol for biodistributions was followed from this point (Section 2.4.3).

2.4.4 PET Imaging of Xenograft Uptake

The NOTA-hIFN-MAXdAb and NOTA-hIFN-CTRLdAb were radiolabelled with Ga-68 to a specific activity sufficient for a total activity greater than 5MBq/dose at injection (Section 2.3.2). The purified G-25 eluate was diluted to the final required dose of ~4µg per 200µl in PBS supplemented with 1%(w/v) BSA or used directly. The 200µl dose was injected into the tail vein of a female SCID

Beige HepG2 xenograft bearing mice (Section 2.4.2). The dose syringe was both weighed and the dose radioactivity measured in a Capintec CRC-15PET radioisotope dose calibration chamber before and after injection. The mouse was left for one hour.

The mouse was anaesthetised using isofluorane, placed on the heated bed of a Siemens Inveon Micro PET/CT system and PET images were acquired for 2 hours, followed by a CT scan. PET images were reconstructed using the OSEM3D algorithm. The images were analysed using Siemens Analysis software.

Once the scans were complete, the mice were sacrificed by cervical dislocation and a biodistribution dissection was performed as described in Method 2.4.3.

2.5 TaqMan Gene Expression

2.5.1 RNA Isolation

The HepG2 tumours samples from the NOTA-hIFN-MAXdAb, NOTA-hIFN-CTRLdAb, NOTA-hIFN(A)-HidAb, NOTA-hIFN(A)-MidAb, NOTA-hIFN(C)-MidAb, NOTA-hIFN(E)-MidAb and NOTA-hIFN(A)-LodAb biodistribution studies, as well as tumours from untreated mice, were used for the TaqMan study.

All steps were performed using aseptic technique to prevent RNA contamination, and samples kept on ice. Working solutions for a Qiagen RNeasy Maxi Kit were prepared and xenograft tissue samples preserved in RNAlater were thawed from -80C on ice. The RNAlater was decanted off carefully and each xenograft tissue transferred into a gentleMACS M tube containing 7.5ml of Buffer RLT. The tissue was homogenised using a gentleMACS dissociator.

The homogenate was centrifuged at 5000g for 10min. The supernatant was removed with a pipette (taking care not to disturb the fatty top layer) and transferred into a 15ml tube. An equal volume of 70% EtOH was added and the mixture vigorously shaken to resuspend all precipitates. The sample was decanted onto a RNeasy Maxi Column in a 50ml centrifuge tube, before centrifugation at 5000xg for between 5 and 20min and the discarding of the flow-through. 15ml of Buffer RW1 was added to the column and it was again centrifuged for 5min at 5000g, followed by

discarding the flow-through. 10ml Buffer RPE was added to the column and it was centrifuged for 2min at 5000g, followed by discarding the flow-through. 10ml Buffer RPE was added to the column and it was centrifuged for 5min at 5000g to dry the silica-gel membrane, followed by discarding the flow-through.

The column was eluted into a fresh 50ml centrifuge tube by pipetting 1.2ml RNase-free ddH_2O directly onto the silica-gel membrane, allowing it to stand for 1min, followed by centrifugation at 5000g for 3min. This step was repeated with another 1.2ml of RNase-free ddH_2O to maximise the RNA yield.

2.5.2 Reverse-Transcription PCR

An Applied Biosystems High Capacity complementary DNA (cDNA) Reverse Transcription Kit was utilised to formulate a 2X Master Mix containing MultiScribe Reverse Transcriptase for a 300µl reverse transcription (RT)-PCR reaction per xenograft RNA sample (Table 2.8). The RT-PCR was run using a Bio-Rad DNA Engine Tetrad 2 Peltier Thermal Cycler (Table 2.9). The resultant cDNA concentration was measured using UV spectrophotometry at 280nm.

Table 2.8
RT-PCR Reaction Mix Recipe

Reagent	Components	Volume (µl)
RT-PCR Master Mix	10X RT Buffer	12
	25X dNTP Mix	12
	10X RT Random Primers	30
	MultiScribe Reverse Transcriptase	15
	RNase Free ddH_2O	63
Purified Tumour Tissue RNA	-	150

Table 2.9
RT-PCR to Amplify cDNA for TaqMan

Step	Temperature (°C)	Time (min:s)	# Cycles
Reverse Transcription	25	10	1
Amplification	37	120	1
Hold	4	∞	-

2.5.3 TaqMan Array

The TaqMan Array Human Interferon Pathway Fast 96-well plate was prepared by centrifugation at 1000rpm for 1min. The TaqMan reaction mix was prepared with ~100ng cDNA (Table 2.10) and TaqMan Universal PCR Master Mix, and thoroughly mixed by gentle inversion. A 10µl aliquot of the TaqMan reaction mix was pipetted into each well of the TaqMan Array plate using a multi-pipette with constant agitation of the stock solution to ensure homogeneity. The plate was sealed with a MicroAmp Optical Adhesive Film and centrifuged at 1000rpm for 1min. The plate was loaded into an Applied Biosystems StepOnePlus, and the software programmed to perform a Standard assay protocol (Table 2.11)* for a 96-Well plate with a 10µl sample volume and to collect fluorescence data at the end of each cycle. Plates were analysed by normalisation to the expression levels of control gene glyceraldehyde-3-phophate (*GAPDH*) utilising the ΔCt-method in Microsoft Excel.

Table 2.10
TaqMan Reaction Mix Recipe

Reagent	Volume (µl)
TaqMan Universal PCR Master Mix	540
RNase Free ddH_2O	270
Tumour Tissue cDNA	270

Table 2.11
TaqMan Thermal Cycling Standard Assay

Step	Temperature (°C)	Time (min:s)	# Cycles
AMPErase UNG Activation	50	2:00	1
AmpliTaq Gold Activation	95	10:00	1
Melt	95	0:15	40
Anneal / Extend	60	1:00	40

* The TaqMan Array plates utilised were of the Fast variety, but as the TaqMan Universal PCR Mix was not a Fast grade reagent, the Standard protocol was chosen

III

HepG2 Xenograft Targeting of ^{68}Ga-NOTA-hIFN-dAb

Does fusion of hIFN to an ASGPR targeting dAb increase tumour specific uptake of hIFN in a HepG2 xenograft model?

3.1 INTRODUCTION

The ability of dAb fusions to target xenograft tissue *in vivo* had never previously been shown. Therefore, the specific uptake of a ^{68}Ga-NOTA-hIFN-dAb in an *in vivo* HepG2 model was to be used to validate the model as the basis for further uptake modelling work using biodistribution and PET-CT studies. This would was intended to be demonstrated with pre-made fusion proteins hIFN-MAXdAb with its ASGPR and hIFNAR affinity (Table 3.1) compared to hIFN-CTRLdAb with its lack of ASGPR affinity. Furthermore, it was not known whether any observed ASGPRdAb-mediated specific uptake could result in increased efficacy of the fused hIFN, so this was also to be investigated by TaqMan gene expression analysis. Foremost however, the experimental process for producing functional NOTA-conjugated hIFN-dAbs, and subsequent Ga-68 labelling had also to be established. The following chapter details the results of the experimental development (Figure 3.0) towards quantifying the *in vivo* targeting of ^{68}Ga-NOTA-hIFN-dAbs to HepG2 xenografts.

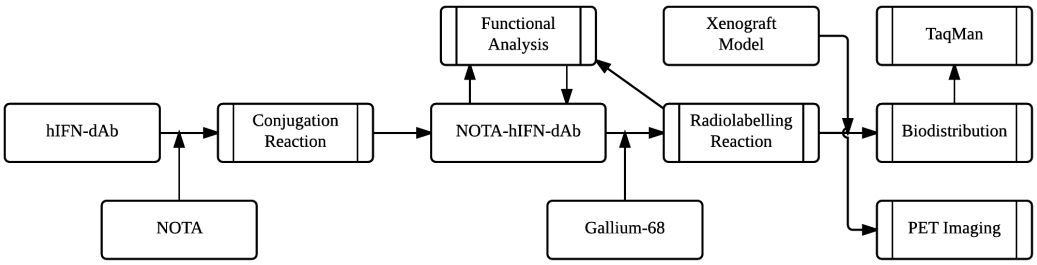

Figure 3.0 – Outline of Experimental Development
Experimental steps involved in producing validated ^{68}Ga-NOTA-hIFN-dAbs and subsequent *in vivo* modelling, towards establishing effective xenograft targeting and optimised potency.

3.2 *IN VITRO* ASSAYS

3.2.1 Tool Fusion Proteins

Two tool HEK293e expressed hIFN-dAb fusion proteins called hIFN-MAXdAb and hIFN-CTRLdAb were supplied for the project* based on their contrasting affinities for ASGPR (Table 3.1).

Table 3.1
Tool hIFN-dAbs and constituent controls

Fusion Protein	Molecular Mass (Da)	Targeting Affinity	
		ASGPR	hIFNAR
hIFN-MAXdAb	32547	YES	YES
hIFN-CTRLdAb	32877	NO	YES
MAXdAb	13299	YES	NO
hIFN	20090	NO	YES

The fusion protein hIFN-MAXdAb is a 32.5kDa dual-targeted fusion protein, comprised of a high affinity ASGPR targeting dAb called MAXdAb fused to the C-terminus of wild-type hIFNα2b (henceforth referred to as hIFN) (Figure 3.1). The hIFN-MAXdAb fusion protein was therefore designed to bind the two target receptors† ASGPR and hIFNAR and thus in theory any tissue expressing either, or both, of these receptors.

The protein hIFN-CTRLdAb is a 32.9kDa single-target fusion protein, comprised of a V_H domain protein scaffold with no known specific receptor or tissue affinity‡ called CTRLdAb and hIFN. The hIFN-CTRLdAb fusion protein was therefore designed to only specifically bind hIFNAR.

* Kindly supplied by Dr Adam Walker and Dr Edward Coulstock at GSK
† Not necessarily simultaneously (Section 1.4.4)
‡ Personal communication with Dr Adam Walker

Figure 3.1 – Comparison of the Amino Acid Sequences of hIFN-MAXdAb and hIFN-CTRLdAb

Aligned amino acid sequences of hIFN-MAXdAb and hIFN-CTRLdAb highlighting the protein composition including sequence parental origin – hIFN, MAXdAb and CTRLdAb – sequence homology and loci of lysine residues.

Additionally, the individual MAXdAb and hIFN proteins were included as positive controls for ASGPR and hIFNAR targeting respectively.

Hence, the two fusion proteins are highly homologous in structure but differ in their respective ability to bind ASGPR. The hIFN-CTRLdAb was therefore a suitable control for potential ASGPR-mediated tissue uptake of the hIFN-MAXdAb fusion.

3.2.2 NOTA Conjugation Reactions

Covalent bioconjugation of the chelator NOTA to hIFN-MAXdAb and hIFN-CTRLdAb would allow radiolabelling with Ga-68, thus functioning as a radiotracer for the biodistribution of hIFN-dAbs *in vivo*. The bifunctional chelator SCN-Bn-NOTA enabled the coupling of the NOTA to sterically unhindered primary amine groups on the protein by nucleophilic substitution under basic reaction conditions, forming an isothiourea bond. The aim of these experiments was thus to purify predominantly homogenous, singly conjugated NOTA-hIFN-MAXdAb and NOTA-hIFN-CTRLdAb (Methods 2.2).

3.2.2.1 Sodium Bicarbonate Dialysis Buffer Exchange

The recovery from the dialysis tube was greater than 90% with the remaining losses incurred on the membrane. The concentration decreased during dialysis, probably due to a positive osmotic potential across the membrane (Table 3.2).

Table 3.2
NOTA Conjugation Metrics

Fusion Protein	Theoretical pI	Stock Concentration (µM)	Post Dialysis Concentration (µM)	Post Dialysis Recovery (%)
hIFN-MAXdAb	8.46	27.0	24.3 ±1.25	91.0 ±3.70
hIFN-CTRLdAb	6.60	204	200 ±8.08	92.0 ±1.73

n≥3

3.2.2.2 SCN-Bn-NOTA Conjugation Reaction Development

The SCN-Bn-NOTA acylation conjugation reaction comprised the pH9.2 bicarbonate buffer dialysed fusion protein with a 10:1 molar excess of SCN-Bn-NOTA. The reaction was performed at room temperature in the dark with gentle rocking for 4 hours, followed by refrigeration.

The molar excess of SCN-Bn-NOTA was a balance between ensuring sufficient NOTA conjugation to enable high efficiency radiolabelling, whilst not promoting conjugation of multiple NOTA groups to individual fusion protein units. A 20:1 molar excess of SCN-Bn-NOTA did not improve In-111 labelling versus a 10:1 molar excess. This indicated that the amount of fusion protein was a limiting factor above 10:1, perhaps as all available conjugation sites were saturated. Furthermore as the likelihood of multiple conjugations was increased, a 20:1 molar excess was deemed not advantageous. On the other hand, a 5:1 molar ratio yielded a lower radiolabelling efficiency, which indicated that this was an insufficient concentration of NOTA. The lower concentration likely decreased the initial rate of reaction, which, in addition to the high pH, potentially increased the competing hydrolysis of SCN-Bn-NOTA. Hydrolysed thiocarbamic acid SCN-Bn-NOTA

derivative can no longer react by alkylation (Introduction 1.7.4.1), decreasing the yield of NOTA-hIFN-dAb. Hence, a 10:1 molar excess of NOTA was utilised.

The reaction time of four hours was to maximise reaction time whilst minimising protein degradation from room temperature incubation and acknowledged the likely low reactive half-life of the NOTA owing to hydrolysis. The pH of 9.2 offered a balance between promoting conjugation with lysine groups in an unprotonated state (Introduction 1.7.4), without overly favouring hydrolysis nor erring too close to the predicted pI of the fusion proteins (Table 3.2). Also, the reaction was performed in the dark to minimise potential photolytic degradation via the benzyl group. Rocking ensured reaction homogeneity and likely improved the reaction kinetics. However, the effects of these variables were not quantitatively analysed.

3.2.2.3 Protein A Purification of NOTA Conjugates

Protein A is a recombinant protein derived from a microbial surface component recognising adhesive matrix molecule adhesin proteins expressed on the surface of *Staphylococcus aureus* bacteria, covalently attached to a Sepharose matrix[467]. Protein A has a high affinity for VH3 family protein sequences (Introduction 1.2.1), and hence can be utilised to purify VH3 derived dAb fusions by packed bed affinity capture chromatography.

Purification of the NOTA-hIFN-dAbs served to remove excess SCN-Bn-NOTA, increase the protein concentration and buffer exchange into NaAc. Any contamination from SCN-Bn-NOTA or other species thereof would have reduced subsequent radiolabelling efficiencies by complexing the radioactive metal. An increase in concentration would likely enable higher achievable specific activities owing to lower reaction volumes and higher hIFN-dAb reaction concentrations therein. The hIFN-dAbs were reported to be highly stable, monomeric and less aggregation-prone, in slightly acidic NaAc buffer* and therefore the NaAc elution method enabled convenient protein purification in pH4.5 0.14M NaAc. Hence, the aim was to achieve maximum concentrations with no SCN-Bn-NOTA breakthrough.

The elution was fractionated into six elutions with the most concentrated fraction being utilised for further experimentation (Table 3.3). Protein lost at each

* Unpublished data Dr Adam Walker & Dr Edward Coulstock, GSK.

stage of the purification was monitored, with minimal detectable protein losses by SDS-PAGE (Appendix Figure 6.7). There was no detectable SCN-Bn-NOTA breakthrough observed by AM iTLC (Appendix Figure 6.15) nor SE-HPLC (data not shown).

Table 3.3
NOTA-hIFN-dAb Purification Metrics

NOTA Conjugate	Pre-Purification Conc. (µM)	Post-Purification Fraction Concentrations (µM)						Post-Purification Total Recovery (%)
		1	2	3	4	5	6	
NOTA-hIFN-MAXdAb	24.3 ±1.25	0.0 ±0.0	14.5 ±7.40	50.9 ±9.44	24.9 ±8.20	6.1 ±3.90	0.0 ±0.0	86.0 ±3.61
NOTA-hIFN-CTRLdAb	200 ±8.08	0.0 ±0.0	12.2 ±10.24	48.9 ±33.5	18.9 ±6.20	3.73 ±3.83	0.74 ±1.47	61.8 ±13.7

n≥3

Almost 90% of the NOTA-hIFN-MAXdAb was recovered from the purification process over the four-fraction elution peak. Any loss in protein was attributed to loss on plasticware or aggregation. There was an average of 53% ±7 of recovered protein present in the most concentrated fraction for NOTA-hIFN-MAXdAb. On the other hand, only an average of 62% of loaded NOTA-hIFN-CTRLdAb was recovered. However, this was offset by 61% ±16 recovery in the top fraction. The NOTA-hIFN-MAXdAb top fraction was on average two times more concentrated than the original dialysed hIFN-MAXdAb protein, whereas the NOTA-hIFN-CTRLdAb elution concentration was below the 204µM starting concentration. In both instances the elution concentration achieved in the top fraction was sufficient for subsequent radiolabelling.

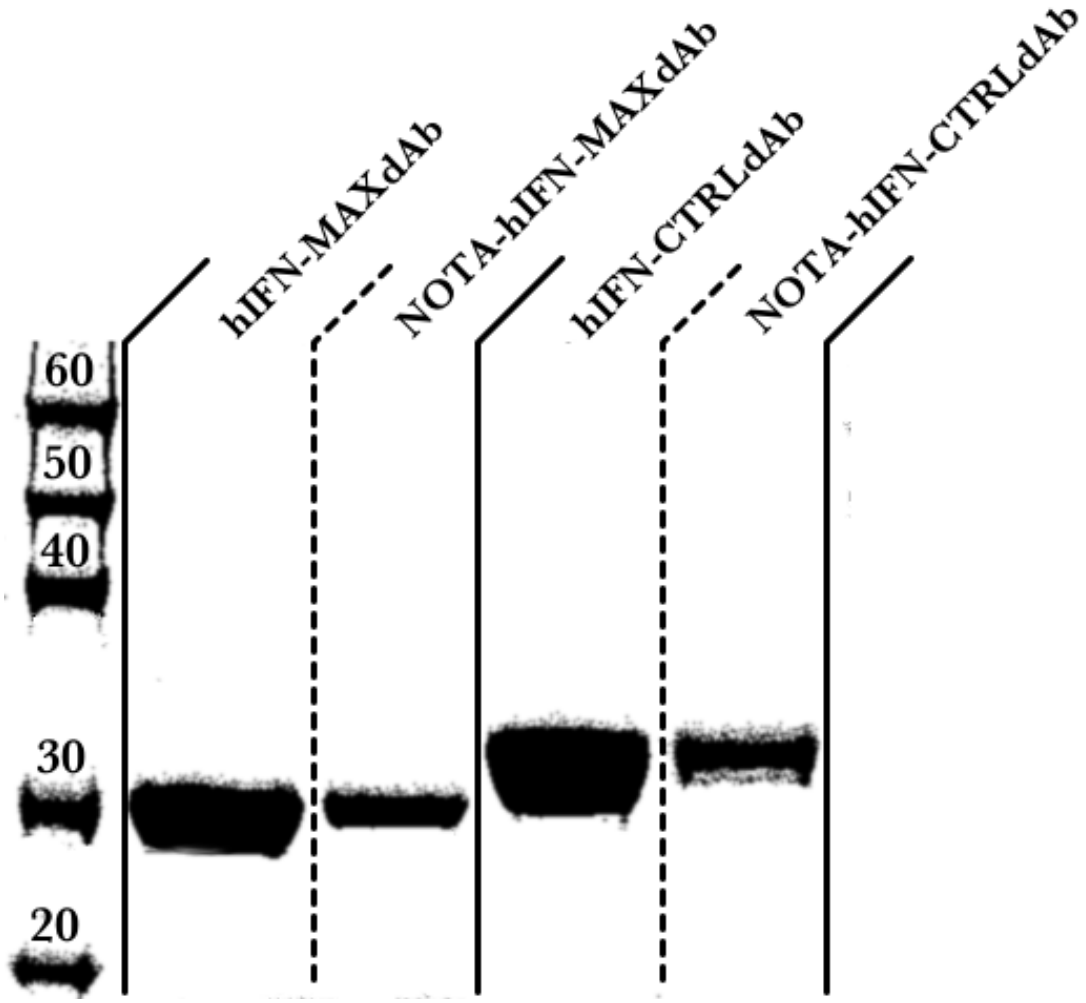

Figure 3.2 – Non-Reducing SDS-PAGE of pre-conjugation and post-Protein A purification hIFN-dAbs

hIFN-dAb fusion proteins migrate as predicted to an apparent molecular mass of between 30-33kDa, without any detectable aggregation either before undergoing the conjugation reaction with SCN-Bn-NOTA or subsequently after Protein A purification.
hIFN-MAXdAb (3μg), NOTA-hIFN-MAXdAb (1μg), hIFN-CTRLdAb (3μg), and NOTA-hIFN-CTRLdAb (1μg) with Novex Sharp Pre-stained Protein Standard.

The high variability reflected the improvements achieved as the protocol was refined. The maximum achieved concentrations of the top fractions, for instance, improved with each batch production up to a maximum of 59.5μM for hIFN-MAXdAb and 98.9μM for hIFN-CTRLdAb*, which represented increases from the first batches of 46% and 211% respectively. This was possibly due in particular to switching to utilising UltraPure reagents without Chelexing, leading to a more reliable elution buffer pH.

* These were the batches utilised *in vivo* (Section 3.5.1)

Non-reducing SDS-PAGE also confirmed that the concentrated fractions of hIFN-dAb did not promote protein aggregation as only a monomeric species at the expected molecular masses (Table 3.1) of approximately 30-33kDa were obtained (Figure 3.2).

Hence, the Protein A purification protocol was successful in the recovery of concentrated NOTA-hIFN-MAXdAb and NOTA-hIFN-CTRLdAb proteins.

3.2.2.4 Mass Spectrometry

Electrospray ionisation time of flight (ESI-TOF) MS was used to analyse the composition of the NOTA-hIFN-dAb species present in the top fraction from Protein A purification (Table 3.3). The MS data showed that the purified stock of NOTA-hIFN-MAXdAb was a heterogeneous mix of species composed of a number of glycosylation and NOTA-conjugated species (Table 3.4, Figure 3.3, Table 3.5).

Table 3.4
Mass Spectrum of hIFN-MAXdAb Post NOTA Conjugation

Peak Mass	Protein Identity	O-linked Glycan	Percentage of Total Protein (%)	
32547*	hIFN-MAXdAb	N/A	N/A	N/A
33197		GalNAc-Gal-Neu5Ac	4.8	39.1
33491		GalNAc-Gal-Neu5Ac$_2$	31.6	
33511			2.7	
33648	NOTA-hIFN-MAXdAb	GalNAc-Gal-Neu5Ac	3.2	60.9
33942		GalNAc-Gal-Neu5Ac$_2$	31.0	
33996			5.3	
34392	NOTA$_2$-hIFN-MAXdAb		15.0	
34445			3.7	
34842	NOTA$_3$-hIFN-MAXdAb		2.7	

*hIFN-MAXdAb predicted mass based on amino acid sequence for reference

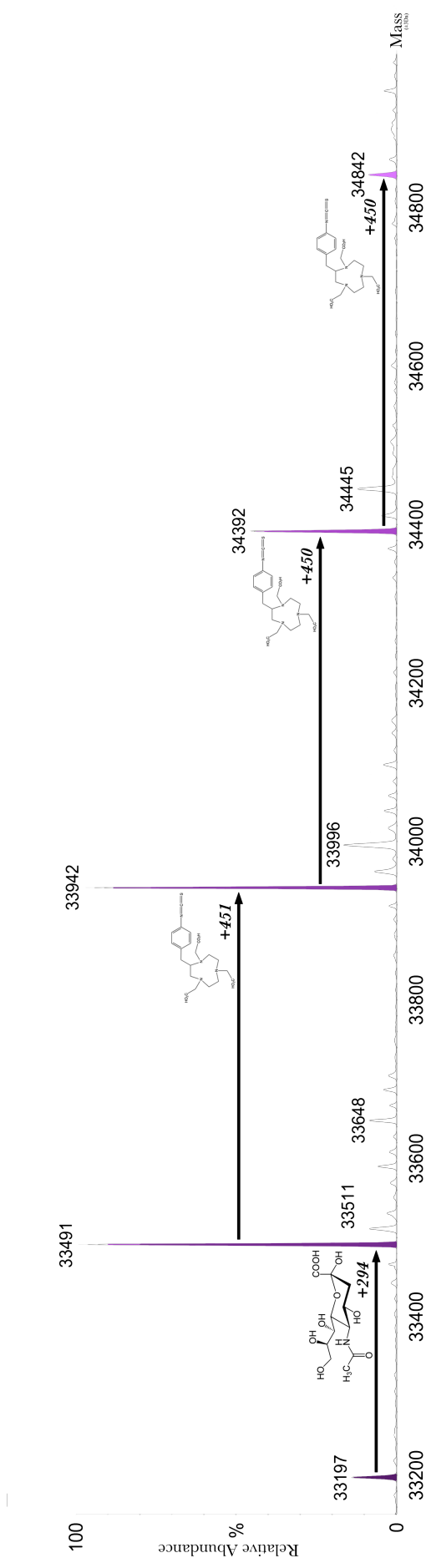

Figure 3.3 – Mass Spectrum of NOTA-hIFN-dAb

Mass spectrum of Protein A purified Post-Conjugation reaction 50µg/ml NOTA-hIFN-MAXdAb Fraction 3. Multiple glycosylated and NOTA- conjugated species identified including: 33197 hIFN(GalNAc-Gal-Neu5Ac)-MAXdAb, 33491 hIFN(GalNAc-Gal-Neu5Ac$_2$)-MAXdAb, 33942 NOTA-hIFN(GalNAc-Gal-Neu5Ac$_2$)-MAXdAb, 34392 NOTA$_2$-hIFN(GalNAc-Gal-Neu5Ac$_2$)-MAXdAb, and 34842 NOTA$_3$-hIFN(GalNAc-Gal-Neu5Ac$_2$)-MAXdAb. Performed with a XYZ ESI-TOF MS.

Table 3.5
Group Molecular Masses

Group Name	Group Mass (Da)
(Lys)-SCN-Bn-NOTA	+451
(Thr)-GalNAc-Gal-Neu5Ac	+948
(Gal)-Neu5Ac	+294
Cr^{3+}	+53/54
(Lys)-OH	+16

*brackets indicate parent molecule attachment and do not count to mass

The hIFN-MAXdAb has no N-linked glycosylation sites (Figure 3.1), only an O-glycosylation site present at Thr109 in the hIFNα2b portion of the hIFN-MAXdAb (Introduction 1.5.1). The expected molecular mass of the hIFN-MAXdAb protein was 32547Da, whereas the first detectable species above the analysis relative-abundance threshold was 33197Da (Figure 3.3) representing a difference of 943Da, and accounted as a 948Da O-GalNAc-Gal-Neu5Ac glycan (Table 3.5). There was a discrepancy of 5Da between the predicted value and the measured hIFN(GalNAc-Gal-Neu5Ac)-MAXdAb glycoprotein but it was decided the 5Da was within an acceptable margin of error because foremost the 'expected value' was estimated from the amino acid sequence, the literature supported the presence of O-GalNAc-Gal-Neu5Ac[239] and the machine error was ±3Da. This hIFN(GalNAc-Gal-NeuAc)-MAXdAb species accounted for 12.3% of the total unconjugated hIFN-MAXdAb glycoprotein (Table 3.4). There was also a conjugated 33648kDa NOTA-hIFN(GalNAc-Gal-Neu5Ac)-MAXdAb species.

The predominant glycosylation state was O-GalNAc-Gal-Neu5Ac$_2$, which was consistent with previous observations[239], as demonstrated by the 294Da mass increase from the presence of an additional Neu5Ac. The three NOTA-conjugated species of hIFN(GalNAc-Gal-Neu5Ac$_2$)-MAXdAb were identified by a mass increase of 450/451Da corresponding to 33942Da NOTA-hIFN-MAXdAb, 34392Da NOTA$_2$-hIFN-dAb, and 34842Da NOTA$_3$-hIFN-MAXdAb. These three NOTA-hIFN(GalNAc-Gal-Neu5Ac$_2$)-MAXdAb fully-sialyted glycoprotein species account for 94.7% of the NOTA-conjugated species representing 57.7% of the total purified NOTA-hIFN-MAXdAb stock. Of these conjugated species 62.9% were singly conjugated, accounting for 36.3% of the total purified NOTA-hIFN-MAXdAb stock.

Therefore, the most abundant species was NOTA-hIFN(GalNAc-Gal-Neu5Ac$_2$)-MAXdAb.

The 33511Da minor peak from the 33491Da parental hIFN-MAXdAb peak with an increase in mass of 20Da was consistent with a small modification such as the hydroxylation of a lysine group which were free to react in the unconjugated hIFN-MAXdAb. The 33996Da and 34445Da minor peaks of the respective parental 33942Da NOTA-hIFN-dAb and 34392Da NOTA$_2$-hIFN-dAb peaks showed an average increase in mass of 53.5Da. This was explained as the potential chelation of an iron or chromium ion isotope[468], which may have been present as a contaminant from the MS machine. There was no indication that there was metal contamination in the stock sample based on subsequent labelling successes. Therefore all the measurable +~53.5Da minor peaks were assumed to be congruent with their parental peak.

The main caveat regarding this data was that it could only be viewed as an accurate reflection of the composition of species that actually ionised and were detected on the machine. A different species ratio or the presence of other species could not be ruled out, although it clearly indicated heterogeneity.

The presence of the multiple conjugated NOTA$_2$-hIFN-MAXdAb and NOTA$_3$-hIFN-MAXdAb species complicated potential quantitation of targeting *in vivo* as there will would not be a 1:1 relationship between detected radioactive events and the number of NOTA-hIFN-dAb molecules. However there was the possibility to apply the determined proportions to create a correction factor.

Furthermore, the locus of the NOTA conjugation on the hIFN-MAXdAb structure was uncontrolled. Therefore the exact lysine group(s) being conjugated were unknown. The conjugated lysine group may have been situated in or adjacent to a dAb CDR or hIFN receptor interaction domain. Therefore this uncontrolled potential to affect hIFN-MAXdAb function was a concern. The hIFN-MAXdAb sequence was known to contain fourteen lysine groups with three within the CDR sequences (Figure 3.1), although this gave no indication of their accessibility in a tertiary conformation. There are several lysines essential to hIFN function[469], and so the hIFN function appeared to be most at risk from undirected NOTA conjugation. Therefore if there were any observed differences between hIFN-MAXdAb and

NOTA-hIFN-MAXdAb *in vitro* then it was bore in mind that it may be due to a NOTA group impinging on a functional site.

The asialoglycoproteins hIFN(GalNAc-Gal-Neu5Ac)-MAXdAb and NOTA-hIFN(GalNAc-Gal-Neu5Ac)-MAXdAb species were acknowledged for their potential for unintended ASGPR interactions through the O-GalNAc-Gal-Neu5Ac and subsequent degradation of the protein through the endocytotic lysosomal pathway. However as there was only one NOTA-hIFN(O-GalNAc-Gal-Neu5Ac)-MAXdAb species, which accounted for 3.2% of total NOTA-hIFN-MAXdAb stock. Any asialoglycan mediated targeting of ASGPR was thought unlikely to be of noticeable magnitude and moreover controlled for by the NOTA-hIFN-CTRLdAb which also has O-linked glycosylation.

These conjugation complications could have potentially been avoided with a different chelation strategy. A pH of 7.5 would have promoted less lysine ε-amine deprotonation, whilst simultaneously increasing the likelihood of N-terminal α-amine conjugation and thus decreasing the likelihood of multiple conjugations whilst avoiding the pI of both hIFN-MAXdAb and hIFN-CTRLdAb (Table 3.2) to prevent possible aggregation. The N-terminus is part of the hIFN portion of the fusion protein and is sterically unhindered by the fusion protein superstructure, so the lower pH may have been a feasible option.

Another expedient approach would be to control the conjugation through the introduction of a cysteine group at the C-terminus to enable conjugation by thiol reaction, such as with maleimido-mono-amide-NOTA. A similar approach was successfully applied to C-terminally conjugate a nanobody to DTPA[470]. However, introducing a new amino acid residue into the sequence risks adding more complications, altering the hIFN-MAXdAb tertiary structure and thus function, plus cysteine could promote dimer formation.

In conclusion, the purified NOTA-hIFN-MAXdAb was a heterogeneous mix of unconjugated and multiple conjugated species in addition to two glycosylation states. This equated to an average of 0.86 NOTAs per hIFN-MAXdAb. The predominating species was O-linked glycosylated NOTA$_1$-hIFN-MAXdAb and the majority of the protein was NOTA conjugated. Therefore, as a tracer for *in vivo* biodistribution and imaging, the hIFN-MAXdAb conjugation was successful. The heterogeneous stock will continue to be referred to as NOTA-hIFN-MAXdAb.

The NOTA-hIFN-CTRLdAb fraction proved more troublesome because mass spectra were not obtained by either ESI-TOF MS nor Liquid Chromatography Time of Flight MS. Previously, treatment with Endo-H_f under reducing conditions to remove the glycosylation had been observed to improve mass spectrum acquisition of DOTA conjugated dAb fusions*; however in this instance that method failed to yield interpretable data. The O-linked glycosylation of hIFNα2b is not high-mannose and so Endo-H_f was not liable to be effective.

Hence, it was only possible to speculate that the $NOTA_x$-hIFN-CTRLdAb profile was similar to that of the NOTA-hIFN-MAXdAb (Table 3.4). The two proteins differ by 43AA in their dAb sequences (Figure 3.1), including three lysine residues, and so the conjugation profiles had the potential to be different given the likely different ε-amino groups' pK_a within the likely differing tertiary structures. However, a similar radiolabelling pattern with In-111 for both conjugates provided confidence that NOTA-hIFN-CTRLdAb was generated.

3.2.3 Biacore Surface Plasmon Resonance

Surface Plasmon Resonance (SPR) as detected in this study with a Biacore machine, allowed label-free real-time observation of interactions between the target ligand immobilised on the surface of an adherent substrate matrix coated gold chip and the protein analytes flowed over the surface in solution. Subsequently kinetic and affinity parameters based on the detected on-rate, off-rate and binding equilibrium could be computed from the observed sensogram binding curves. This was achieved by analysing the binding curves of several analyte concentrations to create a model of the binding interaction, from which the kinetic parameters were fitted. In this investigation, as hIFN-MAXdAb was designed to have dual affinity for both the ASGPR and hIFNAR, Biacore was utilised to determine the binding parameters for both ASGPR-H1-CRD and hIFNAR2 (Method 2.2.2).

* Personal communication by Dr Edward Coulstock

3.2.3.1 ASGPR Binding Assay

Immobilised CRD from the ASGPR-H1 comprised of a 160AA portion of the ECD was used to enable *in vitro* modelling of the interaction of NOTA-hIFN-dAb with ASGPR-H1. A recombinant ASGPR-H1-CRD was expressed and purified (Appendix Figure 6.8)[471] with a highly pure final recovery of 700µg.

A Biacore S-Series CM5 chip was coated with approximately 500RU of the recombinant ASGPR-H1-CRD ligand by amine coupling to the carboxymethylated dextran surface in pH5.5 NaAc*†. Sample analytes NOTA-hIFN-MAXdAb, hIFN-MAXdAb, MAXdAb, and hIFN (Table 3.1) were prepared in HBS-P+ in a serial dilution series and run on a Biacore T200‡ (Figure 3.5). The resultant binding curves were analysed by Biacore Evaluation software assuming a 1:1 Langmuir binding model.

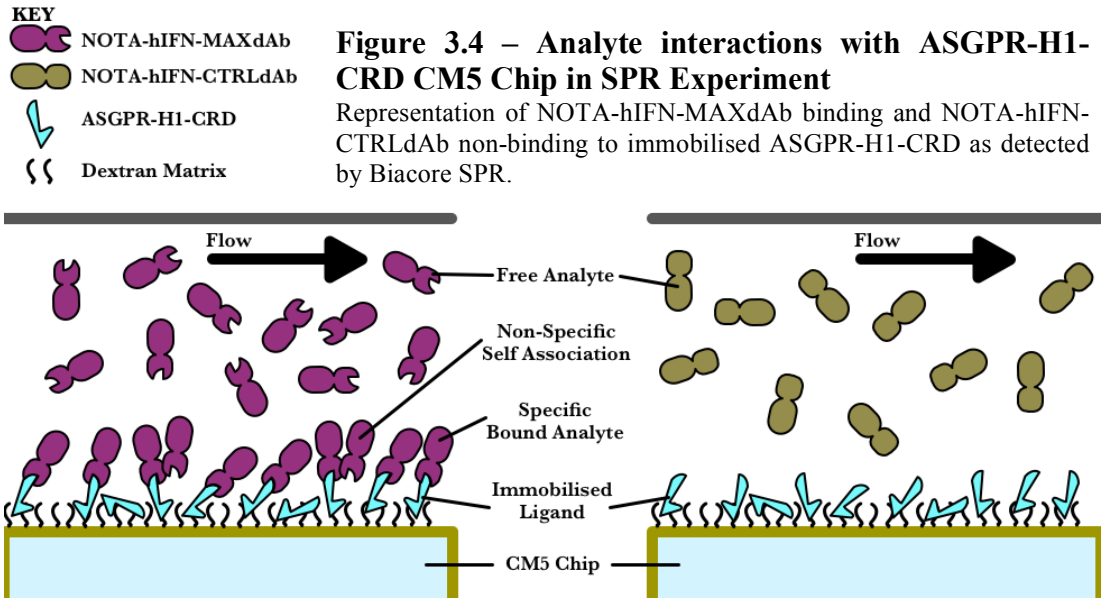

Figure 3.4 – Analyte interactions with ASGPR-H1-CRD CM5 Chip in SPR Experiment
Representation of NOTA-hIFN-MAXdAb binding and NOTA-hIFN-CTRLdAb non-binding to immobilised ASGPR-H1-CRD as detected by Biacore SPR.

The differences between the analytes' binding interactions with ASGPR-H1-CRD were exemplified at a concentration of 10nM (Figure 3.5). Qualitatively the results conveyed the MAXdAb's ability to confer ASGPR-H1-CRD binding to the hIFN protein as part of a fusion protein. Without the MAXdAb, the hIFN protein alone demonstrated no discernable affinity for the ASGPR-H1-CRD. Moreover, this ASGPR-H1-CRD binding capability was overall maintained in spite of

* Kindly provided by Peggy Luong and Dr Thil Batuwangala
† Established by pH Scouting (data not shown)
‡ The Biacore T200 provides high sensitivity to binding interactions, a high rate of data collection (hertz) and advanced curve integration algorithms for accurate K_D computation

heterogeneous NOTA conjugated species. Conversely, as intended, the CTRLdAb fusion proteins had no detectable binding affinity for ASGPR-H1-CRD. The apparent differences in the magnitude of the binding curves of MAXdAb, hIFN-MAXdAb and NOTA-hIFN-MAXdAb were attributed to an increase in the molecular mass increasing the SPR signal. Hence, qualitatively, the data demonstrated that the analyte binding reflected the expected ASGPR binding properties (Table 3.1).

Quantitative analysis of the binding kinetics (Table 3.6) was performed by sampling a range of analyte concentrations from 100nM to 0.01nM* (Figure 3.6) over multiple experiments†, as calculated by integrative analysis by the BIAevaluation software.

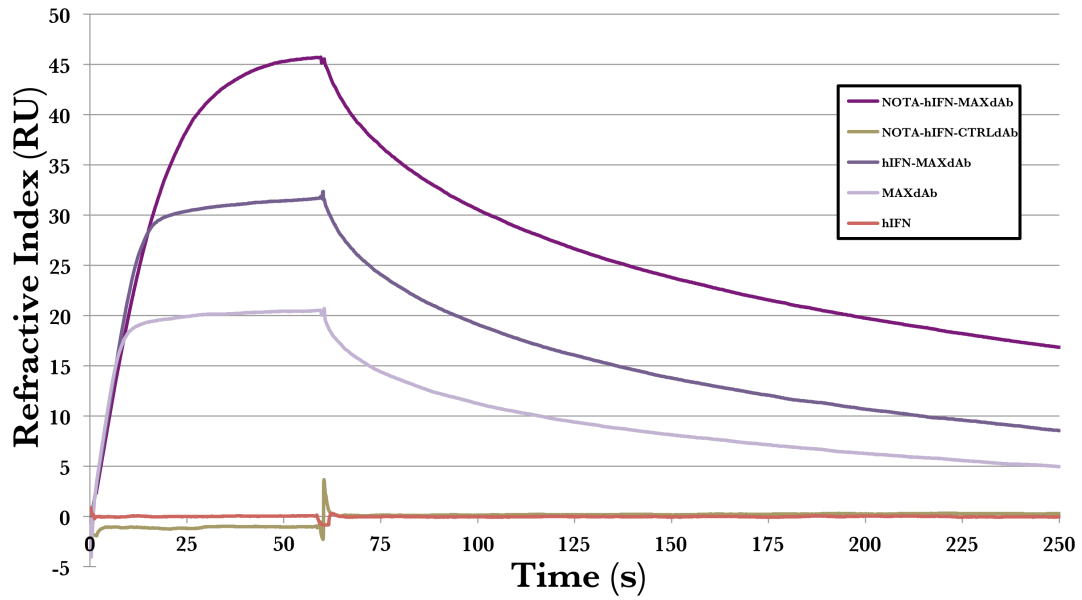

Figure 3.5 – Biacore T200 SPR Analysis of Analytes' binding interaction with recombinant ASGPR-H1-CRD

Biacore T200 SPR with ASGPR-H1-CRD immobilised on a CM5 chip assessed the ASGPR-H1-CRD binding curves of 10nM analytes NOTA-hIFN-MAXdAb, NOTA-hIFN-CTRLdAb, hIFN-MAXdAb, MAXdAb and hIFN injected over the chip surface at 30µlmin^{-1}. The data shows MAXdAb can bind ASGPR-H1-CRD and can confer this property to hIFN as part of a fusion protein, compared to the CTRLdAb and hIFN alone showing no binding to ASGPR-H1-CRD.

* In practice only analyte concentrations ranging from 10nM to 0.03nM were utilised to compute the kinetic data as higher concentrations decreased the goodness of fit for the modelled data

† Between 4 and 10 experiments with n=3 for each data point

Table 3.6
Biacore T200 ASGPR-H1-CRD Binding Kinetics

Protein	K_{on} ($x10^7$ $M^{-1}s^{-1}$)	K_{off} ($x10^{-2}$ s^{-1})	K_D (nM)	R_{max} (RU)	Chi^2 (RU^2)
NOTA-hIFN-MAXdAb	1.78 ±0.67	1.26 ±0.40	0.73 ±0.13	44.5 ±12.0	0.40 ±0.25
hIFN-MAXdAb	21.0 ±8.50	6.78 ±2.67	0.33 ±0.03	30.6 ±10.0	0.03 ±0.01
MAXdAb	23.8 ±9.68	5.48 ±2.15	0.24 ±0.04	20.6 ±5.59	0.04 ±0.03

n≥4, SD values displayed

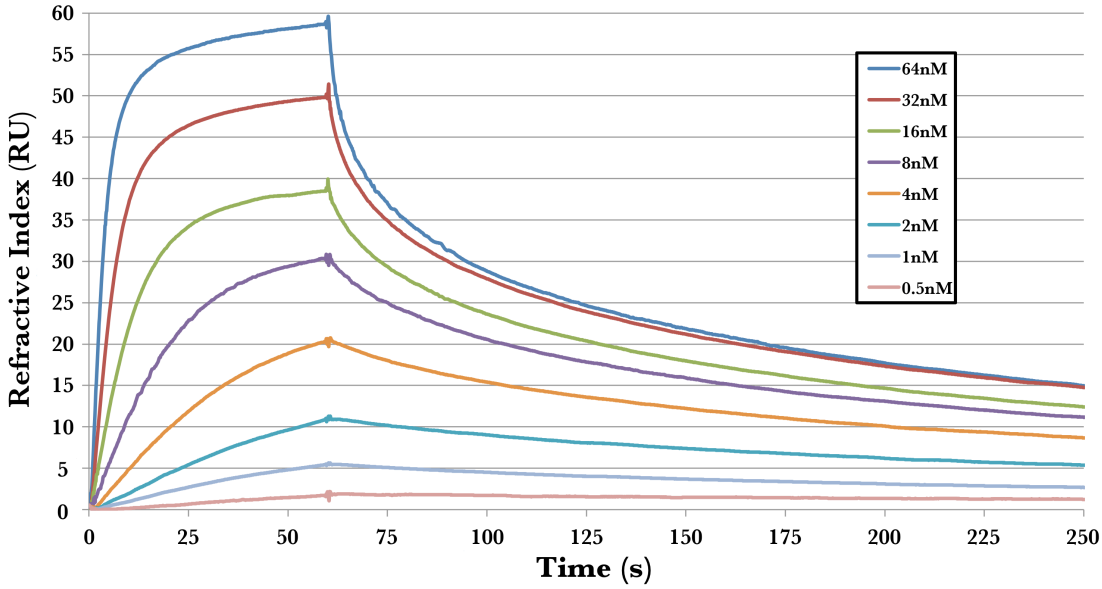

Figure 3.6 – Biacore T200 SPR Analysis of NOTA-hIFN-MAXdAb binding to ASGPR-H1-CRD
Biacore T200 SPR with ASGPR-H1-CRD immobilised on a CM5 chip assessed the ASGPR-H1-CRD binding kinetics of a 64-0.5nM 1:2 serial dilution of NOTA-hIFN-MAXdAb injected over the chip surface at 30µlmin^{-1}.

NOTA-hIFN-MAXdAb's 0.73nM K_D binding affinity for ASGPR-H1-CRD was considered high*. The binding interaction profile consisted of a fast on-rate (k_{on}) combined with a fast off-rate (k_{off}) which suggested a strong, transient interaction between the MAXdAb component and ASGPR-H1-CRD (Table 3.6, Figure 3.6). The implications for the NOTA-hIFN-MAXdAb *in vivo* were favourable as it suggested that the NOTA-hIFN-MAXdAb could potentially rapidly concentrate in

* Drug-target binding affinities are generally considered high between 0.1nM-10nM

ASGPR-expressing tissues but would be readily re-released for hIFN-mediated interaction with hIFNAR. The data also compared favourably with the published binding affinity result of 0.6nM for an ASGPR binding dAb fusion[74].

Comparison of NOTA-hIFN-dAb with hIFN-MAXdAb and MAXdAb demonstrated significant ($p=0.00008$) differences in the binding kinetics of each protein for ASGPR-H1-CRD (Table 3.6, Appendix Figures 6.9 & 6.10). The presence of NOTA conjugates significantly decreased the MAXdAb's K_D for ASGPR-H1-CRD. There was a significant ($p=0.002$) decrease in the k_{on} with the presence of NOTA conjugates, which appeared to be offset by a significant ($p=0.004$) improvement in the k_{off} rate. This suggested the result likely reflected the overall binding of the heterogeneous NOTA-hIFN-MAXdAb stock, whereby the 61% subset of NOTA-conjugated species decreased the overall binding efficiency value. The addition of NOTA may have impeded binding to ASGPR-H1-CRD, but once the NOTA-hIFN-MAXdAb was bound the NOTA conjugation served to increase the stability of the interaction. The presence of NOTA may have modified the tertiary structure of the NOTA-hIFN-MAXdAb fusion protein subset to the extent that the CDRs of the MAXdAb had an ameliorated binding alignment with the ASGPR-H1-CRD epitope.

Indeed, although the differences were mathematically significant, they were not of practical qualitative significance as the NOTA-hIFN-MAXdAb overall still bound the ASGPR-H1-CRD at a sub 1nM K_D binding affinity in spite of NOTA conjugation, and the crucial factor for this study was the highly significant ($p<0.0001$) contrast with the non-ASGPR binding NOTA-hIFN-CTRLdAb.

The SD values showed low variance and so there was a high degree of confidence that the kinetic values were consistent. The low R_{max} below 50RU was an indication the observed results were unlikely augmented by the mass-transport effect*, which enhanced confidence in the robustness of the result. Furthermore, the low Chi^2 values below $0.5RU^2$ equating to less than 1% of the Rmax† indicated a high confidence in the curve fit, and so any differences between data points and fitted values may have been just due to background noise.

* The mass-transport effect is the phenomena whereby the analyte accumulates at the chip surface by diffusion from the bulk solution, caused by the reduced flow rate close to the chip surface, thus creating false positive ligand association results.

† Less than 10% of the R_{max} is considered appropriate

Nevertheless, the SDs showed that there was some sensitivity to sample concentration change, as reflected in the k_{on} and k_{off} values (Table 3.6). However, the results were not attained consecutively but over many months and so the small variability appeared to be temporal. This correlated with variation in the R_{max} indicating a decrease in chip binding capacity over time.

There was an observed lack of steady-state equilibrium during the association phase (0-60s) with binding continuing after the apparent ligand saturation point had been reached. This was most pronounced in the NOTA-hIFN-MAXdAb data due to the slower k_{on} (Figure 3.6). A possible explanation was that the reaction conditions were conducive to non-specific MAXdAb-mediated self-associations, a property known to afflict dAb technologies (Introduction 1.2.1), and so there was an accumulation on the chip surface of dimers over time. Another explanation was that there was a second, lower-affinity epitope on ASGPR-H1-CRD for MAXdAb that had a considerably lower k_{on} rate, which would also account for the continuing increase in binding signal. In both explanations though it was the saturation of the specific ASGPR binding that appeared to make this secondary interaction kinetically favourable.

In summary, NOTA-hIFN-MAXdAb demonstrated a 0.73nM binding affinity for the recombinant ASGPR-H1-CRD in this *in vitro* Biacore SPR analysis model. The addition of NOTA significantly affected the binding kinetics of the hIFN-MAXdAb fusion protein, notwithstanding a significant improvement in k_{off}. However in practical terms the modulation was not meaningful as the K_D remained significantly higher than the non-binding control NOTA-hIFN-CTRLdAb.

3.2.3.2 hIFNAR Binding Assay

A Biacore CM5 chip was coated with approximately 500RU of recombinant R&D Systems hIFNAR2 ligand by amine coupling to the carboxymethylated dextran surface in pH4.0 NaAc*. Sample analytes NOTA-hIFN-MAXdAb, NOTA-hIFN-CTRLdAb, hIFN-MAXdAb, MAXdAb and hIFN were prepared in HBS-P+ at in a logarithmic 1:3/1:3.33 serial dilution series and run on a Biacore 3000† (Figure 3.7). The resultant binding curves were analysed by Biacore Evaluation software assuming a 1:1 Langmuir binding model.

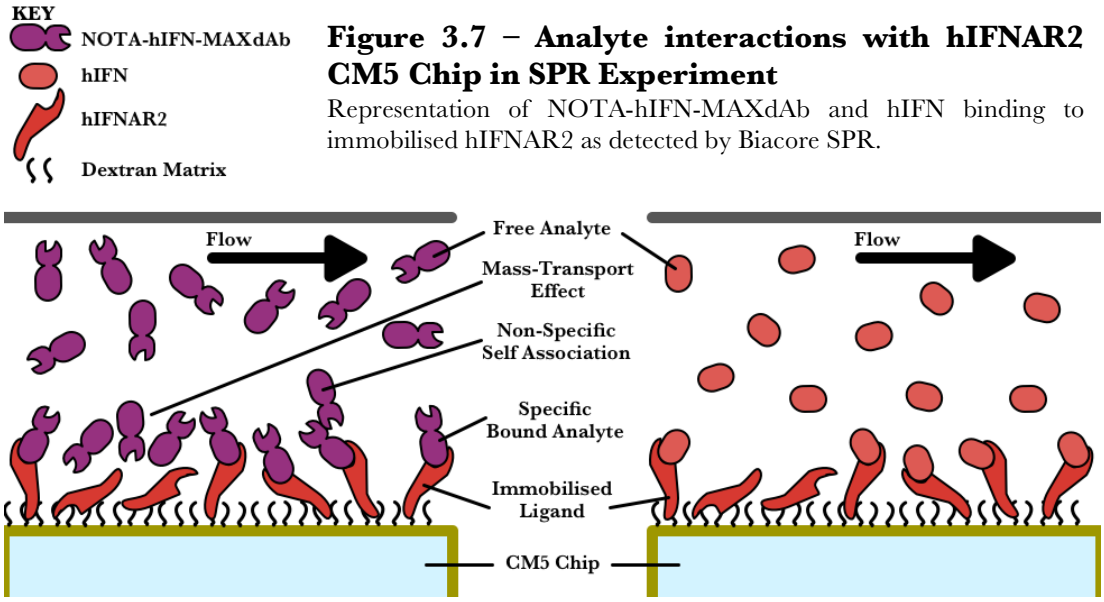

Figure 3.7 – Analyte interactions with hIFNAR2 CM5 Chip in SPR Experiment
Representation of NOTA-hIFN-MAXdAb and hIFN binding to immobilised hIFNAR2 as detected by Biacore SPR.

The binding profiles of the analytes against hIFNAR2 were exemplified at 250nM (Figure 3.8). A qualitative analysis of the profiles showed that the NOTA-hIFN-MAXdAb and the NOTA-hIFN-CTRLdAb had an intrinsic binding capacity for the hIFNAR2. However, there was a strong suggestion that their binding to hIFNAR2 was reduced by the NOTA conjugation as their magnitudes were substantially reduced.

The hIFN positive control showed rapid binding before reaching a constant equilibrium. The hIFN-MAXdAb showed a similar binding profile to the hIFN, albeit with a greater intensity owing to its increased mass and lack of equilibrium (Section 3.2.3.1). The MAXdAb negative control appeared to show some non-specific interaction with the chip surface.

* Established by pH Scouting (data not shown)
† The Biacore 3000 was utilised as a Biacore T200 was unavailable.

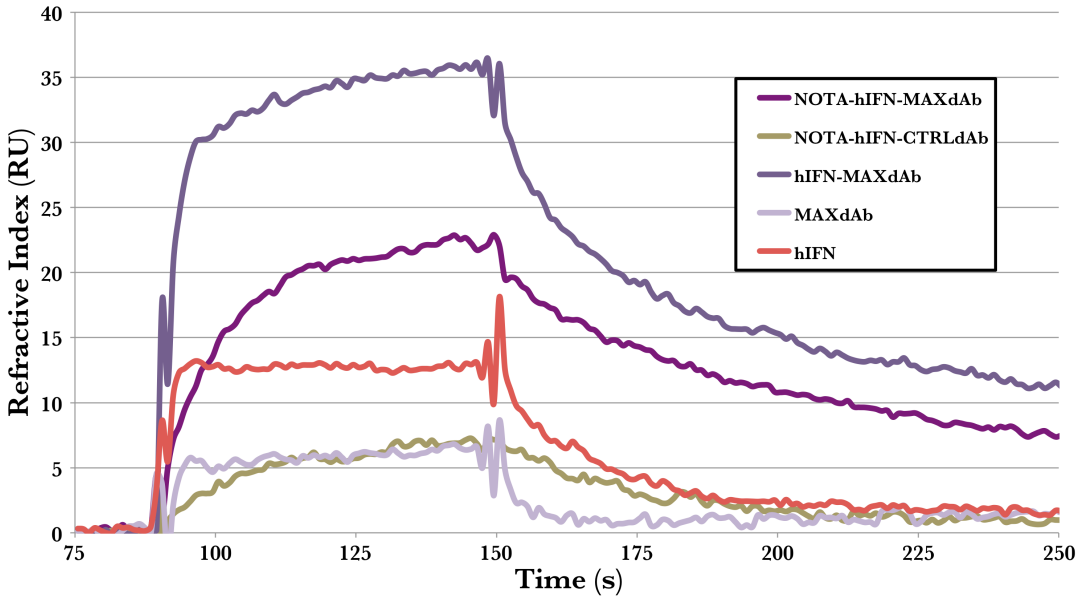

Figure 3.8 – Biacore 3000 SPR Analysis of Analytes' binding interaction with recombinant hIFNAR2

Biacore 3000 SPR with hIFNAR2 immobilised on a CM5 chip assessed the hIFNAR2 binding curves of 250nM analytes – NOTA-hIFN-MAXdAb, NOTA-hIFN-CTRLdAb, hIFN-MAXdAb, MAXdAb and hIFN – injected over the chip surface at 30µlmin^{-1}. The data shows hIFN can bind hIFNAR2 and can confer this property to MAXdAb and CTRLdAb as part of the respective fusion proteins, which compares to the MAXdAb alone showing no measurable binding to hIFNAR2 above background noise.

Quantitative analysis of the binding kinetics (Table 3.7) was performed by sampling a range of analyte concentrations from 100nM to 0.01nM over multiple experiments. The kinetic data confirmed a significant ($p=0.02$) decrease in K_D with the presence of NOTA conjugated species decreasing hIFNAR binding. For instance, the NOTA-hIFN-MAXdAb binding affinity was over a 1000-fold reduced at 46.9µM compared to 30nM for hIFN-MAXdAb. The source of this effect was attributable to a significant ($p=0.002$) decrease in the k_{on} association rate of hIFN-MAXdAb and NOTA-hIFN-MAXdAb of $29.2x10^4$ $M^{-1}s^{-1}$ to $0.02x10^4 M^{-1}s^{-1}$, respectively. This contrasted with the k_{off} values of hIFN-MAXdAb and NOTA-hIFN-MAXdAb which were not significantly ($p=0.79$) different at $0.88x10^{-2}$ s^{-1} and $0.83x10^{-2}$ s^{-1}, respectively. This showed that once bound to the hIFNAR2 the NOTA-hIFN-MAXdAb would actually dissociate significantly ($p=0.01$) slower than hIFN alone. The mechanism for this extra binding stability was not clear, but it was evidently related to the presence of the MAXdAb in the dAb fusion protein as the NOTA-hIFN-CTRLdAb and the hIFN both had similar, faster k_{off} values. Thus, the data suggested that the negative

effect of NOTA conjugation was related to the association phase of binding and once bound, the NOTA-hIFN-CTRLdAb bound strongly to the hIFNAR2.

Table 3.7
Biacore 3000 hIFNAR2 Binding Kinetics

Protein	K_{on} (x10^4 $M^{-1}s^{-1}$)	K_{off} (x10^{-2} s^{-1})	K_D (μM)	R_{max} (RU)	Chi^2 (RU^2)
NOTA-hIFN-MAXdAb	0.02 ±0.00	0.83 ±0.02	46.9 ±20.9	8020 ±2490	0.38 ±0.07
hIFN-MAXdAb	29.2 ±3.81	0.88 ±0.23	0.03 ±0.01	22.5 ±5.93	0.53 ±0.03
NOTA-hIFN-CTRLdAb	0.03	2.97	86.4	3460	0.26
hIFN	354 ±77.3	3.26 ±0.55	0.01 ±0.00	10.8 ±0.50	0.25 ±0.04

n≤3, SD values displayed

To control for their differing ASGPR targeting, NOTA-hIFN-MAXdAb and NOTA-hIFN-CTRLdAb were intended to have equal hIFN activity (Figure 3.1). Indeed they were both shown to share similar k_{on} rates and double-digit μM K_D values (Table 3.7). However, they differed in their k_{off} rates as NOTA-hIFN-CTRLdAb dissociated 3.6 times faster than NOTA-hIFN-MAXdAb. The CTRLdAb has three fewer lysine residues in its sequence than MAXdAb, and so perhaps the conjugation of hIFN-CTRLdAb was weighted towards the lysines of the hIFN as a result. The hIFN function may have thus been affected to a greater extent in the NOTA-hIFN-CTRLdAb from NOTA conjugation. Therefore, although the binding affinities remained non-significantly different overall, the difference in k_{off} was noted for possible ramifications on the potency of the NOTA-hIFN-CTRLdAb. A different conjugation strategy may have circumvented this control drawback.

The hIFN positive control K_D of less than 10nM conformed to previously published K_D values[263,269,472]. Furthermore, in one study pegylated hIFN (an increase in molecular weight of 40kDa) demonstrated a two-fold decrease in binding affinity compared to the hIFN alone[472], which is not dissimilar to the three-fold decrease witnessed between hIFN-MAXdAb and hIFN.

The data appeared to be relatively noisy compared to the ASGPR-H1-CRD binding data (Table 3.7). Indeed the Chi^2 values ranged from 0.21-0.56RU^2 equated

to less than 1% of the Rmax* thus indicating confidence in the curve fit, but also an increase in signal-noise. The increased noise was the decreased R_{max} making background noise more significant (p=0.009), which in addition to the decreased binding affinities was attributable to the decreased sensitivity of the Biacore 3000.

The very high R_{max} of the NOTA-hIFN-MAXdAb and NOTA-hIFN-CTRLdAb were indicative of mass-transport effects, which may have also accounted for the apparently poor respective K_D values. The mass-transport effect may have precluded confidence in the hIFNAR2 K_D quantitation, however it did not undermine the qualitative assessment that NOTA-hIFN-MAXdAb had a higher k_{on} affinity than NOTA-hIFN-CTRLdAb.

As was seen with the ASGPR-H1-CRD experiments (Section 3.2.3.1), the lack of steady state equilibrium was also apparent for the hIFNAR2 binding, particularly for the NOTA-hIFN-MAXdAb result. As the hIFN alone binding was unaffected by this problem, this suggested that this was a dAb-mediated problem.

In summary, NOTA-hIFN-MAXdAb and NOTA-hIFN-CTRLdAb were shown to interact with the hIFNAR2 in this *in vitro* Biacore SPR analysis model. The k_{off} data supported that NOTA conjugated dAb fusions can bind hIFNAR2. However, the addition of NOTA appeared to have significantly decreased the k_{on} of the hIFN-mediated interaction with hIFNAR2 resulting in lower K_D values of NOTA-hIFN-MAXdAb and NOTA-hIFN-CTRLdAb for hIFNAR2 compared to hIFN alone. Moreover, the very high Rmax undermined the confidence in the binding values of the NOTA conjugates.

* Less than 10% of the R_{max} is considered appropriate

3.2.4 HEK-Blue hIFN Potency Assay

The HEK-Blue hIFNα/β *in vitro* cellular assay was utilised as a highly sensitive reporter assay for the activation of the hIFN signalling pathway and thus the quantification of hIFN bioactivity. HEK-Blue cells stably transfected with the human IFN signalling pathway (Figure 3.9) plus ISRE dependent ISG54 promoter linked to a secreted embryonic alkaline phosphatase (SEAP) reporter gene were cultured. Secreted SEAP was detected in the supernatant by the addition of QUANTI-Blue medium, which turns purple/blue with an OD640 proportional to the amount of SEAP present, and thus is also proportional to the potency of the hIFN bioactivity. Hence, sampling a logarithmic concentration dilution series of the relevant analytes of 1:3/1:3.33 1nM-3fM and incubating with HEK-Blue cells, followed by plotting the resultant spectrophotometric OD readouts allowed the derivation of the EC50 values of the respective analytes (Method 2.2.3).

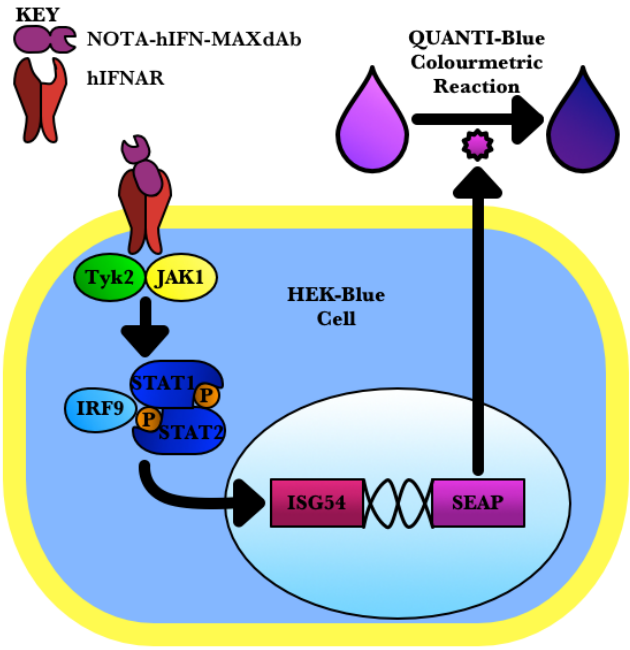

Figure 3.9 – HEK-Blue hIFN Potency Assay
Representation of NOTA-hIFN-MAXdAb stimulating the production of SEAP through binding the IFNAR of a HEK-Blue cell, with subsequent colourimetric readout after the addition of QUANTI-Blue reagent.

The normalised data* demonstrated only minor differences in the potency of the hIFN-dAb fusions compared to hIFN alone (Table 3.8, Figure 3.10). The NOTA-hIFN-MAXdAb was only 68.9% less potent than the hIFN alone (Table 3.8) in spite of the apparent 1000 fold poorer binding affinity for the hIFNAR2 (Table 3.7). Also, the unconjugated hIFN-MAXdAb showed a 45% increase in potency over

* The data across different plates was normalised using the hIFN control on each plate, thus controlling for the any differences in colourimetric development time, so that plates could be cross compared.

hIFN. The lack of significant difference between the potency values of the heterogeneously 60.9% conjugated NOTA-hIFN-MAXdAb stock (Figure 3.3, Table 3.4) and the homogeneous 100% unconjugated hIFN-MAXdAb stock demonstrated that although NOTA conjugation lead to a significant decrease in hIFNAR2 K_D, the NOTA had not overall inhibited the potency of hIFN-MAXdAb.

Table 3.8
HEK-Blue hIFN Bioactivity Reporter Assay

Protein	EC50 (pM)
NOTA-hIFN-MAXdAb	6.79
hIFN-MAXdAb	2.78
MAXdAb	-
NOTA-hIFN-CTRLdAb	37.5
hIFN-CTRLdAb	6.87
hIFN	4.02

n≥6

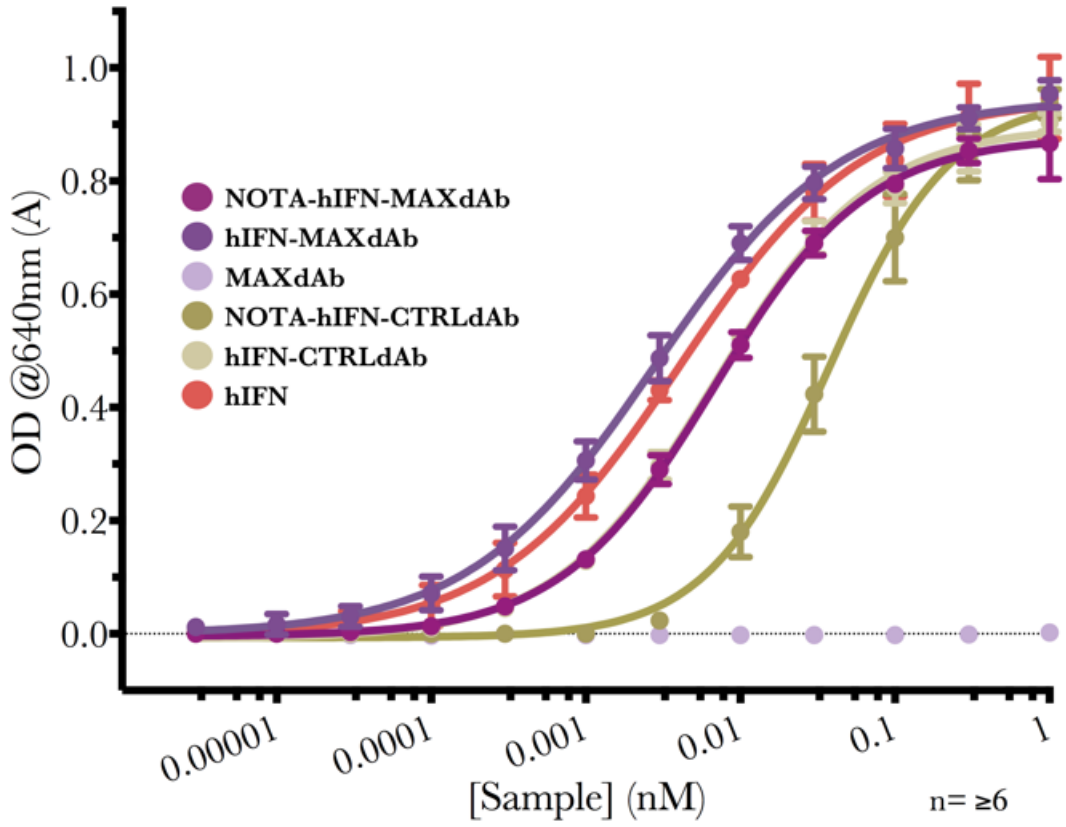

Figure 3.10 – HEK-Blue hIFN Potency Assay
HEK-Blue *in vitro* reporter assay for hIFN bioactivity utilised to calculate EC50 values of hIFN-dAb fusions and controls – NOTA-hIFN-MAXdAb, hIFN-MAXdAb, MAXdAb, NOTA-hIFN-CTRLdAb, hIFN-CTRLdAb, and hIFN – demonstrating a decrease in potency with the presence of NOTA but broadly comparable potencies to hIFN alone.

These results suggested that the k_{off} may be the most important factor influencing the potency of the hIFN-MAXdAbs as both NOTA-hIFN-MAXdAb and hIFN-MAXdAb had improved k_{off} rates for hIFNAR2 than hIFN but significantly lower k_{on} rates and concomitant lower K_D binding affinities. This suggested their k_{off} rates disproportionately maintained the NOTA-hIFN-MAXdAb and hIFN-MAXdAb potencies at a similar level to hIFN alone. This result conformed to the model of the hIFN interaction with hIFNAR (Introduction 1.5.2) whereby hIFNAR1 binding is the rate limiting step for signalling and therefore one could hypothesise that a slow k_{off} increases the likelihood of formation of the full hIFN-hIFNAR JAK-STAT signalling complex, thus compensating for the low k_{on} rates.

The exception to these small potency changes was NOTA-hIFN-CTRLdAb because its potency decreased more than four-fold compared to unconjugated hIFN-CTRLdAb. However, considering the NOTA-hIFN-CTRLdAb had such poor kinetics (slow on-rate, and fast off-rate) in the Biacore SPR experiments (Section 3.2.3.2), this had impacted its potency to a lesser extent than was anticipated. Again it was apparent that large differences in the binding affinity and kinetic values are not linked to significant knock-on effects on the potency. Although it was nevertheless an unwelcome variable, *in vivo* this difference with the potency of NOTA-hIFN-MAXdAb was expected to be even less relevant owing to a blood concentration in the nM range, far in excess of the pM EC50. It appeared reasonable to assume that this pM difference in potency between NOTA-hIFN-MAXdAb and NOTA-hIFN-CTRLdAb was unlikely to be a significant determinant of hIFN-mediated bioactivity *in vivo*, but rather the binding affinities for ASGPR. Hence, this decrease in potency was deemed within acceptable limits and did not preclude NOTA-hIFN-CTRLdAb as an effective control for NOTA-hIFN-MAXdAb.

In summary, the HEK-Blue hIFN reporter assay data has shown that the NOTA-hIFN-MAXdAb and NOTA-hIFN-CTRL-dAb remain bioactive in spite of the presence of NOTA. The pM potencies demonstrate the effectiveness of NOTA-hIFN-MAXdAb for activating the hIFN pathway.

3.2.5 Flow Cytometry

Flow Cytometry was utilised in this investigation to profile cell binding of the hIFN-dAb derivative analytes to populations of the ASGPR-positive hIFNAR-positive cell line HepG2 (Figure 3.11) and the ASGPR-negative hIFNAR-positive U937 histiocytic lymphoma monocyte cell line. The two cell lines, differing in their ASGPR expression, were chosen to establish the whole cell binding capabilities of hIFN-MAXdAb, NOTA-hIFN-MAXdAb, hIFN-CTRLdAb and NOTA-hIFN-CTRLdAb as well the MAXdAb and hIFN controls, and how the presence of ASGPR influences this binding (Method 2.24).

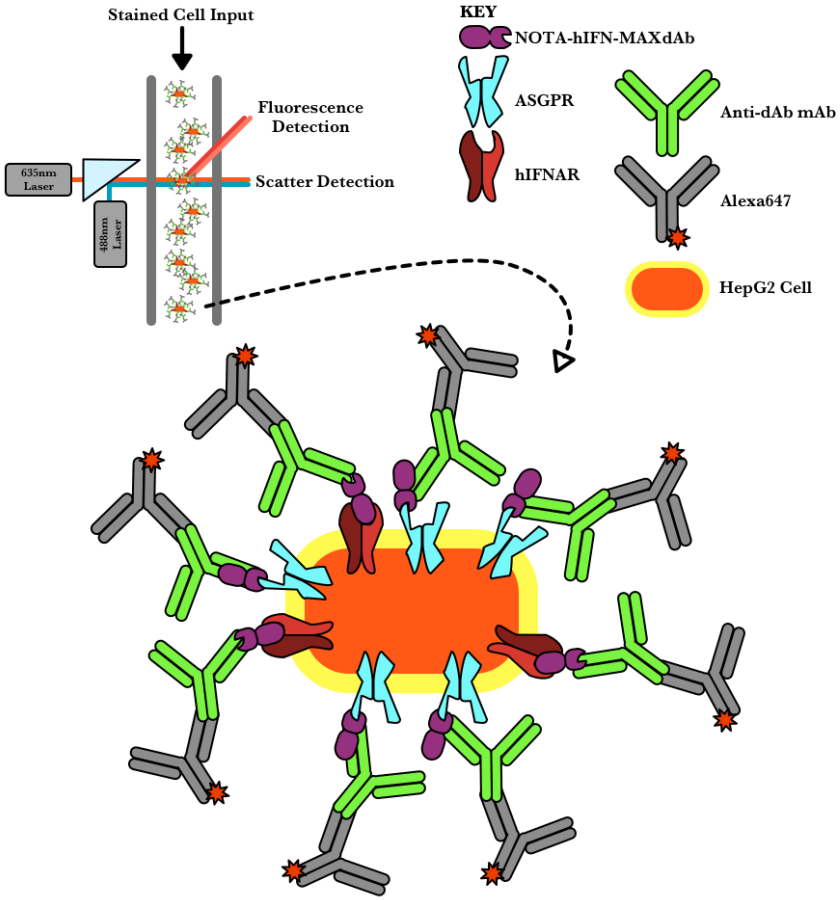

Figure 3.11 – Flow Cytometry with HepG2 cells
Representation of NOTA-hIFN-MAXdAb binding HepG2 cells by both ASGPR and hIFNAR, detected by the secondary anti-dAb mAb and tertiary Alex647 fluorescence.

3.2.5.1 HepG2 Whole Cell Binding

The data confirmed that HepG2 cells express both ASGPR and hIFNAR (Table 3.9, Figure 3.12). There was a strong indication that ASGPR expression levels were significantly ($p<0.0001$) higher than the hIFNAR levels on HepG2 cells, and the broad peak indicated that there was a range of ASGPR expression levels within the cell population. Moreover, that hIFNAR2 expression was higher than hIFNAR1, as was expected (Introduction 1.5.2).

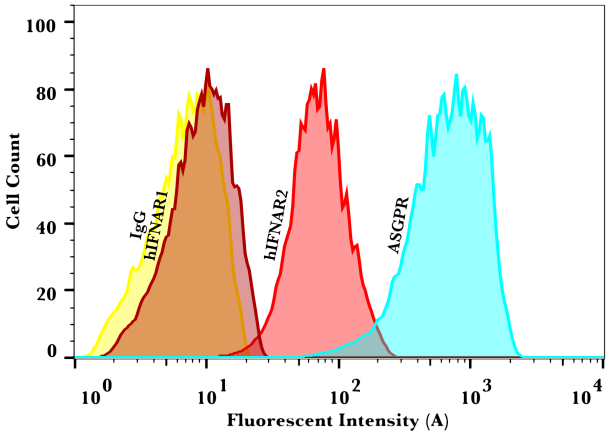

Figure 3.12 – Flow Cytometry for Receptor detection on HepG2
Histogram of flow cytometric analysis of live HepG2 cell staining with anti-receptor mAbs – α-ASGPR, α-hIFNAR1, and α-hIFNAR2 – plus an irrelevant-IgG non-specific control, detected with anti-mAb Alexa647. Data demonstrates that HepG2 cells express hIFNAR1, hIFNAR2 and ASGPR at respectively increasingly levels.

Table 3.9
Flow Cytometric Analysis of hIFN-dAbs' HepG2 Cell Binding

Protein Analyte	Detection mAbs	Staining	Mean Fluorescence Intensity (MFI)
NOTA-hIFN-MAXdAb	α-hIFN	PI + Alexa647	671 ±261
hIFN-MAXdAb			977 ±291
MAXdAb	α-dAb		1373 ±122
NOTA-hIFN-CTRLdAb	α-hIFN		23.3 ±2.19
hIFN-CTRLdAb			35.5 ±1.84
hIFN			101 ±2.33
RECEPTOR CTRLS	α-ASGPR		814 ±50.0
	α-hIFNAR1		12.5 ±2.12
	α-hIFNAR2		92.5 ±14.6
ANTIBODY CTRLS	α-dAb		9.86 ±1.37
	α-hIFN		10.47 ±0.65
	IgG		9.45 ±1.54
STAINING CTRL			10.17 ±1.46

n≥2

The hIFN-dAb HepG2 binding data (Figure 3.13) demonstrated that MAXdAb could significantly (p=0.005) increase HepG2 cell binding of a hIFN-dAb *in vitro*, such as NOTA-hIFN-MAXdAb compared to NOTA-hIFN-CTRLdAb and up to ten-fold higher binding than hIFN alone (Table 3.9). It was thus reasonable to conclude that this improved HepG2 binding was mediated by MAXdAb's ASGPR affinity. Indeed, the MAXdAb alone also had a high binding to the HepG2 cells (Figure 3.14).

Comparison with the irrelevant IgG1 control showed that there was some specific binding of the NOTA-hIFN-CTRLdAb to the HepG2 cells (p=0.02) (Figure 3.13). However, this was twenty-nine fold less than NOTA-hIFN-MAXdAb, which strongly suggested that hIFN-mediated binding via hIFNAR likely did not form a major part of the NOTA-hIFN-MAXdAb HepG2 cell binding. This result was therefore consistent with the 0.73nM K_D for ASGPR and 46.9μM K_D for hIFNAR2 of NOTA-hIFN-MAXdAb, and the relative expression levels of the ASGPR and hIFNAR2 (Figure 3.12). Furthermore, the NOTA-hIFN-CTRLdAb binding was

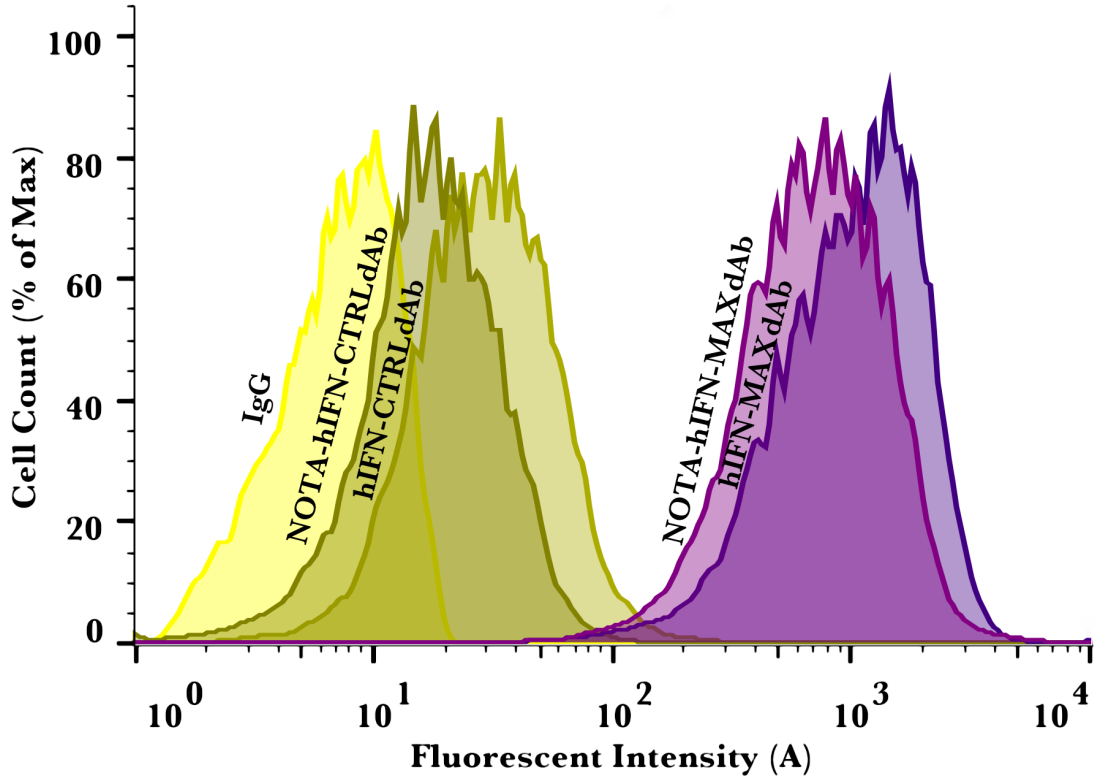

Figure 3.13 – Flow Cytometry of hIFN-dAb Fusions with HepG2
Histogram of flow cytometric analysis of live HepG2 cell staining with hIFN-dAb fusions – NOTA-hIFN-MAXdAb, hIFN-MAXdAb, NOTA-CTRLdAb and hIFN-CTRLdAb – detected with anti-hIFN mAb and anti-mAb Alexa647, plus an irrelevant-IgG representing non-specific binding. Data demonstrates that MAXdAb-mediated HepG2 cell binding significantly increases binding versus CTRLdAb, with NOTA conjugation not significantly altering binding.

significantly ($p<0.0001$) lower than hIFN alone to HepG2 cells (Figure 3.14). This was consistent with the lesser binding kinetics for NOTA-hIFN-CTRLdAb compared to hIFN (Table 3.7).

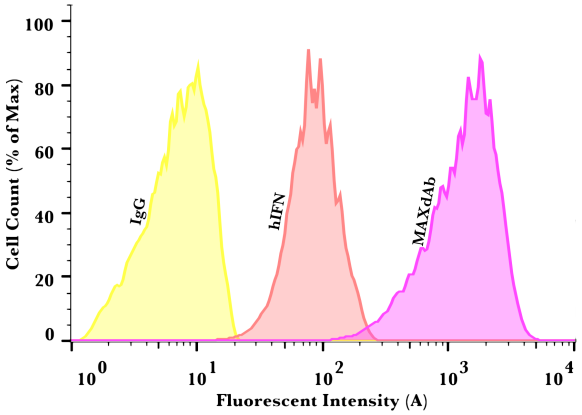

Figure 3.14 – Flow Cytometry of MAXdAb & hIFN with HepG2
Histogram of flow cytometric analysis of live HepG2 cell staining with MAXdAb and hIFN alone detected with anti-dAb anti-hIFN mAb respectively and anti-mAb Alexa647, plus an irrelevant-IgG representing non-specific binding. Data demonstrates that MAXdAb can bind to HepG2 cells to a greater extent than hIFN alone, seemingly reflecting receptor copy number.

Consistent with the previous data, it was apparent that NOTA conjugation for hIFN-MAXdAb and hIFN-CTRLdAb appeared to have decreased their ability to bind to ASGPR on HepG2 whole cells (Figure 3.13) with a non-significant ($p=0.25$) decrease of 31.3% and a significant ($p=0.002$) decrease of 34.4%, respectively. The non-significance of the NOTA-hIFN-MAXdAb binding decrease is owing to the highly variable total cell binding values which is likely due to the influence of ASGPR receptor number on the binding.

3.2.5.2 U937 Whole Cell Binding

The U937 cell line was selected for its lack of ASGPR expression. Indeed, the U937 control stainings (Table 3.10, Figure 3.15) showed the lack of detectable ASGPR as the cell staining was not different to the non-specific staining with the irrelevant IgG. The presence of hIFNAR2 and hIFNAR1 was confirmed with the latter appearing to be less strongly expressed, as was seen on the HepG2 cells.

The U937 data backed up the conclusions from the HepG2 cells. The difference between the NOTA-hIFN-MAXdAb and NOTA-hIFN-CTRLdAb was reduced (Figure 3.16), thus indicating specific ASGPR binding was the driver behind the high binding of NOTA-hIFN-MAXdAb to HepG2 cells. As the U937 cells had a different expression level of hIFNAR compared to the HepG2 cells (Figure 3.15) and likely a different cell surface protein expression profile, it was not an ideal control for

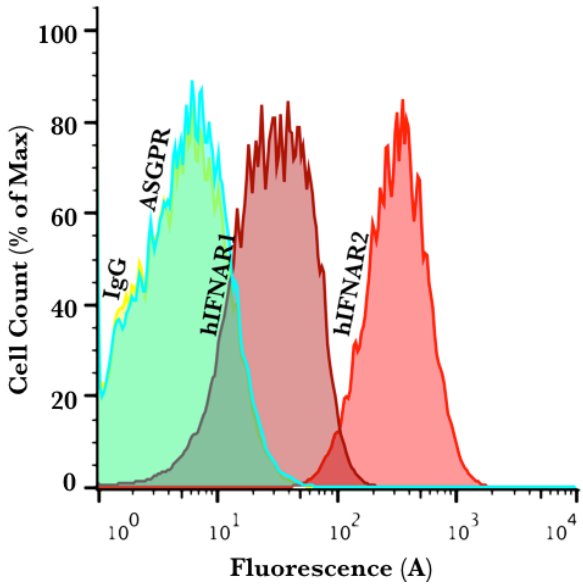

Figure 3.15 – Flow Cytometry for Receptor detection on U937 cell line

Histogram of flow cytometric analysis of live U937 cell staining with anti-receptor mAbs – α-ASGPR, α-hIFNAR1, and α-hIFNAR2 – plus an irrelevant-IgG non-specific control, detected with anti-mAb Alexa647. Data demonstrates that U937 cells express hIFNAR1, hIFNAR2 at respectively increasingly levels but do not express detectable levels of ASGPR above background staining.

specific ASGPR binding. For instance, it did not entirely rule out that the observed HepG2 cell binding could have been non-specific MAXdAb-mediated cell binding. Comparison of ASGPR-positive and ASGPR-negative cell lines from the same parental lineage whether transfection, siRNA or full recombination derived, may have provided more robust data for the effect of ASGPR on cell binding.

The MAXdAb appeared to have some non-specific affinity for the U937 cells (Table 3.10). It had no hIFN and so ought not to have bound. This was consistent with the non-specific binding seen in the hIFNAR2 Biacore SPR data (Section 3.2.3.2). Nevertheless, staining with the anti-dAb mAb secondary alone showed anti-dAb itself is somewhat non-specifically cross-reactive with the U937 cells (Table 3.10)

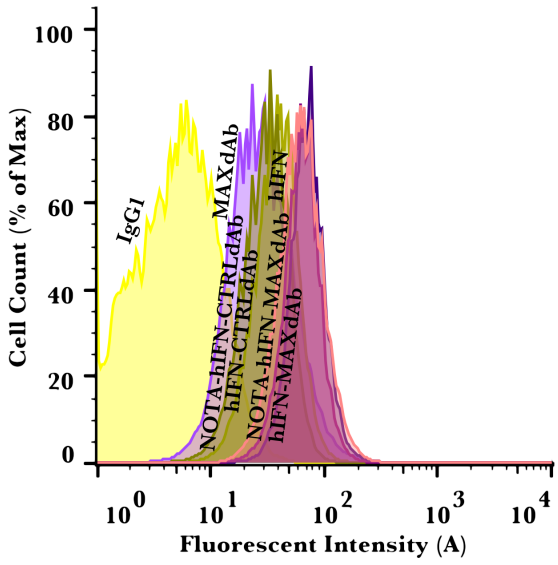

Figure 3.16 – Flow Cytometry of hIFN-dAb Fusions with U937

Histogram of flow cytometric analysis of live U937 cell staining with hIFN-dAb fusions – NOTA-hIFN-MAXdAb, hIFN-MAXdAb, NOTA-CTRLdAb and hIFN-CTRLdAb – detected with anti-dAb mAb and anti-mAb Alexa647, plus MAXdAb, hIFN and an irrelevant-IgG representing non-specific binding. Data demonstrates that with only hIFN-mediated cell binding, there is no significant difference in binding between NOTA-hIFN-MAXdAb, hIFN-MAXdAb, NOTA-hIFN-CTRLdAb and hIFN-CTRLdAb with binding no greater than hIFN alone.

and so likely accounted for some of the staining signal in the MAXdAb sample.

The pattern of hIFNAR binding seen on the U937 cells reflected the HEK-Blue hIFN potency results with hIFN-MAXdAb > hIFN > NOTA-hIFN-MAXdAb > hIFN-CTRLdAb > NOTA-hIFN-CTRLdAb. This further evidenced the assertion that K_D for hIFNAR2 was not an accurate reflection of binding to the full hIFNAR (Section 3.2.4). In light of the apparent MAXdAb alone binding, the higher binding of the hIFN-MAXdAb compared to hIFN may be due to some MAXdAb-mediated non-specific binding to the U937 cells.

In summary, the flow cytometry results showed that NOTA-hIFN-MAXdAb could bind whole HepG2 cells. This was most likely through its MAXdAb-mediated binding to ASGPR with an indication that hIFN-mediated hIFNAR binding was less relevant to total cell binding. These binding results also reflected the relative surface expression of ASGPR and hIFNAR1, indicating that receptor copy number was an important variable. The data suggested that NOTA-hIFN-CTRLdAb bound HepG2 cells through its hIFN-mediated hIFNAR only and so was considerably less targeted to HepG2 cells as a result. The results indicated that any observed HepG2 tissue targeting *in vivo* would likely be driven by ASGPR binding, and concordantly that any observed significant difference between NOTA-hIFN-MAXdAb and NOTA-hIFN-CTRLdAb uptake in a HepG2 xenograft would likely be overwhelmingly ASGPR-targeting mediated. Furthermore, the results show that HepG2 cells were an appropriate choice for *in vivo* xenograft modelling with hIFN-ASGPRdAbs.

3.2.6 Radioligand Binding Assay

A radioligand binding assay allowed the *in vitro* quantitation of specific binding of the radioligands ^{68}Ga-NOTA-hIFN-MAXdAb and ^{68}Ga-NOTA-hIFN-CTRLdAb to their target receptors ASGPR and hIFNAR on a population of whole HepG2 cells (Method 2.2.5). This was achieved through incubating the HepG2 cells with the radioligands, removing unbound radioligand through a series of wash steps, and then measuring the bound radioactivity of the cells. The specific binding was determined by running two experiments in parallel, measuring both the total binding to the cells and the non-specific binding, with the difference between these values representing the specific binding. The non-specific binding was calculated by

blocking the specific target receptors by pre-treating the HepG2 cells with an excess of cold hIFN-MAXdAb blocking ligand, therefore providing a measure of only non-specific binding such as to other membrane proteins or uptake in the lipid bilayer. Performing these measurements at varying concentrations of radioligand allowed the creation of binding curves for total and non-specific binding, and thus the resolution of the specific binding curve. Subsequently an estimate of K_D could be calculated from the maximum binding B_{max}. The assay was performed in a 96-well format, developed specifically for this work. The binding values were expressed as amount of bound radioligand per amount of assay protein (fmol/mg) to enable assays to be compared in spite of varying cell counts.

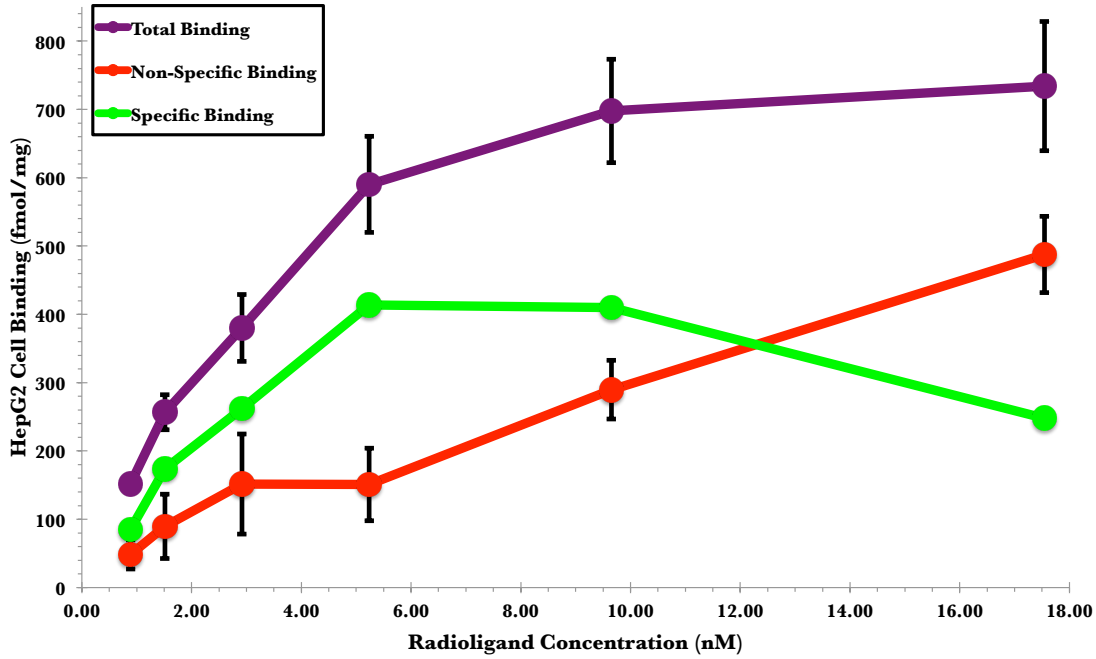

Figure 3.17 – ^{68}Ga-NOTA-hIFN-MAXdAb Binding Assay
Radioligand binding assay with ^{68}Ga-NOTA-hIFN-MAXdAb binding HepG2 cells including total binding (Total Binding) and 1μM blocking with hIFN-MAXdAb (Non-Specific Binding) for the calculation of the Specific Binding. Data shows an apparent B_{max} of 410fmol/mg for Specific Binding, representing a K_D of 1.9nM for HepG2 cell binding. Non-specific binding increases at a linear concentration-dependent rate (R^2=0.98). Specific binding decreases with increasing concentration possibly representing an increase in non-specific self-association.

The total binding appeared to demonstrate a typical single-phase exponential association profile (Figure 3.17). The observed specific binding for ^{68}Ga-NOTA-hIFN-MAXdAb reached saturation between approximately 5nM and 10nM at a B_{max} of approximately 400fmol/mg. This corresponded to a calculated K_D of approximately 1.9nM for HepG2 cell binding. This value was representative of

binding to both ASGPR and hIFNAR. This compared to the Biacore quantitated K_D values for NOTA-hIFN-MAXdAb of 0.7nM for ASGPR (Table 3.6) and 46.9µM for hIFNAR (Table 3.7), with the lower K_D values representing the post-labelling reaction affinities. The K_D value of 1.9nM thus indicated that the majority of HepG2 cell binding is through MAXdAb-mediated ASGPR binding, and concurs with the emerging model established by the flow cytometry data. This hypothesis was further supported by the ^{68}Ga-NOTA-hIFN-CTRLdAb data (representing hIFNAR binding only) which demonstrated no detectable HepG2 binding above non-specific binding at the sampled concentrations (Figure 3.18). Therefore, it appeared that any hIFN-mediated hIFNAR binding to HepG2 cells in the ^{68}Ga-NOTA-hIFN-MAXdAb assay was likely to have a broadly negligible overall influence on total binding and so the observed binding is likely to only reflect MAXdAb-mediated ASGPR HepG2 binding.

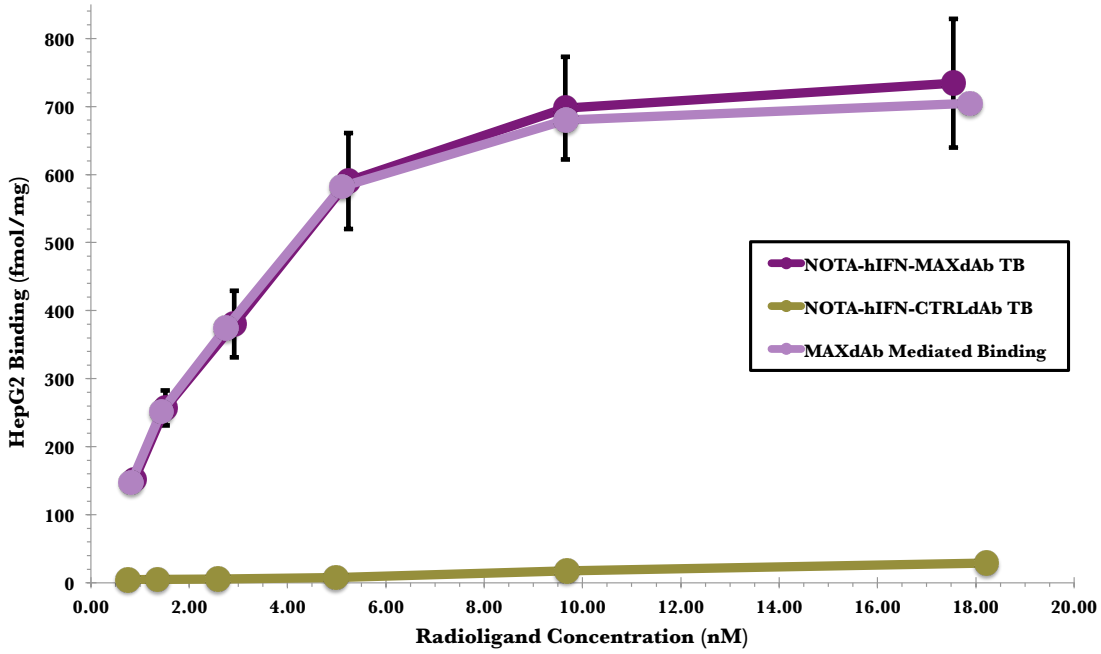

Figure 3.18 – ^{68}Ga-NOTA-hIFN-MAXdAb vs ^{68}Ga-NOTA-hIFN-MAXdAb in a HepG2 Binding Assay

Radioligand binding assays with ^{68}Ga-NOTA-hIFN-MAXdAb and ^{68}Ga-NOTA-hIFN-CTRLdAb total binding to HepG2 cells for the calculation of the MAXdAb mediated binding. This includes both specific and non-specific binding. The data demonstrates that hIFN-mediated binding either specifically to hIFNAR or non-specifically does not significantly ($p>0.05$) contribute to HepG2 binding by ^{68}Ga-NOTA-hIFN-MAXdAb.

A Scatchard plot (Figure 3.19) of the total bound ligand against the ratio of bound and free ligand showed a linear relationship with an $R^2 = 0.92$ that was indicative of the ligand binding with a single affinity. This was supported by a Hill

coefficient of 0.92, which was indicative of binding to one binding site. The Scatchard plot and Hill coefficient data appeared to support the assertion that an ASGPR binding was the primary driver of the observed NOTA-hIFN-MAXdAb HepG2 interaction. The Scatchard plot also indicated a K_D of 4.58nM for HepG2 cells, which again demonstrated that NOTA-hIFN-MAXdAb had a low nM affinity for HepG2 cells.

In summary, the radioligand binding assay provided additional data to support evidence from previous experiments. It concurred with the Biacore SPR data and Flow Cytometry data showing that the predominating MAXdAb-mediated low nM affinity ASGPR HepG2 binding of NOTA-hIFN-MAXdAb contrasts with the low HepG2 binding of the NOTA-hIFN-CTRLdAb.

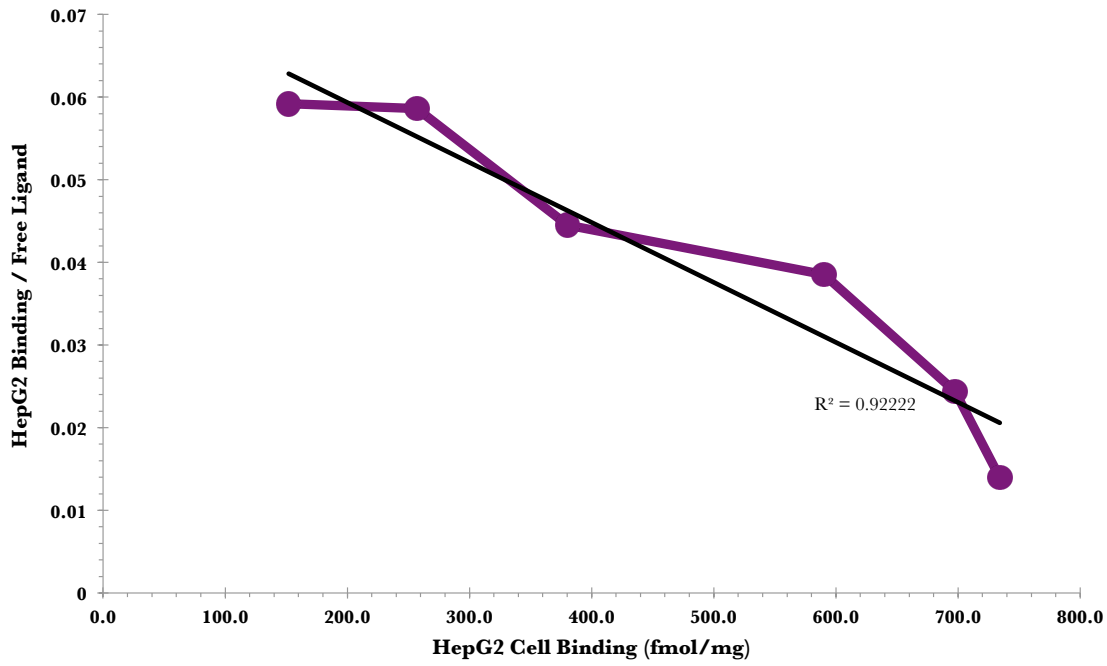

Figure 3.19 – Scatchard Plot of ^{68}Ga-NOTA-hIFN-MAXdAb
Radioligand binding assay with ^{68}Ga-NOTA-hIFN-MAXdAb represented as a Scatchard plot of the ratio of HepG2 bound ligand to the free assay ligand against the total bound protein (fmol/mg). The linear plot demonstrates that the HepG2 binding was with a single affinity, most likely the ASGPR-mediated interaction. The slope indicates a K_D of approximately 4.58nM.

3.4 GA-68 RADIOLABELLING DEVELOPMENT

The chosen radiolabelling strategy for this work was utilising gallium-68 (Introduction 1.7.2) to radiolabel the NOTA conjugated dAb fusions. The Ga-68 radiolabelling of dAb proteins had never been previously performed prior to this investigation. Therefore, the reaction conditions required extensive optimisation to attain high labelling efficiencies at low protein concentrations, in order to achieve the maximum specific activities.

3.4.1 Reaction Development

The EZ IG100 370MBq ^{68}Ge/^{68}Ga generator was used to produce Ga-68 for the radiolabelling reactions (Method 2.3.1). The generator set-up underwent numerous iterations towards a system of elution for efficient collection of the most radioactive fraction and minimised failed runs. Airlocks in particular prevented failed runs and potential damage to the generator due to air in the system.

The optimum radioactive yields were attained from the first elution of the day if the generator was eluted in the previous evening. Regular daily elution also improved labelling reliability, likely by preventing the build up of impurities. Manual injection of 0.1M HCl at a rate of 1ml/min was found to yield the most consistent elution profile. The elution output profile was periodically monitored to attain the highest radioactive fraction possible for reaction (Appendix Figure 6.12) by collecting the eluate conforming to the top of the peak. The generator yields were observed to deteriorate faster than the Ge-68 half-life may suggest (Appendix Figure 6.13) and so generator care was a high priority.

TraceSelect reagents were used for all the reaction reagents, including making all reagents in TraceSelect UltraPure water, which improved the labelling consistency by presumably reducing metal contaminants. The use of LoBind plasticware improved radiolabelling by an estimated 3-5% and also reduced losses during recovery by an unquantified amount, likely due to less protein sticking to the tubes. The order of reactant addition appeared important to prevent colloid formation. Radiolabelling efficiencies improved by adding the buffer to the aliquot of Ga-68 with instant mixing to prevent pockets of high pH, lastly followed by the conjugated protein.

Radiolabelling efficiencies for a time during the investigation dropped markedly. The problem was traced to the use of rubber in syringes and the airlocks. After subsequently switching to non-rubber equivalents the radiolabelling efficiencies were restored.

Initial indications about optimum reaction conditions were explored with NOTA alone labelling. These confirmed that 10 minutes at room temperature was optimum (37˚C increased labelling efficiency but also colloid) and was further observed to label optimally at pH3.5. The sampling of a titration of reaction pHs for hIFN-MAXdAb with 5M NaOH buffering identified pH4.4 as the optimal (Appendix Figure 6.14). The pH4.4 was likely the optimum pH between protein degradation at low pH and colloid formation at higher pH. The colloid was observed to increase up to an average of 13.8% with an increase in pH of only between 0.5 and 1.0 units.

3.4.2 Ga-68 Radiolabelling Reactions

Three reaction condition protocols were optimised based on buffering conditions to maintain the pH 4.4 reaction conditions: 5M NaOH (Appendix 6.1.5.1), 5M NaAc (Appendix 6.1.5.2) and 1M NaAc (Method 2.3.2).

The results demonstrated the contrasting efficacies of the different strategies (Table 3.11). The 5M NaOH method did not achieve sufficiently high specific activities above 0.5MBq/µg for NOTA-hIFN-MAXdAb. Similarly, the 5M NaAc method did not achieve specific activities consistently above 1.25MBq/µg. The logic behind utilising strong 5M NaOH and 5M NaAc buffers was to minimise the volume of the added buffer in the reaction, thus allowing more radioactivity to be included for the maximum potential specific activity. However, in practice both these methods proved unreliable because utilising small volumes increased the likelihood of pH variability and the highly concentrated alkaline was hypothesised to create a temporal pocket of high pH prior to shaking, which would increase colloid. It was apparent from the results that these methods resulted in a significant ($p=0.0002$) 5.8 fold greater formation of colloid when labelling NOTA-hIFN-MAXdAb compared to the 1M NaAc method, and thus the maximum potential labelling efficiencies were not attained.

Table 3.11
Ga-68 Labelling Method Results

Protein[$]	Radiolabelling Method*	Labelling Parameters		
		Radiolabelling Efficiency (%)	Specific Activity (MBq/µg)	Colloid (%)
NOTA-hIFN-MAXdAb	5M NaOH	83.0 ±8.9	0.53 ±0.04	18.3 ±7.47
	5M NaAc	75.8 ±10.3	1.23 ±0.21	23.7 ±7.24
	1M NaAc	88.9 ±2.5	2.37 ±0.08	3.64 ±0.49
NOTA-hIFN-CTRLdAb	5M NaOH	-	-	-
	5M NaAc	87.1 ±1.9	0.77 ±0.18	11.4 ±2.19
	1M NaAc	95.4 ±8.9	2.47 ±0.11	1.28 ±0.92

*Method 2.3.2 & Appendix 6.1.5, n>3, [$]~16µg at 1µM

The 1M NaAc method yielded significantly ($p<0.0001$) higher specific activities for both NOTA-hIFN-MAXdAb and NOTA-hIFN-CTRLdAb, with labelling sufficient for potential PET imaging given consistent specific activities above ~2.4MBq/µg owing to reliably low colloid formation (Table 3.11, Figure 3.20). The increased volume reduced the likelihood of pipetting errors and alleviated the colloid formation problems with reductions up to 85%. Moreover, utilising UltraPure reagents and Lo-Bind Eppendorf tubes further increased the achievable radiolabelling efficiencies at lower concentrations of hIFN-dAb down to 1µM. At this concentration, incubating at 37˚C also helped increase the radiolabelling efficiency consistency (Section 3.6.1).

The NOTA-hIFN-CTRLdAb consistently labelled to a higher specific activity than the NOTA-hIFN-MAXdAb regardless of the method employed. The reason for this was unclear, but was likely to be due to a differing NOTA conjugation state (Section 3.2.2.4).

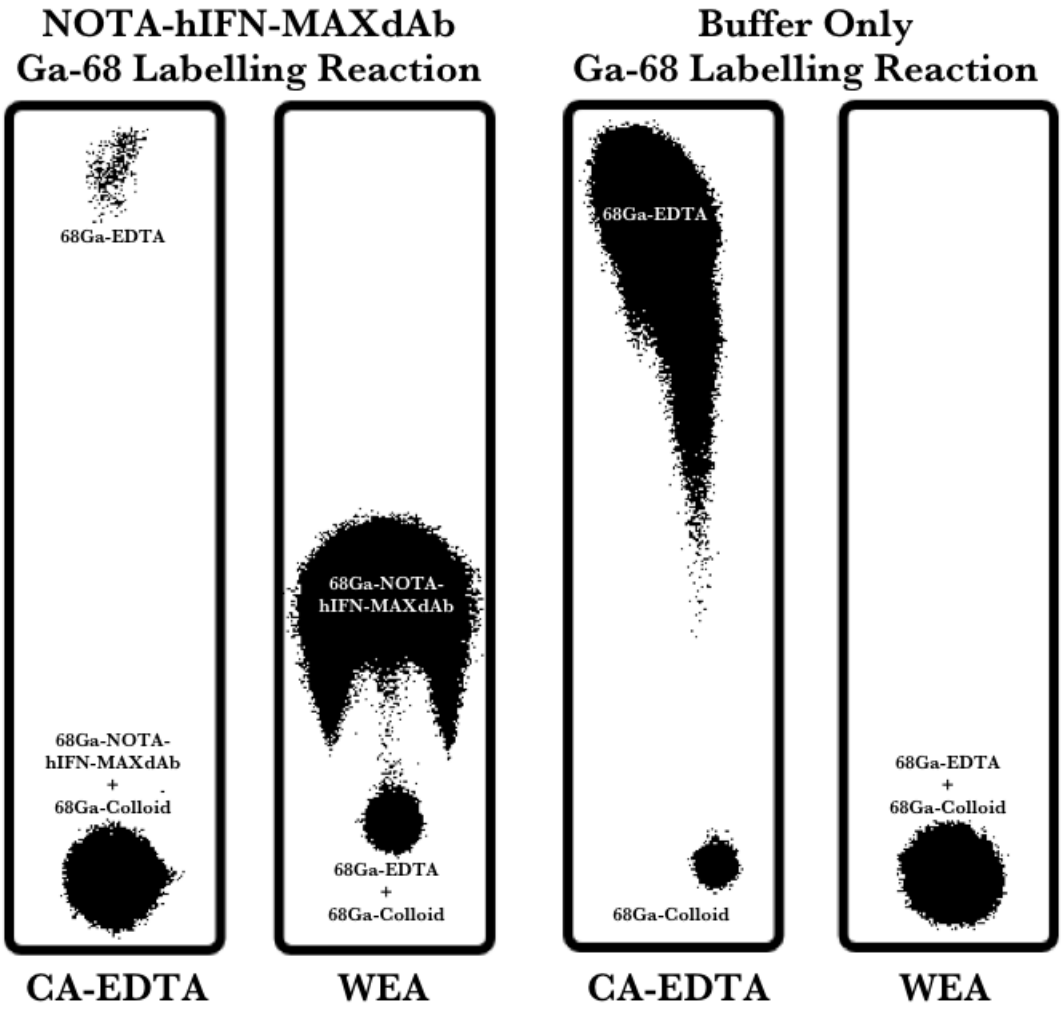

Figure 3.20 – Ga-68 NOTA-hIFN-MAXdAb Radiolabelling Reactions with 1M NaAc Method

Phosphorimaging of typical 0.02M CA-EDTA and WEA-(2%BSA(w/v)) TLCs of a ^{68}Ga-NOTA-hIFN-MAXdAb radiolabelling reaction and a Buffer Only radiolabelling reaction control. The CA-EDTA TLC relative intensities allow the computation of the ^{68}Ga-EDTA as a measure of free Ga-68 whereas the WEA-TLC allows computation of the radiolabelled product – the ^{68}Ga-colloid is calculated from both TLCs.

Biacore SPR analysis (Section 3.2.3.1) was utilised with NOTA-hIFN-MAXdAb to ascertain that the ASGPR binding properties were still active after undergoing the 1M NaAc labelling protocol*. The data demonstrated that there was a negative effect on the MAXdAb-mediated ASGPR binding of the protein after undergoing the radiolabelling reaction (Figure 3.21). The K_D for unreacted NOTA-hIFN-MAXdAb was determined to be 0.85nM† and post-reaction was determined to be 1.66nM ±0.07. This latter decrease in affinity compares with the 1.9nM result from the radioligand binding assays (Section 3.2.6). Hence, the labelling reaction had

* This was performed with just 0.1M HCl rather than Ga-68 eluate

† Compares to 0.73nM from the previous work, which was a fresher batch of conjugated protein

a detrimental effect on the binding affinity but the ASGPR binding was nevertheless maintained at a low nM level.

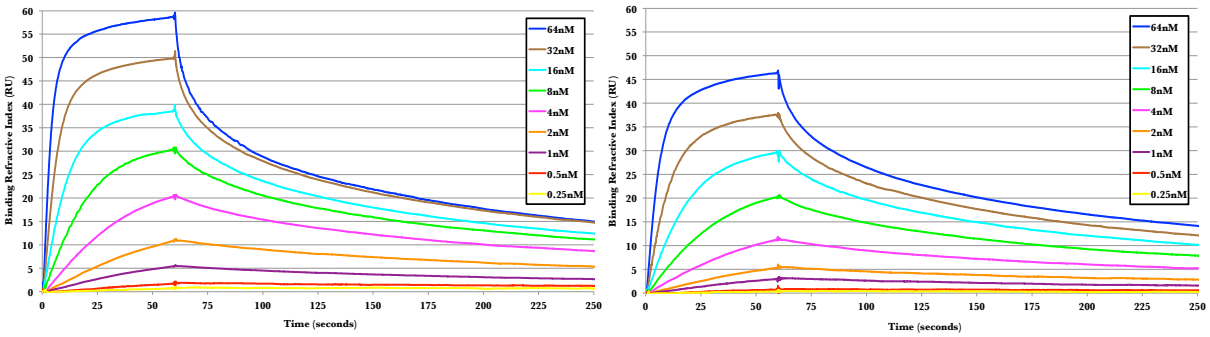

Figure 3.21 – Biacore T200 SPR Analysis of the NOTA-hIFN-MAXdAb pre- and post-reaction
Biacore T200 SPR with ASGPR-H1-CRD immobilised on a CM5 chip assessed the ASGPR-H1-CRD binding kinetics of a 64-0.25nM 1:2 serial dilution of NOTA-hIFN-MAXdAb both pre- and post-reaction with Ga-68 injected over the chip surface at 30µlmin^{-1}. Demonstrates decrease in binding affinity for ASGPR-H1-CRD but MAXdAb function remains active.

In summary, a radiolabelling method involving buffering with 1M NaAc was designed and optimised to enable the reaction of NOTA-hIFN-dAbs with Ga-68 at pH4.4. This achieved reliably high labelling efficiencies and concurrently high specific activities, with only a minor affect on binding affinity.

3.4.3 Further Reaction Optimisation

3.4.3.1 Reaction Purification

The maximum radiolabelling efficiencies and specific activities achieved with the 1M NaAc method were sufficient for *in vivo* work. However, there was still colloid present and free ^{68}Ga-EDTA and so purification of the reaction was optimised (Appendix 6.1.7 & Method 2.3.2).

Filtration with a syringe-driven 0.22µm filter unit was utilised based on the principle that the filter membrane would retain the ^{68}Ga-colloid. This method showed a recovery of 50.6% ±14.0 and in over half of instances there was a net decrease in purity owing to lost ^{68}Ga-NOTA-hIFN-dAb. Hence, this method was not appropriate.

A modified Protein A method for purifying the radiolabelled NOTA-hIFN-dAbs proved ineffectual, with a recovery of 3.4% ±2.1 purified ^{68}Ga-NOTA-hIFN-MAXdAb. This was owing to only about 10% of the loaded radiolabelling reaction

binding to the column and a poor elution profile. This method was also ineffectual because the NaAc buffer still required pH adjustment from pH4.5 to pH7.0.

Illustra NAP-5 column purification was the standard purification method for radiolabelled dAb fusions[74], however the highest yield achieved with ^{68}Ga-NOTA-hIFN-MAXdAb was a 25.8% loaded protein recovery in the 0.7ml fraction with a 68.8% reduction in colloid and overall a 56.8% increase in the purity of the ^{68}Ga-NOTA-hIFN-MAXdAb. This method thus proved again ineffectual in spite of positive purity improvements because there was too much product retained on the column and the recovered fraction was too dilute for PET imaging.

The MiniTrap G25 column purification method yielded consistently pure product (Figure 3.22) at sufficiently high concentrations for subsequent PET imaging.

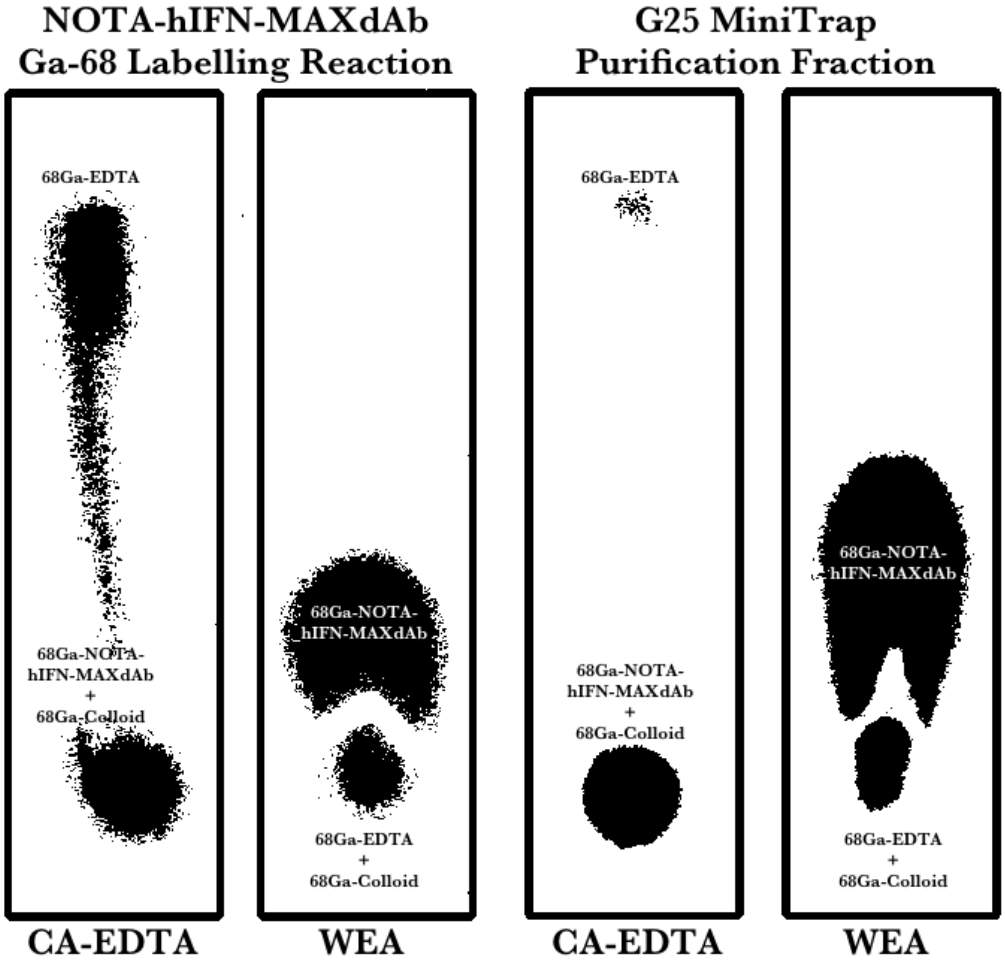

Figure 3.22 – G-25 MiniTrap Purification of a Ga-68 NOTA-hIFN-MAXdAb Radiolabelling Reaction

Example of 0.02M CA-EDTA and WEA (2%BSA(w/v)) TLC phosphoimaging of a ^{68}Ga-NOTA-hIFN-MAXdAb radiolabelling reaction and the primary fraction from the subsequent G-25 MiniTrap purification. The radiochemical impurities were observed to decrease in G-25 with purification, most apparent in the CA-EDTA TLC result.

Radiochemical impurities were decreased by an average of 78.1% ±12.1, allowing ^{68}Ga-NOTA-hIFN-MAXdAb purified up to 97.8% and ^{68}Ga-NOTA-hIFN-CTRLdAb up to 99.4%, as quantified by iTLC (Figure 3.22) and confirmed by HPLC (Figure 3.23). Furthermore, the process simultaneously buffer exchanged into physiological buffer PBS and as a two step method was also rapid.

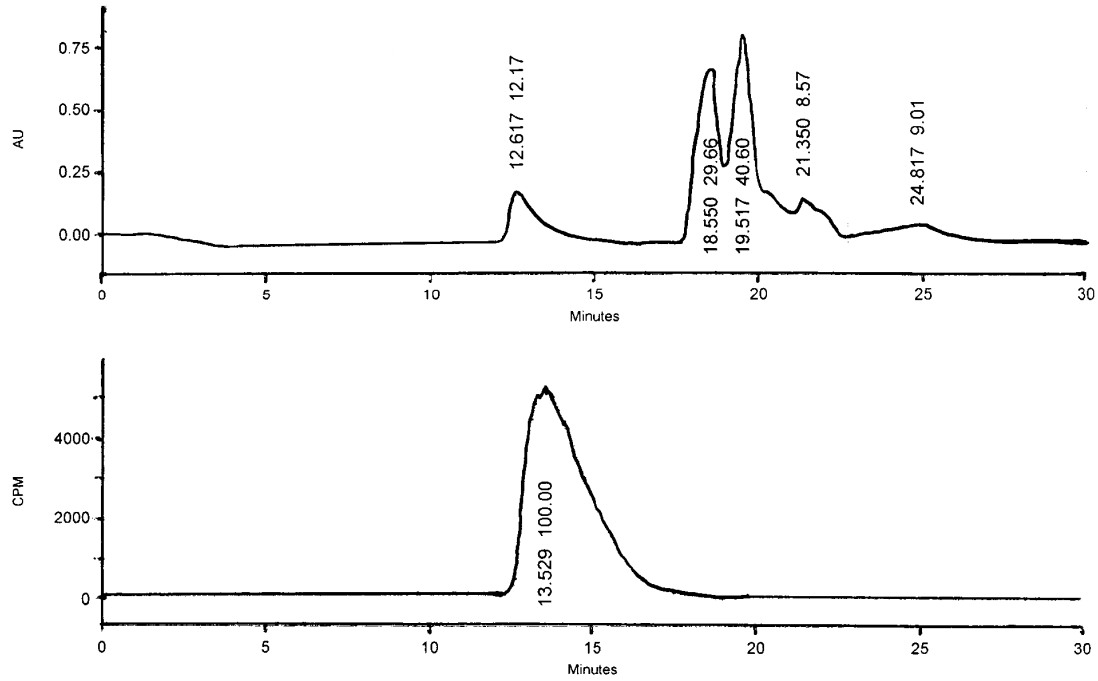

Figure 3.23 – SE-HPLC of G25-Purified ^{68}Ga-NOTA-hIFN-MAXdAb Fraction

SE-HPLC YMC-DIOL-60 column separation, and 220nm UV and radio detection of ^{68}Ga-NOTA-hIFN-MAXdAb purified in the primary fraction of the G25 MiniTrap purification. The observed results demonstrate the 100% purity of the ^{68}Ga-NOTA-hIFN-MAXdAb eluting at 12.62 minutes on the UV trace and as detected on the radio-trace at 13.53 minutes. The remaining UV trace peaks correspond to buffer reagents.

Hence, a method of quickly and reliably purifying the ^{68}Ga-NOTA-dAbs to almost 100% purities was developed utilising MiniTrap G25 columns, whilst also conveniently buffer exchanging into PBS.

3.4.3.2 Cationic Exchange Reactions

The elution of the Ga-68 generator with 0.1M HCl allowed the direct collection of the most radioactive fraction of Ga-68 based on the top of the elution activity peak. However, the eluate is a relatively dilute solution of Ga-68. Therefore, concentrating this fraction and the radioactivity from the whole elution would enable a higher concentration of radioactivity available within the same or a lower reaction

volume, thus potentially allowing higher achievable specific activities. Cationic exchange allowed scrubbing of the Ga-68 from the eluate and then re-elution in a considerably smaller volume (Appendix 6.1.6).

Bond-Elut SCX cationic exchange columns were successfully used to extract the Ga-68 from the eluate. The Ga-68 elution was optimised to elute at a markedly higher concentration in ~40µl of 5M NaCl 0.1M HCl pH1.0. This enabled the average MBq per reaction to increase from 20.4MBq ±2.21 to 49.6MBq ±3.70 in spite of a greater than 400% decrease in reaction volume. Buffering with 1M NaAc to pH4.0 was established as the optimum reaction conditions for labelling NOTA-hIFN-CTRLdAb to high labelling efficiencies followed by G25 purification (Table 3.12).

Table 3.12
Ga-68 Bond-Elut SCX Labelling Method Results

Protein[$]	Radiolabelling Method	Labelling Parameters		
		Radiolabelling Efficiency (%)	Specific Activity (MBq/µg)	Max. Purified (%)
NOTA-hIFN-CTRLdAb	1M NaAc	95.4 ±8.90	2.47 ±0.11	99.4
	SCX	79.1 ±3.70	3.79 ±0.18	99.1

n≥3

The achievable specific activities for ^{68}Ga-NOTA-hIFN-CTRLdAb were increased by over 50%, in spite of a decrease in radiolabelling efficiency, and were efficiently purified to close to 100% radiochemical purity as shown by iTLC (Appendix Figure 6.16).

However, the reduction in labelling efficiency was indicative of a problem. Indeed, when it came to radiolabelling NOTA-hIFN-MAXdAb, the task proved insurmountable. Closer analysis of the NOTA-hIFN-MAXdAb post-reaction by Biacore SPR analysis revealed that the reaction conditions were too stringent and the MAXdAb-mediated ASGPR binding was lost (Figure 3.24). Therefore, it was possible that the high salt conditions may have caused denaturation.

Decreasing the salt concentration in the elution buffer from 5M to 1M (a final reaction concentration of ~3M to ~0.5M respectively) did not ameliorate the loss of ASGPR-binding function. Moreover, below 2.5M, the column elution was less efficient, eluting over a larger volume range.

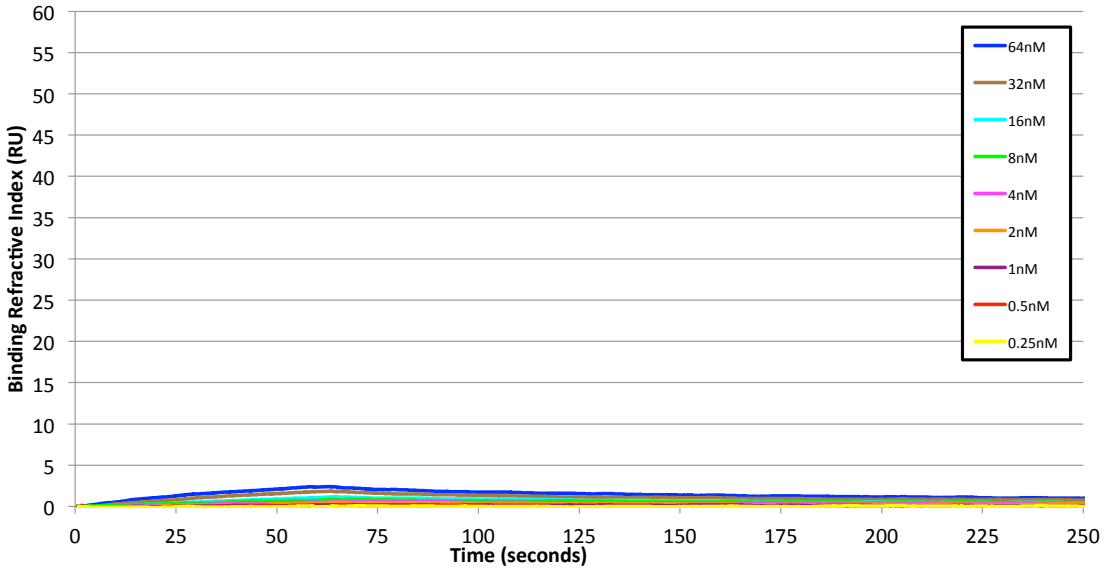

Figure 3.24 – Biacore T200 SPR Analysis of the NOTA-hIFN-MAXdAb post SCX Cationic Exchange Radiolabelling Reaction
Biacore T200 SPR with ASGPR-H1-CRD immobilised on a CM5 chip was carried out to assess the ASGPR-H1-CRD binding kinetics of a 64-0.25nM 1:2 serial dilution of NOTA-hIFN-MAXdAb post-reaction with SCX cationic Ga-68, injected over the chip surface at 30µlmin^{-1}. Result demonstrates that the SCX Ga-68 radiolabelling reaction conditions render the MAXdAb unable to bind ASGPR.

In conclusion, the Bond-Elut SCX cationic exchange protocol may yield high specific activity labelling with proteins that can survive the high salt concentrations but cationic exchange methods proved inappropriate for hIFN-MAXdAb radiolabelling.

3.5 BIODISTRIBUTION STUDIES

Radioligand biodistribution analyses are complicated experiments involving integrating numerous time-critical steps (Appendix Figure 6.3). They were used to quantify *in vivo* NOTA-hIFN-MAXdAb and NOTA-hIFN-CTRLdAb HepG2 xenograft tissue uptake, in addition to uptake in other tissues (Method 2.4.3). SCID Beige HCC HepG2 models were created for this purpose. The uptake values for the dissected tissues were converted to %ID/g so as to control for the mass of the tissue.

3.5.1 Ga-68 Radiolabelling

Utilising the 1M NaAc method developed for the reliable labelling of the NOTA-hIFN-MAXdAb and NOTA-hIFN-CTRLdAb (Method 2.3.2) plus G-25 MiniTrap purification to remove radiochemical impurities, radiolabelled doses of the NOTA-hIFN-dAbs were prepared at RT immediately prior to injection thus maximising the dose radioactivity of the short-lived Ga-68.

The average specific activity achieved with a ~2μM reaction (Table 3.13) for both NOTA-hIFN-MAXdAb (1.40MBq/μg) and NOTA-hIFN-CTRLdAb (1.24MBq/μg) was sufficient for subsequent gamma counting in all instances.

Table 3.13
Ga-68 Radiolabelling for Biodistribution Studies

Protein	Reaction Conc. (μM)	Radiolabelling Efficiency (%)	Specific Activity (MBq/μg)	Radiochemical Purity (%)*
NOTA-hIFN-MAXdAb	2.19	89.2 ±4.56	1.40 ±0.63	98.0 ±1.63
NOTA-hIFN-CTRLdAb	2.08	93.4 ±8.34	1.24 ±0.39	99.4 ±0.50

n≥3, SD values displayed, *post-G25 purification

A final radiochemical purity of greater than 96% was achieved in all instances utilising G-25 MiniTrap purification. The purified fraction was further diluted with PBS(1% BSA (w/v)) to yield the desired mass of radiolabelled protein per 200μl dose as appropriate.

3.5.2 Dosing Biodistribution Study

A dosing study was initially performed to determine whether receptor saturation* was a significant effect with increasing dose. The aim was to have an effective concentration to observe xenograft targeting without saturating the receptors. Doses of 1µg, 6µg and 16µg of ^{68}Ga-NOTA-hIFN-MAXdAb were selected for biodistribution analysis at three hours post-injection.

The 1µg dose demonstrated the highest xenograft tissue uptake values at 2.42%ID/g ±0.69 (Figure 3.25). There was no observed significant difference between 1µg and 16µg (p=0.25), and similarly the 6µg and 16µg doses (p=0.23). There was, however, a minor significant decrease (p=0.03) in the tumour xenograft uptake between 1µg and 6µg. This decrease was not perceived to indicate receptor

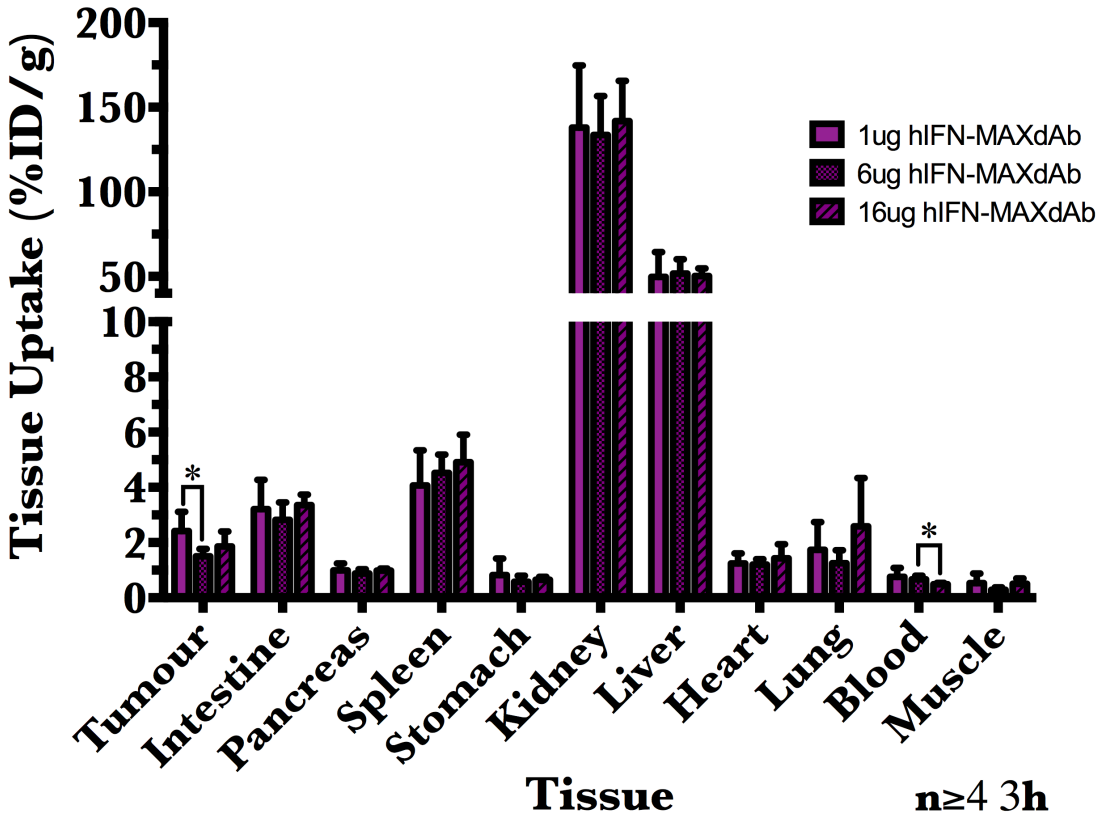

Figure 3.25 – Biodistribution of ^{68}Ga-NOTA-hIFN-MAXdAb in SCID Beige HepG2 Xenograft Model at 3hr with varying dose

Mean %ID/g in selected tissues at 1µg, 6µg, and 16µg injected dose of ^{68}Ga-NOTA-hIFN-MAXdAb at 3 hours post- IV administration as determined by Gamma Counting. No relevant significant differences in tissue uptakes observed at any of the doses tested but for minor decrease in tumour uptake between 1µg and 6µg.

* Non-radiolabelled ligand within the same administered dose outcompeting the radioligand* for receptor binding

saturation because there was not then a concurrent decrease in xenograft uptake from 6μg to 16μg. The xenograft uptake data thus did not appear to present any clear indication about whether receptor saturation was occurring. Nonetheless, it did show that observable xenograft uptake was quantifiable with a 1μg dose of ^{68}Ga-NOTA-hIFN-MAXdAb. The reliability of the radiolabelling reaction to achieve specific activities sufficient for a 1μg dose* was highly reproducible and so there was no impediment to using a 1μg dose. Hence, on the balance of probabilities, it appeared prudent to proceed with further *in vivo* experimentation using a 1μg dosing strategy.

The remaining tissues showed no discernable pattern of uptake relative to the dose and so will be analysed in more detail in further sections. However, the liver and kidney tissues showed very large uptakes.

The liver tissue demonstrated approximately 50%ID/g uptake of the ^{68}Ga-NOTA-hIFN-MAXdAb. This corresponded to an average of 44.9% of the total injected dose (ID). Therefore, the liver was a very large sink for the ^{68}Ga-hIFN-MAXdAb. Some uptake was expected to be attributable to the small amount of remaining ^{68}Ga-colloid impurity in the dose. Moreover, some off-target MAXdAb-mediated cross-reactivity was anticipated because the amino acid sequences of *Homo sapiens* ASGPR1/ASGPR2 and the *Mus musculus* ASGPR1/ASGPR2 are 79%/64% identical and 89%/84% similar, respectively†. Murine ASGPR1/ASGPR2 are also present in the murine liver at a very high level of 222/180FPKM‡, respectively. Hence, the probability of the hypothesised off-target interaction of MAXdAb with murine ASGPR (mASGPR) was high and indeed dAb cross-species reactivity was previously observed *in vitro* with Biacore SPR and *in vivo* with SPECT imaging[74]. There may also be IFNAR cross-reactivity (discussed in Section 3.5.3.3). However, the observed extent of uptake was not anticipated. This was problematic for the model because the mouse liver removed a high proportion of the injected dose from the system. This complicated the model because this dose was unavailable for uptake in the xenograft tissue (Section 3.5.4). In this instance, however, it had no affect on

* Dose is limited by still having adequate radioactivity for gamma counter readings at 3h post-injection
† UniProt analysis performed on P07307 ASGR2_HUMAN and P24721 ASGR2_MOUSE
‡ Average value from three studies for Asgr1 and in *Mus musculus* as determined by www.ebi.ac.uk

the conclusions because the uptake was not significantly (p=0.87) different for each concentration of NOTA-hIFN-MAXdAb and so could be considered a constant.

The highest observed uptake of any tissue sampled was approximately 130%ID/g in kidney and was representative of the 33kDa ^{68}Ga-NOTA-hIFN-MAXdAb being under the renal clearance threshold of 66kDa. This represented an average of 17.2% of the injected dose. This loss was unavoidable without introducing a blocking agent such as serum albumin or performing a nephrectomy. These were, however, deemed likely to just introduce further unknown variables.

In summary, the experiment yielded ambiguous data concerning to effect of dose on tissue uptake and so firm conclusions on receptor saturation could not be drawn. Therefore it appeared logical to continue with the lowest reproducible dose, which was 1µg.

3.5.3 Time Course Biodistribution Study

The NOTA-hIFN-MAXdAb and NOTA-hIFN-CTRLdAb tissue uptake in the SCID Beige HepG2 xenograft model was examined at 1h, 3h and 24h post-injection time points utilising a 1µg dose to determine how tissue uptake changes over time.

3.5.3.1 In-111 Labelling

The ^{68}Ga radiolabelling was not appropriate for a 24h time point and thus In-111 radiolabelling was employed to attain the 24h time point data (Table 3.14).

Table 3.14
In-111 Radiolabelling for Biodistribution Studies

Protein	Reaction Conc. (µM)	Radiolabelling Efficiency (%)	Specific Activity (MBq/µg)	Radiochemical Purity (%)*
NOTA-hIFN-MAXdAb	3.00	94.4	0.91	99.0
NOTA-hIFN-CTRLdAb	3.00	98.7	1.05	100.0

n=1, 3µM reaction, SD values displayed, *post-G25 purification

3.5.3.2 Xenograft Uptake Analysis

The HepG2 xenografts from the SCID Beige model demonstrated significantly different temporal radioligand uptake of the ^{68}Ga-NOTA-hIFN-MAXdAb compared to ^{68}Ga-NOTA-hIFN-CTRLdAb (Figure 3.26) with the uptake of ^{68}Ga-NOTA-hIFN-MAXdAb significantly higher at each time point. Thus this strongly suggested that the MAXdAb-mediated ASGPR binding was responsible for the increased uptake over the non-ASGPR targeted ^{68}Ga-NOTA-hIFN-CTRLdAb.

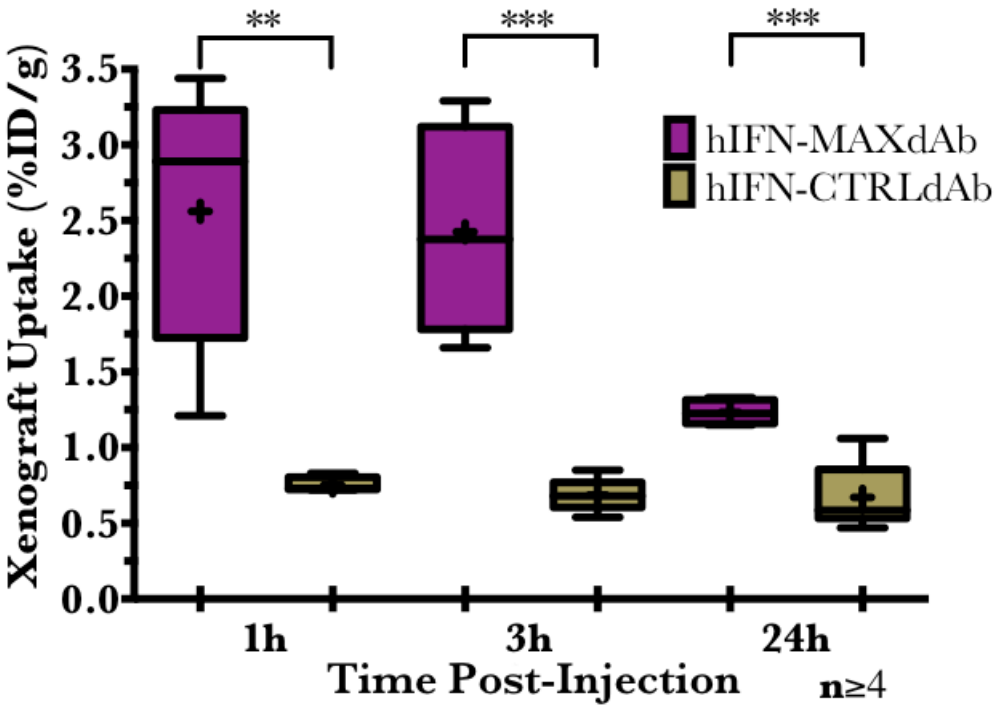

Figure 3.26 – Xenograft Uptake of ^{68}Ga-NOTA-hIFN-MAXdAb and ^{68}Ga-NOTA-hIFN-CTRLdAb in SCID Beige HepG2 Xenograft Model with 1µg dose over time

Mean %ID/g in xenograft tissue at 1µg injected dose of ^{68}Ga-NOTA-hIFN-MAXdAb and ^{68}Ga-NOTA-hIFN-CTRLdAb at 1 and 3 hours post-IV injection, in addition to ^{111}In-NOTA-hIFN-MAXdAb and ^{111}In-NOTA-hIFN-CTRLdAb at 24 hours post-IV-injection, as determined by gamma counting. Demonstrates significantly higher xenograft uptake with MAXdAb-mediated ASGPR targeting compared to only hIFN-mediated hIFNAR targeting.

At 3h the difference between ^{68}Ga-NOTA-hIFN-MAXdAb and ^{68}Ga-NOTA-hIFN-CTRLdAb uptake in the HepG2 xenografts of 2.42%ID/g versus 0.68%ID/g, respectively (Table 3.15), was extremely significant ($p=0.0008$) (Figure 3.26). This significance represented a decrease in variability in ^{68}Ga-NOTA-hIFN-MAXdAb uptake at 3h, as denoted by the tighter percentiles and the mean and median converging, compared to 1h post-injection where the range of results was

much greater. The xenograft uptake variability at 1h (Figure 3.26) was thought likely to be due to non-specific uptake promoted by a high blood concentration, as the xenograft to blood ratio was 0.9:1 at 1h prior to effective renal clearance. This contrasted with the uptake of ^{68}Ga-NOTA-hIFN-MAXdAb in the xenograft at 3h being significantly ($p=0.005$) higher than the concentration in blood (Figure 3.27) at a 3.5:1 xenograft to blood ratio. This strongly suggested that xenograft uptake was due to specific binding rather than being an artificial effect of the blood concentration. Therefore, 3h represented a consistent stable uptake value and was likely mediated by specific binding.

There was a significant ($p=0.014$) decrease in xenograft uptake of the NOTA-hIFN-MAXdAb between 3h and 24h (Figure 3.28) from 2.42%ID/g to 1.23%ID/g, which suggested that the half-life in the xenograft is approximately 24 hours. The difference in xenograft uptake versus ^{68}Ga-NOTA-hIFN-CTRLdAb was nevertheless still highly significant ($p=0.0005$) (Figure 3.26), which demonstrated that MAXdAb-mediated ASGPR binding could still promote xenograft retention at 24h. Moreover, the uptake was also extremely significant ($p<0.0001$) compared to the blood

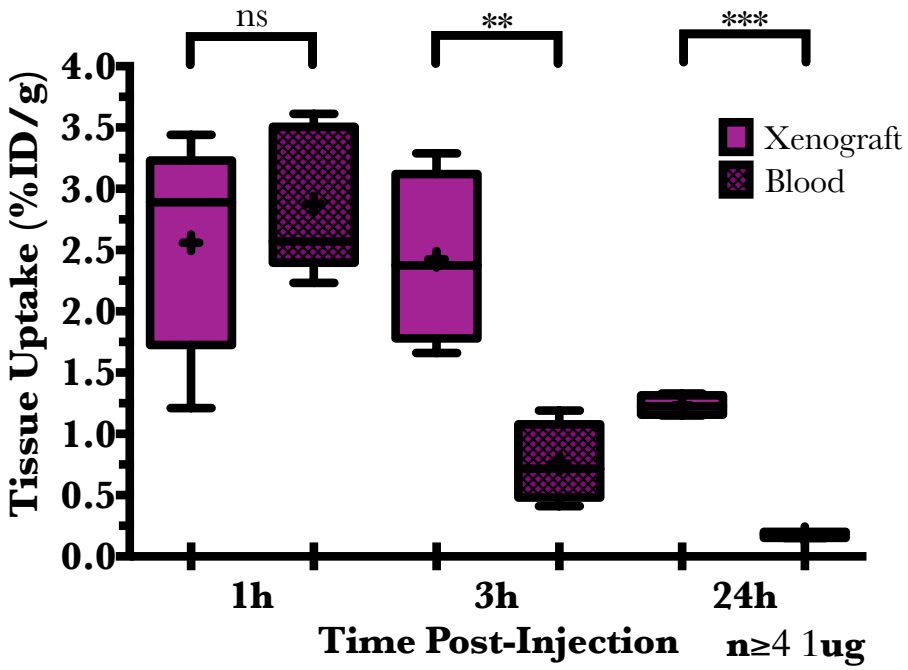

Figure 3.27 – Xenograft Uptake versus Blood Concentration of ^{68}Ga-NOTA-hIFN-MAXdAb in SCID Beige HepG2 Xenograft Model with 1µg dose over time

Mean %ID/g in xenograft tissue and blood at 1µg injected dose of ^{68}Ga-NOTA-hIFN-MAXdAb at 1 and 3 hours post-IV injection, in addition to ^{111}In-NOTA-hIFN-MAXdAb at 24 hours post-IV-injection, as determined by Gamma Counting. Demonstrates significantly higher levels of radioligand in xenograft at 3h and 24h versus in blood, therefore indicating that xenograft uptake is not a product of a high blood concentration.

concentration (Figure 3.27) with a xenograft to blood ratio of 7.1:1. The ^{68}Ga-NOTA-hIFN-CTRLdAb xenograft to blood ratios were 0.71:1 at 1h, 2:1 at 3h and 10.6:1 at 24h, which suggested that there was perhaps some hIFN-mediated hIFNAR targeted xenograft tissue retention with efficient blood wash out.

In conclusion, the xenograft uptake data strongly suggested that MAXdAb-mediated ASGPR targeting increased specific xenograft uptake of a hIFN-dAb fusion versus hIFN-mediated hIFNAR targeting alone.

3.5.3.3 Full Tissue Analysis

The uptake in the liver of the ^{68}Ga-NOTA-hIFN-MAXdAb was consistent with the dosing assay at approximately 50%ID/g (Figure 3.25), and did not show a significant ($p=0.09$) change over time (Table 3.15). The ^{68}Ga-NOTA-hIFN-CTRLdAb on the other hand demonstrated a consistent significant ($p=0.002$) decrease in liver tissue uptake over time. The consistently higher liver retention of NOTA-hIFN-MAXdAb compared to NOTA-hIFN-CTRLdAb was consistent with an additive effect by MAXdAb-mediated ASGPR binding on mouse liver uptake.

However, there was no significant difference ($p=0.12$) in liver uptake at 1h with both equally high. The 24h NOTA-hIFN-CTRLdAb uptake was still 39.5%ID/g. Therefore, it could not be MAXdAb-mediated ASGPR binding that accounted for the majority of liver uptake, but rather was a factor common to both radioligands. Both molecules contained hIFN and so the primary consideration was a cross-reactivity of hIFN with murine IFNAR (mIFNAR) because hIFNAR and mIFNAR are 65.5% similar*. The *in vitro* assays strongly suggested that neither NOTA-hIFN-MAXdAb nor NOTA-hIFN-CTRLdAb had a high affinity for hIFNAR and so a high affinity for mIFNAR seemed unlikely. The mIFNAR copy number in the mouse liver was likely to be cumulatively high so may have resulted in a high retention in spite of the relatively poor kinetics of the hIFN-hIFNAR2 interaction identified *in vitro*. However, this would contradict previous data which showed that a mIFN-CTRLdAb did not demonstrate liver uptake[74] and a reported mIFNAR expression level of only 10.5FMPK in liver compared to 22.5FMPK for spleen for instance.

* UniProt analysis performed on P17181 INAR1_HUMAN and P33896 INAR1_MOUSE, and P48551 INAR2_HUMAN and O35664 INAR2_MOUSE

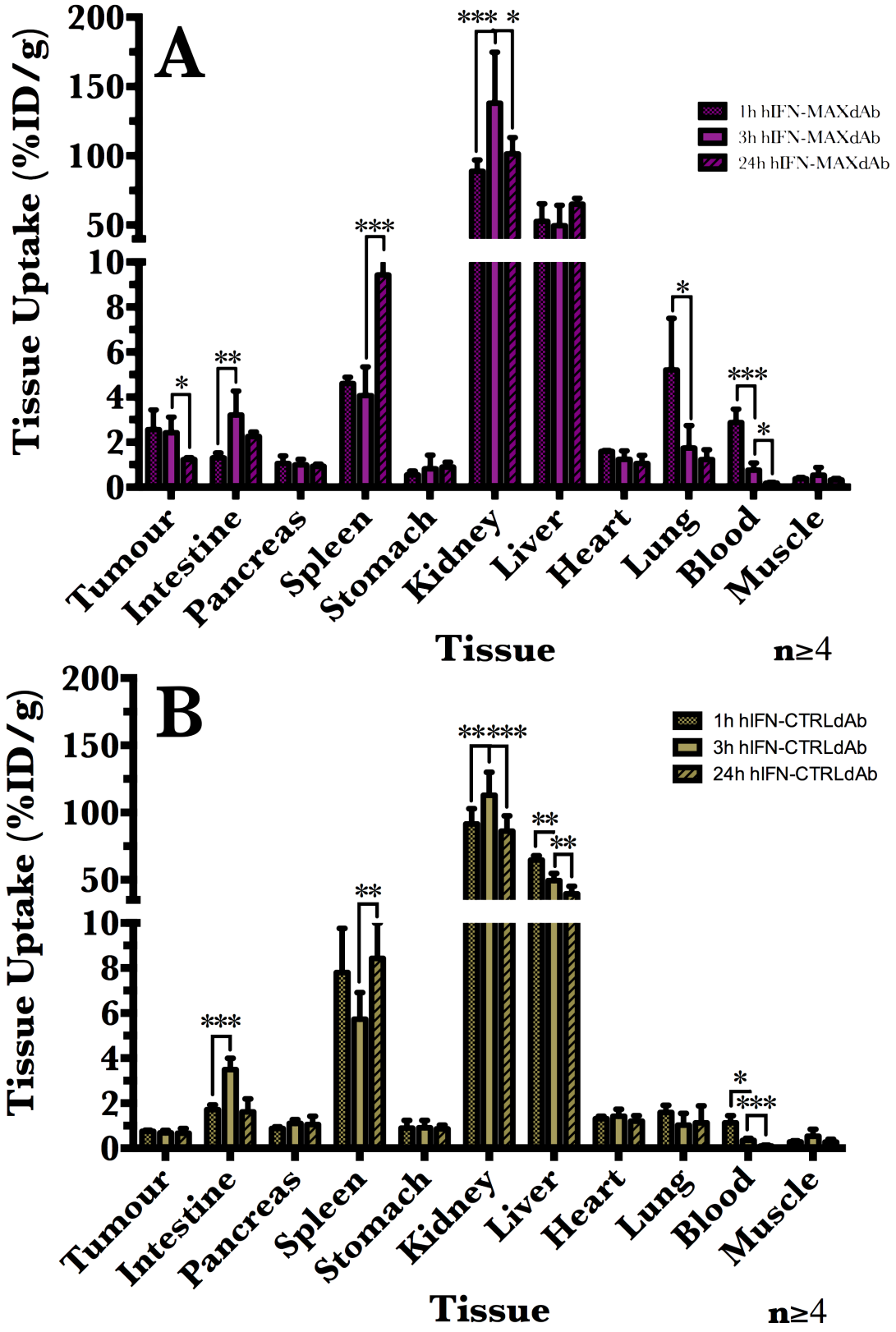

Figure 3.28 – Biodistribution of NOTA-hIFN-MAXdAb and NOTA-hIFN-CTRLdAb in SCID Beige HepG2 Xenograft Model at 1h, 3h and 24h

Mean %ID/g in selected tissues at 1h, 3h, and 24h post 1µg injection of ^{68}Ga/^{111}In-NOTA-hIFN-MAXdAb (A) or ^{68}Ga/^{111}In-NOTA-hIFN-CTRLdAb (B). Various significant differences in biodistribution were observed over time.

The presence of the O-linked glycosylation is also common to both radioligands and so the presence of asialyted sugars, as observed in the NOTA-hIFN-MAXdAb MS results (Section 3.2.2.4), may have resulted in mASGPR-mediated liver uptake and endosomal degradation. This may have partially accounted for the persistently high liver uptake values if the radioactivity was retained in the tissue.

Other considerations included ^{68}Ga-colloid, although this was purified out of the dose prior to injection and so was unlikely to have contributed significantly to the uptake. Hepatic protein degradation pathways may have concentrated the radioligands, however other similar antibody fusion proteins do not concentrate in the liver to the same extent so this seemed an unlikely factor. User error was ruled out owing to the significant differences in xenograft uptake (Figure 3.26) and batch checks by Biacore SPR analysis (data not shown).

Therefore, the unexpected liver uptake of ^{68}Ga-NOTA-hIFN-CTRLdAb was not definitively defined.

Table 3.15
Time Course Biodistribution Analysis Tissue Uptake Values

Tissue (%ID/g)	1h		3h		24h	
	^{68}Ga-NOTA-hIFN-MAXdAb	^{68}Ga-NOTA-hIFN-CTRLdAb	^{68}Ga-NOTA-hIFN-MAXdAb	^{68}Ga-NOTA-hIFN-CTRLdAb	^{111}In-NOTA-hIFN-MAXdAb	^{111}In-NOTA-hIFN-CTRLdAb
Xenograft	2.56 ±0.87	0.75 ±0.05	2.42 ±0.69	0.68 ±0.11	1.23 ±0.08	0.67 ±0.21
Intestine	1.30 ±0.22	1.71 ±0.21	3.21 ±1.06	3.49 ±0.50	2.25 ±0.20	1.61 ±0.58
Pancreas	1.05 ±0.34	0.88 ±0.87	0.99 ±0.25	1.1 ±0.17	0.93 ±0.10	1.05 ±0.37
Spleen	4.61 ±0.27	7.80 ±1.96	4.07 ±1.27	5.73 ±1.18	9.43 ±1.12	8.43 ±1.57
Stomach	0.55 ±0.87	0.89 ±0.35	0.82 ±0.60	0.91 ±0.69	0.89 ±0.22	0.86 ±0.17
Kidneys	88.8 ±8.21	91.5 ±11.5	138 ±36.82	113 ±17.2	102 ±11.7	86.1 ±11.4
Liver	52.8 ±12.65	64.7 ±3.28	49.7 ±14.67	49.4 ±5.35	65.1 ±4.18	39.5 ±5.63
Heart	1.59 ±0.04	1.31 ±0.11	1.24 ±0.37	1.42 ±0.31	1.05 ±0.36	1.2 ±0.25
Lung	5.21 ±2.29	1.59 ±0.32	1.74 ±1.00	1.03 ±0.52	1.23 ±0.43	1.13 ±0.75
Blood	2.87 ±0.60	1.13 ±0.32	0.76 ±0.32	0.35 ±0.09	0.18 ±0.03	0.10 ±0.04
Muscle	0.37 ±0.06	0.28 ±0.05	0.53 ±0.35	0.53 ±0.31	0.32 ±0.07	0.27 ±0.13

~1µg dose, n≥3

The clearance routes for both radioligands were identifiable as kidney and intestine. The kidney uptake in both instances showed a pattern of increasing between 1h and 3h subsequently decreasing between 3h and 24h. For instance from an average of 88.8%ID/g for ^{68}Ga-NOTA-hIFN-MAXdAb at 1h up to 138%ID/g at 3h. This was concurrent with the significant decrease in blood radioligand concentration, and most likely represented the primary route of excretion of

unbound radioligand. However, there was a strong indication of kidney retention given the tissue concentration continuing to be above 80%ID/g for both radioligands at 24 hours post injection. Indeed renal uptake has also been reported for EGFR-targeting nanobodies[473].

The statistically significant increases of both radioligands in the intestine between one and three hours were not through ingestion and so was implicated as hepatobiliary excretion of the breakdown products of the ^{68}Ga-NOTA-hIFN-dAbs after the degradation in the liver. The presence of this effect for both NOTA-hIFN-MAXdAb and NOTA-hIFN-CTRLdAb was thus a common degradation route. Moreover it could have been symptomatic of a breakdown of the Lys-NOTA-^{68}Ga complex either as a chelation unit or Ga-68 alone. The latter would be unlikely as the complex is so stable (Introduction 1.7.4.1). However, given the high liver uptake of both radioligands in the liver it was concluded to be the result of an active breakdown mechanism, perhaps active asialoglycoprotein mASGPR mediated degradation.

The spleen showed a relatively high uptake of both radioligands, although particularly the ^{68}Ga-NOTA-hIFN-CTRLdAb, peaking with a significant increase up to 24h. This was most likely a hIFN-mediated interaction as it is present for both radioligands and the hIFNAR copy number is relatively high. Also, perhaps as the spleen is a primary recycler of Fe^{3+}, free analogous $^{68}Ga^{3+}$ or $^{111}In^{3+}$ from breakdown of the radioligand were also concentrated by ferritin in the spleen*.

A problem with utilising In-111 to label NOTA for the 24hr time point was that ^{111}In-NOTA-hIFN-dAb radioligand was likely not pharmacologically identical to ^{68}Ga-NOTA-hIFN-dAb. However, the assumption was that they were not significantly different. The data appeared to support that assumption, as there were no obviously anomalous results between 1h, 3h and 24h in all tissues. The spleen showed a significant increase in spleen radioactivity between 3h and 24h and so this could have been free In-111 uptake from NOTA-^{111}In dissociation[474,475]. Basic *in vitro* stability experiments showed that the ^{111}In-NOTA-hIFN-MAXdAb radioligand was 99% stable for 24 hours at RT. Nevertheless, if further work were performed utilising this radioligand, analysis of ^{111}In-NOTA-hIFN-dAbs' biodistribution at the earlier time points and a full *in vivo* serum stability analysis would be appropriate.

* This is the principle of Ga-67 scanning (Section 1.7.2.1)

3.5.4 Receptor Blocking

The equivalent of an ASGPR-negative HepG2 xenograft model with blocking the ASGPR specific binding through the injection of an excess of cold MAXdAb ligand was attempted to ascertain whether the observed xenograft uptake of the ^{68}Ga-NOTA-hIFN-MAXdAb radioligand was specific. If the uptake was MAXdAb-mediated by specifically binding ASGPR then the excess of MAXdAb was expected to reduce the observed uptake in the biodistributed xenograft tissue. Therefore, the 1µg ^{68}Ga-NOTA-hIFN-MAXdAb 3hr time point was repeated utilising SCID Beige HepG2 xenograft models both without (0.04mg/kg dose) and with a 347µg excess of concentrated unlabelled MAXdAb* (16.5mg/kg† dose) (Method 2.4.3.1) (Figure 3.29).

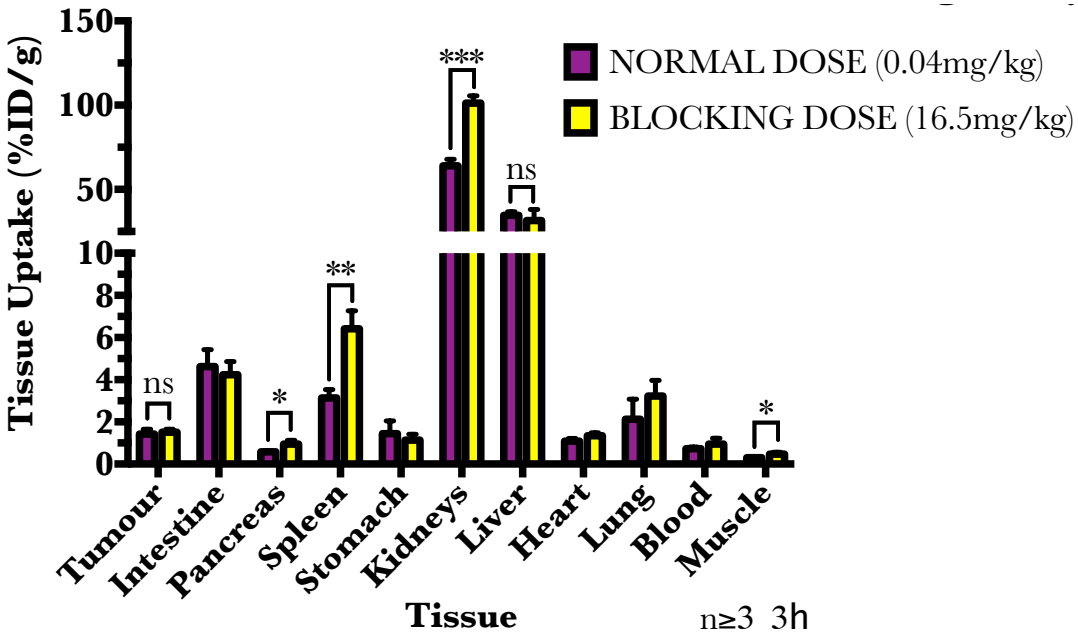

Figure 3.29 – Tissue Uptake of ^{68}Ga-NOTA-hIFN-MAXdAb in SCID Beige HepG2 Xenograft Model with and without MAXdAb Blocking Dose

Mean %ID/g in selected tissues of ^{68}Ga-NOTA-hIFN-MAXdAb at 3h post injection of 1µg dose (0.04mg/kg) or in addition to 347µg of MAXdAb (16.5mg/kg) ASGPR-blocking dose. Demonstrates no significant difference in ASGPR expressing tumour xenograft and liver tissues – although significant differences observed in non-specific tissues such as pancreas, indicating increased bioavailability of radioligand.

* The binding activity of the MAXdAb batch was confirmed *in vitro* using Flow Cytometry and so it was capable of binding ASGPR.

† This was the maximum achievable dose as at higher concentrations the MAXdAb would precipitate out of solution

The results showed no significant difference in ^{68}Ga-NOTA-hIFN-MAXdAb xenograft uptake in spite of the presence of an additional 16.46mg/kg of MAXdAb alone at greater than a 1000-fold excess. Superficially, the data indicated that the ^{68}Ga-NOTA-hIFN-MAXdAb xenograft uptake observed in previous sections was likely due to non-specific interactions. Also, there was an indication that the uptake in liver was also non-specific as there was no significant difference in liver.

However, further analysis revealed there was significantly higher uptake of ^{68}Ga-NOTA-hIFN-MAXdAb with the blocking dose in non-specific tissues such as the pancreas, spleen and muscle, in addition to a highly significant increase in renal filtration. These latter results strongly suggested that there was more ^{68}Ga-NOTA-hIFN-MAXdAb available in the system with the blocking dose at 3hr compared to the normal dose.

The reason for increased systemic availability was not apparent from the %ID/g values. The expression of data as %ID/g is intended to control for tissue mass, but assumes a non-saturable linear horizontal relationship between uptake (%ID) and mass (g). However, when uptake against mass was analysed for liver uptake in this investigation, the relationship was diagonal (Figure 3.30). By comparison, intestinal uptake, for instance, conformed to the expected horizontal relationship (Figure 3.30). The data strongly indicated that the liver was saturable because an increase in mass did not equate to an increase in uptake, with a

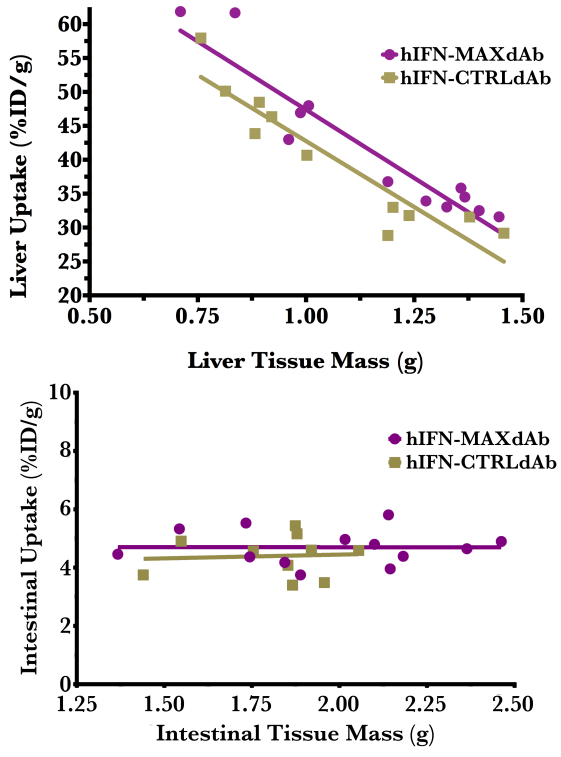

Figure 3.30 – Liver Tissue Uptake and Intestinal Tissue Uptake relative to Tissue Mass

Liver and intestinal uptake (%ID/g) of ^{68}Ga-NOTA-hIFN-MAXdAb and ^{68}Ga-NOTA-hIFN-CTRLdAb plotted against respective tissue mass. Demonstrates non-linear relationship between liver mass and uptake – a larger mass does not equate to a proportional increase in uptake – and the corollary of a linear relationship represented by intestinal mass and uptake.

maximum uptake of 45.4%ID ±2.99 at 1µg injected dose in spite of the masses ranging from 0.71g to 1.45g with a variance of 21.1%. Therefore this would skew the data to give lower %ID/g uptake values for liver at higher masses and so if two groups have different average liver masses then their %ID/g values cannot be directly compared. The concurrent conclusion for uptake being independent of mass was that the capillary endothelium interface expressing ASGPR must be discrete and finite.

Comparison of the liver uptakes from the blocking experiment without correcting for mass revealed a high significant difference in uptake (p=0.002) (Figure 3.31). This suggested that the specific liver uptake of the ^{68}Ga-NOTA-hIFN-MAXdAb had indeed been blocked by the presence of the MAXdAb. Thus there was on average 12.4% more of the ID available systemically in the blocking dose animals. Hence, this potentially explained the non-significant differences in xenograft uptake, and the higher uptake in the kidneys and non-specific tissues. It was possible that the xenograft uptake in the blocking dose animals had been artificially inflated by the increased systemic available dose. Correcting the available dose resulted in a reduced xenograft uptake in the MAXdAb blocking subjects of 2.25%ID/g to 2.61%ID/g in the normally treated subjects.

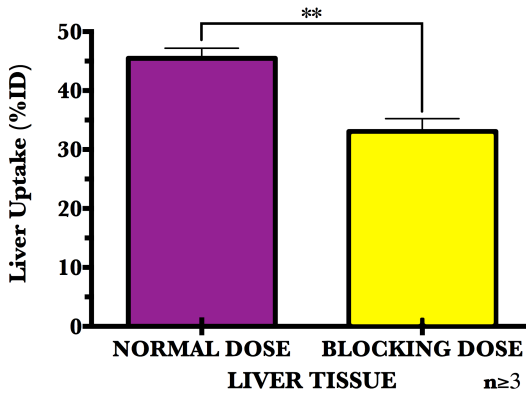

Figure 3.31 – Liver Tissue Uptake of ^{68}Ga-NOTA-hIFN-MAXdAb in SCID Beige HepG2 Xenograft Model with and without MAXdAb Blocking Dose

Mean %ID in liver tissue of ^{68}Ga-NOTA-hIFN-MAXdAb at 3h post injection of 1µg dose (0.04mg/kg) or in addition to 347µg of MAXdAb (16.5mg/kg) ASGPR-blocking dose. Demonstrates the significant decrease in uptake in the presence of a blocking dose indicating the specificity of the liver uptake.

Hence, the blocking result revealed that liver uptake of the NOTA-hIFN-MAXdAb was likely to be partially specific ASGPR binding. Moreover, further highlighted the limitations the liver, as a large sink for specific uptake, places on the model for quantitating xenograft uptake. Hence, the specificity of xenograft uptake was not confirmed by this assay.

3.5.5 TaqMan mRNA Expression Profiling

A significantly higher xenograft uptake of NOTA-hIFN-MAXdAb compared to NOTA-hIFN-CTRLdAb was observed (Section 3.5.3.2) indicating effective targeting, likely due to MAXdAb-mediated ASGPR binding. TaqMan was employed to link targeting to a quantifiable measure of the bioactivity of the attached hIFN* (Methods 2.5). The expression levels of various mRNA sequences from genes associated with the downstream effector proteins of the hIFN pathway (Introduction 1.5.3) were measured.

The mRNA was isolated from homogenised cryo-preserved xenograft tissue from the biodistribution experiments (Section 3.5.3.2) and applied to TaqMan array plates containing sequence-specific primers and TaqMan MGB probe (6-FAMTM dye-labelled). Plates were normalised to the expression levels of control *GAPDH* utilising the ΔC_t-method to yield relative gene copy numbers expressed as percentage values for each gene[476].

In addition to the xenograft samples from the hIFN-MAXdAb and hIFN-CTRLdAb treated models, xenografts from SCID Beige HepG2 xenograft models receiving only a 200µl PBS injection were utilised to attain a baseline level of expression for all mRNAs.

The data demonstrated that both hIFN-MAXdAb and hIFN-CTRLdAb had modified the HepG2 xenograft transcriptome when compared to the untreated control xenograft tissue (Table 3.16, Figure 3.32). It was also apparent that the increased MAXdAb-mediated tumour xenograft uptake with hIFN-MAXdAb versus hIFN-CTRLdAb appeared to broadly correlate with a greater xenograft response (Figure 3.33).

The mRNA copy numbers of several IFN pathway proteins were modified, such as IRF9 and STAT1 (Introduction 1.5.3). Upregulation of these proteins would be necessary for the integration of the IFN signalling pathways into creating an anti-proliferative proteome. IRF9 was up 516% with hIFN-MAXdAb, which would be required for formation of the ISRE for promoting ISG transcription. STAT1 mRNA copies were increased by 231% with hIFN-MAXdAb, which would be integral to JAK-STAT signalling by forming part of the ISRE, promoting transcription of the

* Monetary limitations prevented performing TaqMan on more than one xenograft for each variable

IFNϒ stimulated genes as a phosphorylated homodimer and cross-talk with the ERK signalling pathway to inhibit cell replication. Therefore increasing IRF9 and STAT1 mRNA copy numbers may have increased their translation and thus ameliorated limitations on IFN signal amplification.

Table 3.16
Percentage Difference in mRNA Copy Number relative to untreated Xenograft Tissue

	Fusion Protein	
Gene Name	**hIFN-MAXdAb (1.69%ID/g)**	**hIFN-CTRLdAb (0.60%ID/g)**
ARHGEF Family	-25.8	-4.8
CREB Family	-20.1	3.5
EIF4 Family	-35.7	-55.2
HIST Family	-3.7	64.5
IFNAR1/2	-34.9	-4.7
IFNGR1/2	-28.4	-10.1
IRF9	516	475
IRS1	-42.6	-19.6
JAK1/2	-40.3	-5.1
MAPK Family	-28.5	-2.8
MTOR	-15.4	-51.7
NET1	26.2	-42.7
PI3K Family	-35.7	-15.0
PRKCD	-30.7	10.1
RAC1	-44.9	-17.1
RPS6 Family	-33.3	-7.9
STAT1	230.9	89.9
TYK2	-10	21.6
VAV2/3	-17	-7.4

Percentage differences compared to untreated control xenograft tissues
red = decrease, green = increase

There was also evidence for the down-regulation of the hIFN signalling complex with an observed decrease in all four of the IFNα receptor complex proteins' mRNA gene copy numbers. IFNAR1, IFNAR2, Tyk2 and Jak1 were down by an average of 28.4% with hIFN-MAXdAb. This observation was concurrent with the evidence that hIFN self-regulates by inhibiting the hIFNAR complex (Introduction 1.5.2). Moreover, down-regulating Jak1 may have inhibited the phosphorylation of PI3K.

There was no evidence that the synthesis of mRNA encoding the various IFN subtypes was increased, as may have been expected. This could have been due to the lack of alternative pathways converging to amplify the signal for IFN production, such as the detection of dsRNA by PKR increasing the activity of NFκB or TLR stimulated pathways. Further, perhaps the downregulation of the mTOR pathway preventing IRF7 translation[477] or it may be that the genes have a low copy number relative to protein expression.

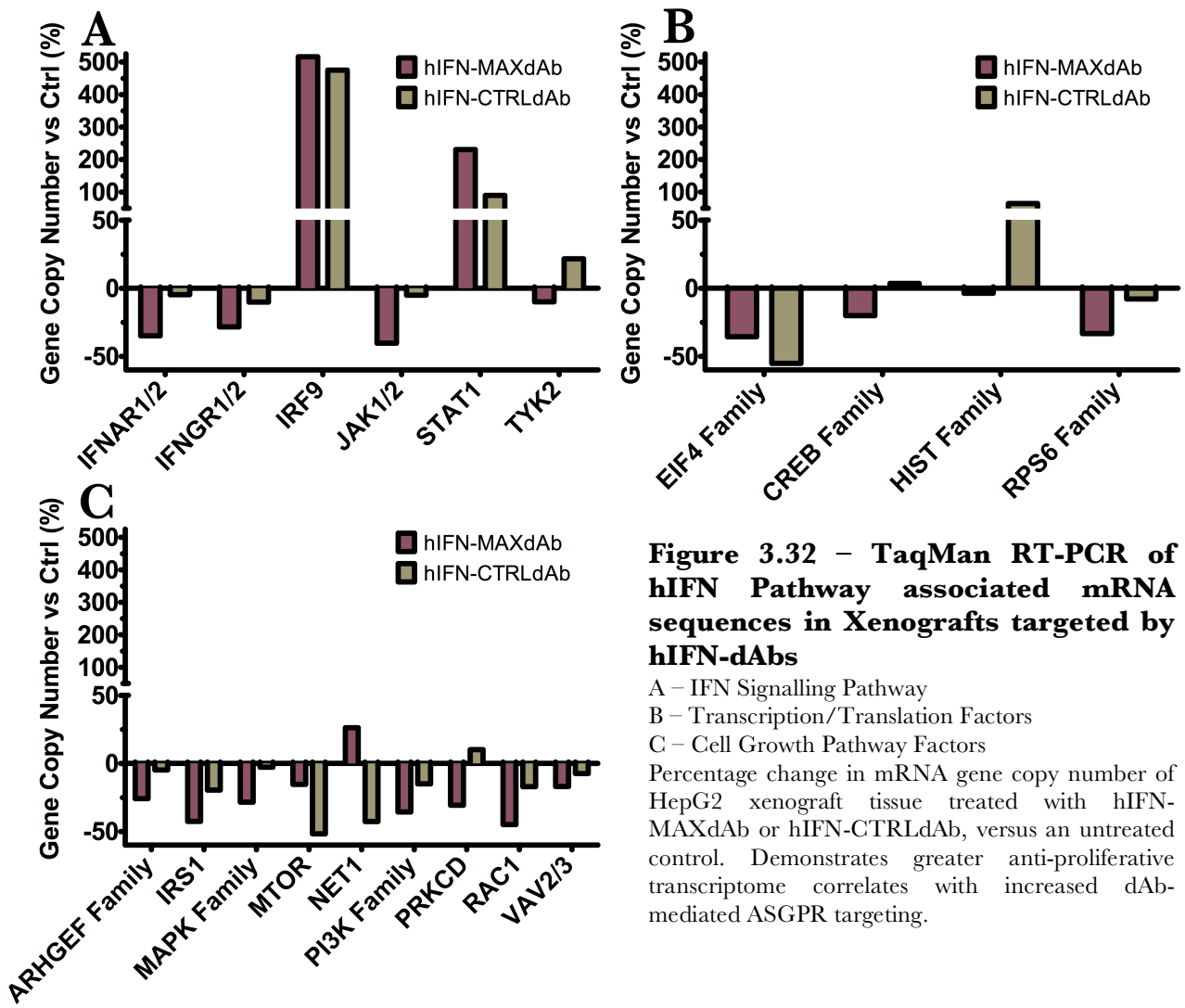

Figure 3.32 – TaqMan RT-PCR of hIFN Pathway associated mRNA sequences in Xenografts targeted by hIFN-dAbs

A – IFN Signalling Pathway
B – Transcription/Translation Factors
C – Cell Growth Pathway Factors
Percentage change in mRNA gene copy number of HepG2 xenograft tissue treated with hIFN-MAXdAb or hIFN-CTRLdAb, versus an untreated control. Demonstrates greater anti-proliferative transcriptome correlates with increased dAb-mediated ASGPR targeting.

There was a decrease in copy number of PI3K family members with NOTA-hIFN-MAXdAb treatment, in addition to a decrease in PI3K-activating IRS1. As PI3K is responsible for conducting cell survival growth signals by the indirect phosphorylation of AKT, which in turn inhibits the action of numerous pro-apoptotic factors such as p53 (Introduction 1.5.4), down-regulation of PI3K may have primed the HepG2 xenograft tissue for apoptosis.

PRKCD is known to be anti-apoptotic in instances of cytokine mediated cell death and so the decrease of PRKCD in hIFN-MAXdAb treated xenograft tissue inferred an apoptotic HepG2 phenotype. By contrast there was an increase in mRNA transcription of NET1, a protein associated with instigating RhoB-mediated cell death after DNA damage[478], in the hIFN-MAXdAb treated xenograft tissue further indicating an apoptotic phenotype.

The initiation of transcription through the MAP/ERK pathway was possibly curtailed through the decrease in genes encoding MAPK related genes, ARHGEF family, RAC1, VAV2/3, in addition to the CREB transcription factors. The MAP/ERK pathway is associated with uncontrolled growth in malignant tumours and therefore a decrease in the pathway's mRNA potentially represented a stalling of cell growth.

The global initiation of translation was possibly inhibited by the decreases in the transcription of the genes encoding the mTOR pathway including MTOR, EIF4 related genes and RPS6 related genes. This may have represented an efficient stress response that resulted in the discrete translation of only mRNA sequences crucial to cell survival.

Generally the data showed high hIFN-MAXdAb and low hIFN-CTRLdAb uptake correlated with concomitant effects on mRNA expression, with hIFN-MAXdAb just having a stronger effect (Figure 3.33). However, there were some interesting exceptions that may have indicated hIFN-MAXdAb and hIFN-CTRLdAb stimulated discrete cellular phenotypes as a result of their differing localised xenograft concentrations. For instance, the MTOR and EIF4 family of genes showed a greater decrease in the hIFN-CTRLdAb targeted xenograft, which may have resulted in a greater retardation of translation. The hIFN-CTRLdAb also differed from the hIFN-MAXdAb with a decrease in NET1 mRNA, an increase in PRKCD mRNA and a large increase in histone mRNA. These differences indicated

that there was even tighter control on protein expression with hIFN-CTRLdAb, such as the increase in transcription suppressing histone transcripts and a repression of the apoptotic phenotype, as evidenced by the decrease in pro-apoptotic NET1 and increase in anti-apoptotic PKRCD.

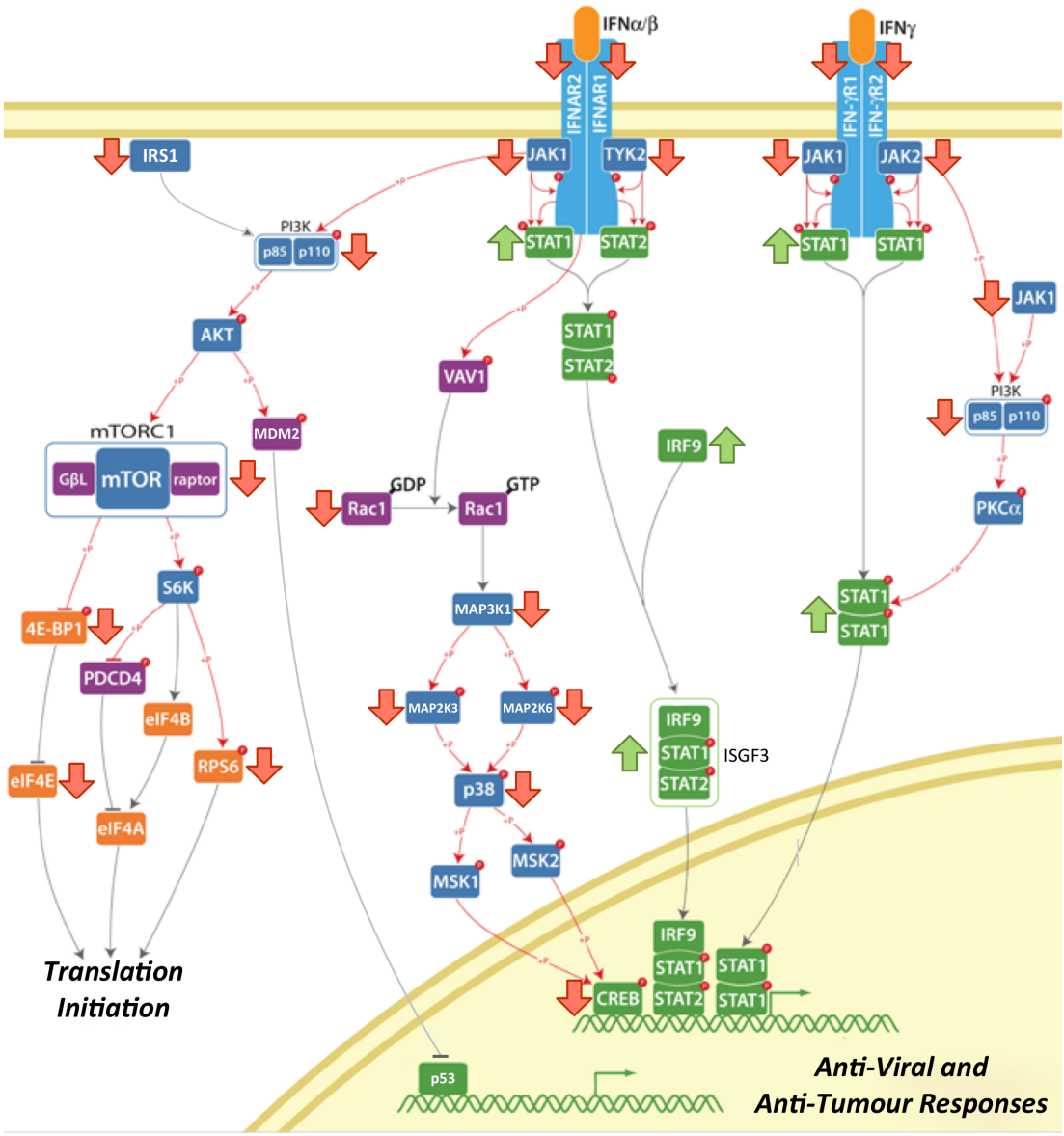

Figure 3.33 – TaqMan mRNA Copy Number Changes in HepG2 Xenografts with hIFN-MAXdAb or hIFN(A)-ASGPRdAb Treatment

Percentage increases (green arrows) and decreases (red arrows) in mRNA gene copy number of HepG2 xenograft tissue treated with hIFN-MAXdAb or the hIFN(A)-ASGPRdAbs versus an untreated control. Diagram represents the anti-proliferative transcriptome instigated by the action of the hIFN pathway including upregulation of mRNAs encoding hIFNα/β and hIFNγ pathway components, self-regulation through down-regulation of receptor mRNA, and the down regulation of translation and survival pathways.

It could also have been argued that the differences in the response to hIFN-CTRLdAb were related to its decreased potency compared to hIFN-MAXdAb (Section 3.2.4) of 37.5pM and 6.79pM, respectively, rather than the differences in uptake. However, the resultant concentrations in the xenografts were likely to be in the nM range given the uptake concentrations of 0.60%ID/g and 1.69%ID/g, respectively, and so above the effective concentrations required for interacting effectively with the IFNAR complex.

TaqMan data always carries a caveat regarding mRNA expression levels not necessarily equating to the encoded protein expression level and the action of RNases such as OAS instigated RNase L. However, the conclusions in this instance do not hinge on the upregulation of one gene but rather are a reflection of a trend across whole gene families covering several regulatory pathways, providing a broad and consistent consensus of the instigation of an anti-proliferative state in the xenograft. Therefore, the results, although not statistically significant, are rendered qualitatively significant owing to the comprehensive examination of the hIFN related transcriptome. The results could have been augmented by proteomics analyses such as by matrix-assisted laser desorption/ionization (MALDI) MS, ELISA or western blotting.

The TaqMan results correlated with the reported discrete cellular responses relative to the temporal ternary structure stability of the IFNAR-IFN interaction[263]. This would be a restrained low-toxicity antiviral response to low hIFN concentrations and an apoptotic anti-proliferative response to higher hIFN concentrations. The data thus strongly suggested that in this model, through increased xenograft uptake mediated by MAXdAb ASGPR targeting, hIFN could be a more efficacious instigator of anti-proliferation. Hence, hIFN-MAXdAb is a more effective potential targeted anti-cancer agent than non-targeted fused hIFN.

3.6 PET-CT IMAGING

SCID Beige HepG2 HCC xenograft models were created for *in vivo* PET-CT quantitation of NOTA-hIFN-MAXdAb and NOTA-hIFN-CTRLdAb xenograft targeting. However, in order to improve image interpretation xenografts were grown on the shoulder* and the injected radiolabelled protein was allowed to distribute for one hour prior to imaging to allow some clearance through the bladder for greater uptake resolution.

3.6.1 Ga-68 Radiolabelling

NOTA-hIFN-MAXdAb and NOTA-hIFN-CTRLdAb were Ga-68 radiolabelled utilising the high specific activity 1M NaAc radiolabelling protocol to attain the highest radioactivity possible from the purification (Table 3.17). The reaction was incubated at 37˚C, achieving highly reliable specific activities with minimum radiochemical impurities (Method 2.3.2). These results enabled sufficient activity for imaging 3 hours post-injection. The injected dose was approximately 4µg as a result of balancing activity with the lowest possible dose.

Table 3.17
Ga-68 Radiolabelling for PET-CT Imaging

Protein	Reaction Conc. (µM)	Radiolabelling Efficiency (%)	Specific Activity (MBq/µg)	Radiochemical Purity (%)*	Injected Activity (MBq)	Injected Mass (µg)
NOTA-hIFN-MAXdAb	1.1	90.1 ±1.72	1.99 ±0.09	97.3 ±0.92	6.22 ±0.53	3.92 ±0.48
NOTA-hIFN-CTRLdAb	1.1	98.4 ±0.60	2.33 ±0.12	99.4 ±0.07	7.37 ±0.65	3.88 ±0.28

n≥3, SD values displayed, *post-G25 purification

* Flank tumour imaging proved unfeasible, as the high background radioactive signal from the uptake in the liver, kidneys and bladder did not allow thresholds capable of visualising tumour uptake.

3.6.2 PET-CT Quantitation of Xenograft Uptake

The xenograft dose uptake between one hour and three hours post-injection was examined by reconstruction of the PET-CT images as 10 minute frames, with manual selection of the xenograft tissue as a region of interest (ROI), in addition to a muscle ROI as a control. After the two hour acquisition, the subjects were sacrificed and biodistributions performed for comparison at three hours post-injection.

The PET-CT data demonstrated tumour uptake of 68Ga-NOTA-hIFN-MAXdAb and a relatively lower uptake of 68Ga-NOTA-hIFN-CTRLdAb over the two-hour imaging period (Table 3.18). This could be visualised through thresholding the data to highlight the xenograft uptake (Figure 3.34). At three hours, the PET-CT results corroborated a pattern of significantly ($p=0.03$) higher uptake of ^{68}Ga-NOTA-hIFN-MAXdAb than ^{68}Ga-NOTA-hIFN-CTRLdAb, as seen in the 4µg dose biodistribution results in this instance (Table 3.18) and at a 1µg dose previously (Figure 3.26). The ratio of xenograft uptake relative to muscle uptake was maintained for ^{68}Ga-NOTA-hIFN-MAXdAb at about double that of ^{68}Ga-NOTA-hIFN-CTRLdAb.

However, there appeared to be a discrepancy in the magnitude of the results comparing %ID/g and %ID/ml, considering that liver has a density of approximately 1.06g/ml. This could in part be accounted for as overestimation of the area of the xenograft tissue compounded by the presence of blood, which would have been absent from the biodistribution data, as together these factors would both serve to underestimate the %ID/ml values.

Table 3.18
PET-CT Imaging Xenograft Uptake Quantitation and Biodistributions

Protein	Tissue	Biodistribution		PET-CT Imaging	
		Uptake (%ID/g)	Mean Ratio	Uptake (%ID/ml)	Mean Ratio
^{68}Ga-NOTA-hIFN-MAXdAb	Xenograft	1.23 ±0.07	3.9:1	0.56 ±0.09	2.9:1
	Muscle	0.31 ±0.05		0.19 ±0.16	
^{68}Ga-NOTA-hIFN-CTRLdAb	Xenograft	0.65 ±0.17	2.2:1	0.38 ±0.06	1.4:1
	Muscle	0.30 ±0.06		0.28 ±0.10	

n=3, SD values displayed, ~4µg dose, t=3h

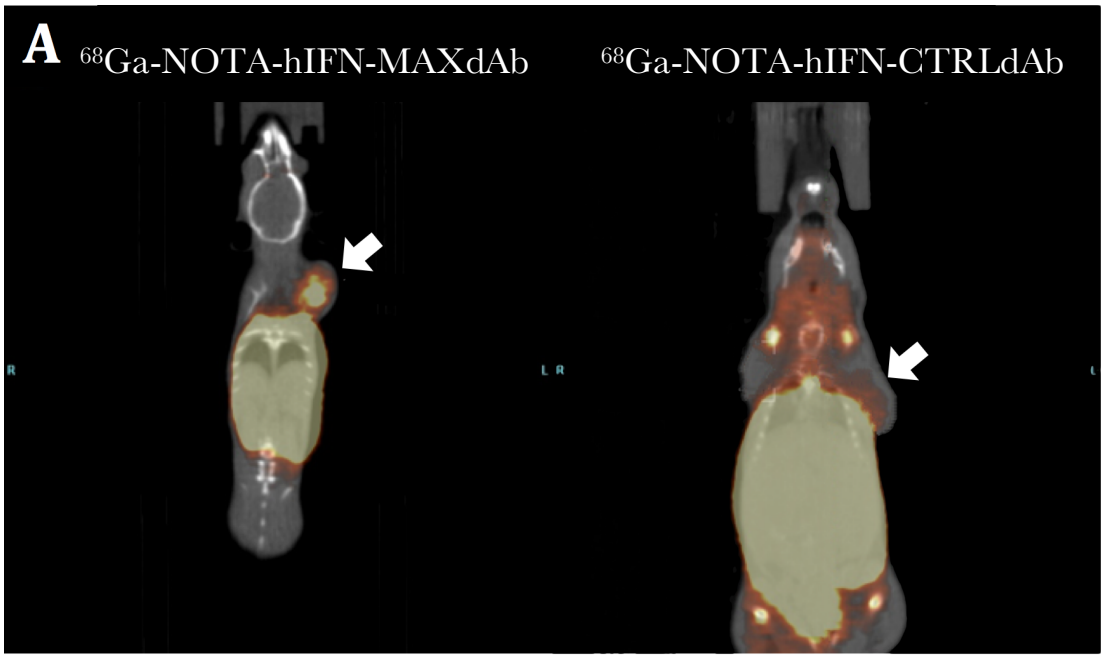

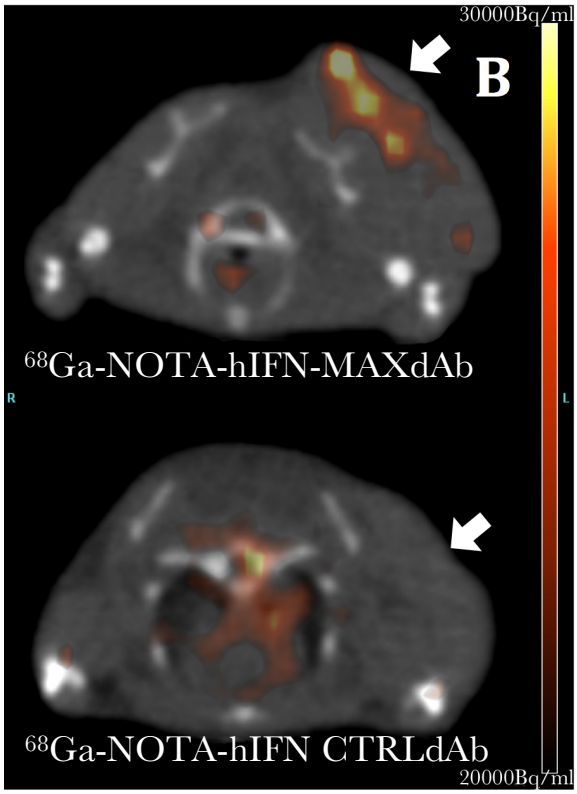

Figure 3.34 – PET-CT Imaging of HepG2 Xenograft Uptake of ^{68}Ga-NOTA-hIFN-MAXdAb and ^{68}Ga-NOTA-hIFN-CTRLdAb

A – Example coronal slice images of HepG2 tumour uptake representing cumulative detected events between one and three hours post-injection of a 4µg dose of ^{68}Ga-NOTA-hIFN-MAXdAb or ^{68}Ga-NOTA-hIFN-CTRLdAb.

B – Example axial slice images of HepG2 tumour uptake representing cumulative detected events between one and three hours post-injection of a 4µg dose of ^{68}Ga-NOTA-hIFN-MAXdAb or ^{68}Ga-NOTA-hIFN-CTRLdAb.

Xenograft tissue indicated with white arrow.

The PET-CT results also showed that between one hour and three hours post-injection the uptake of the radioligands had apparently plateaued (Figure 3.35), with a non-significant decrease in the presence of radioligand over the two hour acquisition. This correlated with the biodistribution results for the xenografts at one hour and three hours, which appeared to show a plateauing of the uptake too and thus that the majority of uptake was in the initial hour post-injection (Figure 3.28). Moreover, the concentration of ^{68}Ga-NOTA-hIFN-MAXdAb was significantly higher ($p<0.001$) than in the muscle tissue throughout the acquisition, whereas the ^{68}Ga-NOTA-hIFN-CTRLdAb concentration was apparently not significantly greater than that of the non-specific muscle control tissue. It was clear though that for more meaningful observations of the kinetics of the tissue clearances then a longer imaging acquisition period would be required.

Overall the PET-CT offered a proof-of-principle demonstration of *in vivo* computation of xenograft uptake that broadly correlated with the *ex vivo* biodistribution data for three hours post-injection. There was a clear indication that quantitative temporal uptake data in xenograft tissue could enable a greater understanding of the uptake dynamics of dAb fusions if analysed over a broader time period.

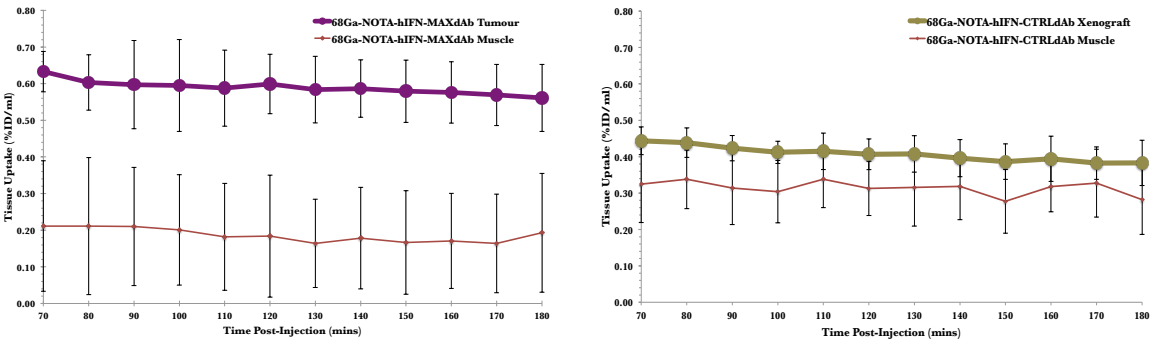

Figure 3.35 – Xenograft Uptake of ^{68}Ga-NOTA-hIFN-MAXdAb and ^{68}Ga-NOTA-hIFN-CTRLdAb between 1h and 3h post-injection

Concentrations of ^{68}Ga-NOTA-hIFN-MAXdAb and ^{68}Ga-NOTA-hIFN-CTRLdAb in HepG2 xenograft tissue and muscle tissue, between 1h and 3h post-injection analysed as 10 minute frames expressed as %ID/ml. The uptake in xenograft tissue of both radioligands appears to have plateaued to a steady decrease with time, with the highest xenograft uptake observed with the ASGPR-targeted ^{68}Ga-NOTA-hIFN-MAXdAb in comparison to ^{68}Ga-NOTA-hIFN-CTRLdAb. Compared to a muscle tissue control, ^{68}Ga-NOTA-hIFN-MAXdAb showed a sustained higher uptake over time to the uptake of ^{68}Ga-NOTA-hIFN-CTRLdAb in xenograft tissue versus muscle uptake. The data demonstrates how PET-CT imaging can be quantitated to provide data on tissue uptake over time, and again demonstrate the superiority of the ASGPR/hIFNAR-targeted ^{68}Ga-NOTA-hIFN-MAXdAb radioligand to target and be retained in HepG2 xenograft tissue versus the hIFNAR-targeted ^{68}Ga-NOTA-hIFN-CTRLdAb. (n=3)

IV

Optimising HepG2 Xenograft Targeting of hIFN-dAbs

What is the optimum combination of hIFN and dAb affinities to maximise hIFN-dAb efficacy in a HepG2 xenograft model?

4.1 INTRODUCTION

In Chapter III, it was demonstrated that MAXdAb could mediate increased xenograft uptake of a hIFN-MAXdAb fusion protein construct compared to the non-targeted hIFN-CTRLdAb. Additionally, this increased uptake correlated with an apparent increase in anti-proliferative bioactivity of the attached hIFN. This now raised the question of whether this observed ASGPRdAb-mediated efficacy could be further refined by the manipulation of the binding affinities of the ASGPRdAb and hIFN for their respective receptors ASGPR and hIFNAR to conclude on the optimum strategy for targeting dAb fusions. This required generating a panel of mutant hIFN-ASGPRdAbs with differing intrinsic binding affinity combinations for ASGPR and hIFNAR followed by the same profiling and modelling experimentation as was performed for hIFN-MAXdAb and hIFN-CTRLdAb (Figure 4.0). This would hopefully enable a more nuanced view of the influence of the two binding affinities on the overall efficacy of hIFN-dAb fusion protein.

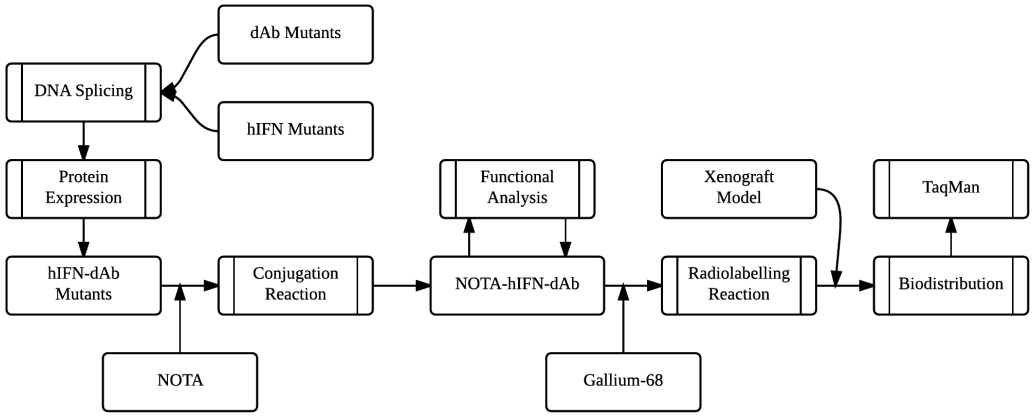

Figure 4.0 – Outline of Experimental Development
Experimental steps involved in producing validated mutant ^{68}Ga-NOTA-hIFN-dAbs and subsequent *in vivo* modelling, towards *in vivo* xenograft targeting quantitation

4.2 MUTANT EXPRESSION & PURIFICATION

4.2.1 Mutant hIFN-dAb Fusion Proteins

Three ASGPRdAb DNA sequences * were selected for their encoded ASGPRdAbs' differing affinities to ASGPR and named HidAb, MidAb, and LodAb (Table 4.1). Three hIFN DNA sequences† were selected from a subset of hIFN site directed mutagenesis sequences designed to reduce the interaction with hIFNAR, and were named hIFN(A), hIFN(C), and hIFN(E). Therefore, spliced combinations of these DNA sequences were intended to yield nine hIFN-dAb fusions (Table 4.1) (Methods 2.1) with differing affinity combinations for the target receptors (Table 4.2).

Table 4.1
Mutant hIFN-ASGPRdAb Fusion Proteins

Protein*	**HidAb** (K_D 5nM)	**MidAb** (K_D 25nM)	**LodAb** (K_D 300nM)
hIFN(A) (K_{off} 0.018 / EC50 0.75pM)	hIFN(A)-HidAb	hIFN(A)-MidAb	hIFN(A)- LodAb
hIFN(C) (K_{off} 0.254 / EC50 36.8pM)	hIFN(C)-HidAb	hIFN(C)-MidAb	hIFN(C)-LodAb
hIFN(E) (K_{off} 0.000 / EC50 16nM)	hIFN(E)-HidAb	hIFN(E)-MidAb	hIFN(E)-LodAb

*Kinetics data for individual proteins kindly provided by Dr Thil Batuwangala and Dr Armin Sepp

4.2.2 hIFN-ASGPRdAb Expression Constructs

High fidelity *Pwo* PCR reactions were performed to clone the individual mutant hIFN and ASGPRdAbs from their holding vectors, before SOE PCR to create a spliced linear constructs of the hIFN-ASGPRdAbs (Table 4.1). DNA gel electrophoresis (Figure 4.1) demonstrated that all sequences were successfully cloned although MidAb was relatively poorly amplified despite repeated attempts to increase yields. However, the DNA present was sufficient to proceed.

All SOE PCR reactions produced banding at the expected MW of ~900kb (Figure 4.2), in addition to various other abortive amplification species from the individual sequences. The hIFN-ASGPRdAb constructs were now amplified in the pCR-Blunt holding vector before being recombined into pDOM50 vectors.

* DNA constructs and original data courtesy of Dr Armin Sepp
† DNA constructs and original data courtesy of Dr Thil Batuwangala

Table 4.2
Mutant hIFN-ASGPRdAb Fusion Proteins

Fusion Protein	Predicted Molecular Weight (Da)	Relative Targeting Affinity	
		ASGPR	hIFNAR
hIFN(A)-HidAb	32476	+++	+++
hIFN(C)-HidAb	32420	+++	++
hIFN(E)-HidAb	32448	+++	+
hIFN(A)-MidAb	32684	++	+++
hIFN(C)-MidAb	32628	++	++
hIFN(E)-MidAb	32656	++	+
hIFN(A)- LodAb	32746	+	+++
hIFN(C)-LodAb	32690	+	++
hIFN(E)-LodAb	32718	+	+

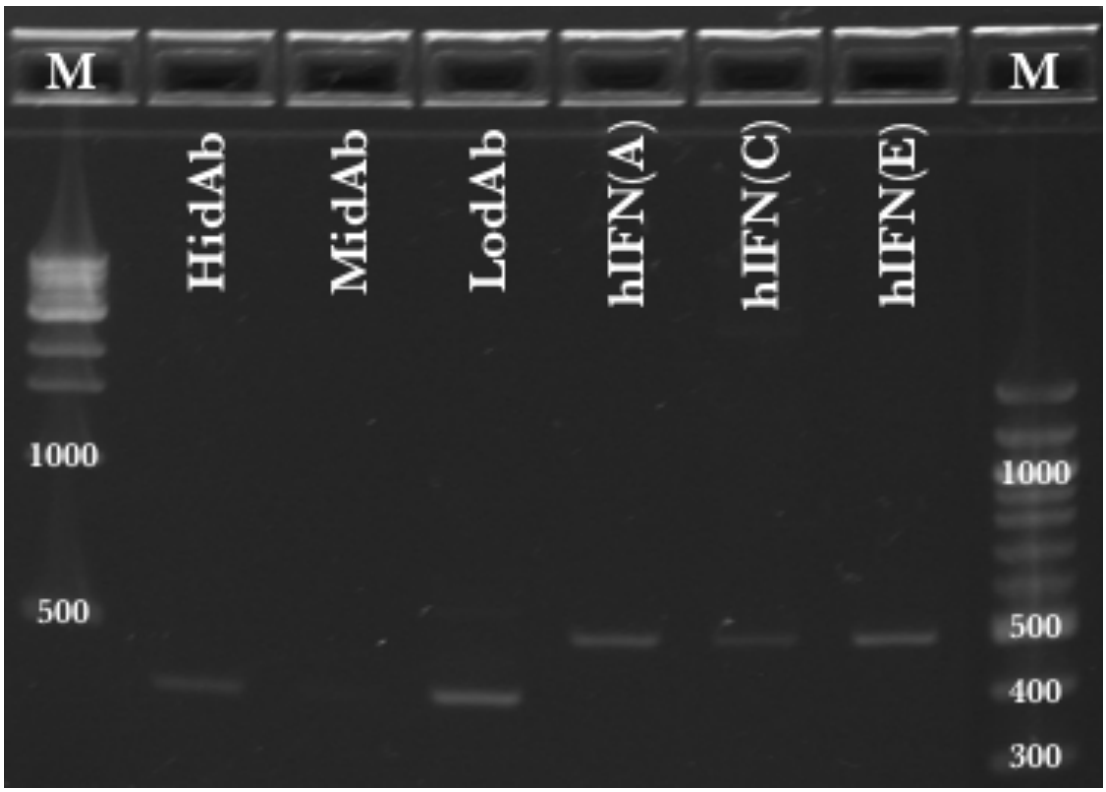

Figure 4.1 – Gel Electrophoresis of PCR Purification products of individual DNA sequences of ASGPRdAb and hIFN mutants
2% Agarose E-Gel showing migration of PCR reaction products encoding HidAb, MidAb and LodAb, in addition to hIFN(A), hIFN(C) and hIFN(E), including the NEB 1kb Marker and NEB 100bp markers (M). Result demonstrates purity of final PCR products.

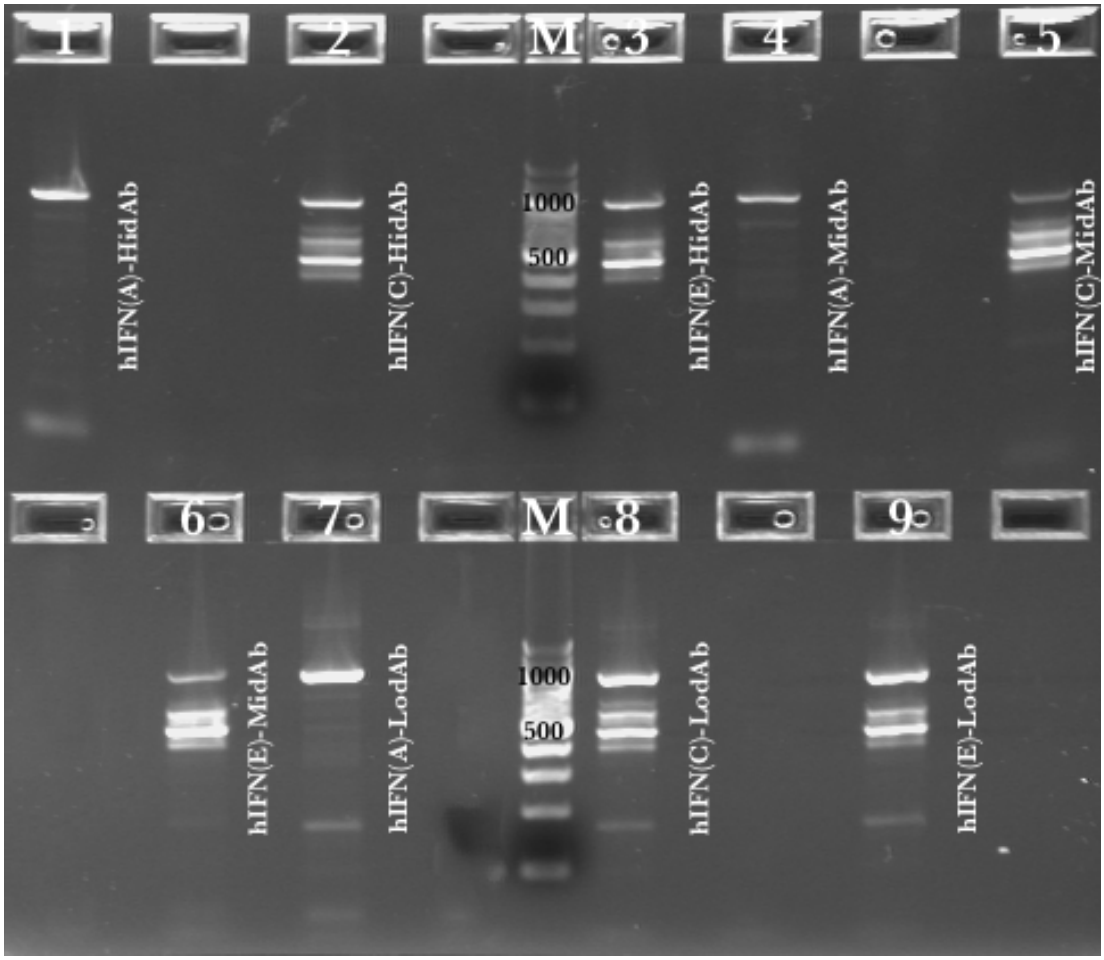

Figure 4.2 – Gel Electrophoresis of SOE PCR products of DNA sequence fusions of ASGPRdAb and hIFN mutants

2% Agarose EX-Gel showing migration of PCR reaction products encoding hIFN(A)-HidAb, hIFN(C)-HidAb, hIFN(E)-HidAb, hIFN(A)-MidAb, hIFN(C)-MidAb, hIFN(E)-MidAb, hIFN(A)-LodAb, hIFN(C)-LodAb and hIFN(E)-LodAb, including the NEB 100bp markers (M). Result demonstrates presence of full genetic fusions at ~900kb for excision and purification

Expression vector pDOM50, based on pTT5 vector derivative with an N-terminal Kozak consensus sequence and a murine-derived secretion V-J2-C signal sequence (Appendix Figure 6.6), was chosen for its proven efficiency for hIFN-dAb expression in HEK293E mammalian cell culture[74*].

High yields of 2.80mg ±0.4 (Table 4.4) purified endotoxin-free transfection grade recombinant pDOM50-hIFN-dAb DNA were subsequently attained by MegaPrep. The supercoiled and uncoiled pDOM50-hIFN-ASGPRdAb plasmids were the only apparent purified products (Figure 4.3).

Sequencing confirmed the final sequences contained all specific mutations, additive sequences such as the mammalian cleavage sequence ACCGGC and the

[*] Dr Andrew Sanderson, GSK, personal communication

double stop codon TAATGA, and were in the correct open reading frame for expression.

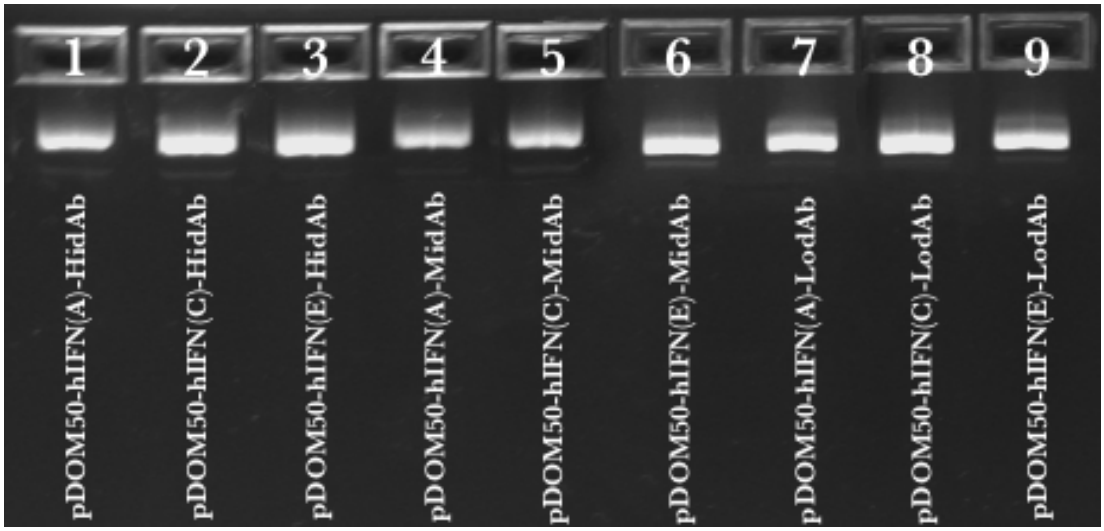

Figure 4.3 – Gel Electrophoresis of MegaPrep DNA products for pDOM50-hIFN-ASGPRdAb expression constructs
2% Agarose E-Gel showing migration of MegaPrep products for the purification of the various pDOM50-hIFN-ASGPRdAb expression constructs. Result demonstrates presence of fully recombinant plasmid products in both super-coiled and uncoiled state.

4.2.3 Expression and Purification of hIFN-ASGPRdAb Mutant Fusion Proteins

The pDOM50-hIFN-ASGPRdAb constructs were utilised to transiently transfect HEK293 mammalian cells with 293Fectin transfection reagent. After 5 days

Table 4.4
Mutant hIFN-dAb Fusion Protein Production Data

Fusion Protein	DNA Expression Construct Yields (mg)	Protein Purification	
		Expression Yield (mg/L)	Post-Conjugation Concentration (μM)
hIFN(A)-HidAb	2.34	48.4	55.4
hIFN(C)-HidAb	3.20	29.0	34.1
hIFN(E)-HidAb	3.49	20.4	49.9
hIFN(A)-MidAb	2.86	32.4	50.6
hIFN(C)-MidAb	2.29	14.2	60.4
hIFN(E)-MidAb	2.53	46.4	84.8
hIFN(A)- LodAb	2.37	35.4	55.1
hIFN(C)-LodAb	2.82	15.2	31.2
hIFN(E)-LodAb	2.58	81.8	60.3

the supernatants of the cultures were harvested. The contents consisted of multiple protein species, including prominent banding for the expressed hIFN-ASGPRdAbs at around 30kDa and a dimer at around 60kDa (Figure 4.4A).

The fusions proteins were purified from the supernatants by ÄKTA chromatography into fractionated eluate from a HiTrap mAb-Select Xtra Protein A column (Figure 4.4B). The peak fractions contained very high concentrations of the respective hIFN-ASGPRdAb species, including unwanted dimers, with some lingering contaminant protein species notable at 50kDa. The most concentrated fractions were pooled.

The resultant stocks of the respective hIFN-ASGPRdAb mutants were >95% pure (Figure 4.4C), although attained at a variety of yields (Table 4.4). The

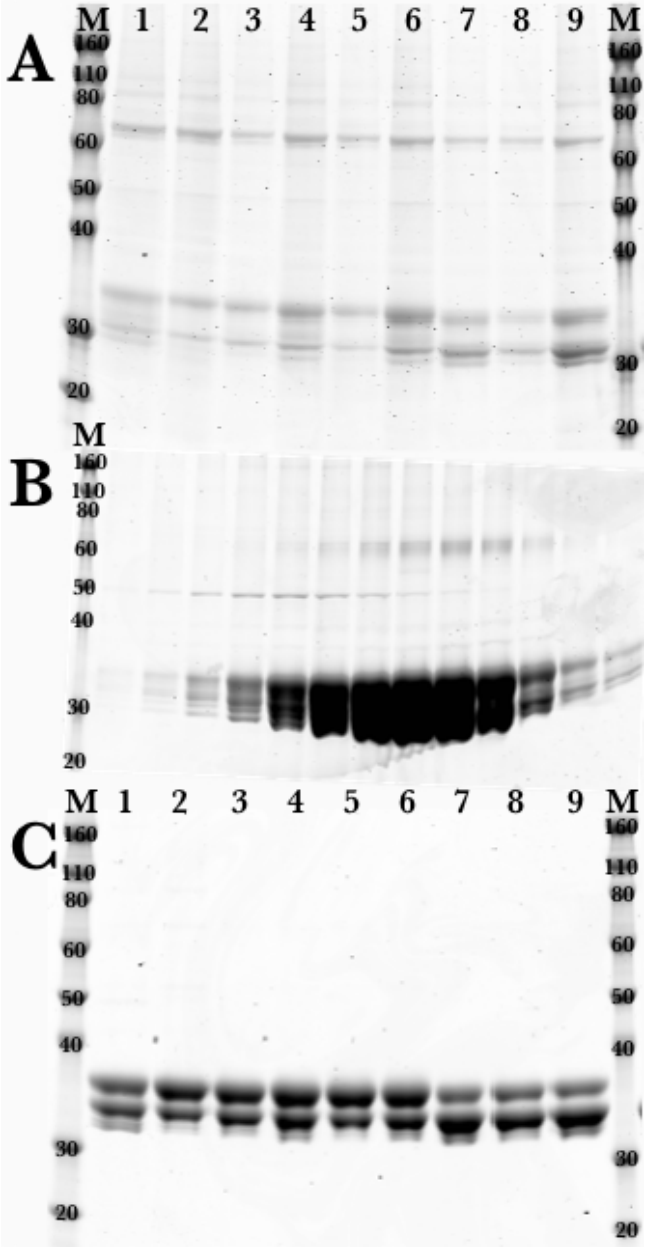

Figure 4.4 – SDS-PAGE of hIFN-ASGPRdAb ÄKTA Purification Steps

1 hIFN(A)-HidAb
2 hIFN(C)-HidAb
3 hIFN(E)-HidAb
4 hIFN(A)-MidAb
5 hIFN(C)-MidAb
6 hIFN(E)-MidAb
7 hIFN(A)-LodAb
8 hIFN(C)-LodAb
9 hIFN(E)-LodAb
M = Novex Sharp Pre-stained Protein Standard.

A – Non-reducing SDS-PAGE of raw HEK293e supernatants containing expressed hIFN-ASGPRdAbs.
(Lanes as above)

B – ÄKTA HiTrap mAb-Select Xtra purified hIFN(A)-HidAb
(Lanes in order fractionated)

C – Reducing SDS-PAGE of ÄKTA HiTrap mAb-Select Xtra purified pooled hIFN-ASGPRdAb stocks post 0.22μM filtering
(Lanes as above)

Results demonstrate full purification of all mutant hIFN-ASGPRdAbs from the heterogeneous protein supernatant to fully purified glycosylation species.

expression yield data broadly showed that the mutant fusion proteins were expressed at above 20mg/L within this HEK293 mammalian expression system, which were average yields for antibody fragments technologies[479]. However, the hIFN(C) lineage fusion mutants had the weakest expression in this system with hIFN(C)-MidAb and hIFN(C)-LodAb achieving yields of approximately 14mg/L, possibly due to poorer transfection efficiencies or secretion properties[480]. These yields were nonetheless sufficient for further experimentation. The concentrations achieved from the HiTrap mAb-Select Xtra stock purifications were significantly ($p=0.0001$) higher than the hIFN-MAXdAb stocks (Table 3.2) and so were known to be sufficient for NOTA conjugation reactions. The SDS-PAGE (Figure 4.4C) indicated the presence of up to four different glycosylation species of hIFN-ASGPRdAb monomer. This was representative of the presence of both N-linked and O-linked glycosylation sites in the hIFN-ASGPRdAb amino acid sequences, as shown by PNGase F and site directed mutagenesis (SDM) experimentation (Appendix 6.2.3).

Hence, all hIFN-ASGPRdAbs were successfully expressed and purified from the HEK293e mammalian expression system.

4.2.4 SCN-Bn-NOTA Conjugation and Purification

For Ga-68 radiolabelling, the hIFN-ASGPRdAb mutant fusion proteins underwent conjugation with SCN-Bn-NOTA (Methods 2.2.1). The conjugation reactions were purified by Protein A batch purification (Table 4.4).

The SDS-PAGE of the resultant most concentrated fractions (Figure 4.5) demonstrated the purity of the attained NOTA-hIFN-ASGPRdAbs. The glycosylation heterogeneity was indicated by the different migration characteristics. The apparent heavier glycosylated products were due to N-linked glycosylation, as was determined by PNGase F enzymatic degradation (Appendix Figure 6.17) and the loss of the glycosylated products after the removal of the NGS glycosylation site by SDM to NGA (Appendix Figure 6.18) (Appendix 6.1.9). There remained a small amount of dimer migrating at approximately 60kDa in each sample in spite of 0.22μm filtration.

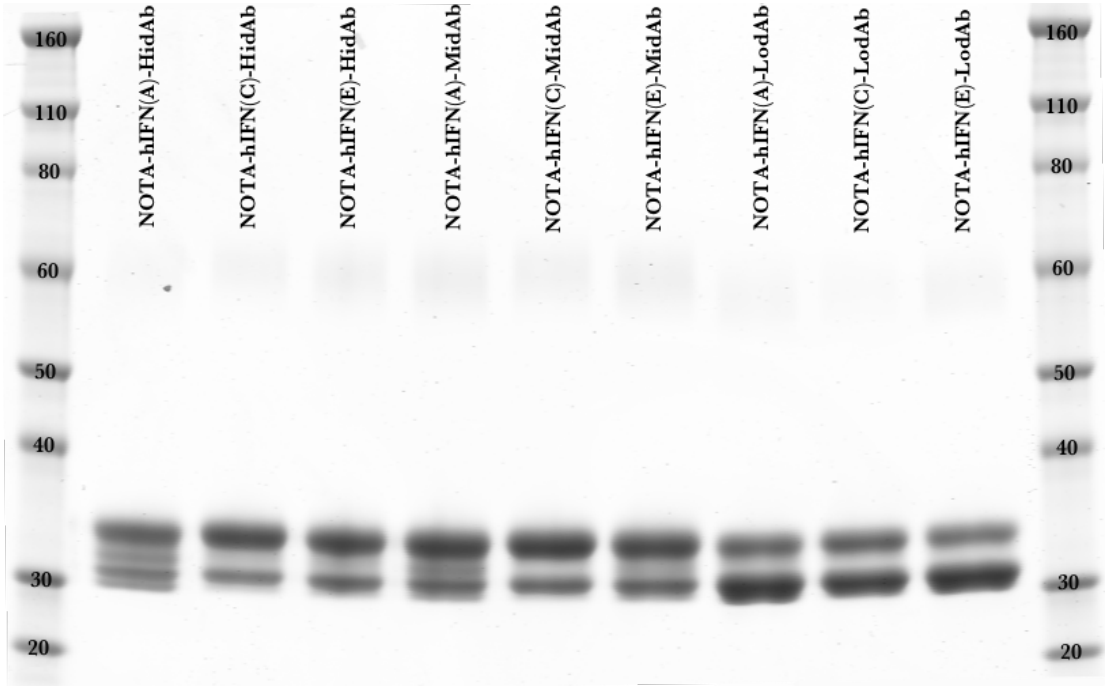

Figure 4.5 – Non-Reducing SDS-PAGE of post-Protein A purification hIFN-ASGPRdAbs

hIFN-ASGPRdAb mutant fusion proteins present as multiple glycosylation species migrate as predicted to an apparent molecular mass of between 30-33kDa, without any significant detectable aggregation after Protein A purification.
All hIFN-ASGPRdAbs at 3µg, with Novex Sharp Pre-stained Protein Standard.

The MS data proved to be of inadequate quality to reliably estimate the levels of NOTA conjugation of the hIFN-ASGPRdAbs as insufficient levels of ionised protein were detected. All traces demonstrated high levels of noise and indistinct mass peaks (Figure 4.6). However, it was possible to determine that NOTA was present on each hIFN-ASGPRdAb as multiple species in a pattern similar to that witnessed for NOTA-hIFN-MAXdAb (Section 3.2.2.4), but at indeterminate overall levels as the N-linked glycosylates were not detected. This was exemplified by NOTA-hIFN(E)-LodAb (Figure 4.6), the trace of which suggested a parental peak (33664) with up to three NOTA conjugation species (34110, 34566, and 35023) and the presence of an asialyted NOTA species (33819).

In conclusion, a purified, heterogeneous, NOTA-conjugated mix of each hIFN-ASGPRdAb was attained for further experimentation.

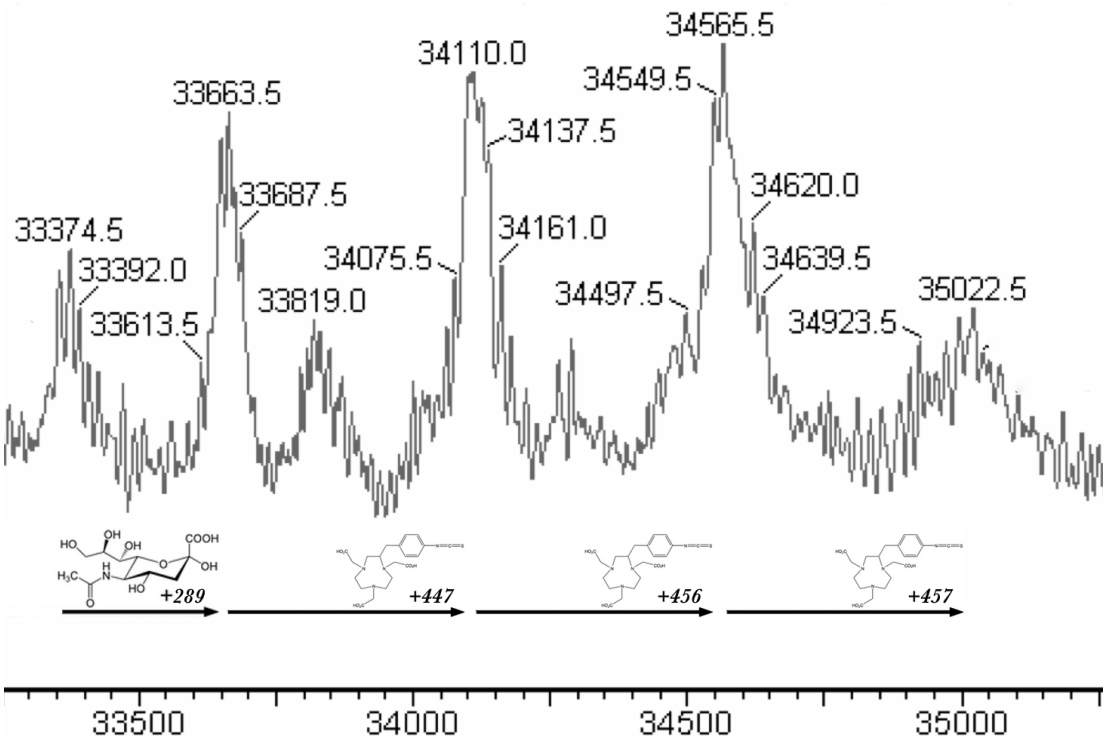

Figure 4.6 – Mass Spectrum of NOTA-hIFN(E)-LodAb

Mass spectrum of Protein A purified post-conjugation, 500µg/ml NOTA-hIFN(E)-LodAb fraction 3. Multiple glycosylated and NOTA- conjugated species identified, but high noise indicates poor ionisation and flight resulting in a reduced robustness

4.4 *IN VITRO* CHARACTERISATION

All the hIFN-ASGPRdAb mutants were designed to have varying dual affinity for both the ASGPR and hIFNAR (Table 4.2). It was necessary to establish the kinetic variables achieved for each of these novel hIFN-ASGPRdAb fusion proteins .

4.4.1 Biacore Surface Plasmon Resonance

Biacore SPR was utilised to determine the binding parameters of each hIFN-ASGPRdAb to both ASGPR-H1-CRD and hIFNAR2 (Methods 2.2.2).

4.4.1.1 ASGPR Binding Assay

Utilising a Biacore T200, the K_D values for the unconjugated hIFN-ASGPRdAbs binding ASGPR-H1-CRD demonstrated that the designed stepwise binding affinity differences (Table 4.2) had been broadly achieved (Table 4.5). The k_{on} values suggested a small effect of the fused hIFN mutant on the association of the hIFN-ASGPRdAb to ASGPR-H1-CRD because the higher the designed hIFN affinity, the faster the rate of association. The k_{off} values appeared not to conform to a discernable pattern. Comparison with the previously determined values (Table 4.2) of 5nM, 25nM and 300nM for HidAb, MidAb and LodAb respectively, and a value of 7.88nM for HidAb observed in this investigation, showed an unfavourable effect on

Table 4.5
Biacore T200 ASGPR Binding Kinetics of Mutant hIFN-ASGPRdAbs

Protein	K_{on} ($x10^4$ $M^{-1}s^{-1}$)	K_{off} ($x10^{-2}$ s^{-1})	K_D (nM)	R_{max} (RU)	Chi^2 (RU^2)
HidAb	113	0.89	7.88	129.4	0.06
hIFN(A)-HidAb	56.9	3.97	69.7	62.6	0.26
hIFN(C)-HidAb	13.4	0.84	63.0	67.5	0.07
hIFN(E)-HidAb	2.10	0.98	468	360	0.19
hIFN(A)-MidAb	11.7	0.94	80.0	30.0	0.06
hIFN(C)-MidAb	6.35	3.97	626	524	0.11
hIFN(E)-MidAb	53.3	0.79	149	36.9	0.02
hIFN(A)-LodAb	23.6	0.20	505	137	0.74
hIFN(C)-LodAb	16.4	6.07	371	179	1.26
hIFN(E)-LodAb	5.03	2.65	528	45.3	0.11

n≤3

K_D by fusing the ASGPRdAbs to the hIFN mutants. For the HidAb fusion proteins it appeared that decreases in the k_{on} rates were responsible for the ten-fold decrease in K_D.

There were two anomalous results for hIFN(E)-HidAb and hIFN(C)-MidAb, where lower K_D values were observed of 468nM and 626nM, respectively, than was expected based on the affinity of the other similar hIFN-HidAb and hIFN- MidAb fusion proteins which averaged 66.4nM and 115nM, respectively. It was apparent from the high R_{max} values that this was likely due to the mass transport effect (Section 3.2.3) as the low Chi^2 values indicated that the data fit was sufficient.

Overall the data confidence level was high and the results indicated the desired binding affinity profile for ASGPR-H1-CRD of HidAb>MidAb>LodAb.

The binding profiles of the analytes against ASGPR pre- and post-conjugation (Figure 4.7) demonstrated an apparent decrease in ASGPR-H1-CRD binding with the conjugation of NOTA. This was exemplified by NOTA-hIFN(A)-HidAb, hIFN(A)-HidAb, NOTA-hIFN(C)-MidAb, hIFN(C)-MidAb, NOTA-hIFN(E)-LodAb, hIFN(E)-LodAb, along with hIFN-MAXdAb and hIFN as positive controls and dAb as a negative control.

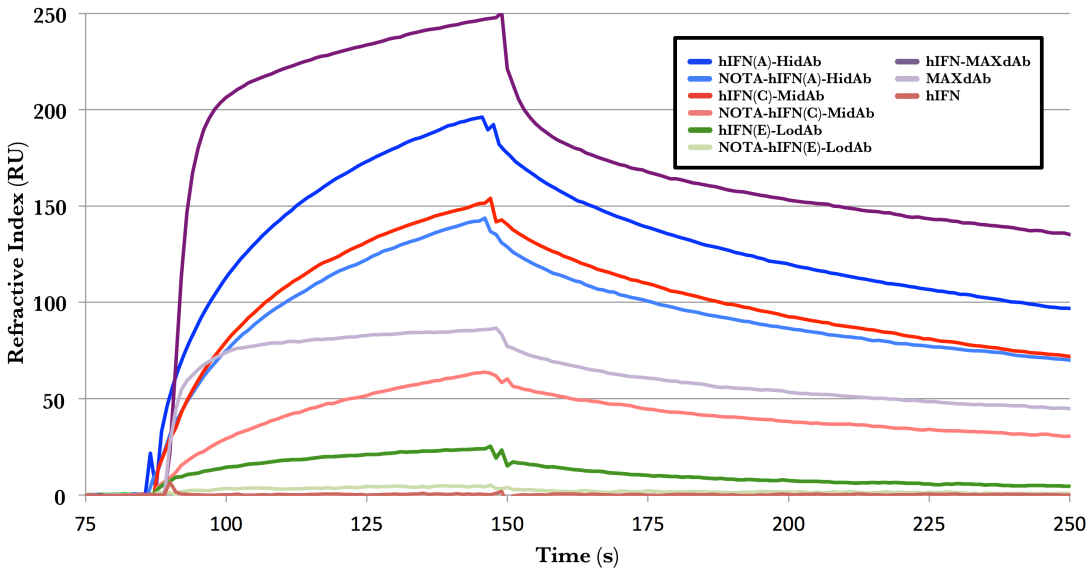

Figure 4.7 – Biacore 3000 SPR Analysis of Analytes' binding interaction with recombinant ASGPR-H1-CRD

Biacore 3000 SPR with ASGPR-H1-CRD immobilised on a CM5 chip assessed the ASGPR-H1-CRD binding curves of 250nM analytes – representative selection of hIFN-ASGPRdAbs, hIFN-MAXdAb, MAXdAb and hIFN – injected over the chip surface at 30µlmin^{-1}. The data shows HidAb, MidAb and LodAb can bind ASGPR-H1-CRD with varying affinities and can confer this property to hIFN as part of a fusion protein, compared to hIFN alone showing no binding to ASGPR-H1-CRD, plus an apparent decrease in affinity with NOTA-conjugation.

The qualitative data for a decrease in affinity for the ASGPR-H1-of the NOTA-hIFN-ASGPRdAbs compared to the hIFN-ASGPRdAbs (Figure 4.7), however, could not be substantiated by quantitative values. The data for the NOTA-hIFN-ASGPRdAbs was performed on a Biacore 3000 and produced unreliable data because good data fits could not be ascertained. This was due to the insensitivity of the readout at low concentrations and the binding data not reaching equilibrium between association and dissociation, as was visible in the 250nM data (Figure 4.7) comparing for example NOTA-hIFN(A)-HidAb with MAXdAb. Based on the evidence from the NOTA-hIFN-MAXdAb, it was possible to suggest that the lack of equilibrium was again due to self-association. However, as observed with the hIFN-MAXdAb and NOTA-hIFN-MAXdAb, the primary NOTA conjugation sites were likely to be on the hIFN portion of the hIFN-ASGPRdAb fusion protein and the effect on the ASGPRdAb portion's K_D for the ASGPR-H1-CRD was likely to be relatively unchanged.

In conclusion, the desired stepwise variations in ASGPR binding affinity were achieved for the unconjugated hIFN-ASGPRdAb mutants. However, the ASGPR binding K_D values for the NOTA-hIFN-ASGPRdAbs could not be obtained, thus FACS analysis was required to confirm if the binding pattern had been maintained post-NOTA conjugation.

4.4.1.2 hIFNAR Binding Assay

The binding profiles of the analytes against hIFNAR2 (Figure 4.8) were exemplified at 250nM by NOTA-hIFN(A)-HidAb, hIFN(A)-HidAb, NOTA-hIFN(C)-MidAb, hIFN(C)-MidAb, NOTA-hIFN(E)-LodAb, hIFN(E)-LodAb, along with hIFN-MAXdAb and hIFN as positive controls and dAb as a negative control. They demonstrated differing binding affinities for hIFNAR were achieved. A qualitative analysis of the profiles showed that the expected stepwise affinity decrease for hIFNAR2 had been achieved, as conferred to the attached ASGPRdAb by the fused hIFN(A), hIFN(C) and hIFN(E). However, there was a suggestion that the binding to hIFNAR2 by each hIFN-ASGPRdAb was reduced by the NOTA conjugation, as their binding magnitudes were reduced post-conjugation.

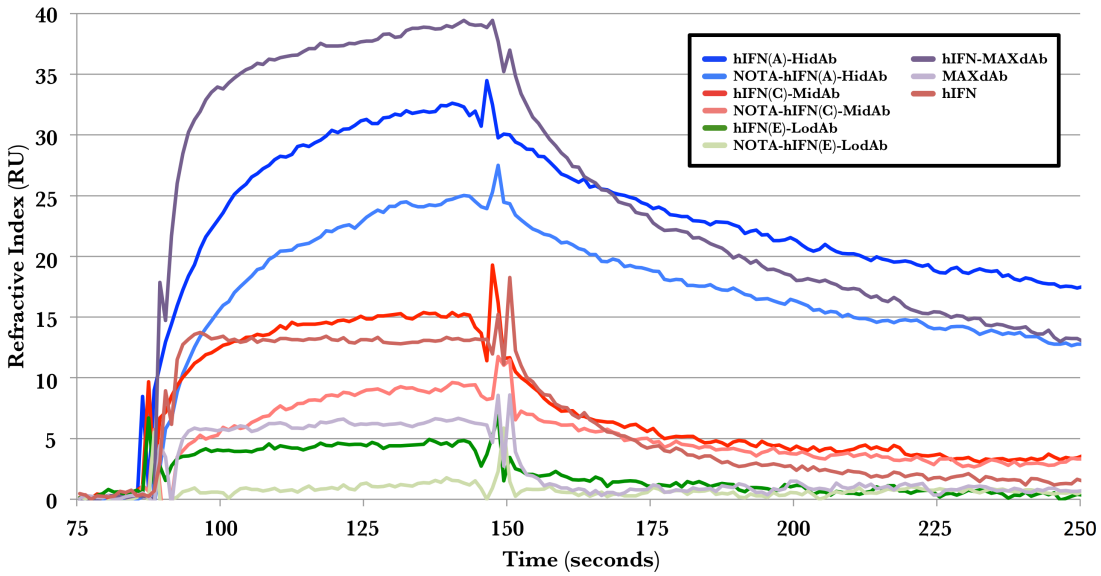

Figure 4.8 – Biacore 3000 SPR Analysis of Analytes' binding interaction with recombinant hIFNAR2

Biacore 3000 SPR with hIFNAR2 immobilised on a CM5 chip assessed the hIFNAR2 binding curves of 250nM analytes – representative selection of hIFN-ASGPRdAbs, hIFN-MAXdAb, MAXdAb and hIFN – injected over the chip surface at 30µlmin^{-1}. The data shows hIFN(A) and hIFN(C) can bind hIFNAR2 with varying affinities and can confer this property to their respective ASGPRdAb as part of a fusion protein, compared to hIFN(E) conferring no such characteristic.

Table 4.6
Biacore 3000 hIFNAR2 Binding Kinetics

Protein	K_{on} (x10^4 M^{-1}s^{-1})	K_{off} (x10^{-2} s^{-1})	K_D (µM)	R_{max} (RU)	Chi^2 (RU^2)
hIFN(A)-HidAb	2.89 ±3.45	0.35 ±0.00	0.42 ±0.49	265 ±299	1.21 ±0.03
NOTA-hIFN(A)-HidAb	3.98 ±1.92	0.46 ±0.07	0.13 ±0.04	55.6 ±13.2	0.49 ±0.02
hIFN(A)-MidAb	9.47 ±2.23	0.56 ±0.05	0.06 ±0.01	30.7 ±1.59	0.57 ±0.08
NOTA-hIFN(A)-MidAb	10.3 ±3.02	1.08 ±0.08	0.11 ±0.00	21.2 ±5.69	0.23 ±0.03
hIFN(A)-LodAb	13.6 ±3.91	0.94 ±0.01	0.07 ±0.02	30.6 ±3.21	0.69 ±0.10
NOTA-hIFN(A)-LodAb	18.2 ±3.99	1.13 ±0.16	0.06 ±0.02	19.0 ±1.53	0.29 ±0.06
hIFN(C)-HidAb	0.87 ±0.00	0.42 ±0.00	0.29 ±0.27	110 ±0.00	0.42 ±0.13
NOTA-hIFN(C)-HidAb	6.31 ±8.34	0.28 ±0.00	0.06 ±0.07	80.0 ±110	0.29 ±0.00
hIFN(C)-MidAb	6.63 ±3.22	0.57 ±0.14	0.10 ±0.04	19.6 ±11.5	0.33 ±0.13
NOTA-hIFN(C)-MidAb	0.02 ±0.00	0.002 ±0.00	0.07 ±0.01	337 ±127	0.27 ±0.00
hIFN(C)-LodAb	8.74 ±0.92	1.70 ±1.07	0.20 ±0.14	27.2 ±9.62	0.54 ±0.42
NOTA-hIFN(C)-LodAb	8.14 ±4.76	4.03 ±1.90	0.53 ±0.35	17.5 ±3.18	0.29 ±0.00

n≤3, SD values displayed

The kinetics data (Table 4.6) did not support the qualitative analysis though because no significant decreases in K_D between the NOTA-conjugated and unconjugated variants were observed. In fact the hIFN(A)-ASGPRdAbs appeared to have improved kinetics post-conjugation. However, the error was often very high.

Furthermore, the average K_D values for the hIFN(A)-ASGPRdAbs and hIFN(C)-ASGPRdAbs did not demonstrate the intended significant decrease in binding affinity for hIFNAR2. Nevertheless, a 1.9-fold decrease in the average k_{on} and a 1.9-fold increase in the average k_{off} were indicative of the K_D hIFNAR2 binding values perhaps not being an accurate reflection of underlying differences in hIFN potency.

NOTA-hIFN(A)-HidAb, NOTA-hIFN(A)-MidAb and NOTA-hIFN(A)-LodAb were intended to have identical binding affinity parameters towards the hIFNAR2 given that each had the same hIFN(A) sequence. Indeed, their respective 0.13μM, 0.11μM, and 0.06μM K_D values did not differ significantly. Similarly, the NOTA-hIFN(C)-HidAb and NOTA-hIFN(C)-MidAb both demonstrated a K_D of 0.06μM whereas at 0.53μM the hIFN(C)-LodAb had a notably lower average affinity for the hIFNAR2. The reason for this latter difference appeared to be owing to a faster off-rate owing to an unknown factor arising from the fusion to the LodAb.

The hIFN(E)-HidAb, hIFN(E)-MidAb and hIFN(E)-LodAb with their planned lack of affinity for hIFNAR yielded no detectable hIFNAR interaction within these reaction conditions.

Overall, the Biacore SPR analysis did not yield high confidence data. The standard deviations were generally large in all instances whereby a number of samples produced data up to an order of magnitude difference between replicates. This reflected the large amount of inconsistency within the data set. The Chi^2 values ranged from 0.02-1.26 for ASGPR and 0.23-1.21 RU^2 for hIFNAR2, in addition to being broadly in excess of 1% of the R_{max}, reflecting a higher noise in the data and thus reduced confidence. The R_{max} results themselves showed that the results were largely free from the additive mass transport effect. The data suggested that the reaction conditions did not suit these particular proteins, perhaps leading to modifications of the tertiary structure or aggregation, which may have accounted for the data inconsistencies.

In conclusion, the Biacore data failed to clearly demonstrate significant quantitative patterns with which to conclude on the effect of NOTA conjugation on the binding affinities of the hIFN-ASGPRdAb mutants for ASGPR and hIFNAR2. However, the qualitative data strongly suggested that the different relative affinities for ASGPR and hIFNAR binding of the hIFN-ASGPRdAbs were distinctly different as intended.

4.4.2 HEK-Blue hIFN Potency Assay

The HEK-Blue hIFNα/β *in vitro* cellular assay was utilised to quantitate the potency of the hIFN-ASGPRdAb mutants as conferred by their fused hIFN(A), hIFN(C) and hIFN(E) proteins (Method 2.2.3, see also Section 3.2.4).

The normalised data* demonstrated that conjugation of NOTA has had a negative effect on the potency of each unconjugated hIFN-ASGPRdAb (Table 4.7) versus the NOTA-hIFN-ASGPRdAb (Table 4.8) (with the exception of NOTA-hIFN(A)-HidAb, which increased slightly), however this effect was not substantial. This data conformed to the pattern of hIFN bioactivity expected with hIFN(A) > hIFN(C) > hIFN(E) (Figure 4.9). Therefore, in spite of non-significantly different K_D values for hIFNAR2 binding for hIFN(A)-ASGPRdAbs and hIFN(C)-ASGPRdAbs (Section 4.4.1), this was not reflected in the potency. This was similar to the lack of correlation between K_D and EC50 seen with the hIFN-MAXdAb (section 3.2.3.4).

The result for the hIFN(E)-ASGPRdAbs were only an estimate based on data projections but the low nM range would conform to the 16nM result registered for hIFN(E) alone†. Therefore, in spite of the hIFN(E)-ASGPRdAbs having had incalculable binding affinities for hIFNAR in the SPR experiments, they were not inactive proteins but rather were severely inhibited in their ability to engage with the hIFNAR binding complex. Therefore, it was noted that they may have a detectable effect on xenografts *in vivo*.

Therefore this data suggested that, from a hIFN potency perspective, the design of the hIFN-ASGPRdAbs having a stepwise difference in hIFN interaction has been successful.

---

* The data across different plates was normalised using the hIFN control on each plate – thus controlling for the any differences in colourimetric development time – so that plates could be cross compared.

† Data for hIFN(E) kindly provided by Dr Thil Batuwangala

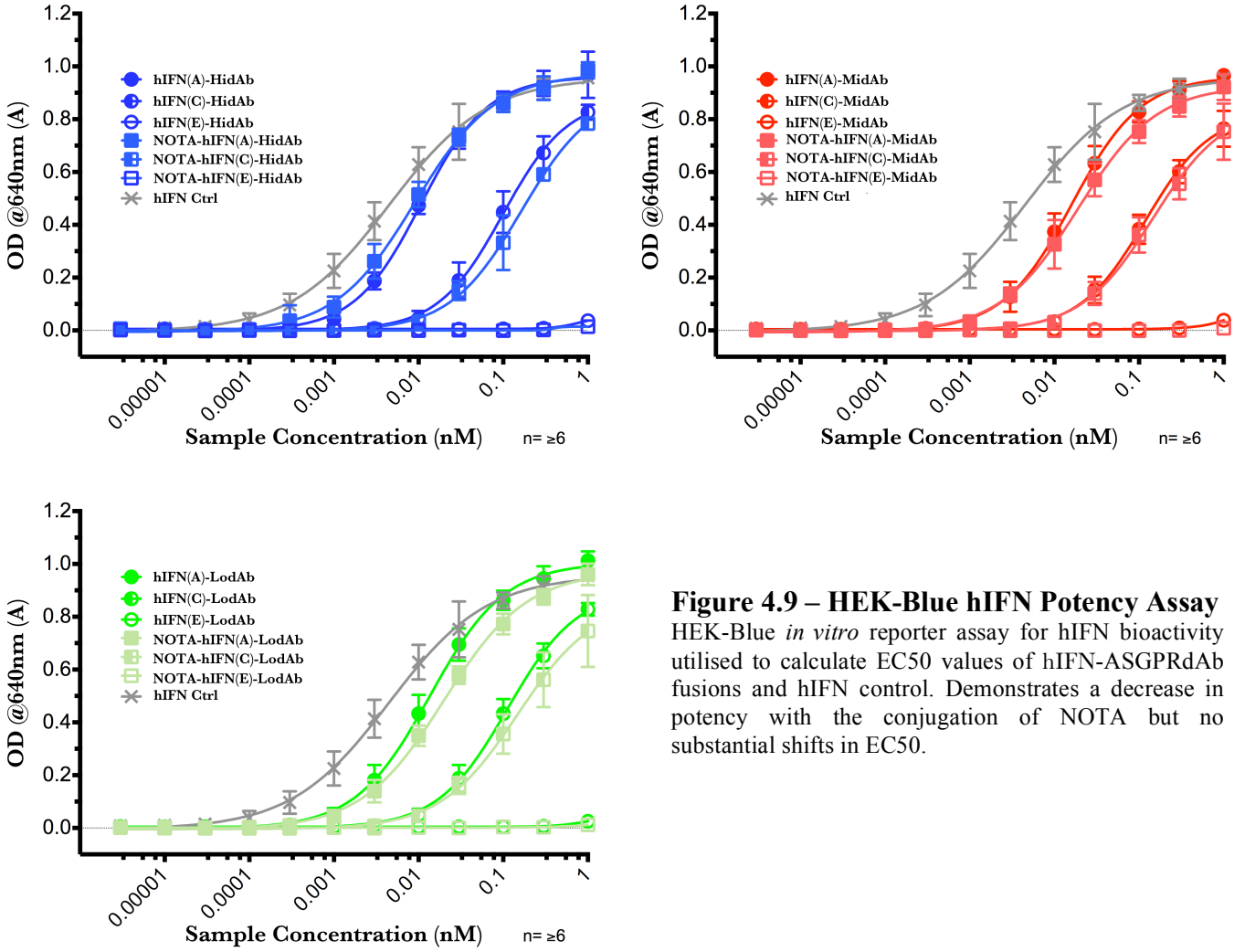

Figure 4.9 – HEK-Blue hIFN Potency Assay
HEK-Blue *in vitro* reporter assay for hIFN bioactivity utilised to calculate EC50 values of hIFN-ASGPRdAb fusions and hIFN control. Demonstrates a decrease in potency with the conjugation of NOTA but no substantial shifts in EC50.

Table 4.7
HEK-Blue EC50 of Unconjugated hIFN-ASGPRdAbs

hIFN-ASGPRdAb	HidAb	MidAb	LodAb
hIFN(A)	10.7	16.2	13.6
hIFN(C)	99.2	118.3	112.5
hIFN(E)	~792	~5499	~897

n≥6, (pM)

Table 4.8
HEK-Blue EC50 of Conjugated NOTA-hIFN-ASGPRdAbs

NOTA-hIFN-ASGPRdAb	HidAb	MidAb	LodAb
hIFN(A)	9.01	19.0	19.9
hIFN(C)	164	145	148
hIFN(E)	~3856	~3676	~3872

n≥6, (pM)

4.4.3 Flow Cytometry

Flow Cytometry was utilised with the hIFN-ASGPRdAb mutants to profile cell binding to the HepG2 and U937 cell lines (Method 2.2.4, see also Section 3.2.5).

The NOTA-hIFN-ASGPRdAb HepG2 semi-quantitative binding data (Table 4.9) demonstrated that the intended affinity profiles were achieved. HidAb conferred to the NOTA-hIFN-HidAb fusions a significantly ($p<0.002$) greater interaction with ASGPR-expressing HepG2 cells than MidAb did to the NOTA-hIFN-MidAb fusions. Concurrently, MidAb (with the exception of the anomalous NOTA-hIFN(E)-MidAb) facilitated significantly ($p<0.0005$) higher HepG2 binding than LodAb did to the NOTA-hIFN-LodAbs. This pattern was visualised by the distinct cell binding peaks above the level of IgG denoted non-specific cell binding (Figure 4.10). This data suggested, as similarly concluded for hIFN-MAXdAb and hIFN-CTRLdAb (Section 3.2.5), that the ASGPRdAb portion of the hIFN-ASGPRdAb fusion protein was the primary determinant of HepG2 cell binding. Indeed, with the presence of the lower affinity hIFN(C) or hIFN(E) mutant analogues in the mutant hIFN-ASGPRdAb there was a clear indication that the hIFN contributed no significant HepG2 binding capability. So, for instance, there was no significant ($p>0.14$) difference between the HepG2 binding values of hIFN(A)-HidAb, hIFN(C)-HidAb and hIFN(E)-HidAb (Table 4.9).

Table 4.9
Flow Cytometric Analysis of NOTA-hIFN-ASGPRdAbs' HepG2 Cell Binding

NOTA-hIFN-ASGPRdAb	HidAb	MidAb	LodAb
hIFN(A)	998 ±195	223 ±111	101 ±15.1
hIFN(C)	794 ±8.00	325 ±21.5	137 ±13.0
hIFN(E)	821 ±111	39.3 ±3.55	73.5 ±4.00

Live/Dead – PI stain, Primary Antibody – α-dAb, Secondary Antibody – Alexa647 α-Murine n=3

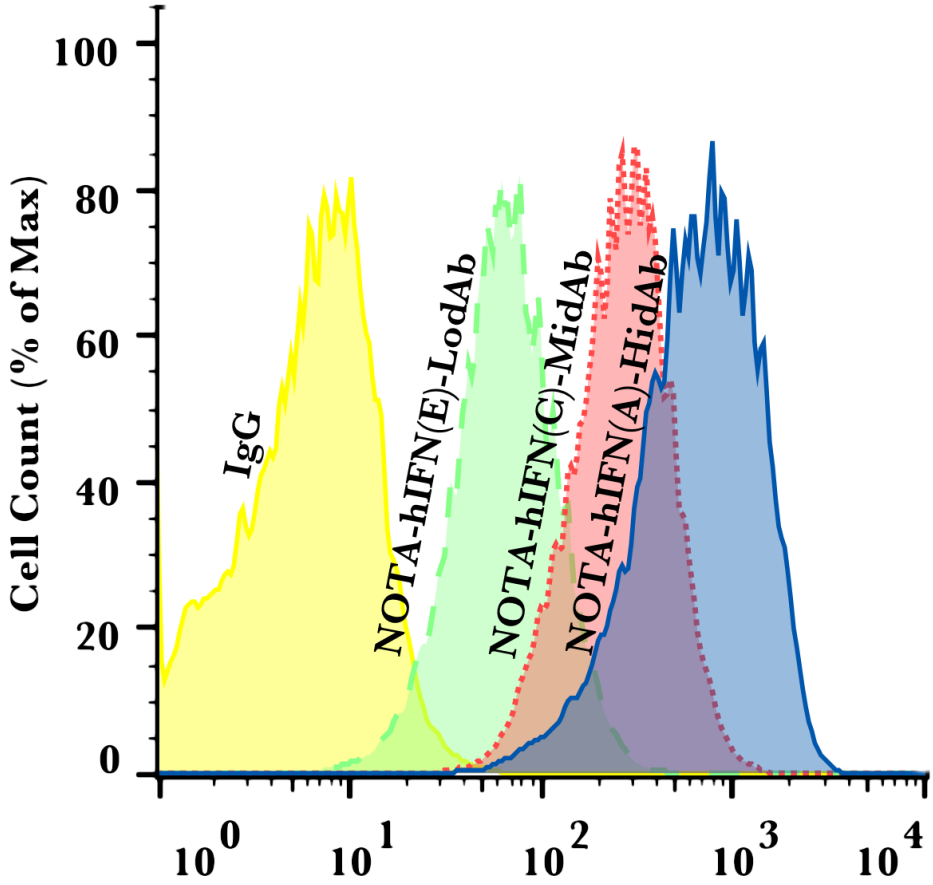

Figure 4.10 – Flow Cytometry of hIFN-dAb Fusions with HepG2
Histogram of flow cytometric analysis of live HepG2 cell staining with representative hIFN-ASGPRdAb fusions – NOTA-hIFN(A)-HidAb, NOTA-hIFN(C)-MidAb, NOTA-hIFN(E)-LodAb – detected with anti-dAb mAb and Alexa647, plus an irrelevant-IgG representing non-specific binding. Data demonstrates that HepG2 cell binding reflects the designed decreasing dAb-mediated ASGPR binding affinities – HidAb > MidAb > LodAb.

However, there was an indication from the U937 binding data that in the absence of ASGPRdAb-mediated ASGPR binding then the hIFN mutants could mediate cell binding via hIFNAR (Figure 4.11) with NOTA-hIFN(A)-HidAb at 46.5A, NOTA-hIFN(C)-MidAb at 13.3A, and hIFN(E)-LodAb at 9.26A. Moreover, the level of binding correlated with the designed affinities of the hIFN mutants (hIFN(A) > hIFN(C) > hIFN(E)) which was a further indication that the designed stepwise affinity for hIFNAR had been achieved. The cell binding of NOTA-hIFN(E)-LodAb was barely above the irrelevant IgG non-specific binging control and so again suggests it has severely inhibited binding to hIFNAR. This was also indicated by the inability to integrate a K_D value (Table 4.6). Nevertheless, it was still observed to be able to bind to some degree, which would explain the estimated nM potency values (Table 4.8).

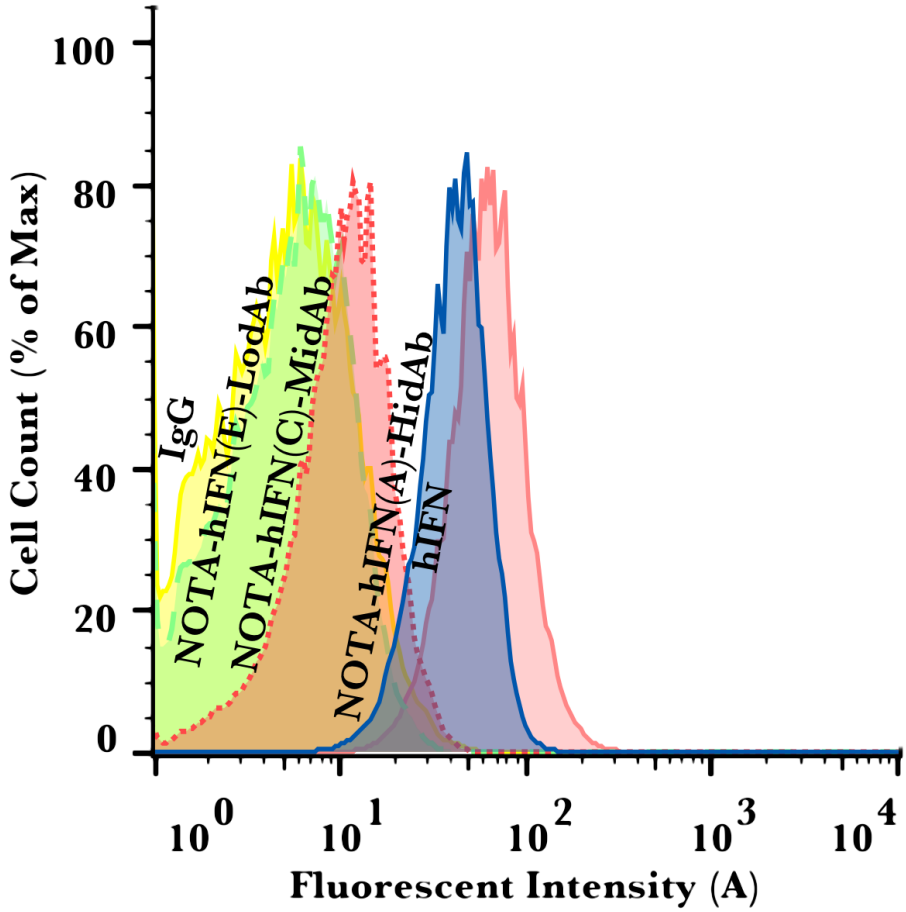

Figure 4.11 – Flow Cytometry of hIFN-dAb Fusions with U937
Histogram of flow cytometric analysis of live U937 cell staining with representative hIFN-ASGPRdAb fusions – NOTA-hIFN(A)-HidAb, NOTA-hIFN(C)-MidAb, NOTA-hIFN(E)-LodAb – detected with anti-dAb mAb and Alexa647, plus an irrelevant-IgG representing non-specific binding. Data demonstrates that U937 cell binding broadly reflects the designed decreasing hIFN-mediated hIFNAR binding affinities – hIFN(A) > hIFN(C) >hIFN(E).

Overall, the flow cytometry data corroborated the conclusions made from the ASGPR binding Biacore SPR data (Section 4.4.1), confirming that the binding pattern of the NOTA-hIFN-ASGPRdAbs through the ASGPRdAb-mediated ASGPR binding was maintained in spite of the presence of the conjugated NOTA.

In conclusion the flow cytometry data strongly suggested that the mutant NOTA-hIFN-ASGPRdAbs could bind to whole HepG2 cells. Moreover, their ability to bind HepG2 cells was likely predominantly mediated by the affinity of the respective ASGPRdAb for ASGPR with hIFN-mediated binding to hIFNAR also contributing to a lesser extent to the overall stepwise binding profile of the mutant hIFN-ASGPRdAb fusion protein subset.

4.5 BIODISTRIBUTION STUDIES

4.5.1 Ga-68 Radiolabelling

Utilising the 1M NaAc method developed for the reliable labelling of the NOTA-hIFN-MAXdAb and NOTA-hIFN-CTRLdAb (Section 3.4.1), Ga-68 radiolabelled doses of the NOTA-hIFN-ASGPRdAbs were prepared at RT immediately prior to injection (Method 2.3.2).

The average specific activity achieved for all mutant NOTA-hIFN-ASGPRdAbs with a 2μM reaction was 1.07MBq/μg ±0.07 with an average efficiency of 85.9% ±2.76 and was thus sufficient for subsequent gamma counting in all instances, which was sufficient for quantifiable biodistribution data at 3 hours post-injection. A final radiochemical purity of greater than 90% was achieved in all instances.

4.5.2 Tissue Uptake Biodistribution Study

HepG2 xenograft SCID Beige models were prepared in the same manner as previously described (Section 3.5.3). The tissue uptake of a 1μg dose of the mutant ^{68}Ga-NOTA-hIFN-ASGPRdAbs was analysed as %ID/g at 3 hours post-injection by gamma counting and tissue mass. All mutants were tested apart from hIFN(C)-HidAb and hIFN(C)-LodAb as there were insufficient SCID Beige animals available.

4.5.2.1 Full Tissue Analysis

The full data set demonstrated that there were differences in tissue uptake potentially related to the mutant ^{68}Ga-NOTA-hIFN-ASGPRdAbs' respective affinities for the ASGPR and hIFNAR receptors (Table 4.10, Figure 4.12,).

In the chapter III, the liver was identified for its specific ASGPR targeted uptake of NOTA-hIFN-MAXdAb and also speculated hIFN-mediated uptake. The liver uptake with the affinity mutants demonstrated ASGPRdAb-mediated differences in uptake (HidAb > MidAb > LodAb). In addition there was also a higher uptake with strong mIFNAR binding mediated by hIFN(A) versus hIFN(E). For instance, the uptake of the ^{68}Ga-NOTA-hIFN(A)-LodAb was significantly ($p<0.0001$) higher than ^{68}Ga-NOTA-hIFN(E)-LodAb with an average of 52.9% more. This strongly suggested that mIFNAR interactions could account for a high proportion of

the liver tissue uptake. A stronger ASGPRdAb mediated uptake was shown to account for a 44.4% increase in liver uptake when comparing uptake of ^{68}Ga-NOTA-hIFN(E)-HidAb and ^{68}Ga-NOTA-hIFN(E)-LodAb. Therefore this suggested that the ASGPRdAb-mediated binding to ASGPR could also further increase liver tissue uptake.

Table 4.10
Mutants Biodistribution Study Tissue Uptake Values

Tissue (%ID/g)	3h						
	^{68}Ga-NOTA-hIFN(A)-HidAb	^{68}Ga-NOTA-hIFN(E)-HidAb	^{68}Ga-NOTA-hIFN(A)-MidAb	^{68}Ga-NOTA-hIFN(C)-MidAb	^{68}Ga-NOTA-hIFN(E)-MidAb	^{68}Ga-NOTA-hIFN(A)-LodAb	^{68}Ga-NOTA-hIFN(E)-LodAb
Xenograft	1.48 ±0.41	1.62 ±0.64	1.59 ±0.39	1.46 ±0.61	1.48 ±0.11	1.36 ±0.27	1.15 ±0.51
Intestine	3.23 ±0.15	4.26 ±0.40	4.13 ±0.20	4.67 ±0.71	3.40 ±0.42	4.10 ±0.61	4.00 ±0.33
Pancreas	0.57 ±0.06	0.75 ±0.10	0.68 ±0.04	0.80 ±0.13	0.83 ±0.11	0.66 ±0.08	0.70 ±0.07
Spleen	5.84 ±0.97	5.01 ±0.48	5.86 ±1.29	4.10 ±0.60	5.27 ±0.79	2.75 ±0.21	2.61 ±0.30
Stomach	0.92 ±0.19	0.73 ±0.12	0.66 ±0.29	1.78 ±1.39	0.58 ±0.19	0.76 ±0.24	0.73 ±0.07
Kidneys	31.9 ±6.29	47.0 ±2.17	47.2 ±3.37	49.6 ±1.13	58.6 ±6.54	88.8 ±8.85	89.4 ±6.74
Liver	39.1 ±2.22	33.1 ±0.97	33.7 ±3.40	29.4 ±0.56	28.9 ±2.77	33.7 ±0.48	18.4 ±1.04
Heart	1.02 ±0.15	1.23 ±0.13	1.07 ±0.13	1.11 ±0.06	1.15 ±0.09	0.89 ±0.08	0.85 ±0.13
Lung	1.65 ±0.77	1.93 ±0.72	1.04 ±0.05	1.16 ±0.11	1.41 ±0.27	1.42 ±0.83	1.52 ±1.29
Blood	1.23 ±0.05	1.25 ±0.29	0.78 ±0.03	1.68 ±0.09	1.42 ±0.10	1.25 ±1.11	0.89 ±0.42
Muscle	0.25 ±0.03	0.33 ±0.04	0.34 ±0.09	0.28 ±0.02	0.36 ±0.03	0.31 ±0.05	0.26 ±0.03

n≥3 (%ID/g)

However, if there was already a strong hIFNAR binding influence, such as from hIFN(A), then the effect of improving ASGPR binding had less impact as demonstrated by only a 13.8% increase in liver uptake between ^{68}Ga-NOTA-hIFN(A)-LodAb and ^{68}Ga-NOTA-hIFN(A)-HidAb. Overall, as the liver uptake is predominantly related to ASGPR and hIFNAR receptor affinity and hIFN observed to have the largest influence on liver tissue uptake, the data strongly suggested that liver uptake was specifically influenced by both the ASGPRdAb and hIFN.

The intestine results show a significant ($p<0.01$) level of variability with no apparent pattern correlating with either ASGPR or hIFNAR receptor affinities. Therefore, as described previously (Section 3.5.2), this may reflect the respective ^{68}Ga-NOTA-hIFN-ASGPRdAbs' susceptibility to degradation in the liver. There is no correlation with liver uptake, and so again suggests that there is an undetermined mechanism of hepatic degradation unrelated to either ASGPR or hIFNAR binding.

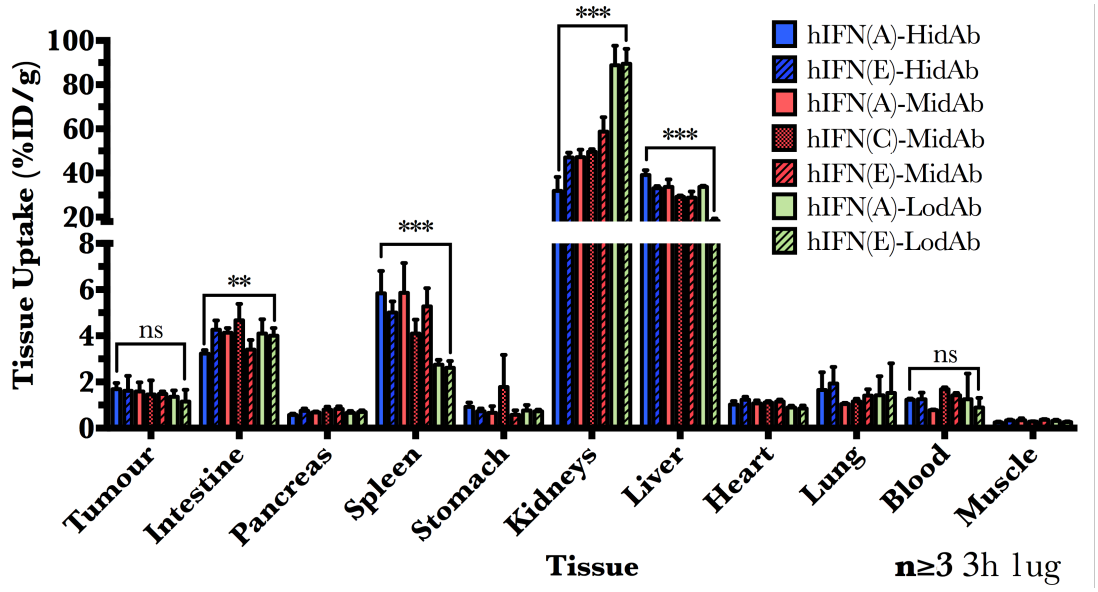

Figure 4.12 – Biodistribution of ^{68}Ga-NOTA-hIFN-MAXdAb in SCID Beige HepG2 Xenograft Model at 3hr with varying dose

Mean %ID/g in selected tissues with 1µg injected dose of ^{68}Ga-NOTA-hIFN-ASGPRdAbs at 3 hours post-IV administration as determined by Gamma Counting. Demonstrates that modifying the affinity of hIFN-ASGPRdAbs for the ASGPR and hIFNAR receptors can significantly change the tissue uptake profile of the fusion protein.

The uptake in the kidneys showed extremely significant differences ($p<0.0001$) for the mutant ^{68}Ga-NOTA-hIFN-ASGPRdAbs with reduced targeting with both to ASGPR and hIFNAR, ranging from 39.1%ID/g for ^{68}Ga-NOTA-hIFN(A)-HidAb up to 89.4%ID/g for ^{68}Ga-NOTA-hIFN(E)-LodAb. This difference was not due to varying kidney size as the average kidney size varied little at 215.4µg ±8.80, but rather appeared to be related to renal filtration (or indeed retention to an unknown extent). This was apparent because for the ^{68}Ga-NOTA-hIFN(A)-HidAb an average of 68.0% of the total ID was accounted for in the harvested tissues whereas by comparison for the ^{68}Ga-NOTA-hIFN(E)-LodAb an average of 56.4% of the total ID was in the harvested tissues. Therefore, assuming the difference was not residing in uncounted tissues, there was increased urinary excretion of the lesser-targeted ^{68}Ga-NOTA-hIFN-ASGPRdAbs. This may perhaps have been accountable for in part by the reduced liver tissue uptake. Hence, targeting to ASGPR increased systemic retention of the mutant hIFN-ASGPRdAbs.

The spleen uptake demonstrated a significant difference ($p<0.001$) between the hIFN-HidAb mutants and the hIFN-LodAb mutants, which was indicative of the spleen tissue uptake being linked to the ASGPRdAb affinity. This was speculated to

be specific ASGPR binding or a non-specific interaction with the white pulp correlating with affinity. These possible hypotheses were supported by the increased bioavailability of the lesser-targeted ^{68}Ga-NOTA-hIFN-ASGPRdAbs not correlating with increased spleen tissue uptake. Hence, it was not increased concentration in the system. Moreover, the levels were significantly higher than in blood. However, this data contradicted the data for ^{68}Ga-NOTA-hIFN-CTRLdAb, which demonstrated a higher uptake in spleen than the ASGPR targeted ^{68}Ga-NOTA-hIFN-MAXdAb. Therefore, the exact nature of the spleen uptake remained unresolved.

4.5.2.2 Xenograft Uptake

The %ID/g data showed the tumour xenograft uptake was observed to not be significantly different (Figure 4.12, Table 4.12), although there was a downward trend with decreasing receptor affinities. However, as demonstrated in the hIFN-MAXdAb blocking study (Section 3.5.4) the liver uptake could have been significantly affecting the bioavailability of the ^{68}Ga-NOTA-hIFN-ASGPRdAbs in the system as a large specific sink. The hypothesis being that a low liver uptake resulted in more radioligand in the system for xenograft uptake, thus potentially inflating xenograft tissue uptake values for lesser targeted radioligands. There was a highly significant difference ($p<0.0001$) in liver uptake over the range of 39.1%ID/g ±2.22 to 18.4%ID/g ±1.04 for the ^{68}Ga-NOTA-hIFN-ASGPRdAbs analysed (Section 4.5.2.1). So for instance, there was an average of 25.2% more ^{68}Ga-NOTA-hIFN(E)-LodAb available for xenograft tumour uptake in the system of the respective SCID Beige model than the respective model with ^{68}Ga-NOTA-hIFN(A)-HidAb owing to the increased specific liver uptake of the latter. Therefore it was appropriate to apply a correction to the xenograft data.

Applying this correction to control for systemic availability by removing the liver counts from the total available %ID, ensured that the xenograft uptake values were relative to the systemic bioavailability of the respective hIFN-ASGPRdAb. This sub-analysis revealed that there was a significant difference ($p=0.04$) between the xenograft uptake between ^{68}Ga-NOTA-hIFN(A)-HidAb and ^{68}Ga-NOTA-hIFN(E)-LodAb of 2.90%ID/g ±0.75 versus 1.56%ID/g ±0.69, respectively, reflecting their respective high and low targeting status (Table 4.13, Figure 4.13).

Table 4.11
Xenograft Tissue Uptake of Mutant ^{68}Ga-NOTA-hIFN-ASGPRdAbs at 3h with Liver Uptake Correction

NOTA-hIFN-ASGPRdAb*	HidAb	MidAb	LodAb
hIFN(A)	2.90 ±0.75	2.67 ±0.52	2.17 ±0.42
hIFN(C)	-	2.31 ±1.00	-
hIFN(E)	2.78 ±1.19	1.48 ±0.12	1.56 ±0.69

n≥3 (%ID/g), *insufficient resources for hIFN(C)-HidAb and hIFN(C)-LodAb

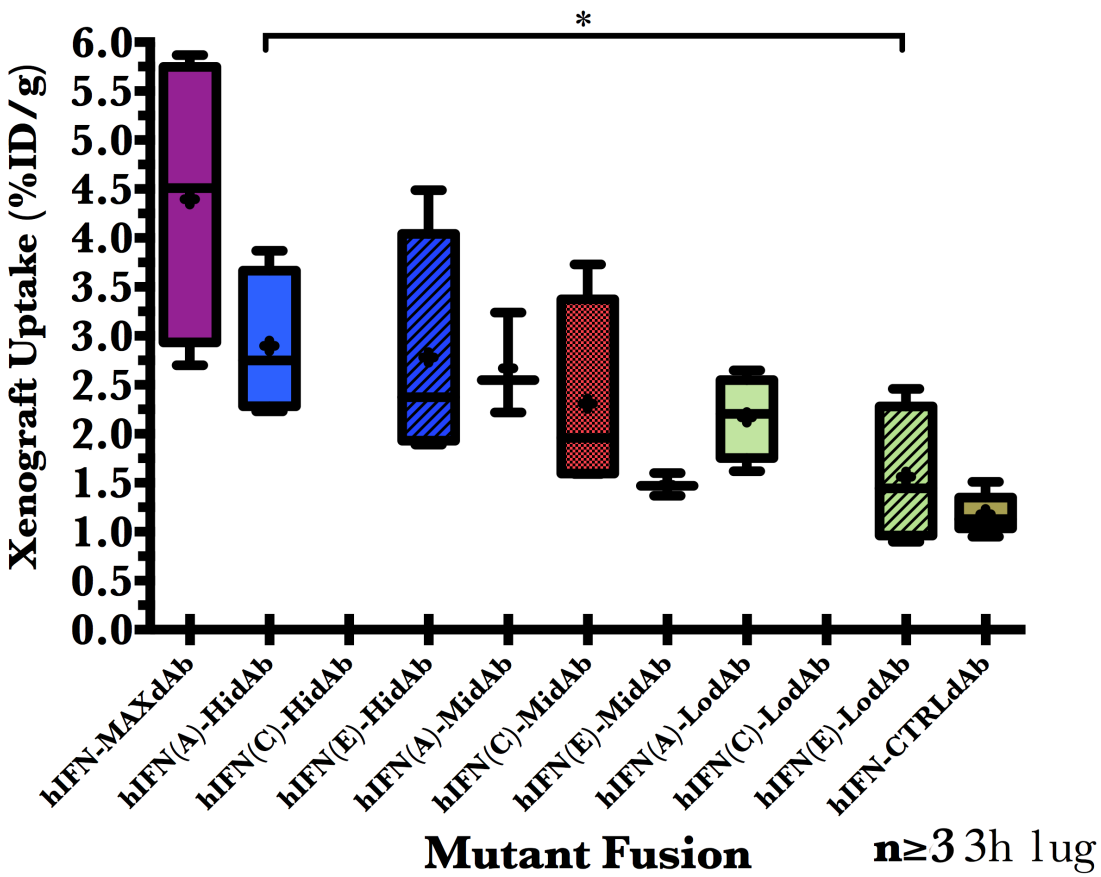

Figure 4.13 – Xenograft Uptake of mutant ^{68}NOTA-hIFN-ASGPRdAbs in SCID Beige HepG2 Xenograft Model

Mean %ID/g (corrected for liver uptake dose) in xenograft tissue at 1µg injected dose of mutant ^{68}Ga-NOTA-hIFN-ASGPRdAbs, plus ^{68}Ga-NOTA-hIFN-MAXdAb and ^{68}Ga-NOTA-hIFN-CTRLdAb, at 3h post-IV injection. Demonstrates significantly higher uptake of fusion protein with increased ASGPR and hIFNAR targeting affinities.

Comparison with the ^{68}Ga-NOTA-hIFN-MAXdAb and ^{68}Ga-NOTA-hIFN-CTRLdAb demonstrated the broadly stepwise decrease in the mean tumour xenograft targeting from the highly targeted hIFN-MAXdAb down through the HidAb, MidAb and LodAb mutant fusions to the hIFN-CTRLdAb (Figure 4.13). This indicated that tumour xenograft uptake of the hIFN-ASGPRdAbs was specific to both the ASGPR and hIFNAR.

However, this hypothesis was undermined by a lack of significant difference between the blood content versus the tumour xenograft (Figure 4.12). This could have been interpreted as the tumour uptake being a product of the highly vascularised nature of the tumour xenograft rather than dAb-mediated specific uptake. Nevertheless, there was no correlation between the blood content and there was an evident pattern of ^{68}Ga-NOTA-hIFN-ASGPRdAb tumour xenograft uptake correlating with ASGPR and hIFNAR affinity, thus suggesting that the blood uptake and tumour xenograft uptake were independent.

An additional conclusion from the lack of significant difference between xenograft uptakes of the mutant ^{68}Ga-hIFN-ASGPRdAbs before liver correction was that this data demonstrated that if there was a large off-target sink for a targeted dAb fusion protein (represented in this data set by the liver uptake) then a reduced receptor affinity was an appropriate strategy to reduce off-target uptake whilst maintaining uptake in the target tissue. So for instance, there was no significant difference ($p=0.71$) in specific xenograft uptake between ^{68}Ga-NOTA-hIFN(A)-HidAb and ^{68}Ga-NOTA-hIFN(A)-MidAb, but ^{68}Ga-NOTA-hIFN(A)-MidAb had a significantly ($p=0.04$) lower liver uptake. Therefore, in spite of its lower affinity for ASGPR, ^{68}Ga-NOTA-hIFN(A)-MidAb was shown to be the optimum choice to reduce off-target uptake.

Hence, in conclusion, this data set provided additional confidence in the assertion that HepG2 xenograft uptake was mediated by ASGPRdAb affinity for ASGPR. Furthermore, that reducing the affinity for ASGPR, and concurrently hIFN's affinity for hIFNAR, could decrease off-target uptake whilst maintaining HepG2 xenograft uptake.

4.5.3 TaqMan mRNA Expression Profiling

The xenograft targeting results for the mutant hIFN-ASGPRdAbs demonstrated an observable affinity dependent uptake in the HepG2 tumour xenograft tissues (Section 4.5.2.2). Previously, it was shown that the significantly different xenograft uptake of hIFN-MAXdAb and hIFN-CTRLdAb was congruent with discrete modifications to the HepG2 xenograft transcriptome with increased anti-viral or anti-proliferative mRNA expression profiles (Section 3.5.5). Therefore, TaqMan was also used to discern the bioactivity of the mutant hIFN-ASGPRdAbs relative to their xenograft uptake (Methods 2.5).

The hIFN-MAXdAb, hIFN(A)-HidAb, hIFN(A)-MidAb, hIFN(A)-LodAb and hIFN-CTRLdAb all had a low pM EC50 hIFN potency but differed in their affinity for the ASGPR receptor (MAXdAb > HidAb > MidAb > LodAb > CTRLdAb, as reflected in their xenograft uptake values (Table 4.12)) and so were compared to elucidate the influence of ASGPR affinity (Figure 4.14). The data demonstrated that the hIFN(A)-HidAb, hIFN(A)-MidAb and hIFN(A)-LodAb instigated a similar pattern of mRNA expression in the HepG2 tumour xenografts to hIFN-MAXdAb but with an even greater effect on mRNA copy number. For instance, on average the hIFN-MAXdAb decreased mRNA related to transcription and translation by 23.2% whereas hIFN(A)-MidAb registered a decrease of 40.3%. Similarly, the mRNA copy number of genes associated with cell survival and motility (excluding NET1) were on average 16.8% lower with the application of hIFN(A)-MidAb compared to hIFN-MAXdAb. For six gene results the lowest affinity targeted hIFN(A)-LodAb had the greatest effect on the respective mRNA copy number. In the modification of apoptotic gene mRNAs such as PRKCD and NET1 the hIFN(A)-MidAb demonstrated the largest anti-tumour effect. There was overall, however, little difference between hIFN(A)-HidAb, hIFN(A)-MidAb, and hIFN(A)-LodAb as each had on average a 29.3% ±2.8 greater effect on cellular mRNA responses compared to hIFN-MAXdAb

Table 4.12
Percentage Difference in mRNA Copy Number relative to untreated Xenograft Tissue

	Fusion Protein						
	hIFN-MAXdAb	**hIFN(A)-HidAb**	**hIFN(A)-MidAb**	**hIFN(C)-MidAb**	**hIFN(E)-MidAb**	**hIFN(A)-LodAb**	**hIFN-CTRLdAb**
Tumour Xenograft Uptake (%ID/g)*	**3.11**	**3.06**	**2.55**	**2.31**	**2.20**	**2.16**	**1.00**
Gene Name							
ARHGEF Family	-25.8	-50.7	-49.6	-40.4	-39.8	-48.3	-4.8
CREB Family	-20.1	-34.3	-39.6	-25.1	-40.1	-41.6	3.5
EIF4 Family	-35.7	-44.0	-55.6	-58.3	-45.9	-37.1	-55.2
HIST Family	-3.7	-8.8	-16.5	25.5	63.6	-10.0	64.5
IFNAR1/2	-34.9	-46.2	-45.1	-43.7	-45.0	-47.1	-4.7
IFNYR1/2	-28.4	-41.4	-41.5	-33.9	-44.3	-43.3	-10.1
IRF9	516	426	344	593	-27	356	475
IRS1	-42.6	-58.2	-51.1	-55.1	-54.8	-58.2	-19.6
JAK1/2	-40.3	-51.9	-49.3	-45.1	-44.8	-48.8	-5.1
MAPK Family	-28.5	-45.5	-43.8	-35.2	-40.9	-45.7	-2.8
MTOR	-15.4	-39.8	-52.3	-46.4	-47.8	-47.9	-51.7
NET1	26.2	13.8	115.3	98.3	36.5	38.9	-42.7
PI3K Family	-35.7	-50.1	-48.4	-43.9	-47.4	-51.2	-15.0
PRKCD	-30.7	-39.1	-38.5	-15.6	-5.3	-25.9	10.1
RAC1	-44.9	-35.4	-39.3	-43.6	-30.1	-49.4	-17.1
RPS6 Family	-33.3	-50.8	-49.3	-36.3	-40.1	-47.6	-7.9
STAT1	230.9	333.0	147.3	328.1	-43.2	251.8	89.9
TYK2	-10.0	-42.3	-39.2	-11.1	-9.3	-39.4	21.6
VAV2/3	-17.0	-55.5	-52.2	-49.6	-37.3	-51.3	-7.4

n=1, *individual xenografts utilised

The higher apoptotic effect of hIFN(A)-MidAb was indicative of an increased concentration of bioavailable hIFN(A)-MidAb in the xenograft in spite of its relatively lower uptake compared to hIFN-MAXdAb with 2.31%ID/g versus 3.11%ID/g respectively. A possible hypothesis for this occurrence was that MAXdAb's higher affinity for ASGPR mediated an increase in degradation of the hIFN-MAXdAb owing to entering the ASGPR degradation pathway (Introduction 1.4.2). Therefore, having a lower affinity for ASGPR, such as with hIFN-MidAb, could have facilitated binding to ASGPR but with a higher rate of subsequent dissociation before degradation could occur. This would enable more interactions with hIFNAR to possibly occur. Moreover, this would likely facilitate greater tissue percolation and thus increase potential hIFNAR interactions.

Therefore, the results indicated that hIFN(A)-MidAb appeared to provide the optimum balance between specific tumour xenograft targeting, relatively low liver uptake and kidney loss, and maximising the potency of the hIFN bioactivity possibly through facilitating increased hIFNAR interaction.

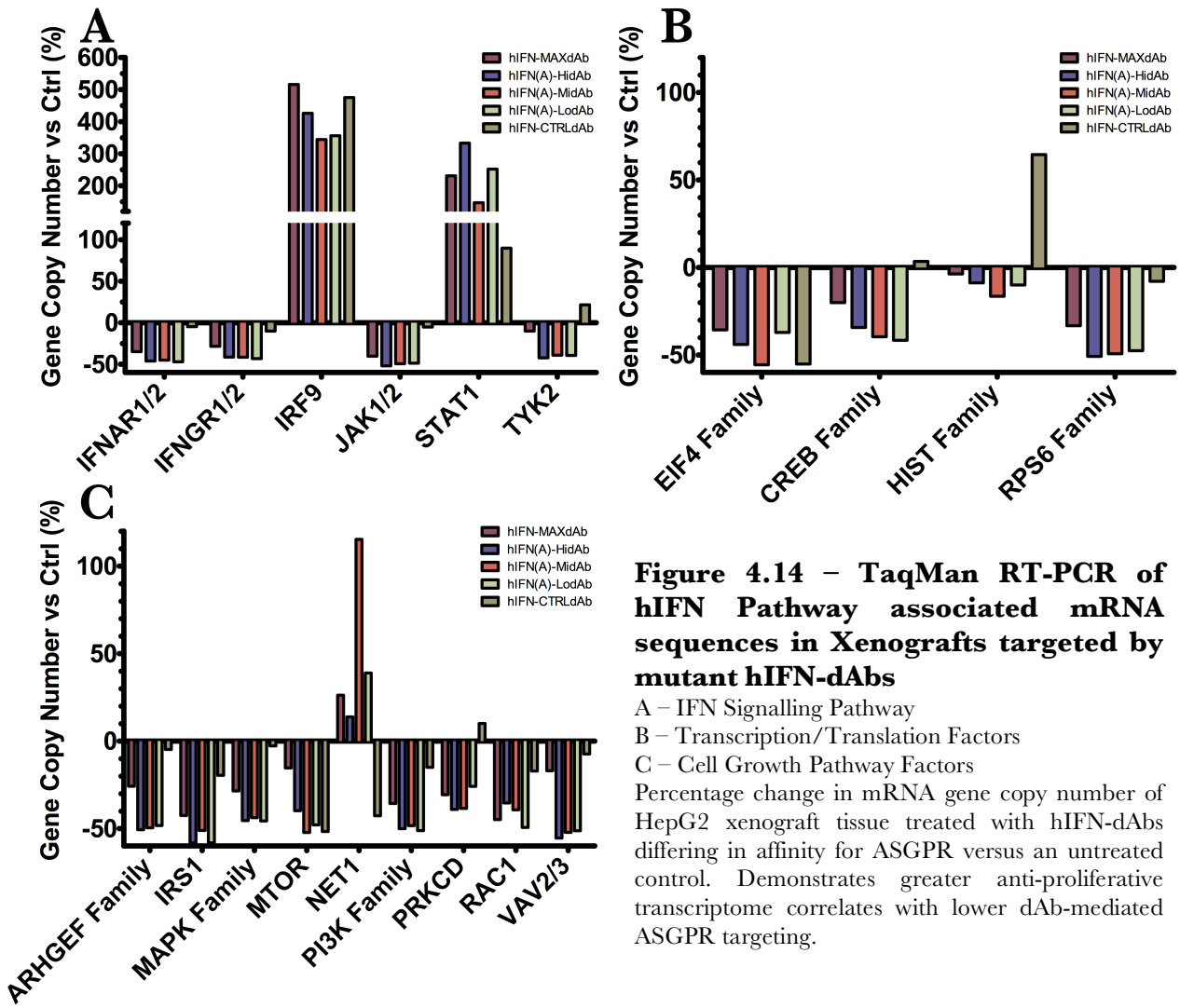

Figure 4.14 – TaqMan RT-PCR of hIFN Pathway associated mRNA sequences in Xenografts targeted by mutant hIFN-dAbs

A – IFN Signalling Pathway
B – Transcription/Translation Factors
C – Cell Growth Pathway Factors
Percentage change in mRNA gene copy number of HepG2 xenograft tissue treated with hIFN-dAbs differing in affinity for ASGPR versus an untreated control. Demonstrates greater anti-proliferative transcriptome correlates with lower dAb-mediated ASGPR targeting.

The hIFN(A)-MidAb, hIFN(C)-MidAb, and hIFN(E)-MidAb differed in their affinities for hIFNAR and also EC50 potency from low pM to high nM (Table 4.8) (hIFN(A) > hIFN(C) > hIFN(E)) and so they were analysed to elucidate the role of reduced hIFN potency on the HepG2 cellular response.

The data demonstrated that in general the mutation of the hIFN did not exclude the adoption of a modified transcriptome by the HepG2 tumour xenograft tissue (Table 4.12, Figure 4.15). This suggested that the concentration of the hIFN-MidAbs and hIFN-LodAbs in the xenografts was sufficient to overcome the deficiencies in potency.

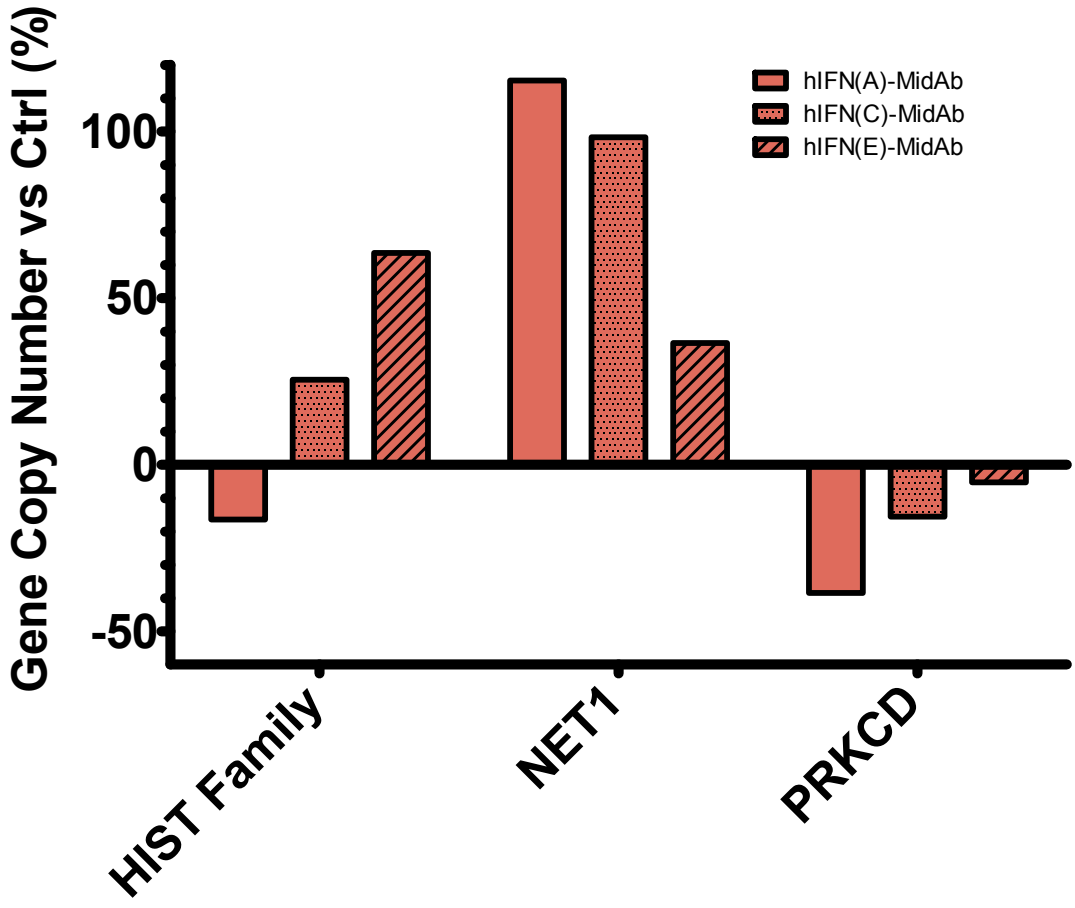

Figure 4.15 – TaqMan RT-PCR of HIST, NET1 and PRKCD mRNA sequences in Xenografts targeted by hIFN-MidAbs
Percentage change in mRNA gene copy number of HepG2 xenograft tissue treated with hIFN-MidAbs differing in affinity for hIFNAR versus an untreated control. Demonstrates greater anti-proliferative transcriptome correlates with higher hIFN potency.

However, there were some crucial differences that indicated there was a discrete effect akin to that observed for the differences between the hIFN-MAXdAb and hIFN-CTRLdAb (Section 3.5.5). Precisely, that the hIFN(C) and hIFN(E) instigated a less apoptotically-primed phenotype as was argued for hIFN-CTRLdAb. For instance, the decrease in anti-apoptotic PRKCD mRNA correlated with the increasing hIFN potencies of the hIFN-MidAbs, as did the decrease in histone mRNA and the increase in pro-cell death NET1 mRNA (Figure 4.15). Hence, this suggested that the hIFN mutants have phenotypically distinct effects on the HepG2 xenograft tissue, with a reduced potency correlating with a reduced apoptotic transcriptome.

This data set was insufficient to make statistically significant assertions as it was performed on single xenografts, but rather identified potential patterns of mRNA expression to further guide the emerging hypothesis that creating the most efficacious dAb fusion may not be a case of having the highest possible affinity for both targets. Nevertheless, several repeats would have needed to be performed before the TaqMan data could have been utilised to conclusively guide dAb fusion design.

Therefore, in conclusion, the data suggested that a reduced affinity for ASGPR compared to MAXdAb could in fact increase the efficacy of the fused hIFN to signal an anti-apoptotic phenotype in HepG2 xenograft cells. This contrasted with a decreased affinity of the hIFN for the hIFNAR appearing to correlate with a less anti-apoptotic transcriptome. Based on this data, it was concluded that hIFN(A)-MidAb was likely the optimum balance of targeting and bioactivity.

V

CONCLUSIONS & FUTURE WORK

5.1 Concluding Discussion

5.1.1 Investigation Overview

This investigation was conceived to investigate the optimum binding affinity strategy for maximising the efficacy of new dAb fusion therapies. This was a necessary line of enquiry owing to the presence of two likely competing binding affinities within the single dAb fusion protein. The hypothesis was thus:

Hypothesis
The efficacy – targeting selectivity and localised potency – of a dAb fusion protein will be significantly influenced by its two intrinsic binding affinities

The hepatic endothelium tissue selective ASGPRdAb and the potent therapeutic hIFN with its contrasting systemically distributed hIFNAR were selected to form the model dAb fusion. A panel of hIFN-ASGPRdAbs with varying engineered binding affinity combinations were to be evaluated (Table 5.1). The chosen *in vivo* model to investigate the differing pharmacology of these hIFN-ASGPRdAbs was a SCID Beige HepG2 xenograft model, facilitated by radiolabelling the dAb fusions with Ga-68 through conjugated NOTA chelator.

Table 5.1
Mutant hIFN-dAb Fusion Proteins' Relative Receptor Affinities

Fusion Protein	Relative Targeting Affinity	
	ASGPR	hIFNAR
hIFN-MAXdAb	++++	+++
hIFN(A)-HidAb	+++	+++
hIFN(C)-HidAb	+++	++
hIFN(E)-HidAb	+++	+
hIFN(A)-MidAb	++	+++
hIFN(C)-MidAb	++	++
hIFN(E)-MidAb	++	+
hIFN(A)- LodAb	+	+++
hIFN(C)-LodAb	+	++
hIFN(E)-LodAb	+	+
hIFN-CTRLdAb	-	+++

5.1.1.1 hIFN-dAb Characterisation

The *in vitro* work focussed on the production of characterised NOTA-conjugated hIFN-ASGPRdAbs for their subsequent use *in vivo*. Where necessary, the hIFN-ASGPRdAbs were genetically engineered, expressed and purified (Sections 4.2.1, 4.2.2 & 4.2.3). Their respective interactions with ASGPR and hIFNAR, and hIFN potency were analysed against isolated target receptors and on whole cells to construct an *in vitro* pharmacokinetic model of the NOTA-hIFN-ASGPRdAbs' behaviour (Figure 5.1).

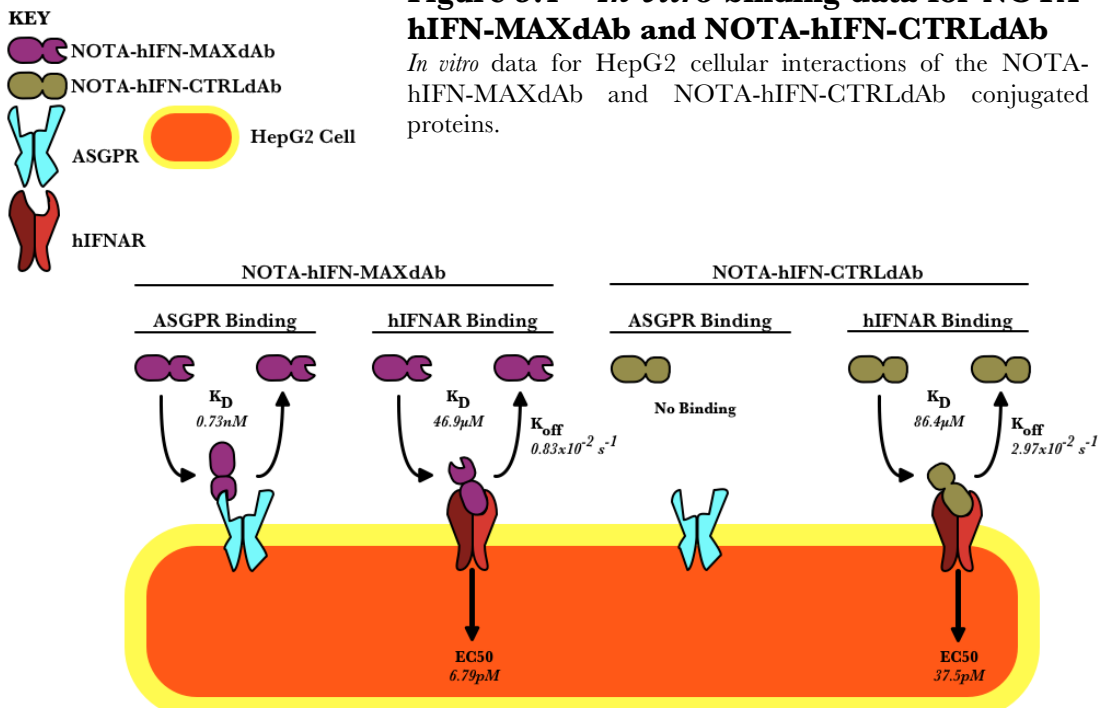

Figure 5.1 – *In vitro* binding data for NOTA-hIFN-MAXdAb and NOTA-hIFN-CTRLdAb
In vitro data for HepG2 cellular interactions of the NOTA-hIFN-MAXdAb and NOTA-hIFN-CTRLdAb conjugated proteins.

The NOTA-conjugation reaction was shown by MS analysis to yield a heterogeneous mix of species, dominated by singly conjugated species (Table 3.4), which were consistently recovered at concentrations of 52.9μM ±14.1 (Table 3.3 & Table 4.4) for subsequent radiolabelling to high specific activities with Ga-68 (Table 3.11) in the instances of hIFN-MAXdAb and hIFN-CTRLdAb. The heterogeneity may have affected the pharmacokinetics of the various species as reflected in the SPR data. However, it did not appear to affect the validity of subsequent results assuming the distribution of the different conjugate species is equal, as the radiotracer will likely still have been proportionally representative of biodistribution of the heterogeneous species (Section 5.2).

The conjugation of NOTA significantly decreased the binding of hIFN-ASGPRdAbs to ASGPR and hIFNAR (Table 3.6 and Table 3.7) including on whole cells (Table 3.9). However, in practical terms the presence of conjugated NOTA did not impact the potency of the hIFN moiety (Figure 3.10 & Figure 4.9), and the desired differences in ASGPR binding were maintained (Figure 3.13 & Figure 4.9).

The exception was a significant decrease in the potency of hIFN-CTRLdAb with NOTA conjugation of 6.87pM to 37.5pM, compared to the decrease from 2.78pM to 6.79pM for hIFN-MAXdAb, which was likely due to increased NOTA conjugation of the hIFN lysines of hIFN-CTRLdAb impacting its interaction with hIFNAR2. This also highlighted that the hIFNAR2 binding was likely driven by the k_{off} of the dAb fusion as the relative potencies (Table 3.8) were ameliorated by slower k_{off} values in spite of reduced K_D values (Table 3.7).

It was shown that HepG2 interactions were predominantly dictated by ASGPR binding *in vitro*. Comparison of MAXdAb, HidAb, MidAb, LodAb and CTRLdAb fusions' binding to whole HepG2 cells showed significant differences (Table 3.9 & Table 4.9, Figure 3.18), which were attributable to dAb-mediated ASGPR binding correlating with the binding affinity for ASGPR. The hIFNAR binding through hIFN, on the other hand, was shown to not contribute significantly to HepG2 binding (Table 4.9). This strongly indicated that HepG2 xenograft uptake *in vivo* would likely be driven by ASGPR binding.

Attaining robust and reproducible *in vitro* data for a number of the dAb fusions proved troublesome, especially in the Biacore SPR analyses. A possible explanation was an apparent concentration dependent self-association dimerisation of the dAb fusions, seemingly promoted by the MAXdAb moiety, as dAbs were known to have the potential to dimerise (Introduction 1.2.1). This was apparent from the lack of equilibrium in the SPR traces (Figure 3.5) and the high non-specific binding in spite of blocking on whole cells (Figure 3.17). Therefore, quantitative kinetic data was not as robust as would have been liked, particularly for the hIFN-ASGPRdAb mutants. This was counteracted by the comprehensive QC analytical package as a whole but unfortunately there was insufficient time for radioligand binding assays with the hIFN-ASGPRdAb mutants.

Thus, *in vitro* it was shown that the hIFN-dAbs selected for investigation had the necessary characteristics for answering the hypothesis *in vivo*.

5.1.1.2 Gallium Radiolabelling

An effective and reliable Ga-68 radiolabelling protocol was optimised from scratch. The most effective reaction conditions were found to be 1M NaAc buffering to pH4.40 in the minimum volume. Radiolabelling NOTA-hIFN-ASGPRdAbs at concentrations as low as 1μM (Table 3.11), for high specific activity radiolabelling up to 2.47MBq/μg and radiolabelling efficiencies up to 98.4%. These reaction conditions enabled specific activities sufficient for quantitative biodistribution analyses (Table 3.15) and PET imaging between one and three hours, with quantifiable measures of xenograft uptake recorded over time (Table 3.18) and quantitative images of xenograft uptake acquired (Figure 3.35).

The Ga-68 radiolabelling specific activities were high enough to attain useful radiotracer data on the biodistribution of all the hIFN-ASGPRdAbs. However, the 1.99MBq/μg for NOTA-hIFN-MAXdAb in Chapter III inhibited experimentation at concentrations below 1μg *in vivo* (Section 3.5.2). Furthermore, in Chapter IV at 1.07MBq/μg the specific activities precluded imaging the mutant hIFN-ASGPRdAbs' biodistribution by PET-CT imaging (Section 4.5.1). Further refining the NOTA conjugation reaction and in particular utilising a higher activity generator could have potentially ameliorated the specific activities by allowing lower reaction concentrations of protein.

In summary, a facile, reliable and reproducible Ga-68 radiolabelling protocol for NOTA conjugated dAb fusions was successfully optimised.

5.1.1.3 hIFN-dAb Xenograft Targeting

The *in vivo* data demonstrated that the HepG2 xenograft targeting of a hIFN-dAb fusion could be significantly increased by selective ASGPR targeting (Figure 3.26, Figure 3.35) with increased xenograft uptake correlating with increasing binding affinity for ASGPR (Figure 4.13). The improved uptake was most pronounced at 3 hours post-injection between the ASGPR targeted hIFN-MAXdAb and the non-ASGPR targeted hIFN-CTRLdAb with 2.42%ID/g ±0.69 vs. 0.68%ID/g ±0.11, respectively. It was also shown that *in vitro* targeting was driven by receptor number.

The ^{68}Ga-NOTA-hIFN-MAXdAb biodistribution analyses for dosing did not comprehensibly determine whether there was self-blocking of xenograft uptake and so a 1μg dose was selected as it provided the highest xenograft uptake in the

experiments and was readily feasible from a practical perspective. Although the *in vitro* data showed the interaction with HepG2 cells was very likely to be a specific interaction (Figure 3.17), the significant *in vivo* xenograft uptakes were analysed for their specificity. The notion that increased uptake was an artificial consequence of high blood concentration was not supported by the data (Figure 3.27), with significant differences after three hours post-injection between the xenograft and blood, with the hIFN-dAbs apparently cleared by renal filtration, liver and perhaps spleen (Figure 3.28). An attempt to block the uptake of hIFN-MAXdAb in the xenografts with an excess of MAXdAb protein proved inconclusive owing to the influence of the murine liver uptake, seemingly masking any differences in xenograft uptake.

PET-CT was demonstrated to enable temporal *in vivo* quantitation of xenograft uptake. The results showed the higher uptake of ^{68}Ga-NOTA-hIFN-MAXdAb between 1h and 3h post-injection compared to ^{68}Ga-NOTA-hIFN-CTRLdAb, and to a control tissue. There was clear potential to develop this technique into compartmental modelling with the correct model.

The primary problem with the chosen model for assessing HepG2 xenograft uptake was the significantly high murine liver uptake. The dAbs were matured for affinity towards human ASGPR and the hIFN variants based on the endogenous human protein with affinity for hIFNAR, so the extent of this uptake was unanticipated. This uptake was significantly influenced by the affinity for ASGPR, as demonstrated by hIFN-MAXdAb versus hIFN-CTRLdAb (Figure 3.28), and most conclusively by the significant decrease in uptake of hIFN-MAXdAb with excess MAXdAb blocking (Figure 3.31). However, the affinity for the hIFNAR was a more significant driver of murine liver uptake, as evidence by the over 50% increase in liver uptake between hIFN(E)-LodAb and hIFN(A)-LodAb (Figure 4.12). Therefore it was likely that cross-reactivity with both mASGPR and mIFNAR was occurring.

The liver was thus shown to act as a significant, apparently saturable sink for the hIFN-dAbs correlating with affinity for both ASGPR and hIFNAR (Figure 3.30. Foremost this will have restricted the maximum attainable xenograft uptake. Moreover, comparing, for instance, hIFN(A)-HidAb with hIFN(E)-LodAb xenograft uptake is more difficult because logically there would be more hIFN(E)-LodAb available in the system owing to decreased liver uptake and thus an increased

likelihood of HepG2 xenograft uptake purely by the virtue that there is more in the system (Figure 4.12). Indeed, once corrected for liver uptake, it transpired there was a significant difference in xenograft uptake (Figure 4.13).

Another perspective on this effect was the liver actually created a convenient proxy for off-target specific uptake. Hence, it was possible to conclude that by reducing the affinity for ASGPR and hIFNAR it was possible to increase uptake in the xenograft tissue relative to off-target uptake, which may reduce side effects whilst maintaining efficacy.

In summary, tissue targeting of hIFN-dAb fusion proteins could be mediated by ASGPRdAbs, increasing uptake in proportion to the affinity for ASGPR. This was in spite of high liver uptake driven by the hIFN. Overall the liver-targeting model itself proved ineffective for picking apart the finer intricacies of targeting with modified binding affinities.

5.1.1.4 Targeting and Efficacy

The increased ASGPRdAb-mediated uptake in HepG2 xenografts was shown to correlate with a hIFN-mediated, increasingly anti-proliferative xenograft mRNA expression profile (Figure 3.32, Figure 3.33). Lower uptake of hIFN-CTRLdAb or a reduced hIFN affinity for hIFNAR, represented by hIFN(C) and hIFN(E), led to an mRNA expression profile akin to an anti-viral response. This is congruent with the established literature detailing the differential hIFN pathway gene expression integration specific to the stimulation of the hIFNAR (Introduction 1.5.1). Thus, there was a strong indication that there could be discretely measurable cellular responses relative to the binding affinities of both the ASGPRdAb and the hIFN.

Indeed there was also a strong indication that the balance between ASGPR targeting affinity for maximum tissue uptake and hIFNAR stimulation is not straightforward. For example, in spite of a higher uptake, the hIFN-MAXdAb did not stimulate a greater increase in anti-proliferative gene transcription compare to hIFN(A)-HidAb or hIFN(A)-MidAb (Table 4.14). Therefore, it was possible to hypothesise that higher binding affinity for ASGPR in fact likely impedes its ability to interact with the hIFNAR. This could be explained by the increased binding affinity for ASGPR increasing the frequency of entering the endosomal degradation pathway rather than the likelihood of dissociation and recycling to the cell surface to interact

with hIFNAR (Introduction 1.4.4.1), or possibly allowing greater xenograft tissue percolation and thus increased hIFNAR interactions.

As the hIFN(C)-MidAb and hIFN(E)-MidAb fusion proteins are not as potent as hIFN(A)-MidAb for producing an anti-proliferative transcriptome, it appeared that in the case of hIFN engineering a reduced hIFNAR binding affinity was counterproductive. However, this need to maximise potency in the target tissue must be balanced with the need to reduce side effects in off-target tissues.

In summary, the results showed that dAb-mediated tissue uptake could increase the anti-proliferative efficacy of the attached therapeutic hIFN but that a too high a binding affinity may be self-defeating.

5.1.2 Final Thoughts

Hypothesis
The efficacy – targeting selectivity and localised potency – of a dAb fusion protein will be significantly influenced by its two intrinsic binding affinities

The data thus strongly indicated that the hypothesis could be accepted. The dAb targeting significantly increased tissue uptake, and thus also localised potency of the attached therapeutic hIFN. The binding affinity of both the dAb and the attached hIFN had a significant influence on the overall efficacy of the fusion protein. A dAb fusion therapeutic may have significant off-target uptake, but reducing the affinity for its target receptor may ameliorate this with the caveat that this may be at the expense of a more potent response in the target tissue.

The implications for future dAb fusion design are evident, with increased consideration for how two binding affinities can be best harnessed for overall efficacy. The ability to target xenograft tissue also indicates that future research could include metastatic cancers or cancer cell subtypes with distinct marker profiles.

5.2 FUTURE WORK

5.2.1 NOTA Conjugations

The NOTA reaction would have perhaps benefitted from a more controlled conjugation strategy. There remained scope for further optimisation of the conjugation reaction to promote a homogeneous singly conjugated species by for instance lowering the reaction to pH7.5 (assuming the pI is avoided) which may promote less lysine ε-amine deprotonation, whilst simultaneously increasing the likelihood of N-terminal α-amine conjugation and thus decreasing the likelihood of multiple conjugations[458]. Another approach to explore is introducing a cysteine group at the C-terminus to enable conjugation by thiol reaction, such as with maleimido-mono-amide-NOTA[470,481,482], in conjunction with necessary stability *in vivo* data[483]. This latter strategy would circumvent the problem of having differing numbers of lysine groups (14 in hIFN-MAXdAb and 11 in hIFN-CTRLdAb), which may have resulted in the decreased hIFN potency of the hIFN-CTRLdAb.

5.2.2 Ga-68 and Sc-44 Radiolabelling

The limiting factor on the specific activities achievable was the concentration of Ga-68 in the fraction utilised for reaction. A larger generator of the order 1.11GBq or higher, compared to the 370MBq utilised in this investigation, would yield higher radioactivities for reaction thus allowing higher achievable specific activities[382,484]. The difference the generator state can make on labelling was apparent from comparing the 1μM/16μg NOTA-hIFN-MAXdAb 1M NaAc Ga-68 labelling optimisation results attained with a relatively new generator (Table 3.11) with the same reactions performed for PET-CT with the same decaying generator. There was a significant ($p<0.0001$) decrease in specific activity from 2.37MBq/μg ±0.08 to 1.99MBq/μg ±0.09 respectively, in spite of a constant radiolabelling efficiency. Hence, experimentation with a larger generator would be a high priority for future work to push the specific activities to the highest possible level achievable.

In order to continue utilising PET-CT for imaging over longer time periods it would be necessary to utilise a longer lived isotope. Sc-44 has a half-life of 3.97 hours, positron emissions constituting 94.3%, a 1.47 E_{MAX} and can be conveniently eluted

from a $^{44}Ti/^{44}Sc$ generator[485]. Therefore, Sc-44 exceeds all the advantages of Ga-68 labelling, particularly with a more suitable half-life. Hence, this could enable greater experimental flexibility for longitudinal *in vivo* imaging.

5.2.3 Serum Stability

The *in vivo* state of the dAb fusions was somewhat in question during the investigation analyses. In future work the blood samples and urine should be subjected to SE-HPLC analysis[486] and iTLC[381] to quantify any breakdown of the dAb fusions and of the ^{68}Ga-NOTA complex. Also, radio-SDS-PAGE could also differentiate between any potential aggregates.

5.2.4 mRNA TaqMan Repeats

The significance of the mRNA TaqMan results was hampered by the lack of repeat data, relying heavily on the agreement of a number of analysed genes to provide legitimacy to the conclusions. Therefore, with further resources allocated to the acquisition of this data it would be straightforward to analyse the mRNA expression profiles of the remaining RNAlater cryo-frozen xenograft tissues.

5.2.4 Evidence of Anti-Proliferative Therapeutic Action

The mRNA data indicated an anti-proliferative phenotype in the xenografts, which correlated with increased xenograft uptake through dAb-mediated ASGPR targeting. Whether the increases in mRNA copy number were translated into anti-proliferative protein expression could be explored *ex vivo* by performing western blotting for proteins such a p53, OAS and PKR, in addition to those genes sampled in the TaqMan experiment. Furthermore, quantitative enzyme-linked immunosorbent assays or MALDI could be easily used to screen for numerous protein markers simultaneously.

Tumour regression analysis would add to the robustness by adding data on a tangible effect on the tumour progression through a repeat dosing regime. This could

perhaps either be by calliper measurements with survival times[149] or time course *ex vivo* size measurements[143]. There is also the possibility of FDG scans to monitor changes in xenograft metabolism[487]. Moreover, xenograft uptake could be monitored over time using PET-CT with a longer time frame beginning from t=0.

The xenograft percolation by the dAb fusions should be assessed by immunohistochemistry. The hypothesis that the increased anti-proliferative phenotype was linked to greater xenograft penetration by the reduced affinity ASGPRdAbs could be assessed. This could be achieved by staining for the dAb or hIFN component, as demonstrated in the flow cytometry experiments. This would also serve to confirm that the uptake is not just free Ga-68. It would also facilitate a greater understanding of the xenograft vascular organisation.

5.2.5 Novel dAb Fusion Tumour PET-CT Modelling & Targets

Novel targets for dAb fusions could be explored whilst improving the *in vivo* model. The full extent of PET-CT's capabilities for *in vivo* compartmental modelling could not be utilised effectively in this investigation. This was due to the low xenograft uptakes compared to the liver from the off-target murine cross-reactive liver uptake and the unquantified effect the liver had on the bioavailability of the dAb fusions for xenograft uptake. There were too many variables. Therefore, to model dAb fusions with *in vivo* PET-CT imaging, target receptors must be chosen that do not have high expression levels in the host. Moreover, MRI facilities are now available so PET-CT-MRI is now a feasible option for further exploration.

Hence, choosing a dAb target that is a high-copy number tumour marker predominantly/exclusively expressed in the xenograft tissue would perhaps provide data with less variables. For instance, targeting xenografts overexpressing HER2[488-490], melanoma xenografts expressing the tumour marker MCSP[142,491], glioblastoma xenografts over-expressing EGFR[141,225], or actively growing xenograft tissue through B-FN[143,145,492]. Such dAbs would require selection by phage-display and subsequent maturation, plus the full analytical package of assays before *in vivo* investigations using the methodology optimised in this investigation.

VI

APPENDICES

6.1 METHODS APPENDIX

6.1.1 Consumable Materials

Table 6.1
Chemical Reagents

Reagent	Manufacturer (Order Number)	Key Data	
		Formula	Mr (g/mol)
293 Freestyle Expression Medium	Gibco (12338-018)	-	-
2X YT Microbial Medium EZMix Powder	Sigma (Y2627)	-	-
Acetate 4.0	GE Healthcare (BR-1003-49)	-	-
Acetate 4.5	GE Healthcare (BR-1003-50)	-	-
Acetate 5.0	GE Healthcare (BR-1003-51)	-	-
Acetate 5.5	GE Healthcare (BR-1003-52)	-	-
Acetic Acid (TraceSelect Ultra)	Sigma Aldrich (07692)	CH_3CO_2H	60.05
Ammonia Solution 35%	Fisher Scientific (A/3280/PB15)	NH_3	17.03
Ammonium Acetate	Sigma Aldrich (A1542)	$CH_3CO_2NH_4$	77.08
Antifoam 204	Sigma Aldrich (A8311)	-	-
Bovine Serum Albumin	Sigma Aldrich (A7906)	-	66463

Cell Dissociation Buffer	Gibco (13151-014)	-	-
Chelex 100 Analytical Grade	Bio-Rad (142-2832)	-	3500
Citric Acid Monohydrate	Sigma Aldrich (C1909)	$HOC(COOH)(CH_2COOH)_2 \bullet H_2O$	210.1
Dulbecco's Modified Eagle Medium	Gibco (41966-029)	-	-
Dulbecco's Phosphate Buffered Saline without $CaCl_2$ and $MgCl_3$	Sigma Aldrich (D8537)	-	-
EDTA	Sigma Aldrich (EDS)	$C_{10}H_{16}N_2O_8$	292.2
EDTA Solution (0.1M)	NHS (BNS10506)	-	-
Ethanol 100%	VWR (20821.321)	$C_2H_6O_2$	46.07
Foetal Bovine Serum (Heat Inactivated)	Gibco (10082147)	-	-
Gallium-68	Eckert & Ziegler (3131-0902)	$^{68}GaCl_3$	176.1
Geneticin	Invitrogen (10131027)	-	-
Glycine 2.0	GE Healthcare (BR-1003-55)	-	-
Glycine 3.0	GE Healthcare (BR-1003-57)	-	-
Guanidine Hydrochloride	Sigma Aldrich (50950)	$CH_6ClN_3 \bullet HCl$	95.53

HBS-P+ Buffer 10X	GE Healthcare (BR-1006-71)	-	-
HEPES	VWR (AAA14777)	$C_8H_{18}N_2O_4S$	238.3
Hydrochloric Acid 30% (TraceSelect Ultra)	Sigma Aldrich (96208)	HCl	36.46
Imidazole	Sigma Aldrich (I2399)	$C_3H_4N_2$	68.06
Indium-111	Mallinckrodt Medical (DRN4901)	$^{111}InCl_3$	221.2
Isofluorane	Baxter International (1001936060)	$C_3H_2ClF_5O$	184.5
L-Glutamine	Sigma Aldrich (G7513)	$C_5H_{10}N_2O_3$	146.1
Methanol	Fisher (M/4056/17)	CH_3OH	32.04
Nickel Chloride	Sigma Aldrich (451193(	$NiCl_2$	129.6
NuPAGE Antioxidant	Invitrogen (NP0005)	-	-
NuPAGE LDS Sample Buffer 4X	Invitrogen (NP0007)	-	-
NuPAGE MOPS SDS Running Buffer 20X	Invitrogen (NP0001)	-	-
p-SCN-Bn-NOTA	Macrocyclics (147597-66-8)	$C_{20}H_{26}N_4O_6S•3HCl$	559.9
Phosphate Buffered Saline 1X	Agilent Technologies	-	-
Propan-2-ol	Fisher Scientific (10497070)	C_3H_8O	60.10

Propidium Iodide	Molecular Probes (P3566)	-	-
Quanti-Blue	Invivogen (rep-qb1)	-	-
Quick Coomassie Stain	Generon (GEN-QC-STAIN-1L)	-	-
Reference Standard pH10.0	Sigma Aldrich (B5020)	-	-
Reference Standard pH4.0	Sigma Aldrich (B5020)	-	-
Reference Standard pH7.0	Sigma Aldrich (B4770)	-	-
RNAlater Solution	Life Technologies (AM7020)	-	-
RPMI 1640 Medium	Gibco (A10491-01)	-	-
Sodium Acetate	Sigma Aldrich (71183)	CH_3COONa	82.03
Sodium Acetate (TraceSelect)	Sigma Aldrich (59929)	CH_3COONa	82.03
Sodium Bicarbonate	Sigma Aldrich (S6014)	$NaHCO_3$	84.01
Sodium Chloride (TraceSelect)	Sigma Aldrich (204439)	NaCl	58.44
Sodium Hydroxide	Sigma Aldrich (S8045)	NaOH	40.00
Sodium Phosphate dibasic	Sigma Aldrich (S7907)	Na_2HPO_4	142.0
Sodium Phosphate monobasic	Sigma Aldrich (S8282)	NaH_2PO_4	120.0

Trypan Blue	Bio-Rad (145-0021)	-	-
Water (TraceSelect Ultra)	Sigma Aldrich (14211-1L-F)	H_2O	18.00
Water (PCR Grade)	Sigma Aldrich (W3500)	H_2O	18.00
Water (Sterile)	Baxter (UKF7114)	H_2O	18.00

Table 6.2
Biological Reagents

Reagent	**Manufacturer (Order Number)**
Alexa Fluor 647 Goat Anti-Mouse IgG	Invitrogen (A21235)
Anti-hIFN Mouse mAb	PBL Interferon Source (21105-1)
Anti-IFNAR1 Mouse mAb	PBL Interferon Source (21375-1)
Anti-IFNAR2 Mouse mAb	PBL Interferon Source (21385-1)
Anti-rat-ASGPR Mouse mAb	Hycult Biotech (HM3020)
Anti-dAb Mouse mAb	GSK In-House (GRITS33516)
BL21(DE3) Competent E. coli	New England Biolabs (C2527)
Blasticidin	Invivogen (ant-bl-1)
DNA 100bp Ladder	New England Biolabs (N3231L)
DNA 1kb Ladder	New England Biolabs (N3232L)
HEK-Blue IFNα/β Cells	Invivogen (hkb-ifnab)
HepG2 Hepatocellular Carcinoma Epithelial Cells	ATCC (HB-8065)
hIFNAR2 Fc Chimera	R&D Systems (4015-AB-050)
IgG_1 Mouse λ Isotype Control	BD Biosciences (553452)
One Shot MAX Efficiency DH5α-T1R Competent E. coli	Invitrogen (12297-016)

Platinum Blue PCR SuperMix	Invitrogen (12580-023)
Pwo Master Mix	Roche (03789403001)
TaqMan Universal PCR Master Mix	Applied Biosystems (4304437)
U-937 Histiocytic Lymphoma Monocyte Cells	ATCC (CRL-1539.2)
WThIFN-His6	GSK (-)
Zeocin	Invivogen (ant-zn-1)

Table 6.3
Lab Consumables

Consumable	**Manufacturer (Order Number)**
0.5ml Protein Lo-Bind Tube	Eppendorf (0030108094)
0.5ml Safe-Lock Microcentrifuge Tube	Eppendorf (0030121023)
1-200µl Gel Loading Tips	Corning (CLS4853)
1-200µl Round Gel Loading Tips	Corning (4853)
1.5ml Safe-Lock Microcentrifuge Tube	Eppendorf (0030 120.086)
1000ml Rapid-Flow 0.2µm Filter Unit	Nalgene (567-0020)
10ml Stripette	Corning (4101)
15ml Tubes	Corning (430791)
2.0ml Protein Lo-Bind Tube	Eppendorf (0030108132)
2.0ml Safe-Lock Microcentrifuge Tube	Eppendorf (0030120094)
250ml Rapid-Flow 0.2µm Filter Unit	Nalgene (568-0020)
25ml Stripette	Corning (4251)
2ml Cryotube	Corning (430488)
300µl Fused Glass Insert Vial	Chromacol (03-FISV)
30ml Tube	Sterilin (128C)
500ml Centrifuge Tube	Corning (431123)

500ml Erlenmeyer Flask	Corning (430422)
500ml Rapid-Flow 0.2µm Filter Unit	Nalgene (566-0020)
50ml Disposable Vacuum Filtration System	Millipore (SCGP00525)
50ml Reagent Reservoir	Corning (4870)
50ml Tubes	Corning (430829)
5ml Stripette	Corning (4051)
96 Square Well Storage Plate	Thermo Scientific (AB-0661)
96 Well V-bottom Plate	Greiner Bio-One (651101)
96-Well Microplate Foils	GE Healthcare (28-9758-16)
96-Well Round Bottom Cell Culture Plate	Corning (3799)
96-Well V-Bottom Microtitre Plate	Sterilin (612V96)
9mm Screw Cap with PTFE pre-cut seal	Chromacol (9-SC(GY)-BST1X)
AirOtop Enhanced Ultra Yield Flask Seal	Thomson (899425)
Anti-Static Microspatula	VWR (231-0106)
Aspirating Pipettes	Corning (4486)
Centrifugal Filter Ultrafree-MC HV	Millipore (UFC30HV25)
Column Adaptor	Phenomenex (AHO-7191)
Counting Slides	Bio-Rad (145-0015)
E-Gel 0.8% Agarose	Invitrogen (G501808)
E-Gel 2% Agarose	Invitrogen (G501802)
E-Gel Double Comb 2% Agarose	Invitrogen (G601802)
E-Gel EX 2% Agarose	Invitrogen (G401002)
FEP Tubing	Sigma Aldrich (58695-U)
Flat Deck Thermo-Fast 96 Detection PCR Plate	Thermo Scientific (AB-1400)
Gas Permeable Microplate Seals	Thermo Scientific (AB-0718)
gentleMACS M Tubes	Miltenyi Biotec (130-093-236)
Glass Vials 16mm (4ml)	GE Healthcare (BR-1002-09)

HiLoad 26/60 Superdex 200 prep grade Column	GE Healthcare (17-1071-01)
Illustra NAP-5 Columns	GE Healthcare (17-0853-01)
Injekt Solo 1ml Syringe	Beckton, Dickinson & Company (?)
Injekt Solo 2ml Syringe	Beckton, Dickinson & Company (A/3280/PB15)
Injekt Solo 5ml Syringe	Beckton, Dickinson & Company (?)
Inoculation Loop	Nunc (254410)
Insulin Syringe 0.5ml with Needle	Terumo (SS05M2913)
iTLC-SG Chromatography Medium	Varian (SGI0001)
IV Safelon Catheter	BD Biosciences (391651)
Kimcare Medical Wipes	Kimberly-Clark Professional (3020)
LabXpert Perm Nylon Cloth Labels	LabXpert (X-131-499)
Maxi GeBAflex-tube 3.5kDa MWCO Dialysis Tube	Gene Bio-Application (D035)
MicroAmp Optical Adhesive Film	Applied Biosystems (4360954)
Midi GeBAflex-tube 3.5kDa MWCO Dialysis Tube	Gene Bio-Application (D010)
Millex-GS 0.22µm Syringe Filter	Millipore (SLGSV255F)
Millex-GV 0.22µm Syringe Filter	Millipore (SLGV004SL)
Minisart 0.2µm Filter	Sartorius Stedim Biotech (16534)
Myjector U-100 Insulin Syringe	Terumo (BS05M2913)
Novex Sharp Pre-Stained Protein Standard	Life Technologies (LC5800)
NuPAGE 12% Bis-Tris Gel 1.0mm x 12 well	Life Technologies (NP0342BOX)
NuPAGE 12% Bis-Tris Gel 1.0mm x 17 well	Life Technologies (NP0349BOX)
Parafilm Wrap	Pechiney Plastic Packaging (PM-992)
PCR Microplate Film	Eppendorf (0030127811)
PD MiniTrap G-25	GE Healthcare (28-9180-07)
Perm Nylon Cloth Tube Label	Brady (X-131-499)
Petri Dish	Sterilin (101VR20)
pH0.0-6.0 Strips	Sigma-Aldrich (P-4661)

pH4.5-10 Strips	Sigma-Aldrich (P-4536)
Plastic Vials 7mm (0.8ml)	GE Healthcare (BR-1002-12)
Poly-Prep Chromatography Columns	Bio-Rad (731-1550)
PP Female-Female Luer Adaptors	Cole-Parmer (EW-45500-22)
PTFE Tubing	GE Healthcare (P5360JE)
PVDF 3-way Valves	Cole-Parmer (EW-31200-80)
Rubber Caps 7mm	GE Healthcare (BR-1005-55)
Rubber Caps Type 2	GE Healthcare (BR-1004-11)
Scintillation Vial & Cap	Sterilin (505)
Sensor Chip CM5	GE Healthcare (BR-1000-12)
Sensor Chip CM5 (Series S)	GE Healthcare (BR-1005-30)
Sepharose 4 FastFlow Protein A	Amersham (17-0974-04)
Septa Caps 16mm	GE Healthcare (BR-1002-11)
Silica Gel 2.5-6.0mm 4-7	Fisher (S/0720/53)
Steriflip 0.22µm 50ml Vacuum Filtration System	Millipore (SCGP00525)
Sterile Disposable Scalpels 10	Swann-Morton (0501)
Strata-XC Cationic Exchange Columns	Phenomenex (8B-S029-TAK)
T175 Flask	Corning (431080)
T25 Flask	Corning (430639)
T75 Flask	Corning (430641)
TaqMan Array Human Interferon Pathway Fast 96-well Plate	Applied Biosystems (4418799)
Titer-Tops Microplate Seals	Diversified Biotech (T-TOPS-50)
Ultrafree MC-HV Centrifugal Filters	Millipore (UFC30HV25)
Vivaspin 20 5kDa MWCO	Sartorius Stedim Biotech (VS2012)
Vivaspin 6 5kDa MWCO	Sartorius Stedim Biotech (VS0611)
YMC-Diol-60 SE-HPLC Column	YMC (DL06505-3008WT)

Table 6.4
Reagent Kits

Consumable	Manufacturer (Order Number)
Amine Coupling Kit	GE Healthcare (BR100050)
BIA Maintenance Kit	GE Healthcare (BR-1006-66)
DC Protein Assay Kit II	Bio-Rad (500-0112)
Endo H_f	New England Biolabs (P0703L)
EndoFree Plasmid MegaPrep	Qiagen (12381)
High Capacity cDNA Reverse Transcription Kit	Applied Biosystems (4375575)
NucleoSpin Plasmid MiniPrep Kit	Macherey-Nagel (740588-250)
PNGase F	New England Biolabs (P0704S)
QIAGEN Plasmid MaxiPrep	Qiagen (12162)
QIAprep Spin MiniPrep	Qiagen (27104)
QIAquick Gel Extraction	Qiagen (28706)
QIAquick PCR Purification	Qiagen (28104)
RNeasy Maxi Total RNA Isolation Kit	Qiagen (75162)
T_4 DNA Ligase Kit	New England Biolabs (M0202L)
Zero Blunt TOPO PCR Cloning Kit, with One Shot MAX Efficiency DH5α-T1R E. coli	Invitrogen (K2820-20)

Table 6.5
Restriction Enzymes

Restriction Enzyme	Units (U/µl)	Buffer	Manufacturer
BamHI	10	SuRE/Cut B	Roche (10220612001)
DpnI	20	CutSmart	New England Biolabs (R0189L)
HindIII	10	SuRE/Cut B	Roche (10656313001)

Table 6.6
Plasmid Vectors

Plasmid Vector	Resistance	Forward Primer	Reverse Primer	Manufacturer
pCR-BLUNT	Kanamycin	M13F	M13R	Invitrogen (Paisley, UK)
pDOM50	Carbenicillin	DT039	DT045	Domantis (-)

Table 6.7
Buffer & Reagent Recipes

Buffer / Reagent	Concentration	pH	Ingredients		
			Chemical	Mass (g)	Volume (ml)
Citric Acid	0.04M	-	Citric Acid Monohydrate	0.42	-
			ddH_2O	-	50
EDTA	0.1M	-	EDTA	1.46	-
			ddH_2O	-	50
EtOH	20%	-	Ethanol 100%	-	10
			ddH_2O	-	40
HCO_3^-	0.05M *	9.2	$NaHCO_3$	3	-
			ddH_2O	-	1000
GuHCl	6M	-	CH_6ClN_3•HCl	573.2	-
			H_2O	-	~1000
HCl	0.1M	-	HCl (TS)	-	10.58
			H_2O (TS)	-	989.4
	5.5M	-	0.1M HCl (TS)		21
			HCl (TS)	-	29
HEPES	1M *	7.0	HEPES	238.3	-
			NaOH 5M	-	
			ddH_2O	-	
Imidazole	25mM	-	Imidazole	0.303	-
			PBS	-	~100
	1M	8.0	Imidazole	6.81	-
			Tris-HCl-NaCl 0.1M	-	~100
NaAc	25mM *	3.3	NaAc (TS)	0.015	-
			CH_3CO_2H (TS)	-	$708x10^{-3}$
			ddH_2O	-	~500
		6.0	NaAc (TS)	0.098	-
			CH_3CO_2H (TS)	-	$33.4x10^{-3}$
			ddH_2O	-	~500
	1M	6.0	NaAc (TS)	7.95	-
			CH_3CO_2H (TS)	-	$178x10^{-3}$
			ddH_2O	-	100
		-	NaAc (TS)	0.978	-
			ddH_2O	-	~2
NaCl	5M	1.0	NaCl (TS)	1.46	-
			HCl 0.1M (TS)	-	~5

NaOH	5M	-	NaOH ddH_2O		
$NiCl_2$	0.25M	-	$NiCl_2$ ddH_2O	3.24 -	- ~100
Tris-HCl-NaCl	0.1M	8.0	Tris NaCl HCl 1M ddH_2O	1.21 0.58 - -	- - 6.45 ~93.6

*+10g/L Chelex (0.2um filtered out)

Table 6.8
HPLC Solvent Recipe

Solvent Name	Reagent	Variables & Measurements			
		Final Concentration	pH	Mass (g)	Volume (ml)
PO_4^{3-} NaCl Buffer	Na_2HPO_4	0.2M	6.8	17.5	-
	NaH_2PO_4			9.23	-
	NaCl	0.15M		8.77	-
	H_2O	-		-	1000

*H_2O = Baxter Water

6.1.2 Method Outlines

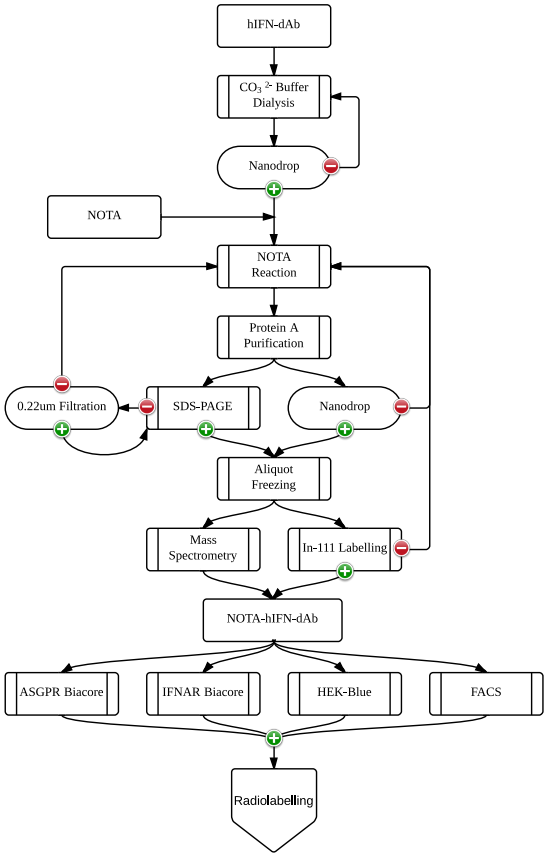

Figure 6.1 – NOTA Conjugation and Analytical *in vitro* Assays

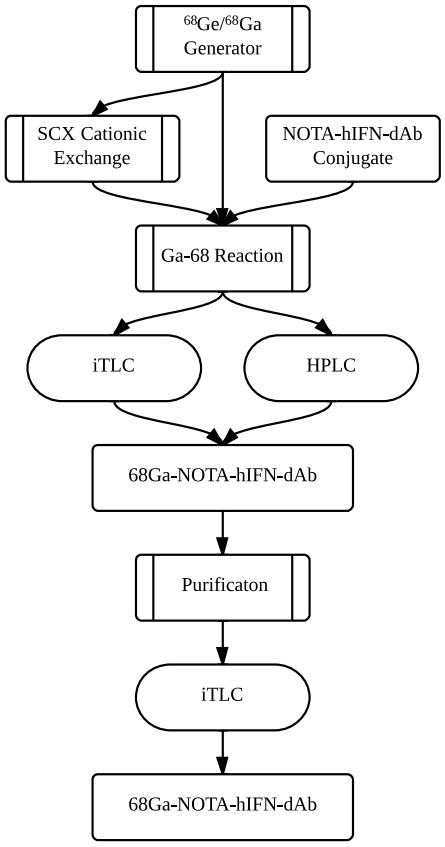

Figure 6.2 – Ga-68 Radiolabelling Reaction

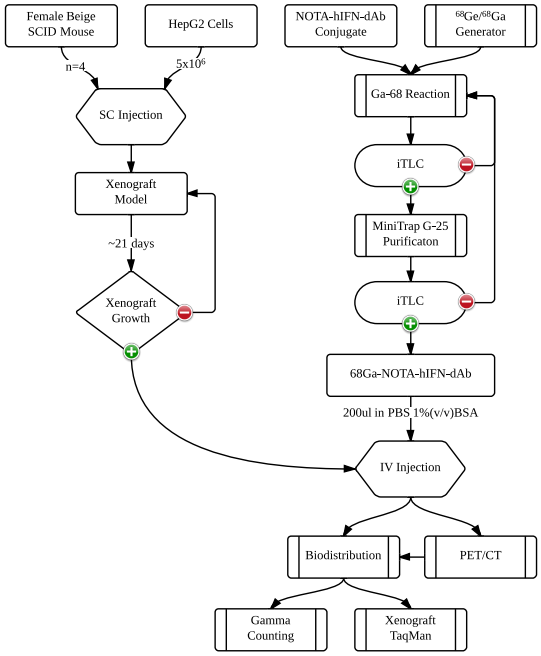

Figure 6.3 – *In vivo* Xenograft Biodistribution Modelling

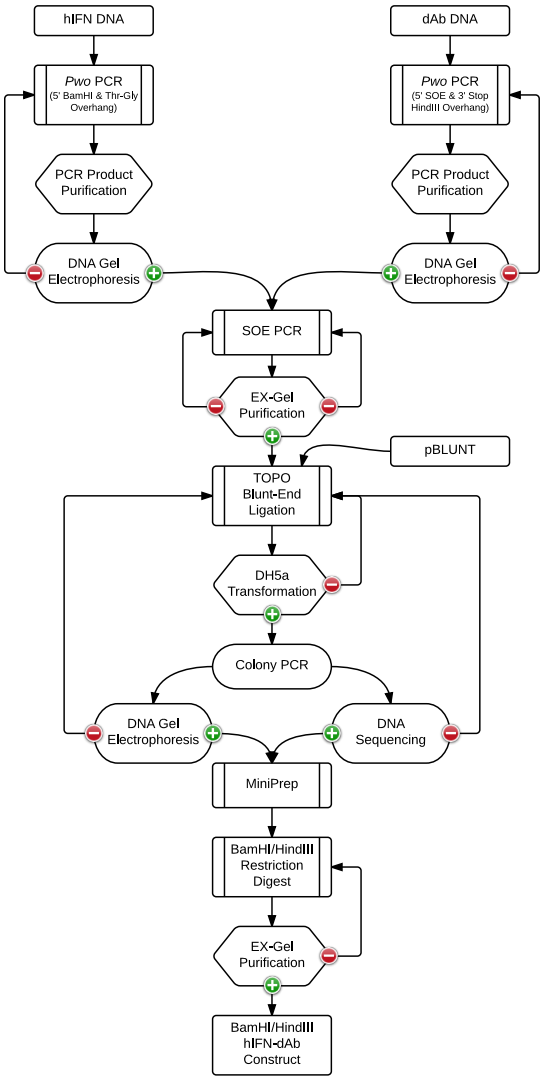

Figure 6.4 – DNA In-Line Fusions

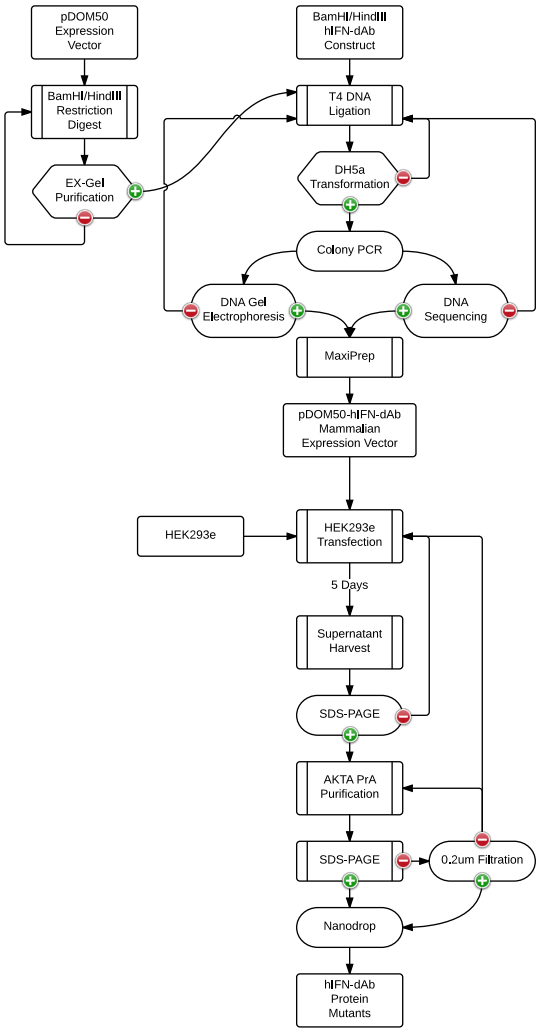

Figure 6.5 – Expression Construct and Protein Expression

6.1.3 Common Molecular Biology Methodologies

6.1.3.1 PCR Product DNA Purification

The Qiagen QIAquick PCR Purification system was utilised to purify PCR products. The samples were pipetted onto QIAquick spin columns and loaded by vacuum filtration. The column was washed with Buffer PB at 5x sample volume and 0.75ml Buffer PE, each followed by microcentrifugation at 13000rpm for 1min. An additional centrifugation at 13000rpm for 1min was performed. The purified DNA was eluted into a fresh 2ml tube by the addition of 50µl cgH2O, which was allowed to settle for 4min, followed by centrifugation at 13000rpm for 1min.

6.1.3.2 Analytical DNA Gel Electrophoresis

A 2% E-Gel Agarose Gel was inserted into an Invitrogen E-Gel iBase™ and was pre-run for the pre-programmed time. Sample aliquots of 10µl were loaded directly into the gel lanes as required. A 10µl 100bp and/or 1kb 1X DNA Ladder mix (2µl 6x DNA Ladder, 2µl 6x Loading Buffer, 8µl double deionized H_2O (ddH_2O)) was also loaded adjacent to the samples, as appropriate. Gels were run at room temperature for ~30min. Gels were imaged with a 600ms ultraviolet (UV) exposure on a Syngene Gene Genius UV imager. Images were captured using Syngene GeneSnap software.

6.1.3.3 Gel Extraction DNA Purification

A 2% SYBRSafe Agarose EX-Gel was loaded into an Invitrogen E-Gel iBase and pre-run for the pre-programmed time. DNA samples were loaded to a maximum of 20µl per well, being split over several wells as necessary. A 10µl 100bp and/or 1kb 1X DNA Ladder mix (2µl 6x DNA Ladder, 2µl 6x Loading Buffer, 8µl ddH_2O) was also loaded adjacent to the samples, as appropriate. Gels were run at room temperature for ~30min. Gels were imaged with a 600ms UV exposure on a Syngene Gene Genius UV imager. Images were captured using Syngene GeneSnap software.

The EX-Gel was loaded onto an Invitrogen Safe Imager to illuminate DNA banding for excision. A fresh clean scalpel blade was used to excise each DNA band of interest contained within the agarose, and were transferred to 2ml polypropylene tubes. The Qiagen QIAquick Gel Purification system was utilised to purify DNA

from the gel samples. Tubes were weighed to establish the volume of the extracted gel band, and QB buffer added to 3x sample volume before incubation in a 42°C waterbath for ~10min with intermittent vortex agitation to ensure all agarose was dissolved. The QB-agarose-DNA mix was loaded onto a QIA-column and microcentrifuged at 13000rpm for 1min. The column was washed by centrifugation at 13000rpm for 1min with 0.5ml Buffer QB followed by 0.75ml Buffer PE. An extra centrifugation at 13000rpm for 1min was performed to remove any remnants of buffers. DNA elution was achieved by the addition of 50µl cgH_2O, which was allowed to settle for 4min, followed by centrifugation at 13000rpm for 1min into a fresh 2ml tube.

6.1.3.4 DH5α E. coli Cell Transformation

All procedures were carried out utilising sterile technique. A 50µl vial of Invitrogen One Shot MAX Efficiency DH5α-T1R chemically Competent E. coli was thawed on ice. The E. coli were transformed by the gentle addition of 1µl of recombinant DNA plasmid sample with incubation on ice for 20min to 1hr. The vial was then immersed for 35s in a waterbath heated to precisely 42°C and immediately returned to ice for ~10min.

The transformed E. coli were revived with the addition of 250µl room temperature optimal broth with catabolite suppression (SOC) Medium, before incubation at 37°C for 1hr with horizontal shaking at 250rpm. Aliquots of this starter culture were spread onto selective 2YT Agar plates pre-warmed 37°C at varying concentrations using the 'Franz' technique to ensure single transformed DH5α colony growths. Infected plates were incubated inverted at 37°C for ~20hours or until discrete colonies could be identified.

6.1.3.5 Colony Screening *Taq* PCR

Six colonies were preselected from the agar plates based on their lack of proximity to other colonies, large relative size and shape regularity. They were partially picked using a pipette tip, which was then immersed in an individual plated PCR reaction mixture.

The 96-well plated 50µl PCR reaction mixtures consisting of one colony pick, 48µl *Taq* SuperMix, 1µl sense primer and 1µl α-sense primer underwent PCR

thermal cycling in a Bio-Rad DNA Engine Tetrad 2 Peltier Thermal Cycler as outlined in Table 6.6.

The temperature decrease between the denature step and anneal step was slowed using a cooling gradient of 2.5C/s. The PCR machine lid temperature tracked at least 5°C above sample temperature.

Table 6.9
***Taq* PCR for Colony Screening**

STEP	TEMPERATURE (°C)	TIME (min:s)	# CYCLES
Initial Denaturation	94	2:00	1
Denature	94	0:30	30
Anneal	55	0:30	
Extension	72	2:00	
Final Extension	72	10:00	1
Soak	4	∞	1

6.1.3.6 DNA Sequencing

The DNA (25ng) was made up with cgH_2O as appropriate to a volume ≥25µl/well in a Flat Deck Thermo-Fast 96 Detection PCR Plate. Plates were heat-sealed with using a Thermo Scientific ALPS 3000. Raw sequence data was acquired utilising an Applied Biosciences 3730xl DNA analyser with addition of appropriate primers, and conducted by GSK GenePortal Sequencing Service (Stevenage, UK). The raw data files were analysed using Biosoft Bioedit software.

6.1.3.7 DNA MiniPrep

All procedures were carried out utilising sterile technique. The Qiagen QIAprep MiniPrep system was utilised. A positive colony was picked from a plate to inoculate 5ml of 50µg/ml selective 2YT Broth in a 15ml tube. The tube lid was loosely reattached and the culture incubated overnight at 37°C for 16 hours with shaking at 250rpm.

The E. coli cells were harvested centrifuging the cell culture for 15min at 3600rpm 4°C, with the supernatants subsequently decanted to waste. Pellets were thoroughly resuspended in 250µl Buffer P1 and transferred to a 2ml tube. Cells were lysed by the addition of 250µl Buffer P2, with inversion mixing, until homogenously blue in colour as indicated by LyseBlue. Introduction of 350µl Buffer N3 neutralised the reaction mix with immediate inversion mixing until homogeneously colourless.

The mixes were microcentrifuged for 10min at 13000rpm to remove lysed cellular debris. The supernatants were loaded onto QIAprep spin columns and 400mbar vacuum filtrated. The columns were washed with 500µl Buffer PB, followed by 750µl Buffer PE, with microcentrifugation for 1min at 13000rpm. An extra microcentrifugation for 1min at 13000rpm was performed to remove any remnants of buffers. DNA elution was achieved by the addition of 100µl H_2O, which was allowed to settle for 4min, before microcentrifugation for 1min at 13000rpm into a fresh 2ml tube. The DNA was stored at -20°C.

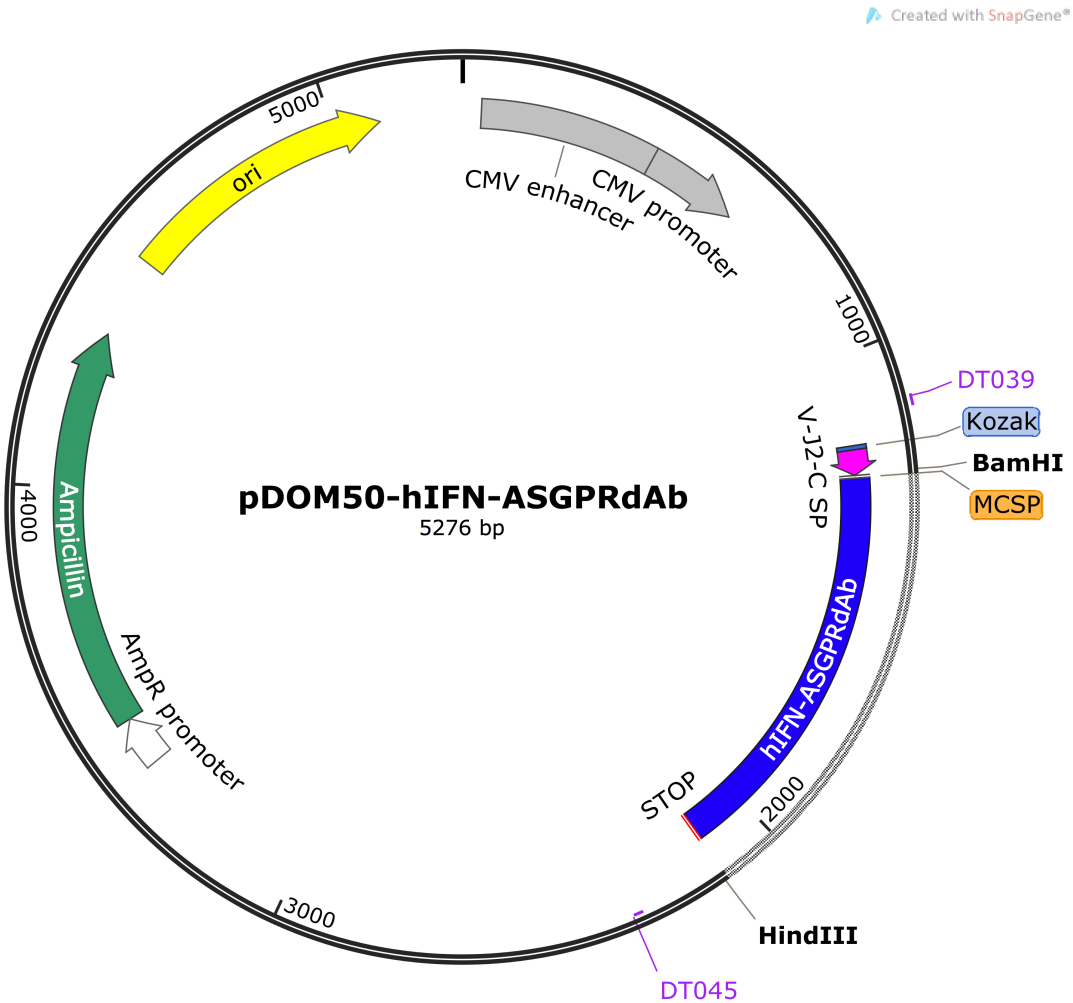

Figure 6.6 – pDOM50-hIFN-ASGPRdAb Expression Vector Construct
The hIFN-ASGPR expression unit was cloned into the pDOM50 plasmid vector as a BamHI/HindIII fragment. The vector contains an Ampicillin/Carbenicillin resistance gene for prokaryotic cell selection.

6.1.3.8 Restriction Digest

The 50µl reaction mix of 40µl DNA (~1µg), 5µl 10X Buffer, 2.5µl ddH_2O and finally 1.25µl of each relevant restriction enzyme (Appendix Table 6.5) was incubated at 37°C for 12 hours followed by incubation at 4°C.

6.1.3.9 DNA MegaPrep

All procedures were carried out utilising sterile technique. The Qiagen EndoFree MegaPrep system was utilised.

A positive colony was picked from a plate to inoculate a 15ml starter culture of 50µg/ml selective (Table 6.6) 2YT Broth in a 50ml tube. The tube lid was loosely reattached and the culture incubated at 37°C for 8hours with shaking at 250rpm. The entire starter culture was then added to 500ml of 50µg/ml selective 2YT Broth in a 2L glass baffled flask for overnight incubation with 250rpm shaking.

E. coli cells were harvested by centrifuging the culture for 30min at 3600rpm 4°C with the supernatants decanted to waste. Cells were fully resuspended by vigorous pipetting and vortex in 50ml Buffer P1 containing 100µg/ml RNase A. Addition of 50ml Buffer P2 lysed the cells by gentle swirl mixing and incubation for 5min at room temperature, until homogenously blue in colour as indicated by LyseBlue. Cell debris was precipitated by adding 50ml chilled neutralisation buffer P3 with gentle inversion mixing until homogeneously colourless.

The mixture was immediately transferred to the QIAfilter Mega-Giga cartridge attached to a 500ml Schott bottle, allowing the precipitate to accumulate at the meniscus over 10min. A 400mbar vacuum was applied to filter the lysate from the precipitate. A 50ml Buffer FWB2 aliquot was then added to the QIAfilter cartridge, and the precipitate carefully washed without dispersal with a 400mbar vacuum applied to pull through all remaining liquid. The filtered lysate was mixed with 12.5ml Buffer ER by inversion mixing, followed by 30min incubation on ice.

A QIAGEN-tip 2500 resin column was equilibrated with 35ml Buffer QBT by gravity flow. The chilled filtered lysate was applied to the column by gravity flow. The QIAGEN-tip was subsequently washed with 200ml Buffer QC by gravity flow. The previous three steps' eluates were discarded. Plasmid DNA was eluted from the column with 30ml buffer QN into a sterile 50ml tube.

The DNA was precipitated through the addition of 21ml Propan-2-ol, gently mixed, and immediately centrifuged for 1 hour at 3600rpm 4°C. The supernatant was decanted without disturbing the pellet. The pellet was washed with endotoxin-free 70% ethanol and centrifuged again for 20min at 3600rpm 4°C. The supernatant was carefully decanted without disturbing the pellet. The pellet was now allowed to air dry with excess accumulations of ethanol being swabbed away with a Kimcare tissue wrapped around forceps, with great care taken not to touch the pelleted DNA.

The DNA was redissolved in 1ml buffer TE, and transferred to a fresh 2ml eppendorf.

The eluted DNA was resolved by DNA Gel Electrophoresis (Appendix 6.1.3.1), the concentration measured via a 1:100 TE dilution sample by UV spectrophotometry at 260nm and DNA sequencing performed. The DNA was stored at -20°C.

6.1.3.10 SDS-PAGE

Proteins were resolved by SDS-PAGE analysis, performed utilising the Invitrogen NuPAGE SDS-PAGE System. The set up was optimised for proteins between 30kDa-36kDa, as described.

A Pre-Cast NuPAGE 12% Bis-Tris Gel was loaded into an XCell SureLock Mini-Cell containing 1X MOPS Running Buffer. If protein samples were reduced, 200µl NuPAGE antioxidant was added into the cathode chamber.

A 9µl aliquot of sample protein (normally 2µg) was mixed with 3µl 4x LDS Sample Buffer in a 96-Well plate. The plate was sealed with a PCR Microplate Film, the plate gently vortexed and centrifuged for 1min at 1000rpm. The plate was loaded into a Bio-Rad DNA Engine Tetrad 2 Peltier Thermal Cycler and heated to 70°C for 10min. The plate was again centrifuged for 1min at 1000rpm. A 10µl sample was loaded into a gel well using gel loading tips. A 10µl Novex Sharp Pre-Stained molecular weight marker aliquot was loaded adjacent to samples.

Gels were run at 160V for 58min at room temperature or until the dye front reached the base of the gel. Post electrophoresis the gel was rinsed in ddH_2O and the wells trimmed. The gel was stained in Generon Quick Coomassie Stain for 1hr at room temperature with 70rpm rocking. The gel was washed twice with ddH_2O at 2 hour intervals with 70rpm rocking. Gels were imaged with the Licor Odyssey Imager at 700nm with 64dpi high quality settings and analysed with Image Studio software.

6.1.3.11 Protein Ethanol Flash Freezing

Purified proteins were aliquoted into 0.5ml Lo-Bind tubes. An ethanol bath was prepared by placing dry ice in a vat of 100% ethanol. The protein tubes were arranged in a rack, and then immersed in the chilled ethanol. The tubes were then immediately placed in -20°C storage.

6.1.3.12 Biacore Chip Coating

A Biacore CM5 chip was primed with degassed HBS-P+ buffer until a stable baseline sensogram was attained. The receptor ligand was diluted 1:200 in GE Healthcare Biacore Acetate immobilisation buffers pH4.0, pH4.5, pH5.0 and pH5.5. The pH Scouting application wizard was run, with a rack arranged as prescribed with ligand samples, 1M Ethanolamine-HCl surface regeneration, and 2min ligand-surface contact time. The buffer pH conducive to maximum stable RU gain was chosen.

The Biacore CM5 chip was primed with degassed HBS-P+ buffer until a stable baseline sensogram was attained. The receptor ligand was diluted 1:200 in the optimum pH Acetate buffer. The Surface Preparation Immobilisation application wizard was run, with a rack arranged as prescribed with ligand samples, NHS/EDC surface activation and 1M Ethanolamine-HCl. Flow cell (FC) 1 was assigned as a blank reference cell, and the receptor ligands assigned as appropriate to FC2-4. The target RUs was set at 500* and the flow at 50µl/min. A final RU ±20% was accepted and the surface tested with 100nM analyte with Glycine 3.0 regeneration.

6.1.3.13 Biacore 3000 Program Method

```
! MICROPLATE FULL RUN by ALEX PAPPLE
! Timestamp:     08-may-13 10:00
! Software:      BIACORE 3000 Control Software
! Version:       3.2
! Configuration: IFC6
! ----

DEFINE LOOP cycle

    LPARAM  %sample   %position     %volume

BLANK_HBS-P+            R2H12 30
DMS6305_0.98nM          R2G9  30
DMS6305_1.95nM          R2G8  30
DMS6305_3.91nM          R2G7  30
DMS6305_7.81nM          R2G6  30
DMS6305_15.63nM   R2G5  30
DMS6305_31.25nM   R2G4  30
DMS6305_62.5nM          R2G3  30
DMS6305_125.0nM   R2G2  30
DMS6305_250.0nM   R2G1  30
BLANK_HBS-P+            RR6   30
BLANK_HBS-P+            R2B1  30
END

DEFINE APROG analyse
    PARAM %sample   %position %volume
```

* Optimum binding kinetic data generally achieved with minimal coated RUs

```
    KEYWORD sample %sample
    CAPTION sample %sample
    FLOW 30
    RPOINT baseline

  * KINJECT %position   %volume  300
    QUICKINJECT RR2   5
END

MAIN
  RACK 1 MICRO
  RACK 2 MICRO
  RACK R Reag_A

  DETECTION 2-1,3-1,4-1

  LOOP cycle STEP
    APROG analyse %sample %position   %volume

  ENDLOOP
  APPEND Standby
END
```

6.1.4 Mammalian Cell Culture

6.1.4.1 Cell Sub-Culturing

For adherent cells HEK-Blue and HepG2 (Table 6.10) the following protocol was followed:

The necessity for passaging was determined by light microscopy. If the cell monolayer was <70% confluent, the media would be replaced with an equal volume of fresh media (Table 6.10 & Table 6.11). If the cell monolayer was ≥70% confluent, the cells would be passaged.

Cell culture medium and dissociation buffer were pre-heated to 37°C. Fresh T175 flasks were filled with culture medium for a final volume of 28ml. Antibiotic pressure was added as appropriate (Table 6.10).

The old media was aspirated followed by a 10ml sterile PBS monolayer wash at room temperature. A 5ml dissociation medium aliquot was added to detach cells in combination with incubation in a humidified incubator at 37°C 5%-CO_2 for 10min. An additional 10ml of cell culture medium was added to the flask and the cells completely resuspended by gentle pipetting shear force and washing of the T175 cell culture surface. A fraction of the cell resuspension was used to inoculate the fresh T175 flasks to complete the passage. Excess cells were aspirated to waste. Cells were cultured in a humidified incubator at 37°C 5%-CO_2.

For the suspended cell line U937 the following protocol was followed:

The necessity for passaging was determined by light microscopy. If the cell density was <70% confluent, the media would not be changed. If the cell density was ≥70% confluent, the cells would be passaged. Cell culture medium and dissociation buffer were pre-heated to 37°C. Fresh T175 flasks were filled with culture medium for a final volume of 30ml. The old cell-containing media was pipetted into a 50ml tube. The cell suspension was centrifuged at 1250rpm 4°C for 5min. The supernatant was aspirated and the cell pellet resuspended in 20ml fresh culture medium. 1ml was used to inoculate the T175 flasks to complete the passage. Cells were cultured in a humidified incubator at 37°C 5%-CO_2.

Table 6.10
Sub-culturing Cell Lines

Cell Line	Culture	Dissociation Medium	Passage Dilution	Selection Pressure
HEK-Blue	Adherent	Culture Medium	1/15	Blasticidin (30µg/ml) Zeocin (100µg/ml)
HepG2	Adherent	Cell Dissociation Buffer	1/6	-
U937	Suspension	-	1/20	-

6.1.4.2 Defrosting Cell Lines for Culture

The culture medium was pre-heated to 37°C in a waterbath. The cell cryotube was removed from liquid nitrogen vapour storage into dry ice. A 10ml aliquot of culture medium was pipetted to a 15ml tube.

The cell cryotubes was rapidly thawed by immersion in 37°C water and the thawed contents immediately pipetted to a 15ml tube containing 10ml media. The tube was centrifuged at 1250rpm 4°C for 5min. The supernatant was aspirated to waste. The cell pellet was resuspended in 5ml culture medium. The resuspension was transferred to T25 flask and incubated in a humidified incubator at 37°C 5%-CO_2.

Cells were passaged as appropriate to respective cell line via a T75 flask, before proceeding with T175 full-scale culture.

Table 6.11
Culture Medium Recipes

Cell Line	Reagents	Volume (ml)
HEK-Blue	DMEM	500
	HI-FBS	50
	L-Glutamine*	5
HepG2	DMEM	500
	HI-FBS	50
U937	RPMI-1640	500
	HI-FBS	50

*Final concentration = 2mM

6.1.4.3 Liquid Nitrogen Cryopreservation

The cell sub-culturing protocol was followed to attain pelleted cells. Cells were resuspended in 15ml of cell culture medium supplemented with 5% (v/v) DMSO and immediately aliquoted in 1.5ml fractions into 2ml cryotubes and placed into dry ice. Cryotubes were stored at -80°C for one week before transferring to liquid nitrogen vapour phase storage.

6.1.4.4 Trypan Blue Live/Dead Cell Counting

The total live cell count was determined by very gently shake mixing 20µl of cell suspension with 20µl of 0.4% Trypan Blue solution, pipetting into the chamber of a TC10 Counting Slide (n=2), and read with a Bio-Rad TC10 Automated Cell Counter. The output values of total cell count and viability were used to compute the total live cell count.

6.1.5 Alternative Radiolabelling Strategies

All the following strategies' radiolabelling efficiencies were quantitated by 0.02M CA-EDTA iTLC and WEA-iTLC, in addition to SE-HPLC (Method 2.3.2 & Appendix 6.1.8).

6.1.5.1 5M NaOH ^{68}Ga-NOTA-hIFN- dAb Labelling

The generator was eluted with 0.1M HCl at a rate of 1ml/min. A 500µl fraction covering the top of the elution peak was collected in a 2ml tube followed by the addition of 8.2µl 5M NaOH and vigorous shaking. A 25µl aliquot of NOTA conjugated protein was pipetted into a 2ml polypropylene tube and a 225µl aliquot of

the pH-adjusted $^{68}GaCl_3$ was carefully pipetted from the high activity fraction followed by gentle swirling to ensure homogeneity and the total activity measured. The reaction was incubated at room temperature for 10min. The reaction was quenched by addition of 13.16µl 0.1M EDTA.

6.1.5.2 5M NaAc ^{68}Ga-NOTA-hIFN-dAb Labelling

The generator was eluted with 0.1M HCl at a rate of 1ml/min. A 500µl fraction covering the top of the elution peak was collected in a 2ml tube containing 17.5µl of 5M NaAc pH5.5, and mixed vigorously. An aliquot of NOTA conjugated protein relative to the final desired reaction concentration in a total reaction volume of 250µl was pipetted into a 2ml polypropylene tube and made up to 25µl using ddH_2O. A 225µl aliquot of the pH-adjusted $^{68}GaCl_3$ was carefully pipetted from the high activity fraction followed by gentle swirling to ensure homogeneity and the total activity measured. The reaction was incubated at room temperature for 10min. The reaction was quenched by addition of 13.16µl 0.1M EDTA.

6.1.6 Bond-Elut SCX Cationic Exchange ^{68}Ga-NOTA-hIFN-dAb Labelling

This method was adapted from the work of Schultz et al[493,494]. All buffers were formulated with TraceSelect reagents.

An Agilent Technologies Bond Elut SCX 100mg 1ml Cationic Exchange Column* was equilibrated with 1ml of 5.5M HCl, followed by washing with 10ml ddH_2O and liquid expulsion with air. The pre-equilibrated column was affixed to the generator outflow by a column-luer adaptor.

A 5ml aliquot of 0.1M HCl was injected into the generator at 2ml/min, and thus through the attached SCX column. Remaining 0.1M HCl in the column was expelled with air and the waste checked for Ga-68 breakthrough. The SCX column was eluted by the injection of 5M NaCl 0.1M HCl pH1.0 buffer totalling 0.5ml. The elution was collected as drop-wise fractions in 0.5ml polypropylene tubes.

* Columns were adapted for this system set-up by cutting off the shaft of the cartridge above the matrix using a clean scalpel

Elution fractions 2 and 3 were combined, and 40µl pipetted into a 0.5ml Lo-Bind tube. This was followed by 25µl of 1M NaAc buffer, pipetted slowly with gentle swirling to ensure homogeneity. NOTA conjugated protein for 2µM in a total reaction volume of 60µl with remaining volume capacity made up with 0.14M NaAc pH4.5. The reaction mix was given a gentle shake and the total activity measured. The reaction was incubated at room temperature for 10min. A control reaction with a relevant volume of 0.14M pH4.5 NaAc replacing the protein was run in parallel.

A PBS equilibrated PD MiniTrap G-25 column was subsequently used to purify labelled product from radiochemical impurities and NaCl into PBS (Method 2.3.2). Labelling was quantified by CA-EDTA and WEA iTLC plus SE-HPLC (Method 2.3.3 & Appendix 6.1.8)

6.1.7 Radiolabelled NOTA-hIFN-dAb Purification

6.1.7.1 0.22µm Filtration Purification

The entire radiolabelling reaction was passed through a Millipore Millex 0.22µm syringe filter using a 1ml syringe and positive pressure, the eluate was collected in a 2ml tube.

6.1.7.2 Protein A Spin Purification

0.1ml of Protein A Sepharose 4 FastFlow was bedded on a Millipore Ultrafree Centrifugal Filter and equilibrated with 15CV 25mM pH6 NaAc with centrifugation at 12000rpm for 1min.

The radiolabelling reaction was loaded onto the column before microcentrifugation at 12000rpm for 1min. The eluate was reloaded twice more with centrifugation at 12000rpm for 1min. The column was washed with 15CV 25mM pH6 NaAc with centrifugation at 12000rpm for 1min. The column was eluted with fractions of 1CV 25mM pH3.3 NaAc into 0.02CV 1M pH6 NaAc in a 2.0ml polypropylene tube. The fractions were measured for radioactive recovery.

6.1.7.3 Illustra NAP-5 Column Purification

A clamped GE Healthcare illustra NAP-5 column was equilibrated with 10ml PBS without Ca^{2+}/Mg^{2+} by gravity flow. The whole radiolabelling reaction was loaded onto the column by gravity flow. The purified radiolabelled product was eluted in a 0.7ml PBS primary fraction by gravity flow.

6.1.8 Radioactive SE-HPLC

A Beckman Coulter System Gold HPLC machine's liquid lines and pumps were purged of air and YMC-Diol-60 SE-HPLC column equilibrated with phosphate elution buffer (Table 6.8). The UV detector and GABI Raytest activity monitor were calibrated to the local conditions. A constant elution rate of 0.5ml/min was maintained and a 20µl sample injected onto a 200µl loop. The UV elution spectrums at $A_{260,}$ and 280nm, and the gamma radiation signal were recorded for 30min using Beckman Coulter 32 Karat analysis software.

6.1.9 Additional Methodologies

6.1.9.1 SDM of hIFN-ASGPRdAbs to Mutate NGS Glycosylation Site to NGA

Three of the nine hIFN-ASGPRdAb mutants underwent SDM: hIFN(A)-HidAb, hIFN(C)-MidAb and hIFN(E)-LodAb.

The 50µl PCR reaction mixture of 1µl (~25ng) the pCR-BLUNT-hIFN-ASGPRdAb, 1µl (0.25µM) sense primer GCGATTGGCCGCAACGGGGCGC-AGACATACTACGCAGACTCC, 1µl (0.25µM) anti-sense primer GGAGTCTGCGTAGTATGTCTGCGCCCCGTTGCGGCCAATCGC, 25µl Roche *Pwo* MasterMix, 22µl cgH_2O underwent PCR thermal cycling in a Bio-Rad DNA Engine Tetrad 2 Peltier Thermal Cycler as outlined in Table 6.6.

Table 6.12
SDM *Pwo* PCR to mutate NGS Glycosylation to NGA

Step	Temperature (°C)	Time (min:s)	# Cycles
Initial Denaturation	94	2:00	1
Denature	94	0:30	30
Anneal*	55	1:00	
Extension	68	5:00	
Final Extension	68	15:00	1
Soak	4	∞	1

The temperature decrease between the denature step and anneal step was slowed using a cooling gradient of 2.5°C/s. The PCR machine lid temperature tracked at least 5°C above sample temperature. The amplified DNA (~2µg) was then

subjected to DPNI (25U) restriction digest in CutSmart buffer (Appendix 6.1.3.8). The cut plasmids were EX-Gel purified (Appendix 6.1.3.3).

The encoded SDM mutants were then expressed and purified following the exact same process as Methods 2.1.1.3 and 2.1.3. The result was proteins hIFN(A)-HidAb(SDM), hIFN(C)-MidAb(SDM) and hIFN(E)-LodAb(SDM).

6.1.9.2 PNGase F Deglycosylation Assay

All reagents were defrosted prior to beginning the assay aliquoting. The assay was performed in two stages (Table 6.13). The denaturation stage consisted of 2µg glycoprotein, 1µl 10X Glycoprotein Dithiothreitol (DTT) Denaturing Buffer with cgH_2O added to a final volume of 10µl. Following the denaturation step, 2µl 10X G7 Reaction Buffer, 2µl NP40, 1µl PNGase F and 5µl cgH_2O were added to the relevant samples. The incubations were performed in a Bio-Rad DNA Engine Tetrad 2 Peltier Thermal Cycler.

Table 6.13
PNGase F Deglycosylation

Step	Temperature (°C)	Time (hours:min)	# Cycles
Denaturation	95	00:10	1
Incubation	4	∞	1
ADD PNGase F Stage Reagents			
PNGase F	37	12:00	1
Incubation	4	∞	1

Controls, each totalling 20µl, included 'glycoprotein only', 'denaturing step only', and 'PNGase F only' (no glycoprotein). Assays were analysed by SDS-PAGE (Appendix 6.1.3.10) including 200µl NuPAGE antioxidant buffer in the cathode chamber.

6.1.9.3 ASGPR-H1-CRD Expression and Purification

A recombinant ASGPR-H1-CRD, the binding target of the ASGPRdAbs, was expressed by HEK293e mammalian cellular expression of the pDOM50-ASGPR-H1-CRD vector* (in the same manner as Method 2.1.2), except purified by Nickel-Sepharose immobilised metal ion affinity chromatography (IMAC) into

* Kindly provided by Dr Thil Batuwangala, GSK.

several fractions, polished by ÄKTA chromatography and concentrated by 5kDa MWCO spin concentrated.

Washed Nickel Sepharose High Performance HisTrap HP resin was resuspended in 50ml ddH_2O and added to a 2L Duran Bottle along with the 250ml harvested ASGPR-H1CRD expression supernatant and 1L of ddH_2O. The mixture was incubated for ~16hrs overnight on a roller in a cold room at 4°C.

The Nickel Sepharose was allowed to settle for ~1hr to the bottom of the bottle at 4°C, and the supernatant was carefully removed by pipette. The Nickel Sepharose was resuspended in ~10CV of 25mM Imidazole- PBS and bed in a 25ml Bio-Rad Poly-Prep Chromatography Column. The Nickel Sepharose was further washed with 20CV 25mM Imidazole-PBS.

The column was eluted in a total of 5 1CV fractions using increasing concentrations of Imidazole in 100mM Tris-HCl-NaCl (50mM, 100mM, 250mM, 500mM & 1M). A sample of each fraction was then analysed by SDS-PAGE for the presence of the purified protein. A 50µl sample was removed at each stage of the purification process from all waste flows for analysis on SDS-PAGE (Appendix6.1.3.10) to monitor potential protein loss.

All fractions containing ASGPR-H1-CRD were pooled into a VivaSpin-20 5kDa MWCO protein concentrator spin filter and centrifuged at 4600rpm 4°C until <1ml remained. The concentrated protein dialysed with a GeBAflex-Midi 800µl 3.5kDa-MWCO Dialysis Tube into PBS for 3hrs at room temperature, with three buffer changes.

All lines and pumps of an ÄKTA Purifier were purged with 6M GuHCl followed by EtOH 20% by executing the SamlplePumpPurify protocol. The pooled partially purified ASGPR-H1-CRD sample was injected into a Superloop. The method parameters, as assigned in UNICORN software, included a continuous 0.05M pH5 NaAc 0.15M NaCl buffer flow rate of 2.5ml/min with a 2CV>x<4CV column equilibration followed by 9.8ml Superloop load, and 2ml fraction collection in a 96-well Deep-Well plate with a serpentine elution pattern. The plate was sealed and stored at 4°C.

SDS-PAGE was performed on those wells containing protein eluate as indicated by UV the elution trace to qualify the amount of protein present and purity (Appendix 6.1.3.10). All fractions with a high concentration of ASGP-H1-CRD were pooled and 0.22µm filtered. The concentration was determined by UV

spectrophotometry at 280nm and purity by SDS-PAGE. Samples were aliquoted and stored at -20°C.

6.3 Results Appendix

6.3.1 Analytical QC Data

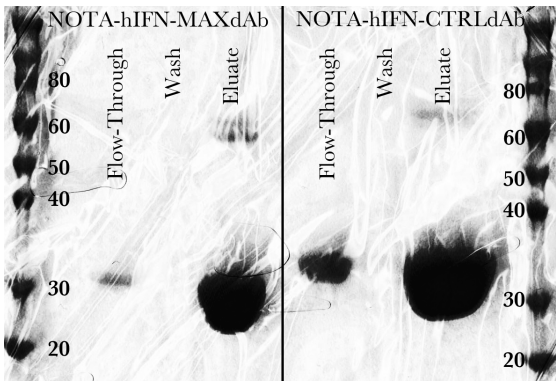

Figure 6.7 – Non-Reducing SDS-PAGE of Protein A Batch Purification steps
SDS-PAGE of samples (1µl) from each step of the purification of NOTA-hIFN-MAXdAb and NOTA-hIFN-CTRLdAb by the Protein A batch method, including the Novex Sharp Pre-stained Protein Standard. Result demonstrates the efficiency of protein recovery by the Protein A batch method as shown by the concentrated recovery in the final eluate and the minimal losses in the flow-through from the load step and the lack of detectable loss during the wash steps.

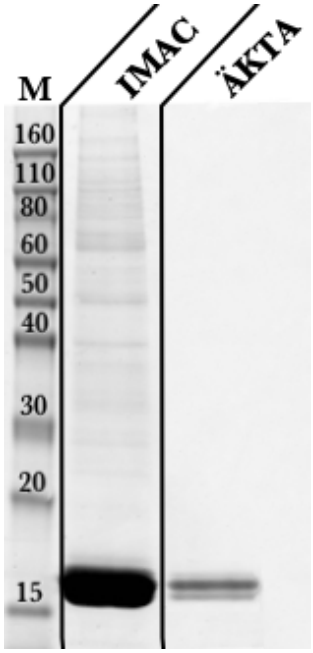

Figure 6.8 – Non-Reducing SDS-PAGE of IMAC purified and ÄKTA polished ASGPR-H1-CRD
Ni_2-Sepharose IMAC co-purification of ASGPR-H1-CRD (raw eluate) with multiple high molecular weight species, followed by ÄKTA purification resulting in two ASGPR-H1-CRD species (8.34µM, 1.3µg loaded). The purity of the final product was confirmed by SDS-PAGE (Figure 3.4) as a mix of two species at approximately the predicted mass of 17.2kDa. The two species were attributed to glycosylation as a similar banding pattern had been previously attributed to differing post-translational modifications. ASGPR is known to be glycosylated *in vivo* and so multiple glycosylation states with a mammalian expression system was not an unexpected result. As the conditions were non-reducing there was also a possibility they were two different stable structural isoforms with their respective differing migration or cleavage product
M = Novex® Sharp Pre-stained Protein Standard.

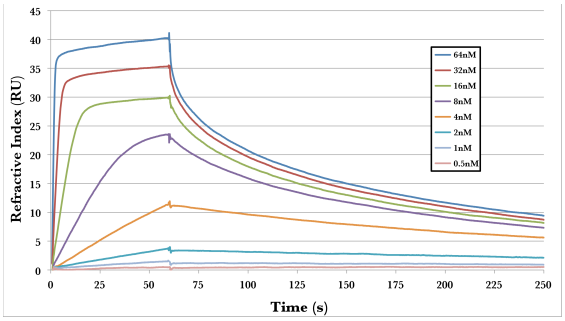

Figure 6.9 – Biacore T200 SPR Analysis of hIFN-MAXdAb
Biacore T200 SPR with ASGPR-H1-CRD immobilised on a CM5 chip assessed the ASGPR-H1-CRD binding kinetics of a 64-0.5nM 1:2 serial dilution of hIFN-MAXdAb injected over the chip surface at 30µlmin^{-1}.

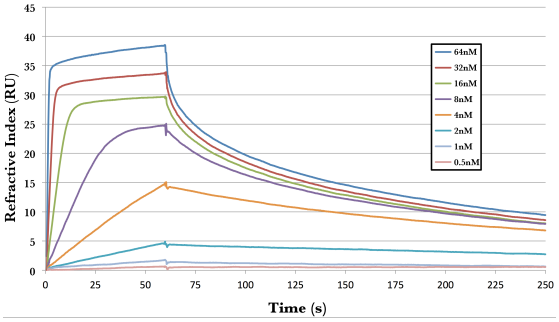

Figure 6.10 – Biacore T200 SPR Analysis of MAXdAb
Biacore T200 SPR with ASGPR-H1-CRD immobilised on a CM5 chip assessed the ASGPR-H1-CRD binding kinetics of a 64-0.5nM 1:2 serial dilution of MAXdAb injected over the chip surface at 30µlmin^{-1}.

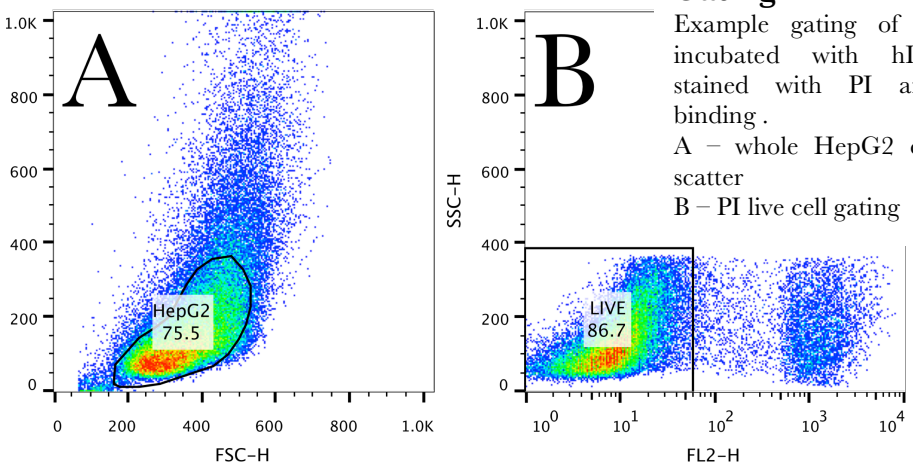

Figure 6.11 – Flow Cytometry HepG2 Cell Gating
Example gating of HepG2 cells incubated with hIFN-MAXdAb stained with PI and Alexa647 binding .
A – whole HepG2 cell gating by scatter
B – PI live cell gating

6.3.2 Gallium Labelling Data

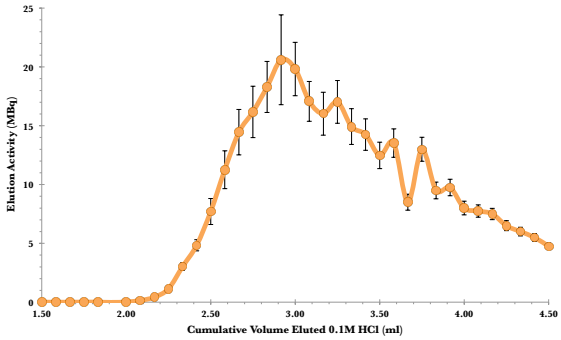

Figure 6.12 – EZ IG100 $^{68}Ge/^{68}Ga$ Generator Elution Profile
Elution profile of generator set-up measured in ~0.1ml fractions (exact volume determined by mass in weighed tubes) up to ~4.5ml. Profile shows, in this instance, a 0.5ml eluate fraction between ~2.7ml and ~3.2ml ought to be collected for maximum activity. n≥3

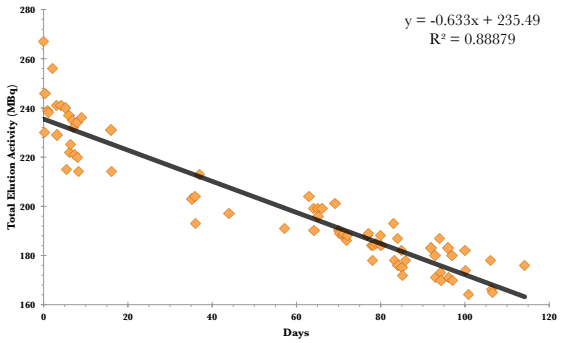

Figure 6.13 – EZ IG100 $^{68}Ge/^{68}Ga$ Generator Decay Monitoring
Total activity eluted in full 10ml elutions over time, as monitored for 115 days up to three times daily. Demonstrates temporally variable yield, which is decreasing with an apparent half life of the Ge-68 core of 161 days compared to the Ge-68 half-life of 271 days.

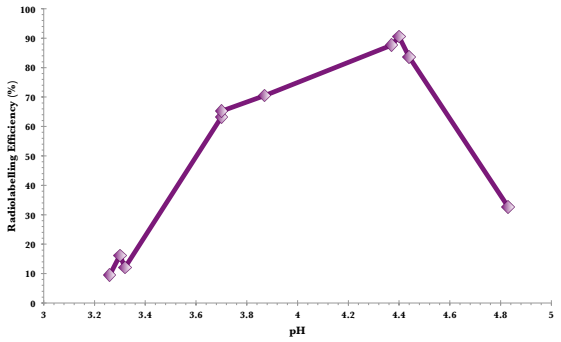

Figure 6.14 – Optimum pH Scouting for NOTA-hIFN-MAXdAb Ga-68 Radiolabelling
NaOH 5M Ga-68 radiolabelling reactions for NOTA-hIFN-MAXdAb with varying pH (monitored with a calibrated pH meter) at a final concentration of 4μM and at room temperature. The results indicated that pH4.4 provided the optimal radiolabelling pH.

Figure 6.15 – AM-iTLC Example
AM-iTLC of ^{68}Ga-NOTA-hIFN(A)-HidAb pre-EDTA quench for examining NOTA contamination from inefficient Protein A purification. Result demonstrates no substantial NOTA break-through into purified eluate, which would appear approximately two-thirds up the strip.

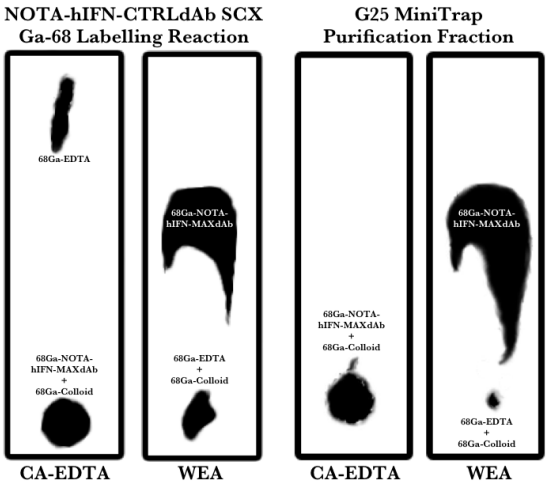

Figure 6.16 – G-25 MiniTrap Purification of a SCX Cationic Exchange Ga-68 NOTA-hIFN-CTRLdAb Radiolabelling Reaction

Phosphorimaging of typical 0.02M CA-EDTA and WEA (2%BSA(w/v)) iTLCs of a ^{68}Ga-NOTA-hIFN-MAXdAb radiolabelling reaction utilising the SCX Cationic Exchange method and the primary fraction from the subsequent G-25 MiniTrap purification. The observed results show the effective Ga-68 radiolabelling utilising the cationic exchange concentrated Ga-68 and effective removal of radiochemical impurities by purification.

6.3.3 Site Directed Mutagenesis Data

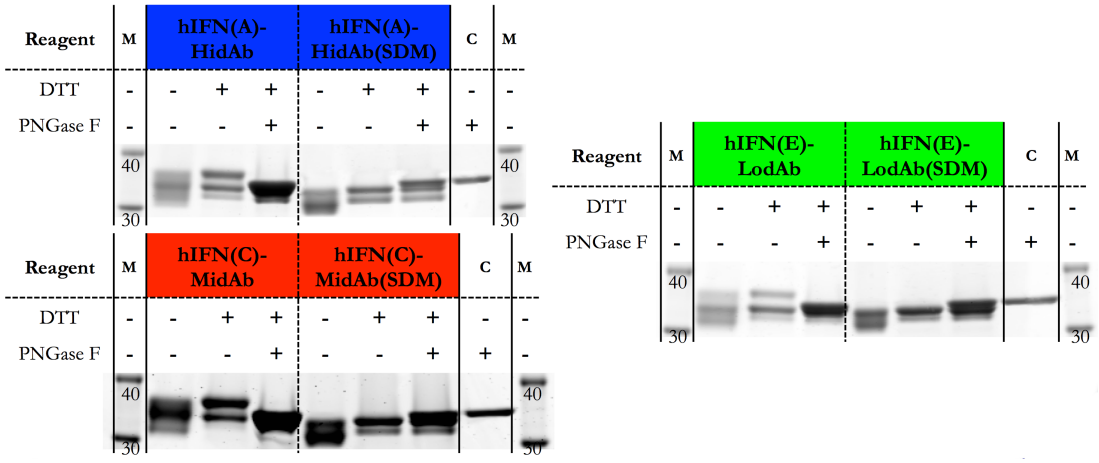

Figure 6.17 – SDS-PAGE of PNGaseF Assay with Mutant hIFN-ASGPRdAbs including SDM Mutants lacking N-linked Glycosylation

SDS-PAGE of hIFN-ASGPRdAb mutants – hIFN(A)-HidAb, hIFN(C)-MidAb and hIFN(E)-LodAb – and their respective SDM mutant variants lacking N-linked glycosylation – hIFN(A)-HidAb(SDM), hIFN(C)-MidAb(SDM) and hIFN(E)-LodAb(SDM) – having undergone PNGaseF deglycosylation, including DTT-only control and untreated controls alongside the PNGaseF protein control (36kDa) and Novex Sharp Pre-stained Protein Standard. The reduced hIFN-ASGPRdAbs show a tri-banding pattern migrating between ~32-38kDa, whereas the SDM mutants have a clear dual banding pattern migrating ~32-34kDa. Through the action of PNGaseF, the heaviest band of the hIFN-ASGPRdAb samples is lost and the banding now matches that of the SDM mutants, upon which PNGaseF appears to have no effect. The results overall demonstrate that one of the glycosylation species is N-linked glycosylation because the species represented by the heaviest migrating band is lost through the action of PNGaseF or SDM.

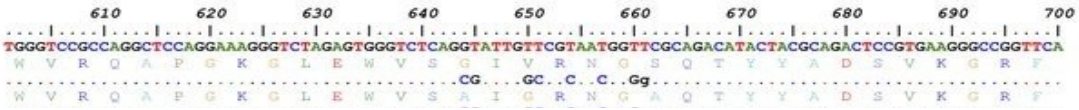

Figure 6.18 – Sequencing of NGS to NGA SDM Mutant

GC rich SDM primer has introduced single T>G mutation in the DNA sequence of the SDM mutant thus mutating the serine residue to an alanine residue in the final protein sequence, removing the N-linked glycosylation site.

VII

REFERENCES

1. Ward ES, Güssow D, Griffiths AD, Jones PT, Winter G. Binding activities of a repertoire of single immunoglobulin variable domains secreted from Escherichia coli. *Nature.* 1989;341(6242):544-546.
2. Fujimori K, Vovell D, Fletcher J, Weinstein J. Modeling analysis of the global and microscopic distribution of immunoglobulin-G, F(ab')2, and Fab in tumors. *Cancer Research.* 1989;49(20):5656-5663.
3. Adams G, Schier R, Marshall K, et al. Increased affinity leads to improved selective tumor delivery of single-chain Fv antibodies. *Cancer Research.* 1998;58(3):485-490.
4. Adams GP, Schier R, McCall AM, et al. High affinity restricts the localization and tumor penetration of single-chain Fv antibody molecules. *Cancer Research.* 2001;61(12):4750-4755.
5. Sulkowski M, Zeuzem S, Lawitz E, et al. Efficacy and safety of albinterferon alfa-2b in combination with ribavirin in treatment naive patients with chronic hepatitis C genotype 1. *Hepatology.* 2009;50(4):333A-333A.
6. Yang X, Zhang X, Fu ML, et al. Targeting the tumor microenvironment with interferon-β bridges innate and adaptive immune responses. *Cancer Cell.* 2014;25(1):37-48.
7. Schmidt SR. *Fusion protein technologies for biopharmaceuticals : applications and challenges.* Hoboken, New Jersey: Wiley; 2013.
8. Franklin EC. Structure and function of immunoglobulins. *Acta Endocrinol Suppl (Copenh).* 1975;194:77-95.
9. Bargou R, Leo E, Zugmaier G, et al. Tumor regression in cancer patients by very low doses of a T cell-engaging antibody. *Science.* 2008;321(5891):974-977.
10. Kortt A, Guthrie R, Hinds M, et al. Solution properties of Escherichia-coli - expressed VH domain of anti-neuraminidase antibody NC41. *Journal of Protein Chemistry.* 1995;14(3):167-178.
11. Ewert S, Huber T, Honegger A, Pluckthun A. Biophysical properties of human antibody variable domains. *Journal of Molecular Biology.* 2003;325(3):531-553.
12. Jespers L, Schon O, James L, Veprintsev D, Winter G. Crystal structure of HEL4, a soluble, refoldable Human V-H single domain with a germ-line scaffold. *J Mol Biol.* 2004;337(4):893-903.
13. Greenberg A, Avila D, Hughes M, Hughes A, Mckinney E, Flajnik M. A new antigen receptor gene family that undergoes rearrangement and extensive somatic diversification in sharks. *Nature.* 1995;374(6518):168-173.
14. Hamers-Casterman C, Atarhouch T, Muyldermans S, et al. Naturally occurring antibodies devoid of light chains. *Nature.* 1993;363(6428):446-448.
15. Davies J, Riechmann L. 'Camelising' human antibody fragments: NMR studies on VH domains. *FEBS Lett.* 1994;339(3):285-290.
16. Muyldermans S, Atarhouch T, Saldanha J, Barbosa JA, Hamers R. Sequence and structure of VH domain from naturally occurring camel heavy chain immunoglobulins lacking light chains. *Protein Eng.* 1994;7(9):1129-1135.
17. Nguyen VK, Desmyter A, Muyldermans S. Functional heavy-chain antibodies in Camelidae. *Adv Immunol.* 2001;79:261-296.
18. Ewert S, Cambillau C, Conrath K, Plückthun A. Biophysical properties of camelid V(HH) domains compared to those of human V(H)3 domains. *Biochemistry.* 2002;41(11):3628-3636.
19. van der Linden R, Frenken L, de Geus B, et al. Comparison of physical chemical properties of llama V-HH antibody fragments and mouse monoclonal antibodies. *Biochimica et Biophysica ACTA-protein structure and molecular enzymology.* 1999;1431(1):37-46.
20. Dumoulin M, Conrath K, Van Meirhaeghe A, et al. Single-domain antibody fragments with high conformational stability. *Protein Science.* 2002;11(3):500-515.
21. Holt LJ, Herring C, Jespers LS, Woolven BP, Tomlinson IM. Domain antibodies: proteins for therapy. *Trends Biotechnol.* 2003;21(11):484-490.
22. Davies J, Riechmann L. Antibody VH domains as small recognition units. *Biotechnology.* 1995;13(5):475-479.
23. Tanha J, Xu P, Chen Z, et al. Optimal design features of camelized human single-domain antibody libraries. *Journal of Biological Chemistry.* 2001;276(27):24774-24780.
24. Jespers L, Schon O, Famm K, Winter G. Aggregation-resistant domain antibodies selected on phage by heat denaturation. *Nat Biotechnol.* 2004;22(9):1161-1165.

25. Barthelemy PA, Raab H, Appleton BA, et al. Comprehensive analysis of the factors contributing to the stability and solubility of autonomous human VH domains. *J Biol Chem.* 2008;283(6):3639-3654.
26. Tanha J, Dubuc G, Hirama T, Narang S, MacKenzie C. Selection by phage display of llama conventional V-H fragments with heavy chain antibody VHH properties. *Journal of Immunological Methods.* 2002;263(1-2):97-109.
27. Perchiacca JM, Ladiwala ARA, Bhattacharya M, Tessier PM. Aggregation-resistant domain antibodies engineered with charged mutations near the edges of the complementarity-determining regions. *Protein Engineering Design & Selection.* 2012;25(10):591-601.
28. Dudgeon K, Famm K, Christ D. Sequence determinants of protein aggregation in human VH domains. *PEDS.* 2009;22(3):217-220.
29. Reiter Y, Schuck P, Boyd L, Plaksin D. An antibody single-domain phage display library of a native heavy chain variable region: Isolation of functional single-domain VH molecules with a unique interface. *J Mol Biol.* 1999;290(3):685-698.
30. Dudgeon K, Rouet R, Kokmeijer I, et al. General strategy for the generation of human antibody variable domains with increased aggregation resistance. *Proc Natl Acad Sci U S A.* 2012;109(27):10879-10884.
31. Perchiacca JM, Lee CC, Tessier PM. Optimal charged mutations in the complementarity-determining regions that prevent domain antibody aggregation are dependent on the antibody scaffold. *Protein Engineering Design & Selection.* 2014;27(2):29-39.
32. Hoogenboom HR, Winter G. By-passing immunisation. Human antibodies from synthetic repertoires of germline VH gene segments rearranged in vitro. *J Mol Biol.* 1992;227(2):381-388.
33. Tomlinson IM, Walter G, Marks JD, Llewelyn MB, Winter G. The repertoire of human germline VH sequences reveals about fifty groups of VH segments with different hypervariable loops. *J Mol Biol.* 1992;227(3):776-798.
34. Scott JK, Smith GP. Searching for peptide ligands with an epitope library. *Science.* 1990;249(4967):386-390.
35. Smith GP. Filamentous fusion phage: novel expression vectors that display cloned antigens on the virion surface. *Science.* 1985;228(4705):1315-1317.
36. Winter G, Griffiths AD, Hawkins RE, Hoogenboom HR. Making antibodies by phage display technology. *Annu Rev Immunol.* 1994;12:433-455.
37. Marks JD, Hoogenboom HR, Griffiths AD, Winter G. Molecular evolution of proteins on filamentous phage. Mimicking the strategy of the immune system. *J Biol Chem.* 1992;267(23):16007-16010.
38. Winter G. Synthetic human antibodies and a strategy for protein engineering. *FEBS Lett.* 1998;430(1-2):92-94.
39. McCafferty J, Griffiths AD, Winter G, Chiswell DJ. Phage antibodies: filamentous phage displaying antibody variable domains. *Nature.* 1990;348(6301):552-554.
40. Hoogenboom HR. Selecting and screening recombinant antibody libraries. *Nat Biotechnol.* 2005;23(9):1105-1116.
41. Hoogenboom HR, Chames P. Natural and designer binding sites made by phage display technology. *Immunol Today.* 2000;21(8):371-378.
42. Sidhu SS. *Phage display in biotechnology and drug discovery.* Boca Raton: CRC Press/Taylor & Francis; 2005.
43. Rodi DJ, Soares AS, Makowski L. Quantitative assessment of peptide sequence diversity in M13 combinatorial peptide phage display libraries. *J Mol Biol.* 2002;322(5):1039-1052.
44. Kay BK, Adey NB, He YS, Manfredi JP, Mataragnon AH, Fowlkes DM. An M13 phage library displaying random 38-amino-acid peptides as a source of novel sequences with affinity to selected targets. *Gene.* 1993;128(1):59-65.
45. Baker M. Protein engineering: navigating between chance and reason. *Nat Methods.* 2011;8(8):623-626.
46. Jacob J, Kelsoe G, Rajewsky K, Weiss U. Intraclonal generation of antibody mutants in germinal centres. *Nature.* 1991;354(6352):389-392.
47. Nobel-Foundation T. 2012. Accessed 10/03/2012, 2012.
48. Köhler G, Milstein C. Continuous cultures of fused cells secreting antibody of predefined specificity. *Nature.* 1975;256(5517):495-497.
49. Köhler G, Milstein C. Derivation of specific antibody-producing tissue culture and tumor lines by cell fusion. *Eur J Immunol.* 1976;6(7):511-519.

50. Shulman M, Wilde CD, Köhler G. A better cell line for making hybridomas secreting specific antibodies. *Nature.* 1978;276(5685):269-270.
51. Riechmann L, Clark M, Waldmann H, Winter G. Reshaping human antibodies for therapy. *Nature.* 1988;332(6162):323-327.
52. Morrison S, Johnson M, Herzenberg L, Oi V. Chimeric human-antibody molecules - mouse antigen-binding domains with human constant region domains. *PNAS.* 1984;81(21):6851-6855.
53. Jones P, Dear P, Foote J, Neuberger M, Winter G. Replacing the complementarity-determining regions in a human-antibody with those from a mouse. *Nature.* 1986;321(6069):522-525.
54. Anderson P. Tumor necrosis factor inhibitors: Clinical implications of their different immunogenicity profiles. *Seminars in Arthritis and Rheumatism.* 2005;34(5):19-22.
55. Ghetie V, Ward ES. Transcytosis and catabolism of antibody. *Immunol Res.* 2002;25(2):97-113.
56. Leibson P. Signal transduction during natural killer cell activation: Inside the mind of a killer. *Immunity.* 1997;6(6):655-661.
57. Duncan AR, Winter G. The binding site for C1q on IgG. *Nature.* 1988;332(6166):738-740.
58. Tutuncu Z, Kavanaugh A, Zvaifler N, Corr M, Deutsch R, Boyle D. Fc gamma receptor type IIIA polymorphisms influence treatment outcomes in patients with inflammatory arthritis treated with tumor necrosis factor alpha-blocking agents. *Arthritis and Rheumatism.* 2005;52(9):2693-2696.
59. Arora T, Padaki R, Liu L, et al. Differences in binding and effector functions between classes of TNF antagonists. *Cytokine.* 2009;45(2):124-131.
60. Abuchowski A, McCoy J, Palczuk N, Vanes T, Davis F. Effect of covalent attachment of polyethylene-glycol on immunogenicity and circulating life of bovine liver catalase. *Journal of Biological Chemistry.* 1977;252(11):3582-3586.
61. Glue P, Fang JW, Rouzier-Panis R, et al. Pegylated interferon-alpha2b: pharmacokinetics, pharmacodynamics, safety, and preliminary efficacy data. Hepatitis C Intervention Therapy Group. *Clinical Pharmacology & Therapeutics.* 2000;68(5):556-567.
62. Manns MP, McHutchison JG, Gordon SC, et al. Peginterferon alfa-2b plus ribavirin compared with interferon alfa-2b plus ribavirin for initial treatment of chronic hepatitis C: a randomised trial. *Lancet.* 2001;358(9286):958-965.
63. Bruno S, Stroffolini T, Colombo M, et al. Sustained virological response to interferon-alpha is associated with improved outcome in HCV-related cirrhosis: a retrospective study. *Hepatology.* 2007;45(3):579-587.
64. Fee C, Van Alstine J. PEG-proteins: Reaction engineering and separation issues. *Chemical Engineering Science.* 2006;61(3):924-939.
65. Peters TJ, Peters T, Jr. *All about albumin: Biochemistry, genetics, and medical applications.* 1996.
66. Chaudhury C, Mehnaz S, Robinson J, et al. The major histocompatibility complex-related Fc receptor for IgG (FcRn) binds albumin and prolongs its lifespan. *Journal of Experimental Medicine.* 2003;197(3):315-322.
67. Walker A, Dunlevy G, Rycroft D, et al. Anti-serum albumin domain antibodies in the development of highly potent, efficacious and long-acting interferon. *Protein Engineering Design & Selection.* 2010;23(4):271-278.
68. Osborn BL, Olsen HS, Nardelli B, et al. Pharmacokinetic and pharmacodynamic studies of a human serum albumin-interferon-alpha fusion protein in cynomolgus monkeys. *J Pharmacol Exp Ther.* 2002;303(2):540-548.
69. Rustgi VK. Albinterferon alfa-2b, a novel fusion protein of human albumin and human interferon alfa-2b, for chronic hepatitis C. *Curr Med Res Opin.* 2009;25(4):991-1002.
70. Kanda T, Imazeki F, Yokosuka O. New antiviral therapies for chronic hepatitis C. *Hepatol Int.* 2010;4(3):548-561.
71. Arend W, Malyak M, Guthridge C, Gabay C. Interleukin-1 receptor antagonist: Role in biology. *Annual Review of Immunology.* 1998;16:27-55.
72. Holt LJ, Basran A, Jones K, et al. Anti-serum albumin domain antibodies for extending the half-lives of short lived drugs. *Protein Eng Des Sel.* 2008;21(5):283-288.
73. Dunlevy G, Holmes S, Hong Z, Sepp A, Walker A, Domantis Ltd. Liver targeting molecules. U.S. Patent Application US20130078216 A1. 2011/01/13.
74. Coulstock E, Sosabowski J, Ovecka M, et al. Liver-Targeting of Interferon-Alpha with Tissue-Specific Domain Antibodies. *PLoS ONE.* 2013;8(2).

75. Maloney DG, Grillo-López AJ, White CA, et al. IDEC-C2B8 (Rituximab) anti-CD20 monoclonal antibody therapy in patients with relapsed low-grade non-Hodgkin's lymphoma. *Blood.* 1997;90(6):2188-2195.
76. Reff ME, Carner K, Chambers KS, et al. Depletion of B cells in vivo by a chimeric mouse human monoclonal antibody to CD20. *Blood.* 1994;83(2):435-445.
77. Johnson P, Glennie M. The mechanisms of action of rituximab in the elimination of tumor cells. *Semin Oncol.* 2003;30(1 Suppl 2):3-8.
78. Holbro T, Civenni G, Hynes NE. The ErbB receptors and their role in cancer progression. *Exp Cell Res.* 2003;284(1):99-110.
79. Slamon DJ, Godolphin W, Jones LA, et al. Studies of the HER-2/neu proto-oncogene in human breast and ovarian cancer. *Science.* 1989;244(4905):707-712.
80. Vogel C, Cobleigh MA, Tripathy D, et al. First-line, single-agent Herceptin(R) (trastuzumab) in metastatic breast cancer. a preliminary report. *Eur J Cancer.* 2001;37 Suppl 1:25-29.
81. Eiermann W. Trastuzumab combined with chemotherapy for the treatment of HER2-positive metastatic breast cancer: pivotal trial data. *Ann Oncol.* 2001;12 Suppl 1:S57-62.
82. Sliwkowski MX, Lofgren JA, Lewis GD, Hotaling TE, Fendly BM, Fox JA. Nonclinical studies addressing the mechanism of action of trastuzumab (Herceptin). *Semin Oncol.* 1999;26(4 Suppl 12):60-70.
83. Drebin JA, Link VC, Stern DF, Weinberg RA, Greene MI. Down-modulation of an oncogene protein product and reversion of the transformed phenotype by monoclonal antibodies. *Cell.* 1985;41(3):697-706.
84. Hale G, Bright S, Chumbley G, et al. Removal of T-cells from bone-marrow for transplantation - a monoclonal anti-lymphocyte antibody that fixes human-complement. *Blood.* 1983;62(4):873-882.
85. Hersh CM, Cohen JA. Alemtuzumab for the treatment of relapsing-remitting multiple sclerosis. *Immunotherapy.* 2014;6(3):249-259.
86. Goldstein N, Prewett M, Zuklys K, Rockwell P, Mendelsohn J. Biological efficacy of a chimeric antibody to the epidermal growth factor receptor in a human tumor xenograft model. *Clinical Cancer Research.* 1995;1(11):1311-1318.
87. Yang X, Jia X, Corvalan J, Wang P, Davis C. Development of ABX-EGF, a fully human anti-EGF receptor monoclonal antibody, for cancer therapy. *Critical Reviews in Oncology Hematology.* 2001;38(1):17-23.
88. Price TJ, Peeters M, Kim TW, et al. Panitumumab versus cetuximab in patients with chemotherapy-refractory wild-type KRAS exon 2 metastatic colorectal cancer (ASPECCT): a randomised, multicentre, open-label, non-inferiority phase 3 study. *Lancet Oncology.* 2014;15(6):569-579.
89. Amado RG, Wolf M, Peeters M, et al. Wild-type KRAS is required for panitumumab efficacy in patients with metastatic colorectal cancer. *Journal of Clinical Oncology.* 2008;26(10):1626-1634.
90. Messersmith WA, Ahnen DJ. Targeting EGFR in colorectal cancer. *New England Journal of Medicine.* 2008;359(17):1834-1836.
91. Kurahashi Y, Sugahara M, Ago H, et al. Crystallization and preliminary diffraction studies of prostaglandin E-2-specific monoclonal antibody Fab fragment in the ligand complex. *Acta Crystallographica.* 2008;64:1027-1030.
92. Lindhofer H, Mocikat R, Steipe B, Thierfelder S. Preferential species-restricted heavy/light chain pairing in rat/mouse quadromas. Implications for a single-step purification of bispecific antibodies. *J Immunol.* 1995;155(1):219-225.
93. Ruf P, Gires O, Jäger M, Fellinger K, Atz J, Lindhofer H. Characterisation of the new EpCAM-specific antibody HO-3: implications for trifunctional antibody immunotherapy of cancer. *Br J Cancer.* 2007;97(3):315-321.
94. Litvinov SV, Velders MP, Bakker HA, Fleuren GJ, Warnaar SO. Ep-CAM: a human epithelial antigen is a homophilic cell-cell adhesion molecule. *J Cell Biol.* 1994;125(2):437-446.
95. Münz M, Kieu C, Mack B, Schmitt B, Zeidler R, Gires O. The carcinoma-associated antigen EpCAM upregulates c-myc and induces cell proliferation. *Oncogene.* 2004;23(34):5748-5758.
96. Perez P, Hoffman RW, Shaw S, Bluestone JA, Segal DM. Specific targeting of cytotoxic T cells by anti-T3 linked to anti-target cell antibody. *Nature.* 1985;316(6026):354-356.

97. Mack M, Riethmüller G, Kufer P. A small bispecific antibody construct expressed as a functional single-chain molecule with high tumor cell cytotoxicity. *Proc Natl Acad Sci U S A.* 1995;92(15):7021-7025.
98. Skerra A, Plückthun A. Assembly of a functional immunoglobulin Fv fragment in Escherichia coli. *Science.* 1988;240(4855):1038-1041.
99. Huston JS, Levinson D, Mudgett-Hunter M, et al. Protein engineering of antibody binding sites: recovery of specific activity in an anti-digoxin single-chain Fv analogue produced in Escherichia coli. *Proc Natl Acad Sci U S A.* 1988;85(16):5879-5883.
100. Yu CM, Peng HP, Chen IC, et al. Rationalization and Design of the Complementarity Determining Region Sequences in an Antibody-Antigen Recognition Interface. *PLoS ONE.* 2012;7(3).
101. Zardi L, Carnemolla B, Siri A, et al. Transformed human-cells produce a new fibronectin isoform by preferential alternative splicing of a previously unobserved exon. *EMBO Journal.* 1987;6(8):2337-2342.
102. Castellani P, Viale G, Dorcaratto A, et al. The fibronectin isoform containing the ED-B oncofetal domain - a marker of angiogenesis. *International Journal Of Cancer.* 1994;59(5):612-618.
103. Neri D, Carnemolla B, Nissim A, et al. Targeting by affinity-matured recombinant antibody fragments of an angiogenesis associated fibronectin isoform. *Nature Biotechnology.* 1997;15(12):1271-1275.
104. Adams G, McCartney J, Tai M, et al. Highly specific in vivo tumor targeting by monovalent and divalent forms of 741F8 anti-c-ERBB-2 single-chain Fv. *Cancer Research.* 1993;53(17):4026-4034.
105. Schier R, Marks J, Wolf E, et al. In-vitro and in-vivo characterization of a human anti-c-ERBB-2 single-chain Fv isolated from a filamentous phage antibody library. *Immunotechnology.* 1995;1(1):73-81.
106. Van Den Abbeele A, Declercq S, De Ganck A, et al. 2X1P: Gelsolin Nanobody. *Worldwide Protein Data Bank.* 2011.
107. Muyldermans S, Baral TN, Retamozzo VC, et al. Camelid immunoglobulins and nanobody technology. *Vet Immunol Immunopathol.* 2009;128(1-3):178-183.
108. Vincke C, Loris R, Saerens D, Martinez-Rodriguez S, Muyldermans S, Conrath K. General Strategy to Humanize a Camelid Single-domain Antibody and Identification of a Universal Humanized Nanobody Scaffold. *J Biol Chem.* 2009;284(5):3273-3284.
109. Decanniere K, Muyldermans S, Wyns L. Canonical antigen-binding loop structures in immunoglobulins: more structures, more canonical classes? *J Mol Biol.* 2000;300(1):83-91.
110. Jähnichen S, Blanchetot C, Maussang D, et al. CXCR4 nanobodies (VHH-based single variable domains) potently inhibit chemotaxis and HIV-1 replication and mobilize stem cells. *Proc Natl Acad Sci U S A.* 2010;107(47):20565-20570.
111. Maussang D, Mujic-Delic A, Descamps FJ, et al. Llama-derived Single Variable Domains (Nanobodies) Directed against Chemokine Receptor CXCR7 Reduce Head and Neck Cancer Cell Growth in Vivo. *J Biol Chem.* 2013;288(41):29562-29572.
112. Gainkam LOT, Keyaerts M, Caveliers V, et al. Correlation Between Epidermal Growth Factor Receptor-Specific Nanobody Uptake and Tumor Burden: A Tool for Noninvasive Monitoring of Tumor Response to Therapy. *Molecular Imaging and Biology.* 2011;13(5):940-948.
113. Vosjan MJWD, Perk LR, Roovers RC, et al. Facile labelling of an anti-epidermal growth factor receptor Nanobody with Ga-68 via a novel bifunctional desferal chelate for immuno-PET. *Euro J Nucl Med & Mol Imag.* 2011;38(4):753-763.
114. Roovers RC, Laeremans T, Huang L, et al. Efficient inhibition of EGFR signalling and of tumour growth by antagonistic anti-EGFR Nanobodies. *Cancer Immunology Immunotherapy.* 2007;56(3):303-317.
115. Tijink BM, Laeremans T, Budde M, et al. Improved tumor targeting of anti-epidermal growth factor receptor Nanobodies through albumin binding: taking advantage of modular Nanobody technology. *Molecular Cancer Therapeutics.* 2008;7(8):2288-2297.
116. Roovers RC, Vosjan MJWD, Laeremans T, et al. A biparatopic anti-EGFR nanobody efficiently inhibits solid tumour growth. *International Journal of Cancer.* 2011;129(8):2013-2024.
117. Xavier C, Vaneycken I, D'huyvetter M, et al. Synthesis, Preclinical Validation, Dosimetry, and Toxicity of Ga-68-NOTA-Anti-HER2 Nanobodies for iPET Imaging of HER2 Receptor Expression in Cancer. *J Nucl Med.* 2013;54(5):776-784.

118. C. X, C. C. Molecular Imaging of HER2 Expression in Breat Cancer using ^{68}Ga-NOTA Anti-HER2 Nanobodies. 1st World Congress on Gallium-68 and Peptide Receptor Radionuclide Therapy (PRRNT); 2011; Bad Berka.
119. Nord K, Gunneriusson E, Ringdahl J, Ståhl S, Uhlén M, Nygren PA. Binding proteins selected from combinatorial libraries of an alpha-helical bacterial receptor domain. *Nat Biotechnol.* 1997;15(8):772-777.
120. Eigenbrot C, Ultsch M, Dubnovitsky A, Abrahmsen L, Hard T. Structural basis for high-affinity HER2 receptor binding by an engineered protein. *Proc Natl Acad Sci U S A.* 2010;107(34):15039-15044.
121. Orlova A, Feldwisch J, Abrahmsén L, Tolmachev V. Update: affibody molecules for molecular imaging and therapy for cancer. *Cancer Biother Radiopharm.* 2007;22(5):573-584.
122. Nilsson FY, Tolmachev V. Affibody molecules: new protein domains for molecular imaging and targeted tumor therapy. *Curr Opin Drug Discov Devel.* 2007;10(2):167-175.
123. Binz HK, Plückthun A. Engineered proteins as specific binding reagents. *Curr Opin Biotechnol.* 2005;16(4):459-469.
124. Binz HK, Amstutz P, Plückthun A. Engineering novel binding proteins from nonimmunoglobulin domains. *Nat Biotechnol.* 2005;23(10):1257-1268.
125. Jonsson A, Dogan J, Herne N, Abrahmsén L, Nygren PA. Engineering of a femtomolar affinity binding protein to human serum albumin. *Protein Eng Des Sel.* 2008;21(8):515-527.
126. Nygren PA. Alternative binding proteins: affibody binding proteins developed from a small three-helix bundle scaffold. *FEBS J.* 2008;275(11):2668-2676.
127. Tolmachev V, Velikyan I, Sandström M, Orlova A. A HER2-binding Affibody molecule labelled with 68Ga for PET imaging: direct in vivo comparison with the 111In-labelled analogue. *Eur J Nucl Med Mol Imaging.* 2010;37(7):1356-1367.
128. Kramer-Marek G, Shenoy N, Seidel J, Griffiths GL, Choyke P, Capala J. 68Ga-DOTA-affibody molecule for in vivo assessment of HER2/neu expression with PET. *Eur J Nucl Med Mol Imaging.* 2011;38(11):1967-1976.
129. Kramer-Marek G, Kiesewetter DO, Martiniova L, Jagoda E, Lee SB, Capala J. [18F]FBEM-Z(HER2:342)-Affibody molecule-a new molecular tracer for in vivo monitoring of HER2 expression by positron emission tomography. *Eur J Nucl Med Mol Imaging.* 2008;35(5):1008-1018.
130. Kramer-Marek G, Kiesewetter DO, Capala J. Changes in HER2 expression in breast cancer xenografts after therapy can be quantified using PET and (18)F-labeled affibody molecules. *J Nucl Med.* 2009;50(7):1131-1139.
131. Gao J, Chen K, Miao Z, et al. Affibody-based nanoprobes for HER2-expressing cell and tumor imaging. *Biomaterials.* 2011;32(8):2141-2148.
132. Francisco J, Cerveny C, Meyer D, et al. cAC10-vcMMAE, an anti-CD30-monomethyl auristatin E conjugate with potent and selective antitumor activity. *Blood.* 2003;102(4):1458-1465.
133. Bartlett NL, Sharman JP, Oki Y, et al. A Phase 2 Study Of Brentuximab Vedotin In Patients With Relapsed Or Refractory CD30-Positive Non-Hodgkin Lymphomas: Interim Results In Patients With DLBCL and Other B-Cell Lymphomas. *Blood.* 2013;122(21).
134. Lewis Phillips GD, Li G, Dugger DL, et al. Targeting HER2-positive breast cancer with trastuzumab-DM1, an antibody-cytotoxic drug conjugate. *Cancer Res.* 2008;68(22):9280-9290.
135. Van den Mooter T, Teuwen LA, Rutten A, Dirix L. Trastuzumab emtansine in advanced human epidermal growth factor receptor 2-positive breast cancer. *Expert Opin Biol Ther.* 2015;15(5):749-760.
136. Yates SP, Merrill AR. Elucidation of eukaryotic elongation factor-2 contact sites within the catalytic domain of Pseudomonas aeruginosa exotoxin A. *Biochemical Journal.* 2004;379(Pt 3):563-572.
137. Beattie BK, Merrill AR. In vitro enzyme activation and folded stability of Pseudomonas aeruginosa exotoxin A and its C-terminal peptide. *Biochemistry.* 1996;35(28):9042-9051.
138. Beattie BK, Prentice GA, Merrill AR. Investigation into the catalytic role for the tryptophan residues within domain III of Pseudomonas aeruginosa exotoxin A. *Biochemistry.* 1996;35(48):15134-15142.
139. Newton DL, Hansen HJ, Mikulski SM, Goldenberg DM, Rybak SM. Potent and specific antitumor effects of an anti-CD22-targeted cytotoxic ribonuclease: potential for the treatment of non-Hodgkin lymphoma. *Blood.* 2001;97(2):528-535.

140. Samel D, Muller D, Gerspach J, et al. Generation of a FasL-based proapoptotic fusion protein devoid of systemic toxicity due to cell-surface antigen-restricted activation. *J Biol Chem.* 2003;278(34):32077-32082.
141. van de Water JAJM, Bagci-Onder T, Agarwal AS, et al. Therapeutic stem cells expressing variants of EGFR-specific nanobodies have antitumor effects. *Proc Natl Acad Sci U S A.* 2012;109(41):16642-16647.
142. de Bruyn M, Rybczynska AA, Wei Y, et al. Melanoma-associated Chondroitin Sulfate Proteoglycan (MCSP)-targeted delivery of soluble TRAIL potently inhibits melanoma outgrowth in vitro and in vivo. *Mol Cancer.* 2010;9.
143. Halin C, Rondini S, Nilsson F, et al. Enhancement of the antitumor activity of interleukin-12 by targeted delivery to neovasculature. *Nat Biotechnol.* 2002;20(3):264-269.
144. Bremer E, van Dam GM, de Bruyn M, et al. Potent Systemic Anticancer Activity of Adenovirally Expressed EGFR-Selective TRAIL Fusion Protein. *Molecular Therapy.* 2008;16(12):1919-1926.
145. Wagner K, Schulz P, Scholz A, Wiedenmann B, Menrad A. The targeted immunocytokine L19-IL2 efficiently inhibits the growth of orthotopic pancreatic cancer. *Clin Cancer Res.* 2008;14(15):4951-4960.
146. Borsi L, Carnemolla B, Nicolo G, Spina B, Tanara G, Zardi L. Expression of different tenascin isoforms in normal, hyperplastic and neoplastic human breast tissues. *International Journal Of Cancer.* 1992;52(5):688-692.
147. Marlind J, Kaspar M, Trachsel E, et al. Antibody-Mediated Delivery of Interleukin-2 to the Stroma of Breast Cancer Strongly Enhances the Potency of Chemotherapy. *Clinical Cancer Research.* 2008;14(20):6515-6524.
148. Frey K, Zivanovic A, Schwager K, Neri D. Antibody-based targeting of interferon-alpha to the tumor neovasculature: a critical evaluation. *Integrative Biology.* 2011;3(4):468-478.
149. Hemmerle T, Neri D. The Dose-Dependent Tumor Targeting of Antibody-IFNgamma Fusion Proteins Reveals an Unexpected Receptor-Trapping Mechanism In Vivo. *Cancer immunology research.* 2014;2(6):559-567.
150. Ebbinghaus C, Ronca R, Kaspar M, et al. Engineered vascular-targeting antibody-interferon-gamma fusion protein for cancer therapy. *International Journal of Cancer.* 2005;116(2):304-313.
151. Grewal PK, Uchiyama S, Ditto D, et al. The Ashwell receptor mitigates the lethal coagulopathy of sepsis. *Nature Medicine.* 2008;14(6):648-655.
152. Morell AG, Gregoriadis G, Scheinberg IH, Hickman J, Ashwell G. The role of sialic acid in determining the survival of glycoproteins in the circulation. *J Biol Chem.* 1971;246(5):1461-1467.
153. Pricer WE, Hudgin RL, Ashwell G, Stockert RJ, Morell AG. A membrane receptor protein for asialoglycoproteins. *Methods Enzymol.* 1974;34:688-691.
154. Ashwell G, Morell AG. The role of surface carbohydrates in the hepatic recognition and transport of circulating glycoproteins. *Adv Enzymol Relat Areas Mol Biol.* 1974;41(0):99-128.
155. Baenziger JU, Maynard Y. Human hepatic lectin. Physiochemical properties and specificity. *J Biol Chem.* 1980;255(10):4607-4613.
156. Drickamer K. Ca(2+)-dependent sugar recognition by animal lectins. *Biochem Soc Trans.* 1996;24(1):146-150.
157. Schwartz AL, Rup D. Biosynthesis of the human asialoglycoprotein receptor. *J Biol Chem.* 1983;258(18):11249-11255.
158. Meier M, Bider MD, Malashkevich VN, Spiess M, Burkhard P. Crystal structure of the carbohydrate recognition domain of the H1 subunit of the asialoglycoprotein receptor. *J Mol Biol.* 2000;300(4):857-865.
159. Hubbard AL, Wilson G, Ashwell G, Stukenbrok H. An electron microscope autoradiographic study of the carbohydrate recognition systems in rat liver. I. Distribution of 125I-ligands among the liver cell types. *J Cell Biol.* 1979;83(1):47-64.
160. Wall DA, Hubbard AL. Galactose-specific recognition system of mammalian liver: receptor distribution on the hepatocyte cell surface. *J Cell Biol.* 1981;90(3):687-696.
161. Hubbard AL, Stukenbrok H. An electron microscope autoradiographic study of the carbohydrate recognition systems in rat liver. II. Intracellular fates of the 125I-ligands. *J Cell Biol.* 1979;83(1):65-81.
162. Naito M, Wisse E. Filtration effect of endothelial fenestrations on chylomicron transport in neonatal rat-liver sinusoids. *Cell and Tissue Research.* 1978;190(3):371-382.

163. Spiess M. The asialoglycoprotein receptor: a model for endocytic transport receptors. *Biochemistry.* 1990;29(43):10009-10018.
164. Baenziger JU, Fiete D. Galactose and N-acetylgalactosamine-specific endocytosis of glycopeptides by isolated rat hepatocytes. *Cell.* 1980;22(2 Pt 2):611-620.
165. Weis WI, Drickamer K. Structural basis of lectin-carbohydrate recognition. *Annu Rev Biochem.* 1996;65:441-473.
166. Goldstein JL, Anderson RG, Brown MS. Coated pits, coated vesicles, and receptor-mediated endocytosis. *Nature.* 1979;279(5715):679-685.
167. Geuze HJ, Slot JW, Strous GJ, Schwartz AL. The pathway of the asialoglycoprotein-ligand during receptor-mediated endocytosis: a morphological study with colloidal gold/ligand in the human hepatoma cell line, Hep G2. *Eur J Cell Biol.* 1983;32(1):38-44.
168. Loeb JA, Drickamer K. Conformational changes in the chicken receptor for endocytosis of glycoproteins. Modulation of ligand-binding activity by Ca2+ and pH. *J Biol Chem.* 1988;263(20):9752-9760.
169. Tolleshaug H, Berg T, Nilsson M, Norum KR. Uptake and degradation of 125I-labelled asialo-fetuin by isolated rat hepatocytes. *Biochim Biophys Acta.* 1977;499(1):73-84.
170. Schwartz AL, Fridovich SE, Lodish HF. Kinetics of internalization and recycling of the asialoglycoprotein receptor in a hepatoma cell line. *J Biol Chem.* 1982;257(8):4230-4237.
171. Bischoff J, Lodish HF. Two asialoglycoprotein receptor polypeptides in human hepatoma cells. *J Biol Chem.* 1987;262(24):11825-11832.
172. Bovenschen N, Rijken DC, Havekes LM, van Vlijmen BJ, Mertens K. The B domain of coagulation factor VIII interacts with the asialoglycoprotein receptor. *J Thromb Haemost.* 2005;3(6):1257-1265.
173. Wahrenbrock MG, Varki A. Multiple hepatic receptors cooperate to eliminate secretory mucins aberrantly entering the bloodstream: are circulating cancer mucins the "tip of the iceberg"? *Cancer Res.* 2006;66(4):2433-2441.
174. Weigel PH. Galactosyl and N-acetylgalactosaminyl homeostasis: a function for mammalian asialoglycoprotein receptors. *Bioessays.* 1994;16(7):519-524.
175. Dotzauer A, Gebhardt U, Bieback K, et al. Hepatitis A virus-specific immunoglobulin A mediates infection of hepatocytes with hepatitis A virus via the asialoglycoprotein receptor. *J Virol.* 2000;74(23):10950-10957.
176. Treichel U, Meyer zum Büschenfelde KH, Dienes HP, Gerken G. Receptor-mediated entry of hepatitis B virus particles into liver cells. *Arch Virol.* 1997;142(3):493-498.
177. Saunier B, Triyatni M, Ulianich L, Maruvada P, Yen P, Kohn LD. Role of the asialoglycoprotein receptor in binding and entry of hepatitis C virus structural proteins in cultured human hepatocytes. *J Virol.* 2003;77(1):546-559.
178. Tozawa R, Ishibashi S, Osuga J, et al. Asialoglycoprotein receptor deficiency in mice lacking the major receptor subunit. Its obligate requirement for the stable expression of oligomeric receptor. *J Biol Chem.* 2001;276(16):12624-12628.
179. Liu J, Hu B, Yang Y, et al. A new splice variant of the major subunit of human asialoglycoprotein receptor encodes a secreted form in hepatocytes. *PLoS One.* 2010;5(9):e12934.
180. Spiess M, Lodish HF. Sequence of a second human asialoglycoprotein receptor: conservation of two receptor genes during evolution. *Proc Natl Acad Sci U S A.* 1985;82(19):6465-6469.
181. Paietta E, Stockert RJ, Racevskis J. Differences in the abundance of variably spliced transcripts for the second asialoglycoprotein receptor polypeptide, H2, in normal and transformed human liver. *Hepatology.* 1992;15(3):395-402.
182. Chiacchia KB, Drickamer K. Direct evidence for the transmembrane orientation of the hepatic glycoprotein receptors. *J Biol Chem.* 1984;259(24):15440-15446.
183. Spiess M, Lodish HF. An internal signal sequence: the asialoglycoprotein receptor membrane anchor. *Cell.* 1986;44(1):177-185.
184. Shia MA, Lodish HF. The two subunits of the human asialoglycoprotein receptor have different fates when expressed alone in fibroblasts. *Proc Natl Acad Sci U S A.* 1989;86(4):1158-1162.
185. Bider MD, Wahlberg JM, Kammerer RA, Spiess M. The oligomerization domain of the asialoglycoprotein receptor preferentially forms 2:2 heterotetramers in vitro. *J Biol Chem.* 1996;271(50):31996-32001.
186. Beavil AJ, Edmeades RL, Gould HJ, Sutton BJ. Alpha-helical coiled-coil stalks in the low-affinity receptor for IgE (Fc epsilon RII/CD23) and related C-type lectins. *Proc Natl Acad Sci U S A.* 1992;89(2):753-757.

187. McPhaul M, Berg P. Formation of functional asialoglycoprotein receptor after transfection with cDNAs encoding the receptor proteins. *Proc Natl Acad Sci U S A.* 1986;83(23):8863-8867.
188. Oka JA, Herzig MC, Weigel PH. Functional galactosyl receptors on isolated rat hepatocytes are hetero-oligomers. *Biochem Biophys Res Commun.* 1990;170(3):1308-1313.
189. Hsueh EC, Holland EC, Carrera GM, Drickamer K. The rat liver asialoglycoprotein receptor polypeptide must be inserted into a microsome to achieve its active conformation. *J Biol Chem.* 1986;261(11):4940-4947.
190. Henis YI, Katzir Z, Shia MA, Lodish HF. Oligomeric structure of the human asialoglycoprotein receptor: nature and stoichiometry of mutual complexes containing H1 and H2 polypeptides assessed by fluorescence photobleaching recovery. *J Cell Biol.* 1990;111(4):1409-1418.
191. Eto T, Takahashi H. Enhanced inhibition of hepatitis B virus production by asialoglycoprotein receptor-directed interferon. *Nature Medicine.* 1999;5(5):577-581.
192. Trahtenherts A, Benhar I. An internalizing antibody specific for the human asialoglycoprotein receptor. *Hybridoma.* 2009;28(4):225-233.
193. Fagerberg L, Hallstrom BM, Oksvold P, et al. Analysis of the Human Tissue-specific Expression by Genome-wide Integration of Transcriptomics and Antibody-based Proteomics. *Mol Cell Proteomics.* 2014;13(2):397-406.
194. Derrien T, Johnson R, Bussotti G, et al. The GENCODE v7 catalog of human long noncoding RNAs: Analysis of their gene structure, evolution, and expression. *Genome Research.* 2012;22(9):1775-1789.
195. Barbosa-Morais N, Irimia M, Pan Q, et al. The Evolutionary Landscape of Alternative Splicing in Vertebrate Species. *Science.* 2012;338(6114):1587-1593.
196. Brawand D, Soumillon M, Necsulea A, et al. The evolution of gene expression levels in mammalian organs. *Nature.* 2011;478(7369):343-+.
197. Asmann YW, Necela BM, Kalari KR, et al. Detection of Redundant Fusion Transcripts as Biomarkers or Disease- Specific Therapeutic Targets in Breast Cancer. *Cancer Research.* 2012;72(8):1921-1928.
198. Schwartz AL, Rup D, Lodish HF. Difficulties in the quantification of asialoglycoprotein receptors on the rat hepatocyte. *J Biol Chem.* 1980;255(19):9033-9036.
199. Steer CJ, Ashwell G. Studies on a mammalian hepatic binding protein specific for asialoglycoproteins. Evidence for receptor recycling in isolated rat hepatocytes. *J Biol Chem.* 1980;255(7):3008-3013.
200. Pacifico F, Montuori N, Mellone S, et al. The RHL-1 subunit of the asialoglycoprotein receptor of thyroid cells: cellular localization and its role in thyroglobulin endocytosis. *Mol Cell Endocrinol.* 2003;208(1-2):51-59.
201. Pacifico F, Laviola L, Ulianich L, et al. Differential expression of the asialoglycoprotein receptor in discrete brain areas, in kidney and thyroid. *Biochem Biophys Res Commun.* 1995;210(1):138-144.
202. Montuori N, Pacifico F, Mellone S, et al. The rat asialoglycoprotein receptor binds the amino-terminal domain of thyroglobulin. *Biochem Biophys Res Commun.* 2000;268(1):42-46.
203. Abdullah M, Kierszenbaum AL. Identification of rat testis galactosyl receptor using antibodies to liver asialoglycoprotein receptor: purification and localization on surfaces of spermatogenic cells and sperm. *J Cell Biol.* 1989;108(2):367-375.
204. Park JH, Kim KL, Cho EW. Detection of surface asialoglycoprotein receptor expression in hepatic and extra-hepatic cells using a novel monoclonal antibody. *Biotechnol Lett.* 2006;28(14):1061-1069.
205. Valladeau J, Duvert-Frances V, Pin JJ, et al. Immature human dendritic cells express asialoglycoprotein receptor isoforms for efficient receptor-mediated endocytosis. *J Immunol.* 2001;167(10):5767-5774.
206. Seow YY, Tan MG, Woo KT. Expression of a functional asialoglycoprotein receptor in human renal proximal tubular epithelial cells. *Nephron.* 2002;91(3):431-438.
207. Sawamura T, Nakada H, Hazama H, Shiozaki Y, Sameshima Y, Tashiro Y. Hyperasialoglycoproteinemia in patients with chronic liver diseases and/or liver cell carcinoma. Asialoglycoprotein receptor in cirrhosis and liver cell carcinoma. *Gastroenterology.* 1984;87(6):1217-1221.

208. Callewaert N, Van Vlierberghe H, Van Hecke A, Laroy W, Delanghe J, Contreras R. Noninvasive diagnosis of liver cirrhosis using DNA sequencer-based total serum protein glycomics. *Nat Med.* 2004;10(4):429-434.
209. Ise H, Sugihara N, Negishi N, Nikaido T, Akaike T. Low asialoglycoprotein receptor expression as markers for highly proliferative potential hepatocytes. *Biochem Biophys Res Commun.* 2001;285(2):172-182.
210. Hirose S, Ise H, Uchiyama M, Cho CS, Akaike T. Regulation of asialoglycoprotein receptor expression in the proliferative state of hepatocytes. *Biochem Biophys Res Commun.* 2001;287(3):675-681.
211. Eisenberg C, Seta N, Appel M, Feldmann G, Durand G, Feger J. Asialoglycoprotein receptor in human isolated hepatocytes from normal liver and its apparent increase in liver with histological alterations. *J Hepatol.* 1991;13(3):305-309.
212. Arangoa MA, Düzgüneş N, Tros de Ilarduya C. Increased receptor-mediated gene delivery to the liver by protamine-enhanced-asialofetuin-lipoplexes. *Gene Ther.* 2003;10(1):5-14.
213. Nishikawa M, Kawakami S, Yamashita F, Hashida M. Glycosylated cationic liposomes for carbohydrate receptor-mediated gene transfer. *Methods Enzymol.* 2003;373:384-399.
214. Nishikawa M, Yamauchi M, Morimoto K, Ishida E, Takakura Y, Hashida M. Hepatocyte-targeted in vivo gene expression by intravenous injection of plasmid DNA complexed with synthetic multi-functional gene delivery system. *Gene Ther.* 2000;7(7):548-555.
215. Conradt HS, Egge H, Peter-Katalinic J, Reiser W, Siklosi T, Schaper K. Structure of the carbohydrate moiety of human interferon-beta secreted by a recombinant Chinese hamster ovary cell line. *J Biol Chem.* 1987;262(30):14600-14605.
216. Trahtenherts A, Benhar I. An internalizing antibody specific for the human asialoglycoprotein receptor. *Hybridoma (Larchmt).* 2009;28(4):225-233.
217. Cao L, Shen G, Zhu Y, et al. Characterization of a single-chain variable fragment (scFv) antibody directed against the human asialoglycoprotein receptor. *Biotechnol Appl Biochem.* 2006;44(Pt 2):65-72.
218. Mazor Y, Barnea I, Keydar I, Benhar I. Antibody internalization studied using a novel IgG binding toxin fusion. *J Immunol Methods.* 2007;321(1-2):41-59.
219. Dreier T, Lode HN, Xiang R, Dolman CS, Reisfeld RA, Kang AS. Recombinant immunocytokines targeting the mouse transferrin receptor: construction and biological activities. *Bioconjug Chem.* 1998;9(4):482-489.
220. Garcin G, Paul F, Staufenbiel M, et al. High efficiency cell-specific targeting of cytokine activity. *Nature Communications.* 2014;5.
221. Tycko B, Keith CH, Maxfield FR. Rapid acidification of endocytic vesicles containing asialoglycoprotein in cells of a human hepatoma line. *J Cell Biol.* 1983;97(6):1762-1776.
222. Medina SH, Tekumalla V, Chevliakov MV, Shewach DS, Ensminger WD, El-Sayed ME. N-acetylgalactosamine-functionalized dendrimers as hepatic cancer cell-targeted carriers. *Biomaterials.* 2011;32(17):4118-4129.
223. Marchetti M, Monier MN, Fradagrada A, et al. Stat-mediated signaling induced by type I and type II interferons (IFNs) is differentially controlled through lipid microdomain association and clathrin-dependent endocytosis of IFN receptors. *Mol Biol Cell.* 2006;17(7):2896-2909.
224. Claudinon J, Monier MN, Lamaze C. Interfering with interferon receptor sorting and trafficking: impact on signaling. *Biochimie.* 2007;89(6-7):735-743.
225. Bremer E, Samplonius D, Kroesen B, van Genne L, de Leij L, Helfrich W. Exceptionally potent anti-tumor bystander activity of an scFv : sTRAIL fusion protein with specificity for EGP2 toward target antigen-negative tumor cells. *NEOPLASIA.* 2004;6(5):636-645.
226. Bremer E, Kuulen J, Samplonius D, Walczak H, De Leu L, Helfrich W. Target cell-restricted and -enhanced apoptosis induction by a scFv : sTRAIL fusion protein with specificity for the pancarcinoma-associated antigen EGP2. *Int J of Cancer.* 2004;109(2):281-290.
227. Hadden B, Luce HR. *Time.* New York, 1923.
228. Isaacs A, Lindenmann J. Virus interference. I. The interferon. *Proc R Soc Lond B Biol Sci.* 1957;147(927):258-267.
229. Sadler AJ, Williams BR. Interferon-inducible antiviral effectors. *Nat Rev Immunol.* 2008;8(7):559-568.
230. Dunn GP, Old LJ, Schreiber RD. The immunobiology of cancer immunosurveillance and immunoediting. *Immunity.* 2004;21(2):137-148.
231. Takaoka A, Hayakawa S, Yanai H, et al. Integration of interferon-alpha/beta signalling to p53 responses in tumour suppression and antiviral defence. *Nature.* 2003;424(6948):516-523.

232. Takaoka A, Mitani Y, Suemori H, et al. Cross talk between interferon-gamma and -alpha/beta signaling components in caveolar membrane domains. *Science.* 2000;288(5475):2357-2360.
233. Yanai Y, Sanou O, Kayano T, et al. Analysis of the antiviral activities of natural IFN-alpha preparations and their subtype compositions. *Journal of Interferon and Cytokine Research.* 2001;21(10):835-841.
234. Hillyer P, Mane VP, Schramm LM, et al. Expression profiles of human interferon-alpha and interferon-lambda subtypes are ligand- and cell-dependent. *Immunology and Cell Biology.* 2012;90(8):774-783.
235. Larrea E, Aldabe R, Riezu-Boj J, et al. IFN-alpha 5 mediates stronger Tyk2-stat-dependent activation and higher expression of 2 ',5 '-oligoadenylate synthetase than IFN-alpha 2 in liver cells. *Journal of Interferon and Cytokine Research.* 2004;24(8):497-503.
236. Meager A. *The interferons: characterization and application.* Wiley-VCH, Chichester. John Wiley.; 2006.
237. Lee N, Ni D, Brissette R, et al. Interferon-alpha(2) variants in the human genome. *Journal of Interferon and Cytokine Research.* 1995;15(4):341-349.
238. Adolf G, Kalsner I, Ahorn H, Maurerfogy I, Cantell K. Natural human interferon-alpha-2 is O-glycosylated. *Biochemical Journal.* 1991;276:511-518.
239. Nyman T, Kalkkinen N, Tolo H, Helin J. Structural characterisation of N-linked and O-linked oligosaccharides derived from interferon-alpha 2b and interferon-alpha 14c produced by Sendai-virus-induced human peripheral blood leukocytes. *Eur J Biochem.* 1998;253(2):485-493.
240. Mathews CK, Van Holde KE, Ahern KG. *Biochemistry.* 3rd ed. ed. San Francisco, Calif. ; Harlow: Benjamin Cummings; 2000.
241. Ghasriani H, Belcourt PJF, Sauve S, et al. A Single N-Acetylgalactosamine Residue at Threonine 106 Modifies the Dynamics and Structure of Interferon alpha 2a around the Glycosylation Site. *Journal of Biological Chemistry.* 2013;288(1):247-254.
242. Wonderling R, Powell T, Baldwin S, et al. Cloning, expression, purification, and biological activity of five feline type I interferons. *Veterinary Immunology and Immunopathology.* 2002;89(1-2):13-27.
243. Klaus W, Gsell B, Labhardt A, Wipf B, Senn H. The three-dimensional high resolution structure of human interferon alpha-2a determined by heteronuclear NMR spectroscopy in solution. *J Mol Biol.* 1997;274(4):661-675.
244. Waine G, Tymms M, Brandt E, Cheetham B, Linnane A. Structure-function study of the region encompassing residues-26-40 of human interferon-alpha-4 - identification of residues important for antiviral and antiproliferative activities. *Journal Of Interferon Research.* 1992;12(1):43-48.
245. Wetzel R. Assignment of the disulfide bonds of leukocyte interferon. *Nature.* 1981;289(5798):606-607.
246. Beilharz M, Nisbet I, Tymms M, Hertzog P, Linnane A. Antiviral and antiproliferative activities of interferon-alpha1 - the role of cysteine residues. *Journal of Interferon Research.* 1986;6(6):677-685.
247. Radhakrishnan R, Walter L, Hruza A, et al. Zinc mediated dimer of human interferon-alpha(2b) revealed by X-ray crystallography. *Structure with Folding & Design.* 1996;4(12):1453-1463.
248. Shire S. H-dependent polymerization of a human-leukocyte interferon produced by recombinant deoxyribonucleic-acid technology. *Biochemistry.* 1983;22(11):2664-2671.
249. Uzé G, Lutfalla G, Gresser I. Genetic transfer of a functional human interferon alpha receptor into mouse cells: cloning and expression of its cDNA. *Cell.* 1990;60(2):225-234.
250. Novick D, Cohen B, Rubinstein M. The Human Interferon-Alpha/Beta Receptor - Characterization and Molecular-Cloning. *Cell.* 1994;77(3):391-400.
251. Constantinescu SN, Croze E, Wang C, et al. Role of Interferon-Alpha/Beta Receptor Chain-1 in the Structure and Transmembrane Signaling of the Interferon-Alpha/Beta Receptor Complex. *Proc Natl Acad Sci U S A.* 1994;91(20):9602-9606.
252. Cook JR, Cleary CM, Mariano TM, Izotova L, Pestka S. Differential responsiveness of a splice variant of the human type I interferon receptor to interferons. *J Biol Chem.* 1996;271(23):13448-13453.
253. de Weerd NA, Samarajiwa SA, Hertzog PJ. Type I interferon receptors: biochemistry and biological functions. *J Biol Chem.* 2007;282(28):20053-20057.

254. Gazziola C, Cordani N, Carta S, De Lorenzo E, Colombatti A, Perris R. The relative endogenous expression levels of the IFNAR2 isoforms influence the cytostatic and pro-apoptotic effect of IFNalpha on pleomorphic sarcoma cells. *Int J Oncol.* 2005;26(1):129-140.
255. Domanski P, Witte M, Kellum M, et al. Cloning and Expression of a Long Form of the Beta-Subunit of the Interferon Alpha-Beta Receptor That Is Required for Signaling. *Journal of Biological Chemistry.* 1995;270(37):21606-21611.
256. Lutfalla G, Holland SJ, Cinato E, et al. Mutant U5A cells are complemented by an interferon-alpha beta receptor subunit generated by alternative processing of a new member of a cytokine receptor gene cluster. *EMBO J.* 1995;14(20):5100-5108.
257. Pestka S. The interferon receptors. *Semin Oncol.* 1997;24(3 Suppl 9):S9-18-S19-40.
258. Thomas C, Moraga I, Levin D, et al. Structural linkage between ligand discrimination and receptor activation by type I interferons. *Cell.* 2011;146(4):621-632.
259. Chill JH, Quadt SR, Levy R, Schreiber G, Anglister J. The human type I interferon receptor: NMR structure reveals the molecular basis of ligand binding. *Structure.* 2003;11(7):791-802.
260. Piehler J, Schreiber G. Mutational and structural analysis of the binding interface between type I interferons and their receptor Ifnar2. *J Mol Biol.* 1999;294(1):223-237.
261. Uze G, Dimarco S, Mouchelvielh E, et al. Domains of interaction between alpha-interferon and its receptor components. *Journal Of Molecular Biology.* 1994;243(2):245-257.
262. Kalie E, Jaitin DA, Abramovich R, Schreiber G. An interferon alpha2 mutant optimized by phage display for IFNAR1 binding confers specifically enhanced antitumor activities. *J Biol Chem.* 2007;282(15):11602-11611.
263. Kalie E, Jaitin DA, Podoplelova Y, Piehler J, Schreiber G. The Stability of the Ternary Interferon-Receptor Complex Rather than the Affinity to the Individual Subunits Dictates Differential Biological Activities. *J Biol Chem.* 2008;283(47):32925-32936.
264. Cajean-Feroldi C, Nosal F, Nardeux PC, et al. Identification of residues of the IFNAR1 chain of the type I human interferon receptor critical for ligand binding and biological activity. *Biochemistry.* 2004;43(39):12498-12512.
265. Strunk JJ, Gregor I, Becker Y, et al. Ligand binding induces a conformational change in ifnar1 that is propagated to its membrane-proximal domain. *J Mol Biol.* 2008;377(3):725-739.
266. Lewerenz M, Mogensen KE, Uzé G. Shared receptor components but distinct complexes for alpha and beta interferons. *J Mol Biol.* 1998;282(3):585-599.
267. Tanimoto T, Yamamoto S, Taniai M, et al. The combination of IFN-alpha 2 and IFN-alpha 8 exhibits synergistic antiproliferative activity on renal cell carcinoma (RCC) cell lines through increased binding affinity for IFNAR-2. *J Interferon Cytokine Res.* 2007;27(6):517-523.
268. Kumaran J, Wei L, Kotra LP, Fish EN. A structural basis for interferon-alpha-receptor interactions. *FASEB J.* 2007;21(12):3288-3296.
269. Jaitin D, Roisman L, Jaks E, et al. Inquiring into the differential action of interferons (IFNs): an IFN-alpha 2 mutant with enhanced affinity to IFNAR1 is functionally similar to IFN-beta. *Mol Cell Biol.* 2006;26(5):1888-1897.
270. Barbosa-Morais NL, Irimia M, Pan Q, et al. The Evolutionary Landscape of Alternative Splicing in Vertebrate Species. *Science.* 2012;338(6114):1587-1593.
271. Fukuda R, Ishimura N, Hamamoto S, et al. Co-infection by serologically-silent hepatitis B virus may contribute to poor interferon response in patients with chronic hepatitis C by down-regulation of type-I interferon receptor gene expression in the liver. *J Med Virol.* 2001;63(3):220-227.
272. Ota H, Nagano H, Sakon M, et al. Treatment of hepatocellular carcinoma with major portal vein thrombosis by combined therapy with subcutaneous interferon-alpha and intra-arterial 5-fluorouracil; role of type 1 interferon receptor expression. *Br J Cancer.* 2005;93(5):557-564.
273. Morris AG, Lin YL, Askonas BA. Immune interferon release when a cloned cytotoxic T-cell line meets its correct influenza-infected target cell. *Nature.* 1982;295(5845):150-152.
274. Williams BR. Signal integration via PKR. *Sci STKE.* 2001;2001(89):re2.
275. Der SD, Zhou A, Williams BR, Silverman RH. Identification of genes differentially regulated by interferon alpha, beta, or gamma using oligonucleotide arrays. *Proc Natl Acad Sci U S A.* 1998;95(26):15623-15628.
276. Samarajiwa SA, Forster S, Auchettl K, Hertzog PJ. INTERFEROME: the database of interferon regulated genes. *Nucleic Acids Res.* 2009;37(Database issue):D852-857.
277. Yan H, Krishnan K, Lim JT, Contillo LG, Krolewski JJ. Molecular characterization of an alpha interferon receptor 1 subunit (IFNaR1) domain required for TYK2 binding and signal transduction. *Mol Cell Biol.* 1996;16(5):2074-2082.

278. Domanski P, Fish E, Nadeau OW, et al. A region of the beta subunit of the interferon alpha receptor different from box 1 interacts with Jak1 and is sufficient to activate the Jak-Stat pathway and induce an antiviral state. *J Biol Chem.* 1997;272(42):26388-26393.
279. Fu XY, Schindler C, Improta T, Aebersold R, Darnell JE. The proteins of ISGF-3, the interferon alpha-induced transcriptional activator, define a gene family involved in signal transduction. *Proc Natl Acad Sci U S A.* 1992;89(16):7840-7843.
280. Schindler C, Fu XY, Improta T, Aebersold R, Darnell JE. Proteins of transcription factor ISGF-3: one gene encodes the 91-and 84-kDa ISGF-3 proteins that are activated by interferon alpha. *Proc Natl Acad Sci U S A.* 1992;89(16):7836-7839.
281. Fu XY, Kessler DS, Veals SA, Levy DE, Darnell JE. ISGF3, the transcriptional activator induced by interferon alpha, consists of multiple interacting polypeptide chains. *Proc Natl Acad Sci U S A.* 1990;87(21):8555-8559.
282. Kessler DS, Veals SA, Fu XY, Levy DE. Interferon-alpha regulates nuclear translocation and DNA-binding affinity of ISGF3, a multimeric transcriptional activator. *Genes Dev.* 1990;4(10):1753-1765.
283. Malakhova OA, Kim KI, Luo JK, et al. UBP43 is a novel regulator of interferon signaling independent of its ISG15 isopeptidase activity. *EMBO J.* 2006;25(11):2358-2367.
284. You M, Yu DH, Feng GS. Shp-2 tyrosine phosphatase functions as a negative regulator of the interferon-stimulated Jak/STAT pathway. *Mol Cell Biol.* 1999;19(3):2416-2424.
285. Fenner JE, Starr R, Cornish AL, et al. Suppressor of cytokine signaling 1 regulates the immune response to infection by a unique inhibition of type I interferon activity. *Nat Immunol.* 2006;7(1):33-39.
286. Chawla-Sarkar M, Lindner DJ, Liu YF, et al. Apoptosis and interferons: role of interferon-stimulated genes as mediators of apoptosis. *Apoptosis.* 2003;8(3):237-249.
287. Proud CG. PKR: a new name and new roles. *Trends Biochem Sci.* 1995;20(6):241-246.
288. Koromilas AE, Roy S, Barber GN, Katze MG, Sonenberg N. Malignant transformation by a mutant of the IFN-inducible dsRNA-dependent protein kinase. *Science.* 1992;257(5077):1685-1689.
289. Meurs EF, Galabru J, Barber GN, Katze MG, Hovanessian AG. Tumor suppressor function of the interferon-induced double-stranded RNA-activated protein kinase. *Proc Natl Acad Sci U S A.* 1993;90(1):232-236.
290. Chong KL, Feng L, Schappert K, et al. Human p68 kinase exhibits growth suppression in yeast and homology to the translational regulator GCN2. *EMBO J.* 1992;11(4):1553-1562.
291. Chebath J, Benech P, Revel M, Vigneron M. Constitutive expression of (2'-5') oligo A synthetase confers resistance to picornavirus infection. *Nature.* 1987;330(6148):587-588.
292. Zhou A, Hassel BA, Silverman RH. Expression cloning of 2-5A-dependent RNAase: a uniquely regulated mediator of interferon action. *Cell.* 1993;72(5):753-765.
293. Zhou A, Paranjape J, Brown TL, et al. Interferon action and apoptosis are defective in mice devoid of 2',5'-oligoadenylate-dependent RNase L. *EMBO J.* 1997;16(21):6355-6363.
294. Castelli JC, Hassel BA, Wood KA, et al. A study of the interferon antiviral mechanism: apoptosis activation by the 2-5A system. *J Exp Med.* 1997;186(6):967-972.
295. Porta C, Hadj-Slimane R, Nejmeddine M, et al. Interferons alpha and gamma induce p53-dependent and p53-independent apoptosis, respectively. *Oncogene.* 2005;24(4):605-615.
296. Lane DP. Cancer - P53, Guardian of the Genome. *Nature.* 1992;358(6381):15-16.
297. Hsu IC, Tokiwa T, Bennett W, et al. p53 gene mutation and integrated hepatitis B viral DNA sequences in human liver cancer cell lines. *Carcinogenesis.* 1993;14(5):987-992.
298. Scheffner M, Huibregtse JM, Vierstra RD, Howley PM. The HPV-16 E6 and E6-AP complex functions as a ubiquitin-protein ligase in the ubiquitination of p53. *Cell.* 1993;75(3):495-505.
299. Hollstein M, Sidransky D, Vogelstein B, Harris CC. p53 mutations in human cancers. *Science.* 1991;253(5015):49-53.
300. Bunz F, Hwang PM, Torrance C, et al. Disruption of p53 in human cancer cells alters the responses to therapeutic agents. *J Clin Invest.* 1999;104(3):263-269.
301. Levine AJ. p53, the cellular gatekeeper for growth and division. *Cell.* 1997;88(3):323-331.
302. Vousden KH, Lu X. Live or let die: the cell's response to p53. *Nat Rev Cancer.* 2002;2(8):594-604.
303. Friedlander P, Haupt Y, Prives C, Oren M. A mutant p53 that discriminates between p53-responsive genes cannot induce apoptosis. *Mol Cell Biol.* 1996;16(9):4961-4971.

304. Chen X, Ko LJ, Jayaraman L, Prives C. p53 levels, functional domains, and DNA damage determine the extent of the apoptotic response of tumor cells. *Genes Dev.* 1996;10(19):2438-2451.
305. Szak ST, Mays D, Pietenpol JA. Kinetics of p53 binding to promoter sites in vivo. *Mol Cell Biol.* 2001;21(10):3375-3386.
306. David M, Petricoin E, Benjamin C, Pine R, Weber MJ, Larner AC. Requirement for MAP kinase (ERK2) activity in interferon alpha- and interferon beta-stimulated gene expression through STAT proteins. *Science.* 1995;269(5231):1721-1723.
307. Romerio F, Riva A, Zella D. Interferon-alpha2b reduces phosphorylation and activity of MEK and ERK through a Ras/Raf-independent mechanism. *Br J Cancer.* 2000;83(4):532-538.
308. Romerio F, Zella D. MEK and ERK inhibitors enhance the anti-proliferative effect of interferon-alpha2b. *FASEB J.* 2002;16(12):1680-1682.
309. Chao Y, Shih YL, Chiu JH, et al. Overexpression of cyclin A but not Skp 2 correlates with the tumor relapse of human hepatocellular carcinoma. *Cancer Res.* 1998;58(5):985-990.
310. Murphy D, Detjen KM, Welzel M, Wiedenmann B, Rosewicz S. Interferon-alpha delays S-phase progression in human hepatocellular carcinoma cells via inhibition of specific cyclin-dependent kinases. *Hepatology.* 2001;33(2):346-356.
311. Morris A, Zvetkova I. Cytokine research: the interferon paradigm. *J Clin Pathol.* 1997;50(8):635-639.
312. Sato K, Hida S, Takayanagi H, et al. Antiviral response by natural killer cells through TRAIL gene induction by IFN-alpha/beta. *Eur J Immunol.* 2001;31(11):3138-3146.
313. Takeda K, Hayakawa Y, Smyth MJ, et al. Involvement of tumor necrosis factor-related apoptosis-inducing ligand in surveillance of tumor metastasis by liver natural killer cells. *Nat Med.* 2001;7(1):94-100.
314. Kayagaki N, Yamaguchi N, Nakayama M, Eto H, Okumura K, Yagita H. Type I interferons (IFNs) regulate tumor necrosis factor-related apoptosis-inducing ligand (TRAIL) expression on human T cells: A novel mechanism for the antitumor effects of type I IFNs. *J Exp Med.* 1999;189(9):1451-1460.
315. Fanger NA, Maliszewski CR, Schooley K, Griffith TS. Human dendritic cells mediate cellular apoptosis via tumor necrosis factor-related apoptosis-inducing ligand (TRAIL). *J Exp Med.* 1999;190(8):1155-1164.
316. Griffith TS, Wiley SR, Kubin MZ, Sedger LM, Maliszewski CR, Fanger NA. Monocyte-mediated tumoricidal activity via the tumor necrosis factor-related cytokine, TRAIL. *J Exp Med.* 1999;189(8):1343-1354.
317. Kischkel FC, Lawrence DA, Chuntharapai A, Schow P, Kim KJ, Ashkenazi A. Apo2L/TRAIL-dependent recruitment of endogenous FADD and caspase-8 to death receptors 4 and 5. *Immunity.* 2000;12(6):611-620.
318. Sharara AI, Perkins DJ, Misukonis MA, Chan SU, Dominitz JA, Weinberg JB. Interferon (IFN)-alpha activation of human blood mononuclear cells in vitro and in vivo for nitric oxide synthase (NOS) type 2 mRNA and protein expression: possible relationship of induced NOS2 to the anti-hepatitis C effects of IFN-alpha in vivo. *J Exp Med.* 1997;186(9):1495-1502.
319. Lindahl P, Gresser I, Leary P, Tovey M. Interferon treatment of mice: enhanced expression of histocompatibility antigens on lymphoid cells. *Proc Natl Acad Sci U S A.* 1976;73(4):1284-1287.
320. Tough DF, Sun S, Zhang X, Sprent J. Stimulation of naïve and memory T cells by cytokines. *Immunol Rev.* 1999;170:39-47.
321. Smyth MJ, Takeda K, Hayakawa Y, Peschon JJ, van den Brink MR, Yagita H. Nature's TRAIL--on a path to cancer immunotherapy. *Immunity.* 2003;18(1):1-6.
322. Takeda K, Smyth MJ, Cretney E, et al. Critical role for tumor necrosis factor-related apoptosis-inducing ligand in immune surveillance against tumor development. *J Exp Med.* 2002;195(2):161-169.
323. Kaido TJ, Maury C, Gresser I. Host CD4+ T lymphocytes are required for the synergistic action of interferon-alpha/beta and adoptively transferred immune cells in the inhibition of visceral ESb metastases. *Cancer Res.* 1995;55(24):6133-6139.
324. Ferrantini M, Giovarelli M, Modesti A, et al. IFN-alpha 1 gene expression into a metastatic murine adenocarcinoma (TS/A) results in CD8+ T cell-mediated tumor rejection and development of antitumor immunity. Comparative studies with IFN-gamma-producing TS/A cells. *J Immunol.* 1994;153(10):4604-4615.

325. Gresser I, Maury C, Carnaud C, De Maeyer E, Maunoury MT, Belardelli F. Anti-tumor effects of interferon in mice injected with interferon-sensitive and interferon-resistant Friend erythroleukemia cells. VIII. Role of the immune system in the inhibition of visceral metastases. *Int J Cancer.* 1990;46(3):468-474.
326. Gresser I, Kaido T, Maury C, Woodrow D, Moss J, Belardelli F. Interaction of IFN alpha/beta with host cells essential to the early inhibition of Friend erythroleukemia visceral metastases in mice. *Int J Cancer.* 1994;57(4):604-611.
327. Gresser I, Belardelli F, Maury C, Maunoury MT, Tovey MG. Injection of mice with antibody to interferon enhances the growth of transplantable murine tumors. *J Exp Med.* 1983;158(6):2095-2107.
328. Gresser I, Maury C, Vignaux F, Haller O, Belardelli F, Tovey MG. Antibody to mouse interferon alpha/beta abrogates resistance to the multiplication of Friend erythroleukemia cells in the livers of allogeneic mice. *J Exp Med.* 1988;168(4):1271-1291.
329. Sidky YA, Borden EC. Inhibition of angiogenesis by interferons: effects on tumor- and lymphocyte-induced vascular responses. *Cancer Res.* 1987;47(19):5155-5161.
330. Brouty-Boyé D, Zetter BR. Inhibition of cell motility by interferon. *Science.* 1980;208(4443):516-518.
331. Mocellin S, Pasquali S, Rossi CR, Nitti D. Interferon alpha adjuvant therapy in patients with high-risk melanoma: a systematic review and meta-analysis. *J Natl Cancer Inst.* 2010;102(7):493-501.
332. Gutterman JU. Cytokine therapeutics: lessons from interferon alpha. *Proc Natl Acad Sci U S A.* 1994;91(4):1198-1205.
333. Wadler S, Schwartz EL, Goldman M, et al. Fluorouracil and Recombinant Alfa-2a-Interferon - an Active Regimen against Advanced Colorectal-Carcinoma. *Journal of Clinical Oncology.* 1989;7(12):1769-1775.
334. Patt YZ, Yoffe B, Charnsangavej C, et al. Low serum alpha-fetoprotein level in patients with hepatocellular carcinoma as a predictor of response to 5-FU and interferon-alpha-2b. *Cancer.* 1993;72(9):2574-2582.
335. Obi S, Yoshida H, Toune R, et al. Combination therapy of intraarterial 5-fluorouracil and systemic interferon-alpha for advanced hepatocellular carcinoma with portal venous invasion. *Cancer.* 2006;106(9):1990-1997.
336. Katamura Y, Aikata H, Takaki S, et al. Intra-arterial 5-fluorouracil/interferon combination therapy for advanced hepatocellular carcinoma with or without three-dimensional conformal radiotherapy for portal vein tumor thrombosis. *Journal of Gastroenterology.* 2009;44(5):492-502.
337. Burnet M. Cancer: a biological approach. III. Viruses associated with neoplastic conditions. IV. Practical applications. *Br Med J.* 1957;1(5023):841-847.
338. Shankaran V, Ikeda H, Bruce AT, et al. IFNgamma and lymphocytes prevent primary tumour development and shape tumour immunogenicity. *Nature.* 2001;410(6832):1107-1111.
339. Dunn GP, Bruce AT, Ikeda H, Old LJ, Schreiber RD. Cancer immunoediting: from immunosurveillance to tumor escape. *Nat Immunol.* 2002;3(11):991-998.
340. Dunn GP, Bruce AT, Sheehan KC, et al. A critical function for type I interferons in cancer immunoediting. *Nat Immunol.* 2005;6(7):722-729.
341. Smyth MJ. Type I interferon and cancer immunoediting. *Nat Immunol.* 2005;6(7):646-648.
342. Hanahan D, Weinberg RA. The hallmarks of cancer. *Cell.* 2000;100(1):57-70.
343. Hanahan D, Weinberg RA. Hallmarks of cancer: the next generation. *Cell.* 2011;144(5):646-674.
344. Lambert G, Estévez-Salmeron L, Oh S, et al. An analogy between the evolution of drug resistance in bacterial communities and malignant tissues. *Nat Rev Cancer.* 2011;11(5):375-382.
345. Rösch F, Baum RP. Generator-based PET radiopharmaceuticals for molecular imaging of tumours: on the way to Theranostics. *Dalton Trans.* 2011;40(23):6104-6111.
346. Jonkers J, Berns A. Oncogene addiction: sometimes a temporary slavery. *Cancer Cell.* 2004;6(6):535-538.
347. Imai K, Takaoka A. Comparing antibody and small-molecule therapies for cancer. *Nat Rev Cancer.* 2006;6(9):714-727.
348. Hauschild A, Gogas H, Tarhini A, et al. Practical guidelines for the management of interferon-alpha-2b side effects in patients receiving adjuvant treatment for melanoma: Expert opinion. *Cancer.* 2008;112(5):982-994.

349. Antonini MG, Babudieri S, Maida I, et al. Incidence of neutropenia and infections during combination treatment of chronic hepatitis C with pegylated interferon alfa-2a or alfa-2b plus ribavirin. *Infection.* 2008;36(3):250-255.
350. Dusheiko G. Side effects of alpha interferon in chronic hepatitis C. *Hepatology.* 1997;26(3 Suppl 1):112S-121S.
351. Myint AM, Schwarz MJ, Steinbusch HW, Leonard BE. Neuropsychiatric disorders related to interferon and interleukins treatment. *Metab Brain Dis.* 2009;24(1):55-68.
352. Llovet JM, Sala M, Castells L, et al. Randomized controlled trial of interferon treatment for advanced hepatocellular carcinoma. *Hepatology.* 2000;31(1):54-58.
353. Sakon M, Nagano H, Dono K, et al. Combined intraarterial 5-fluorouracil and subcutaneous interferon-alpha therapy for advanced hepatocellular carcinoma with tumor thrombi in the major portal branches. *Cancer.* 2002;94(2):435-442.
354. Bornstein SR, Schuppenies A, Wong M-L, Licinio J. Approaching the shared biology of obesity and depression: the stress axis as the locus of gene-environment interactions. *Molecular Psychiatry.* 2006;11(10):892-902.
355. Ridder S, Chourbaji S, Hellweg R, et al. Mice with genetically altered glucocorticoid receptor expression show altered sensitivity for stress-induced depressive reactions. *Journal of Neuroscience.* 2005;25(26):6243-6250.
356. Ansorge M, Zhou M, Lira A, Hen R, Gingrich J. Early-life blockade of the 5-HT transporter alters emotional behavior in adult mice. *Science.* 2004;306(5697):879-881.
357. International Agency for Research on Cancer W. Globocan 2012: Estimated Cancer Incidence, Mortality and Prevalence Worldwide in 2012. 2012. Accessed 29/11/14.
358. WHO. GAR Hepatitis C. 2011; http://www.who.int/csr/disease/hepatitis/whocdscsrlyo2003/en/index3.html - HCV. Accessed 24/01/11, 2011.
359. Yu MC, Yuan JM, Lu SC. Alcohol, cofactors and the genetics of hepatocellular carcinoma. *J Gastroenterol Hepatol.* 2008;23 Suppl 1:S92-97.
360. Ozturk M. p53 mutation in hepatocellular carcinoma after aflatoxin exposure. *Lancet.* 1991;338(8779):1356-1359.
361. Lee JK, Kim JH, Shin HK. Therapeutic effects of the oriental herbal medicine Sho-saiko-to on liver cirrhosis and carcinoma. *Hepatol Res.* 2011;41(9):825-837.
362. ATCC. Hep G2 [HEPG2] (ATCC® HB-8065™). 2014; http://www.lgcstandards-atcc.org/products/all/HB-8065. Accessed 21/06/14.
363. Zhou X, Zhang M, Yung B, et al. Lactosylated liposomes for targeted delivery of doxorubicin to hepatocellular carcinoma. *Int J of Nanomedicine.* 2012;7:5465-5474.
364. Li Y, Huang G, Diakur J, Wiebe LI. Targeted Delivery of Macromolecular Drugs: Asialoglycoprotein Receptor (ASGPR) Expression by Selected Hepatoma Cell Lines used in Antiviral Drug Development. *Current Drug Delivery.* 2008;5(4):299-302.
365. Phelps ME. *PET : molecular imaging and its biological applications.* New York ; London: Springer; 2004.
366. Ruark AE. Positronium. *Physical Review.* 1945;68:278.
367. Cherry SR, Sorenson JA, Phelps ME. *Physics in nuclear medicine.* 3rd ed. ed. Philadelphia, Pa. ; [London]: W. B. Saunders; 2003.
368. Lauterbur PC. Image formation by induced local interactions. Examples employing nuclear magnetic resonance. 1973. *Clin Orthop Relat Res.* 1989(244):3-6.
369. Hand LN, Finch JD. *Analytical mechanics.* Cambridge: Cambridge University Press; 1998.
370. Kim EE. PET/MRI: Methodology and Clinical Applications. *Journal of nuclear medicine : official publication, Society of Nuclear Medicine.* 2014;55(12):2078.
371. Zaidi H, Ojha N, Morich M, et al. Design and performance evaluation of a whole-body Ingenuity TF PET-MRI system. *Physics in Medicine and Biology.* 2011;56(10):3091-3106.
372. Cumalat J, Cheung H, Hassed J, Smith B, Bross A. Effects of magnetic-fields on the light yield of scintillators. *Nuclear Instruments & Methods in Physics Research.* 1990;293(3):606-614.
373. Shao Y, Cherry S, Farahani K, et al. Simultaneous PET and MR imaging. *Physics in Medicine and Biology.* 1997;42(10):1965-1970.
374. Judenhofer MS, Wehrl HF, Newport DF, et al. Simultaneous PET-MRI: a new approach for functional and morphological imaging. *Nat Med.* 2008;14(4):459-465.
375. Loening AM, Gambhir SS. AMIDE: a free software tool for multimodality medical image analysis. *Molecular imaging.* 2003;2(3):131-137.

376. Ballinger JR. Re: Planar and SPECT imaging in the era of PET and PET-CT: can it survive the test of time? *Eur J Nucl Med Mol Imaging.* 2008;35(12):2340.
377. Alavi A, Basu S. Planar and SPECT imaging in the era of PET and PET-CT: can it survive the test of time? *Eur J Nucl Med Mol Imaging.* 2008;35(8):1554-1559.
378. Mariani G, Bruselli L, Duatti A. Is PET always an advantage versus planar and SPECT imaging? *Eur J Nucl Med Mol Imaging.* 2008;35(8):1560-1565.
379. Green MA, Welch MJ. Gallium radiopharmaceutical chemistry. *Int J Rad Appl Instrum B.* 1989;16(5):435-448.
380. Theobald T, et al. *Sampson's Textbook of Radiopharmacy.* 4 ed. London, UK: Pharmaceutical Press; 2011.
381. Velikyan I, Maecke H, Langstrom B. Convenient preparation of 68Ga-based PET-radiopharmaceuticals at room temperature. *Bioconjug Chem.* 2008;19(2):569-573.
382. Velikyan I. Prospective of Ga-68-Radiopharmaceutical Development. *Theranostics.* 2014;4(1):47-80.
383. Velikyan I. The diversity of (68)Ga-based imaging agents. *Recent Results in Cancer Research.* 2013;194:101-131.
384. McQueen JD, Abbassioun K. Cisternal brain scanning with positron emitting isotopes. *J Neurosurg.* 1968;29(6):597-602.
385. Rufini V, Calcagni ML, Baum RP. Imaging of neuroendocrine tumors. *Semin Nucl Med.* 2006;36(3):228-247.
386. Antunes P, Ginj M, Zhang H, et al. Are radiogallium-labelled DOTA-conjugated somatostatin analogues superior to those labelled with other radiometals? *Eur J Nucl Med Mol Imaging.* 2007;34(7):982-993.
387. Wild D, Schmitt JS, Ginj M, et al. DOTA-NOC, a high-affinity ligand of somatostatin receptor subtypes 2, 3 and 5 for labelling with various radiometals. *Eur J Nucl Med Mol Imaging.* 2003;30(10):1338-1347.
388. Eisenwiener KP, Prata MI, Buschmann I, et al. NODAGATOC, a new chelator-coupled somatostatin analogue labeled with [67/68Ga] and [111In] for SPECT, PET, and targeted therapeutic applications of somatostatin receptor (hsst2) expressing tumors. *Bioconjug Chem.* 2002;13(3):530-541.
389. de Jong M, Breeman WA, Bernard BF, et al. Tumor response after [(90)Y-DOTA(0),Tyr(3)]octreotide radionuclide therapy in a transplantable rat tumor model is dependent on tumor size. *J Nucl Med.* 2001;42(12):1841-1846.
390. de Jong M, Breeman WA, Bernard BF, et al. [177Lu-DOTA(0),Tyr3] octreotate for somatostatin receptor-targeted radionuclide therapy. *Int J Cancer.* 2001;92(5):628-633.
391. de Jong M, Breeman WA, Valkema R, Bernard BF, Krenning EP. Combination radionuclide therapy using 177Lu- and 90Y-labeled somatostatin analogs. *J Nucl Med.* 2005;46 Suppl 1:13S-17S.
392. Liu Z, Niu G, Shi J, Liu S, Wang F, Chen X. (68)Ga-labeled cyclic RGD dimers with Gly3 and PEG4 linkers: promising agents for tumor integrin alphavbeta3 PET imaging. *Eur J Nucl Med Mol Imaging.* 2009;36(6):947-957.
393. Jeong JM, Hong MK, Chang YS, et al. Preparation of a promising angiogenesis PET imaging agent: 68Ga-labeled c(RGDyK)-isothiocyanatobenzyl-1,4,7-triazacyclononane-1,4,7-triacetic acid and feasibility studies in mice. *J Nucl Med.* 2008;49(5):830-836.
394. Li ZB, Chen K, Chen X. (68)Ga-labeled multimeric RGD peptides for microPET imaging of integrin alpha(v)beta (3) expression. *Eur J Nucl Med Mol Imaging.* 2008;35(6):1100-1108.
395. Karacay H, Sharkey RM, Gold DV, et al. Pretargeted radioimmunotherapy of pancreatic cancer xenografts: TF10-90Y-IMP-288 alone and combined with gemcitabine. *J Nucl Med.* 2009;50(12):2008-2016.
396. Goldenberg DM, Rossi EA, Sharkey RM, McBride WJ, Chang CH. Multifunctional antibodies by the Dock-and-Lock method for improved cancer imaging and therapy by pretargeting. *J Nucl Med.* 2008;49(1):158-163.
397. Sharkey RM, McBride WJ, Karacay H, et al. A universal pretargeting system for cancer detection and therapy using bispecific antibody. *Cancer Res.* 2003;63(2):354-363.
398. Sharkey RM, Goldenberg DM. Novel radioimmunopharmaceuticals for cancer imaging and therapy. *Curr Opin Investig Drugs.* 2008;9(12):1302-1316.
399. Klivényi G, Schuhmacher J, Patzelt E, et al. Gallium-68 chelate imaging of human colon carcinoma xenografts pretargeted with bispecific anti-CD44V6/anti-gallium chelate antibodies. *J Nucl Med.* 1998;39(10):1769-1776.

400. Schuhmacher J, Klivényi G, Kaul S, et al. Pretargeting of human mammary carcinoma xenografts with bispecific anti-MUC1/anti-Ga chelate antibodies and immunoscintigraphy with PET. *Nucl Med Biol.* 2001;28(7):821-828.
401. Goodwin DA. Tumor pretargeting: almost the bottom line. *J Nucl Med.* 1995;36(5):876-879.
402. Baes CF, Mesmer RE. *The hydrolysis of cations.* New York ; London: Wiley-Interscience; 1976.
403. Moerlein SM, Welch MJ. The chemistry of gallium and indium as related to radiopharmaceutical production. *Int J Nucl Med Biol.* 1981;8(4):277-287.
404. Markiv A, Anani B, Durvasula RV, Kang AS. Module based antibody engineering: A novel synthetic REDantibody. *Journal of Immunological Methods.* 2011;364(1-2):40-49.
405. Lewis MR, Reichert DE, Laforest R, et al. Production and purification of gallium-66 for preparation of tumor-targeting radiopharmaceuticals. *Nucl Med Biol.* 2002;29(6):701-706.
406. Yamamoto F, Tsukamoto E, Nakada K, et al. 18F-FDG PET is superior to 67Ga SPECT in the staging of non-Hodgkin's lymphoma. *Ann Nucl Med.* 2004;18(6):519-526.
407. Maecke HR, Andre JP. 68Ga-PET radiopharmacy: A generator-based alternative to 18F-radiopharmacy. *Ernst Schering Res Found Workshop.* 2007(62):215-242.
408. Paans AM, van Waarde A, Elsinga PH, Willemsen AT, Vaalburg W. Positron emission tomography: the conceptual idea using a multidisciplinary approach. *Methods.* 2002;27(3):195-207.
409. Wadsak W, Mitterhauser M. Basics and principles of radiopharmaceuticals for PET/CT. *Eur J Radiol.* 2010;73(3):461-469.
410. Miller PW, Long NJ, Vilar R, Gee AD. Synthesis of 11C, 18F, 15O, and 13N radiolabels for positron emission tomography. *Angew Chem Int Ed Engl.* 2008;47(47):8998-9033.
411. Miller PW. Radiolabelling with short-lived PET (positron emission tomography) isotopes using microfluidic reactors. *J Chem Technol Biot.* 2009;84(3):309-315.
412. Wadas TJ, Wong EH, Weisman GR, Anderson CJ. Coordinating radiometals of copper, gallium, indium, yttrium, and zirconium for PET and SPECT imaging of disease. *Chem Rev.* 2010;110(5):2858-2902.
413. Verel I, Visser GW, Boerman OC, et al. Long-lived positron emitters zirconium-89 and iodine-124 for scouting of therapeutic radioimmunoconjugates with PET. *Cancer Biother Radiopharm.* 2003;18(4):655-661.
414. Vosjan MJ, Perk LR, Visser GW, et al. Conjugation and radiolabeling of monoclonal antibodies with zirconium-89 for PET imaging using the bifunctional chelate p-isothiocyanatobenzyl-desferrioxamine. *Nat Protoc.* 2010;5(4):739-743.
415. Blower PJ, Lewis JS, Zweit J. Copper radionuclides and radiopharmaceuticals in nuclear medicine. *Nucl Med Biol.* 1996;23(8):957-980.
416. Lucignani G. Labeling peptides with PET radiometals: Vulcan's forge. *Eur J Nucl Med Mol Imaging.* 2008;35(1):209-215.
417. Cai W, Chen K, He L, Cao Q, Koong A, Chen X. Quantitative PET of EGFR expression in xenograft-bearing mice using 64Cu-labeled cetuximab, a chimeric anti-EGFR monoclonal antibody. *Eur J Nucl Med Mol Imaging.* 2007;34(6):850-858.
418. Maecke HR, André JP. 68Ga-PET radiopharmacy: A generator-based alternative to 18F-radiopharmacy. *Ernst Schering Res Found Workshop.* 2007(62):215-242.
419. Zolle I. *Technetium-99m pharmaceuticals : preparation and quality control in nuclear medicine.* Berlin: Springer; 2007.
420. Yano Y, Anger HO. A Gallium-68 Positron Cow for Medical Use. *J Nucl Med.* 1964;5:484-487.
421. Gleason GI. A positron cow. *Int J Appl Radiat Isot.* 1960;8:90-94.
422. Meyer GJ, Mäcke H, Schuhmacher J, Knapp WH, Hofmann M. 68Ga-labelled DOTA-derivatised peptide ligands. *Eur J Nucl Med Mol Imaging.* 2004;31(8):1097-1104.
423. Velikyan I, Beyer GJ, Långström B. Microwave-supported preparation of (68)Ga bioconjugates with high specific radioactivity. *Bioconjug Chem.* 2004;15(3):554-560.
424. Zhernosekov KP, Filosofov DV, Baum RP, et al. Processing of generator-produced 68Ga for medical application. *J Nucl Med.* 2007;48(10):1741-1748.
425. Asti M, De Pietri G, Fraternali A, et al. Validation of (68)Ge/(68)Ga generator processing by chemical purification for routine clinical application of (68)Ga-DOTATOC. *Nucl Med Biol.* 2008;35(6):721-724.
426. Breeman WA, de Jong M, de Blois E, Bernard BF, Konijnenberg M, Krenning EP. Radiolabelling DOTA-peptides with 68Ga. *Eur J Nucl Med Mol Imaging.* 2005;32(4):478-485.

427. Decristoforo C, Knopp R, von Guggenberg E, et al. A fully automated synthesis for the preparation of 68Ga-labelled peptides. *Nucl Med Commun.* 2007;28(11):870-875.
428. *Production of long lived parent radionuclides for generators: \2076\2078Ge, \2078²Sr, \2079\2070Sr and ¹\2078\2078W.* Vienna: International Atomic Energy Agency; 2010.
429. Wackers FJT, Bruni W, Zaret BL. *Nuclear cardiology, the basics : how to set up and maintain a laboratory.* 2nd ed. ed. Totowa, N.J.: Humana; 2008.
430. Browne E, Firestone RB, Shirley VS. *Table of radioactive isotopes.* New York ; Chichester: Wiley; 1986.
431. Filosofov D, Loktionova N, Rosch F. A Ti-44/Sc-44 radionuclide generator for potential application of Sc-44-based PET-radiopharmaceuticals. *Radiochimica Acta.* 2010;98(3):149-156.
432. Loktionova N, Filosofov D, Pruszynski M, Majkowska A, Rosch F. Ti-44/Sc-44 Generator and synthesis of Sc-44-DOTA-TOC. *Nuclear Medicine and Biology.* 2010;37(6):718-718.
433. Zeisler SK, Becker DW, Pavan RA, Moschel R, Ruhle H. A water-cooled spherical niobium target for the production of [18F]fluoride. *Appl Radiat Isot.* 2000;53(3):449-453.
434. Fani M, André JP, Maecke HR. 68Ga-PET: a powerful generator-based alternative to cyclotron-based PET radiopharmaceuticals. *Contrast Media Mol Imaging.* 2008;3(2):67-77.
435. Stimmel JB, Stockstill ME, Kull FC, Jr. Yttrium-90 chelation properties of tetraazatetraacetic acid macrocycles, diethylenetriaminepentaacetic acid analogues, and a novel terpyridine acyclic chelator. *Bioconjug Chem.* 1995;6(2):219-225.
436. Camera L, Kinuya S, Garmestani K, et al. Evaluation of the serum stability and in vivo biodistribution of CHX-DTPA and other ligands for yttrium labeling of monoclonal antibodies. *J Nucl Med.* 1994;35(5):882-889.
437. McMurry TJ, Pippin CG, Wu C, et al. Physical parameters and biological stability of yttrium(III) diethylenetriaminepentaacetic acid derivative conjugates. *J Med Chem.* 1998;41(18):3546-3549.
438. Li Y, Martell AE, Hancock RD, Reibenspies JH, Anderson CJ, Welch MJ. N,N'-Ethylenedi-L-cysteine (EC) and Its Metal Complexes: Synthesis, Characterization, Crystal Structures, and Equilibrium Constants. *Inorg Chem.* 1996;35(2):404-414.
439. Jung WS, Chung YK, Shin DM, Kim SD. Crystal- and solution-structure characteristics of ethylene-diaminetetraacetatoaluminate(III) and gallate(III). *B Chem Soc Jpn.* 2002;75(6):1263-1267.
440. Eder M, Wangler B, Knackmuss S, et al. Tetrafluorophenolate of HBED-CC: a versatile conjugation agent for Ga-68-labeled small recombinant antibodies. *Eur J Nucl Med Mol I.* 2008;35(10):1878-1886.
441. Blend MJ, Stastny JJ, Swanson SM, Brechbiel MW. Labeling anti-HER2/neu monoclonal antibodies with In-111 and Y-90 using a bifunctional DTPA chelating agent. *Cancer Biother Radio.* 2003;18(3):355-363.
442. Berry DJ, Ma Y, Ballinger JR, et al. Efficient bifunctional gallium-68 chelators for positron emission tomography: tris(hydroxypyridinone) ligands. *Chem Commun (Camb).* 2011;47(25):7068-7070.
443. Ferreira CL, Lamsa E, Woods M, et al. Evaluation of Bifunctional Chelates for the Development of Gallium-Based Radiopharmaceuticals. *Bioconjug Chem.* 2010.
444. Notni J, Simecek J, Hermann P, Wester H-J. TRAP, a Powerful and Versatile Framework for Gallium-68 Radiopharmaceuticals. *Chemistry-A European Journal.* 2011;17(52):14718-14722.
445. Brom M, Joosten L, Laverman P, et al. Preclinical evaluation of 68Ga-DOTA-minigastrin for the detection of cholecystokinin-2/gastrin receptor-positive tumors. *Mol Imaging.* 2011;10(2):144-152.
446. Brom M, Oyen WJ, Joosten L, Gotthardt M, Boerman OC. 68Ga-labelled exendin-3, a new agent for the detection of insulinomas with PET. *Eur J Nucl Med Mol Imaging.* 2010;37(7):1345-1355.
447. Heppeler A, Froidevaux S, Eberle AN, Maecke HR. Receptor targeting for tumor localisation and therapy with radiopeptides. *Curr Med Chem.* 2000;7(9):971-994.
448. Smith-Jones PM, Solit DB, Akhurst T, Afroze F, Rosen N, Larson SM. Imaging the pharmacodynamics of HER2 degradation in response to Hsp90 inhibitors. *Nat Biotechnol.* 2004;22(6):701-706.
449. Smith-Jones PM, Vallabahajosula S, Goldsmith SJ, et al. In vitro characterization of radiolabeled monoclonal antibodies specific for the extracellular domain of prostate-specific membrane antigen. *Cancer Res.* 2000;60(18):5237-5243.

450. Motekaitis RJ, Rogers BE, Reichert DE, Martell AE, Welch MJ. Stability and Structure of Activated Macrocycles. Ligands with Biological Applications. *Inorg Chem.* 1996;35(13):3821-3827.
451. Moore D, Fanwick P, Welch M. Synthesis, characterization, and solid-state structure of a new hexachelating ligand and its complex with gallium(III). *Inorganic Chemistry.* 1989;28(8):1504-1506.
452. Moore DA, Fanwick PE, Welch MJ. A novel hexachelating amino thiol ligand and its complex with gallium(III). *Inorganic Chemistry.* 1990;29(4):672-676.
453. Broan CJ, Cox JPL, Craig AS, et al. Structure and Solution Stability of Indium and Gallium Complexes of 1,4,7-Triazacyclononanetriacetate and of Yttrium Complexes of 1,4,7,10-Tetraazacyclododecanetetraacetate and Related Ligands - Kinetically Stable Complexes for Use in Imaging and Radioimmunotherapy - X-Ray Molecular-Structure of the Indium and Gallium Complexes of 1,4,7-Triazacyclononane-1,4,7-Triacetic Acid. *Journal of the Chemical Society-Perkin Transactions 2.* 1991(1):87-99.
454. Clarke ET, Martell AE. Stabilities of the Fe(III), Ga(III) and in(III) Chelates of N,N',N''-Triazacyclononanetriacetic Acid. *Inorganica Chimica Acta.* 1991;181(2):273-280.
455. Podhradsky D, Drobnica L, Kristian P. Reactions of cysteine, its derivatives, glutathione, coenzyme-A, and dihydrolipoic acid with isothiocyanates. *Experientia.* 1979;35(2):154-155.
456. Eder M, Krivoshein AV, Backer M, Backer JM, Haberkorn U, Eisenhut M. ScVEGF-PEG-HBED-CC and scVEGF-PEG-NOTA conjugates: comparison of easy-to-label recombinant proteins for [Ga-68]PET imaging of VEGF receptors in angiogenic vasculature. *Nuclear Medicine and Biology.* 2010;37(4):405-412.
457. Backer MV, Levashova Z, Patel V, et al. Molecular imaging of VEGF receptors in angiogenic vasculature with single-chain VEGF-based probes. *Nature Medicine.* 2007;13(4):504-509.
458. Hermanson GT. *Bioconjugate techniques.* Third edition. ed. London ; Waltham, MA: Elsevier/AP; 2013.
459. Maeda H, Ishida N, Kawauchi H, Tsujimura K. Reaction of fluorescein-isothiocyanate with proteins and amino acids. I. Covalent and non-covalent binding of fluorescein-isothiocyanate and fluorescein to proteins. *J Biochem.* 1969;65(5):777-783.
460. Rana TM, Meares CF. N-Terminal Modification of Immunoglobulin Polypeptide Chains Tagged with Isothiocyanato Chelates. *Bioconjugate Chemistry.* 1990;1(5):357-362.
461. Wu CC, Jagoda E, Brechbiel M, et al. Biodistribution and catabolism of Ga-67-labeled anti-Tac dsFv fragment. *Bioconjugate Chemistry.* 1997;8(3):365-369.
462. Mirzadeh S, Brechbiel MW, Atcher RW, Gansow OA. Radiometal Labeling of Immunoproteins: Covalent Linkage of 2-(4-Isothiocyanatobenzyl)diethylenetriaminepentaacetic Acid Ligands to Immunoglobulin. *Bioconjugate Chemistry.* 1990;1(1):59-65.
463. Mohsin H, Fitzsimmons J, Shelton T, et al. Preparation and biological evaluation of In-111-, Lu-177- and Y-90-labeled DOTA analogues conjugated to B72.3. *Nuclear Medicine and Biology.* 2007;34(5):493-502.
464. Lu S, Takach E, Solomon M, Zhu Q, Law S, Hsieh F. Mass spectral analyses of labile DOTA-NHS and heterogeneity determination of DOTA or DM1 conjugated anti-PSMA antibody for prostate cancer therapy. *Journal of Pharmaceutical Sciences.* 2005;94(4):788-797.
465. Cuatreca P, Parikh I. Adsorbents for affinity chromatography - use of N-hydroxysuccinimide esters of agarose. *Biochemistry.* 1972;11(12):2291.
466. McMurry J. *Organic chemistry.* 6th ed. Belmont, CA: Thomson-Brooks/Cole; 2004.
467. Kobayashi S, Ueda Y. Comparing Protein A Resins for Monoclonal Antibody Purification. *Biopharm International.* 2013;26(12):28-31.
468. Wieghardt K, Bossek U, Chaudhuri P, Herrmann W, Menke B, Weiss J. 1,4,7-triazacyclononane-n,n',n''-triacetate (TCTA), a hexadentate ligand for divalent and trivalent metal-ions - crystal-structures of [CrIII(TCTA)], [FeIII(TCTA)], and Na[CuII(TCTA)].2NaBr.8H2O. *Inorganic Chemistry.* 1982;21(12):4308-4314.
469. Thomas C, Moraga I, Levin D, et al. Structural Linkage between Ligand Discrimination and Receptor Activation by Type I Interferons. *Cell.* 2011;146(4):621-632.
470. Massa S, Xavier C, De Vos J, et al. Site-Specific Labeling of Cysteine-Tagged Camelid Single-Domain Antibody-Fragments for Use in Molecular Imaging. *Bioconjug Chem.* 2014;25(5):979-988.

471. Treichel U, Schreiter T, Zumbuschenfelde K, Stockert R. High-yield purification and characterization of human asialoglycoprotein receptor. *Protein Expression and Purification.* 1995;6(3):251-255.
472. Flores MV, Hickling TP, Sreckovic S, et al. Preclinical studies of PF-04849285, an interferon-alpha 8 fusion protein for the treatment of HCV. *Antivir Ther.* 2012;17(5):869-881.
473. Gainkam LOT, Caveliers V, Devoogdt N, et al. Localization, mechanism and reduction of renal retention of technetium-99m labeled epidermal growth factor receptor-specific nanobody in mice. *Contrast Media & Molecular Imaging.* 2011;6(2):85-92.
474. Lee J, Garmestani K, Wu C, et al. In vitro and in vivo evaluation of structure-stability relationship of In-111- and Ga-67-labeled antibody via 1B4M or C-NOTA chelates. *Nuclear Medicine and Biology.* 1997;24(3):225-230.
475. Shetty D, Lee Y-S, Jeong JM. (68)Ga-labeled radiopharmaceuticals for positron emission tomography. *Nuclear Medicine and Molecular Imaging.* 2010;44(4):233-240.
476. Stordeur P, Poulin L, Craciun L, et al. Cytokine mRNA quantification by real-time PCR. *Journal of Immunological Methods.* 2002;259(1-2):55-64.
477. Colina R, Costa-Mattioli M, Dowling RJO, et al. Translational control of the innate immune response through IRF-7. *Nature.* 2008;452(7185):323-U322.
478. Srougi MC, Burridge K. The Nuclear Guanine Nucleotide Exchange Factors Ect2 and Net1 Regulate RhoB-Mediated Cell Death after DNA Damage. *PLoS ONE.* 2011;6(2).
479. Zhang J, Liu X, Bell A, et al. Transient expression and purification of chimeric heavy chain antibodies. *Protein Expression and Purification.* 2009;65(1):77-82.
480. Jaeger V, Buessow K, Wagner A, et al. High level transient production of recombinant antibodies and antibody fusion proteins in HEK293 cells. *BMC Biotechnology.* 2013;13.
481. Foerster C, Schubert M, Pietzsch H-J, Steinbach J. Maleimido-Functionalized NOTA Derivatives as Bifunctional Chelators for Site-Specific Radiolabeling. *Molecules.* 2011;16(6):5228-5240.
482. Tolmachev V, Altai M, Sandstrom M, et al. Evaluation of a Maleimido Derivative of NOTA for Site-Specific Labeling of Affibody Molecules. *Bioconjugate Chem.* 2011;22(5):894-902.
483. Lyon RP, Setter JR, Bovee TD, et al. Self-hydrolyzing maleimides improve the stability and pharmacological properties of antibody-drug conjugates. *Nat Biotechnol.* 2014;32(10):1059-1062.
484. Mueller D, Klette I, Baum RP. Purification and labeling strategies for (68)Ga from (68)Ge/(68)Ga generator eluate. *Recent results in cancer research. Fortschritte der Krebsforschung. Progres dans les recherches sur le cancer.* 2013;194:77-87.
485. Roesch F. Scandium-44: benefits of a long-lived PET radionuclide available from the (44)Ti/(44)Sc generator system. *Curr Radiopharm.* 2012;5(3):187-201.
486. Hoffend J, Mier W, Schuhmacher J, et al. Gallium-68-DOTA-albumin as a PET blood-pool marker: experimental evaluation in vivo. *Nucl Med and Biol.* 2005;32(3):287-292.
487. Dandekar M, Tseng JR, Gambhir SS. Reproducibility of F-18-FDG microPET studies in mouse tumor xenografts. *Journal of Nuclear Medicine.* 2007;48(4):602-607.
488. Bertotti A, Migliardi G, Galimi F, et al. A Molecularly Annotated Platform of Patient-Derived Xenografts ("Xenopatients") Identifies HER2 as an Effective Therapeutic Target in Cetuximab-Resistant Colorectal Cancer. *Cancer Discovery.* 2011;1(6):508-523.
489. Olafsen T, Kenanova V, Sundaresan G, et al. Optimizing radiolabeled engineered anti-p185(HER2) antibody fragments for in vivo imaging. *Cancer Res.* 2005;65(13):5907-5916.
490. Adams G, Schier R, McCall A, et al. Prolonged in vivo tumour retention of a human diabody targeting the extracellular domain of human HER2/neu. *British Journal of Cancer.* 1998;77(9):1405-1412.
491. Wang B, Chen Y, Ayalon O, Bender J, Garen A. Human single-chain Fv immunoconjugates targeted to a melanoma-associated chondroitin sulfate proteoglycan mediate specific lysis of human melanoma cells by natural killer cells and complement. *Proc Natl Acad Sci U S A.* 1999;96(4):1627-1632.
492. Borsi L, Balza E, Carnemolla B, et al. Selective targeted delivery of TNF alpha to tumor blood vessels. *Blood.* 2003;102(13):4384-4392.
493. Schultz MK, Mueller D, Baum RP, Watkins GL, Breeman WAP. A new automated NaCl based robust method for routine production of gallium-68 labeled peptides. *Applied Radiation and Isotopes.* 2013;76:46-54.
494. Müller D, Zentralklinik Bad Berka Gmbh. Method and Kit for Preparing a Radiopharmaceutical. U.S. Patent Application US20130310537 A1. 2013/11/21.